A general study of electroabsorption on semi-insulating solids

Muhamad, M. Rasat

Muhamad, M. Rasat (1981) *A general study of electroabsorption on semi-insulating solids*, Durham theses, Durham University. Available at Durham E-Theses Online: http://etheses.dur.ac.uk/7412/

A GENERAL STUDY OF ELECTROABSORPTION

ON SEMI-INSULATING SOLIDS

By

M. RASAT MUHAMAD, B.Sc.

A Thesis submitted to the
University of Durham in Application for the
Degree of Doctor of Philosophy

October 1981.

ABSTRACT

The electroabsorption technique has been used to study the properties of a wide range of semi-insulating materials including CdTe:Cl single crystals, solid solutions of CdS-ZnS, amorphous silicon and polymerized diacetylene Langmuir films. The small change in a sample's optical transmission consequent upon the application of large electric fields has been carefully recorded using phase-sensitive detection equipment.

Measurements on CdTe:Cl samples have established an experimental procedure to cope with the complications of photoconductivity and space charge effects. The electroabsorption spectra in this material are interpreted in terms of the Franz-Keldysh effect, thus allowing the calculation of the reduced effective mass. The result is in good agreement with published data obtained using other methods.

In solid solutions of CdS-ZnS, the observed exciton electroabsorption has been analysed within the context of the Stark theory. This enables the lowest bound exciton states to be located precisely and results the determination of the reduced effective mass of the exciton which is found to vary linearly with the band gap as predicted theoretically.

Electroabsorption spectra for α-Si indicate that only transitions involving localized states respond to electric field modulation. These spectra, which are preparation dependent, have also been interpreted in terms of the Stark effect. An interesting result obtained for glow discharge produced samples has been interpreted in terms of an effective change in the mobility edge with temperature.

The final material discussed in the thesis is the diacetylene molecule; the films were prepared using the Langmuir trough technique developed in Durham. Interpretation of the electroabsorption data for the red polymer form has led to our calculating the static polarizability change between the excited and ground states in this molecule.

The thesis concludes with a summary of possible applications of the electroabsorption technique and suggestions as to how the present work could be extended.

ACKNOWLEDGEMENTS

I gratefully acknowledge the assistance of the large number of people who have helped make this thesis possible. In particular, I would like to thank my supervisor, Professor G. G. Roberts, for his constant advice and encouragement. I am indebted to Dr. M. C. Petty and all other members of the group for their help and useful discussions ; the expert knowledge and skills of the workshop staff, headed by Mr. F. Spence, have been invaluable. In addition, I would like to thank Dr. J.B. Mullin of the Royal Signals and Radar Establishment, Dr. J. Woods and Dr. G.J. Russell of Durham University, Professor W.E. Spear of Dundee University, and Dr. R. A. Street of Xerox Corp.,Palo Alto, for the provision of samples.

I gratefully acknowledge financial support from the University of Malaya and the Government of Malaysia. I also gratefully acknowledge Mrs. S. Mellanby for her advice and patience whilst typing this thesis.

Finally, I am deeply indebted to my parents distant encouragement.

CONTENTS

Chapter 2 THEORETICAL BACKGROUND

Pages

Chapter 3 EXPERIMENTAL TECHNIQUE

Chapter 4 ELECTROABSORPTION IN CADMIUM TELLURIDE

Chapter 5 ELECTROABSORPTION IN SOLID SOLUTIONS OF $Cd_xZn_{1-x}S$

Pages

Chapter 6 ELECTROABSORPTION STUDIES IN AMORPHOUS SILICON

Chapter 7 ELECTROABSORPTION STUDIES IN DIACETYLENE LANGMUIR FILMS

Chapter 8 CONCLUSIONS AND SUGGESTIONS FOR FURTHER WORK

CHAPTER 1

INTRODUCTION

Sixteen years after Zeeman performed his classic experiments showing the splitting of spectral lines in a magnetic field, Stark(1) and Surdo(2), working independently, discovered that a similar effect was present when a spectral source was placed in an electric field. The interpretation of these early experiments on, for example, the Balmer series of hydrogen, is relatively straightforward. Less well understood are the results of equivalent measurements on molecules in a crystalline environment. The linear Stark effect is only observed in those materials possessing a permanent dipole moment. More commonly, scientists have turned their attention to measuring the small changes introduced when the electric field induces a dipole moment - the so-called quadratic Stark effect.

In inorganic crystals where the electrons are relatively mobile, another effect is produced by the electric field. In this case, interband transitions are affected and the small perturbation in the absorption coefficient is termed the Franz(3)-Keldysh(4) effect. The magnitude of change in both cases, the Stark and Franz-Keldysh effects, is extremely small and for the majority of materials, phase-sensitive techniques are required to detect the electroabsorption signal. The method is now well established in modulation spectroscopy but as will be explained in this thesis, great care must be taken to ensure that the data obtained are not due to spurious effects.

The electroabsorption technique has turned out to be a very powerful experimental tool in obtaining information concerning singularities in the energy band structure. It has been used to a lesser extent to learn about impurity state symmetry in crystals and phonon spectra and band tailing effects in disordered solids. In inorganic semiconductors, it is possible to determine the reduced effective mass of the charge carriers. In molecular crystals, where the effective mass formulation breaks down, it is then possible to calculate the static polarizability change between the excited and ground states of the material.

The main objective of this thesis is to demonstrate the versatility of this electric field modulation technique. This has been achieved by studying the change in absorption coefficient introduced when voltages are applied to a wide range of technologically important materials. These include (1) semi-insulating single crystals of CdTe, (2) solid solutions of the II-VI alloy system CdS-ZnS, (3) amorphous films of silicon produced by two different methods, and (4) polymerised diacetylene Langmuir films. Separate chapters are devoted to all of these topics and each exemplifies a particular strength of the technique.

The required theoretical background to the subject is presented in Chapter 2 ; this contains both a brief review of optical absorption mechanisms in solids and a summary of current electroabsorption theory. The experimental technique is described in Chapter 3. Considerable effort has been devoted to developing the instrumentation so that the experimental data so obtained are accurate and may be ascribed purely to the electric field effect. Results on CdTe:Cl are presented in Chapter 4 and are mainly aimed at calculating the reduced effective mass in this material. In addition certain experimental complications including non-uniform field distributions, space charge injection, photo-conductivity effects, and the existence of harmonics in the electroabsorption signal are examined. This particular chapter discusses the various remedies for coping with these complications. Electroabsorption studies in $Cd_xZn_{1-x}S$ are described in Chapter 5 ; these data have been used to study exciton effects in this alloy system. They enable us to calculate for the first time using the electroabsorption technique how the exciton reduced effective mass varies with the alloy component. Chapter 6 is very topical in that it is devoted to electroabsorption studies in the commercially important semiconductor-amorphous silicon. Emphasis is placed on the subtle differences in electroabsorption spectra observed with α-Si obtained from different sources. In the following chapter we describe only the second report to date of electroabsorption studies on Langmuir-Blodgett films. These multilayer films produced by assembling one monolayer on top of another, are ideally suited to our experimental technique. Chapter 7 concentrates on the results we have obtained for the interesting diacetylene molecule. The thesis concludes with a chapter summarizing the most important results obtained during the course of the work and some suggestions for further study.

CHAPTER 2

THEORETICAL BACKGROUND

2.1 INTRODUCTION

The main objective of this work is to study the effect of a large electric field on the optical absorption of some semi-insulating solids. It is therefore necessary to review certain important aspects of the optical absorption mechanism in these systems. This chapter is devoted to this discussion. A survey of optical absorption in crystalline, non-crystalline, and organic molecular solids will in turn be presented in sections 2.2, 2.3 and 2.4, respectively.

In general, there are two mechanisms responsible for absorption of electromagnetic radiation in solids. The first, arising from the acceleration of free carriers by the oscillating electric field, is known as free carrier absorption. The second mechanism is due to excitation of electrons from a valence band to a conduction band or to bound electron-hole states (excitons), and is known as interband or fundamental absorption. Since this work involves only absorption of the second type, this discussion is therefore restricted to the second mechanism only.

2.2 OPTICAL ABSORPTION IN CRYSTALLINE SOLIDS

A study of optical absorption can provide valuable information concerning the band structure of a material. A transition which involves only an optical photon, producing negligible change in the wavevector of the electron, is called a direct transition. If however a photon and one or more phonons are involved, producing a change in the wavevector by the wavevector of the phonon, the transition is called an indirect transition. The limiting factor is that momentum must be conserved in each process.

2.2.1 Direct Transition

This type of transition is pictured as a vertical transition in an E versus k diagram, as shown in Fig 2.1a where the maximum of the valence band and the minimum of the conduction band occur at the same momentum value. The transition at that point is said to be direct allowed and the value of absorption constant increases very rapidly at the energy corresponding to the band gap of the material as illustrated in Fig 2.1b. A large number of materials such as indium phosphide, gallium arsenide and indium antimonide exhibit this property.

For a given photon energy, the absorption coefficient is directly proportional to the density of electrons in the initial states and the density of available final sites. It is also directly proportional to the transitional probability between the initial and final states. In some materials, the transitional probability vanishes at k = 0 due to the relative symmetry of the wavefunction. The transitions are then said to be forbidden at k = 0 but can be allowed at $k \neq 0$, since away from k = 0 the wavefunctions are modified by the interaction between bands.

For direct transitions involving simple parabolic bands, it can be shown that (1)

$$\alpha n_o \hbar\omega = \text{const.}(\hbar\omega - E_g)^m \tag{2.1}$$

where α is the absorption coefficient at photon energy $\hbar\omega$, n_o is the refractive index and E_g is the optical band gap of the material. The value of m equals $\frac{1}{2}$ for an allowed transition and $\frac{3}{2}$ for a forbidden transition as shown in Fig 2.2.

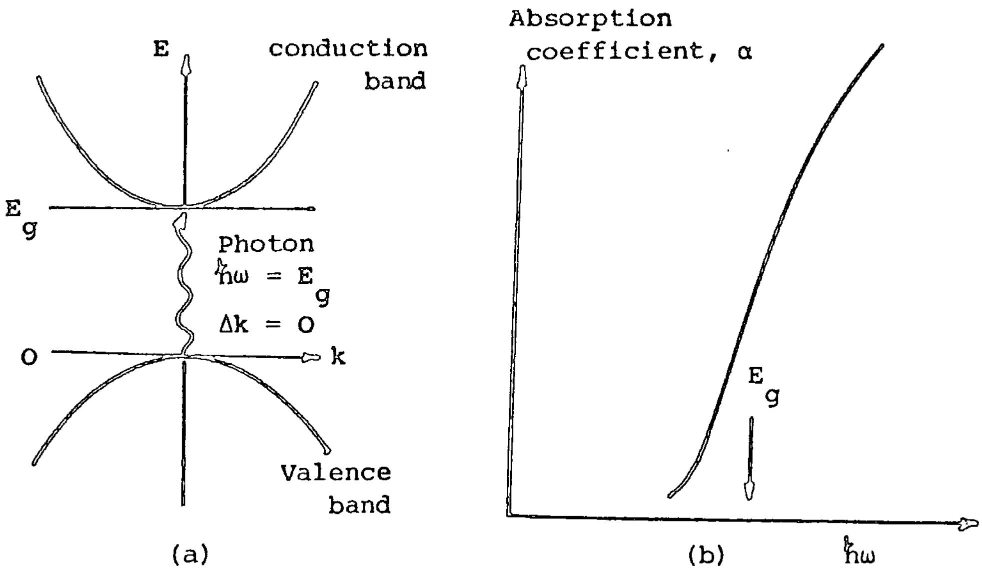

Fig 2.1 (a) Excitation across a direct band gap by photon absorption, and

(b) The absorption spectrum of a direct band gap.

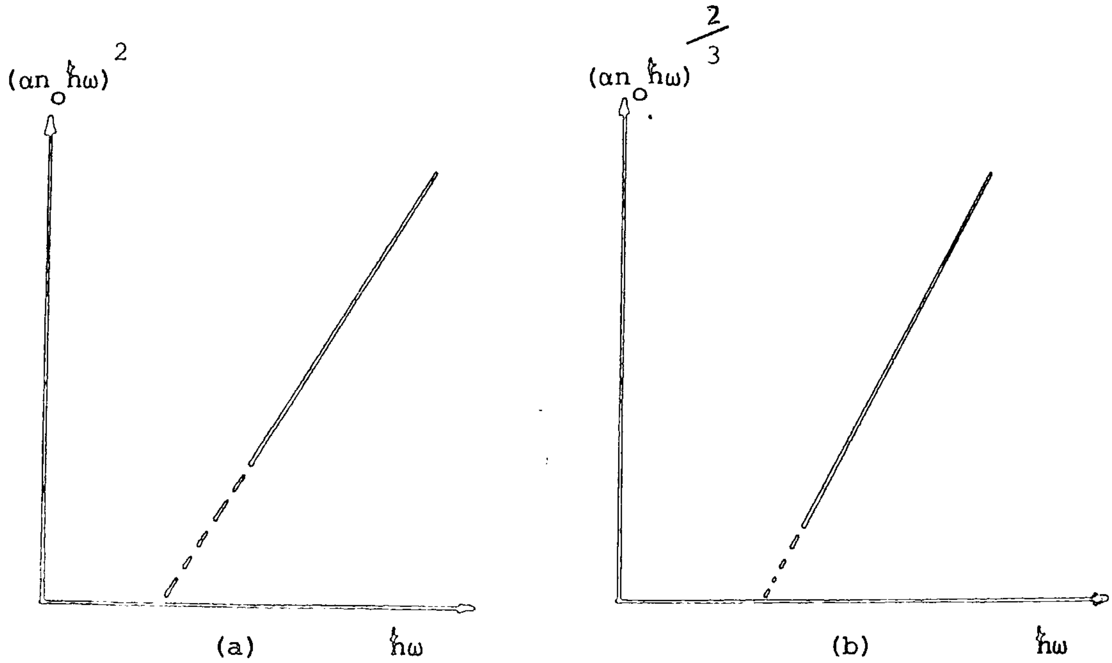

Fig 2.2 Schematic illustration of a direct transition (a) direct allowed and (b) direct forbidden.

2.2.2 Indirect Transition

An electron undergoing an optical transition is sometimes influenced by the interaction with a lattice vibration or phonon, and therefore its wavevector can change during the transition. The momentum change can involve the electron absorbing or emitting a phonon. Such transitions are most likely to occur when the maximum of the valence band and the minimum of the conduction band do not occur at the same point in k-space, i.e. in an indirect band gap material whose band structure is shown schematically in Fig 2.3.

The function which links the initial and final states of an optical transition is called the matrix element. In the case of an indirect transition an optical and an electron-phonon matrix elements are involved.

For a material with a parabolic type band structure with valence band maximum at k = 0 such that only one phonon is involved, it can be shown that the absorption coefficent expression can be written as (2)

$$\alpha n_o \hbar\omega = \frac{\left(\hbar\omega - E_g + E_p\right)^m}{\exp\left(E_{p/kT}\right) - 1} + \frac{\left(\hbar\omega - E_g - E_p\right)^m}{1 - \exp\left(-E_{p/kT}\right)} \qquad (2.2)$$

where E_p is the phonon energy. The parameter m equals 2 for an allowed transition and equals 3 for a forbidden transition as shown in Fig 2.4. Transitions involving more than one phonon are also possible.

The transitional probability for this type of transition is very small, much smaller than for a direct transition. This is however counterbalanced by an increase in the number of possible states from which transitions can be made and the available final states. Germanium provides a good example of a transition of this kind as illustrated in Fig 2.5.

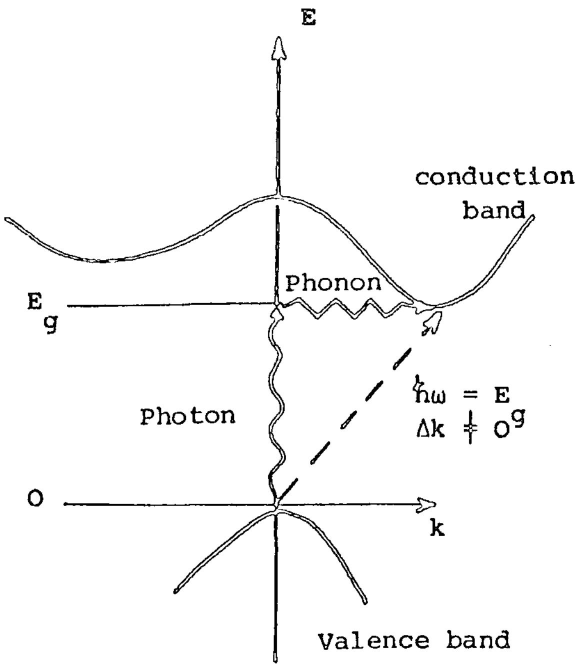

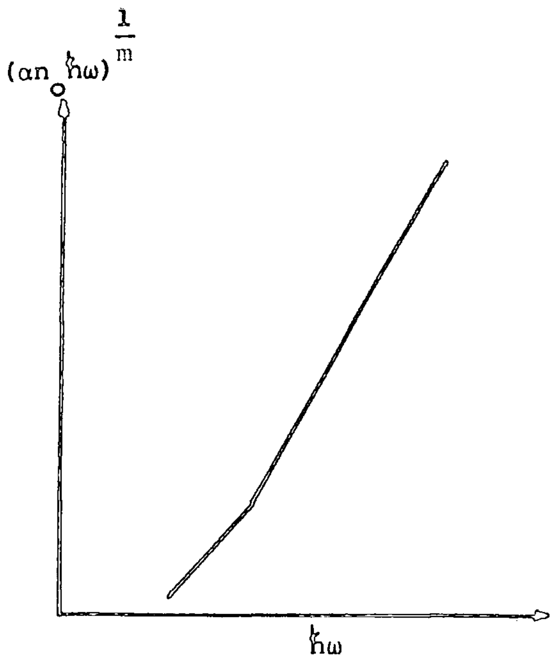

Fig 2.3 Indirect transition process necessitates a phonon interaction in order that the wave vector is conserved.

Fig 2.4 Schematic illustration of an indirect transition with m equal to 2 for allowed and 3 for forbidden transition.

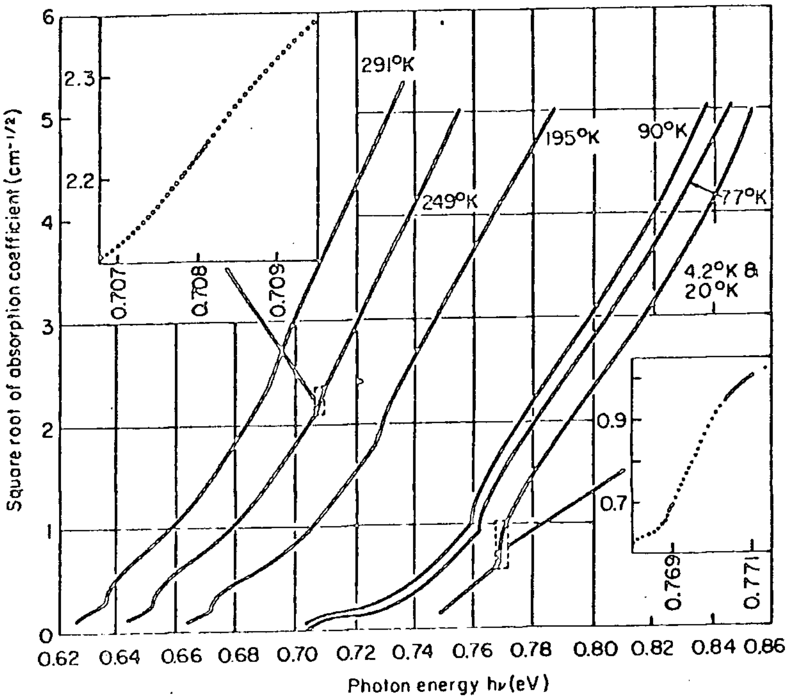

Fig 2.5 The absorption spectrum of Ge at various temperatures.

2.2.3 Absorption due to Excitons

In the previous discussion, little reference was made to excitonic effects. The exciton may be considered as a neutral electron-hole pair which is bound by a Coulombic potential and is free to migrate through the lattice. It is formed by exciting a valence band electron to a state just below the conduction band by the absorption of a photon. The nature of an exciton depends very much on the material.

For solids in which atoms interact weakly, such as molecular crystals, the electronic excitation covers only a few lattices. Even though it is localized, it can propagate through the crystal and provides a means of energy transfer. This picture was first proposed by Frenkel (4) and the pseudo particle is known as a 'Frenkel exciton'. However, in solids which have strong atomic interation such as the majority of inorganic semiconductors, the interaction is no longer localized. Wannier (5) proposed that the exciton may be viewed as a bound electron-hole pair with hydrogenic levels whose energies are modified by the dielectric constant of the solid and also by the carrier reduced effective masses. Analytical studies of the effect of Wannier excitons on the optical absorption by Elliot (7), Knox (8), and Dimmock (9) showed that the energy of formation of an exciton in a bound state is given by

$$E_n = E_g + \frac{\hbar^2 k^2}{2(m_e + m_h)} + \frac{R}{n^2} \qquad (2.3)$$

with n = 1,2,3,...... and R is known as the effective Rydberg such that

$$R = \frac{m^* e^4}{8(\varepsilon_o \varepsilon)^2 h^2} = 13.6 \left(\frac{1}{\varepsilon}\right)^2 \left(\frac{m^*}{m_o}\right) \text{ meV...} \qquad (2.4)$$

m^* is the reduced effective mass of electron-hole pair and ε is the static dielectric constant. The radius (effective Bohr radius) of the exciton is given by

$$a = \frac{\hbar^2 \varepsilon_o}{e^2 m^*} = 5.29 \left(\frac{m_o \varepsilon_o}{m^*} \right) 10^{-9} \text{ cm..} \qquad (2.5)$$

It can be shown that for a direct transition in the presence of an exciton, a series of absorption peaks are expected at energies given by

$$\hbar\omega = E_g - \frac{R}{n^2} \qquad (2.6)$$

and the intensities of each line fall off as n^{-3}.

For a photon energy less than the band gap

$$\alpha = \left[\pi \, A \, R^{\frac{1}{2}} \, e^{\pi\gamma} \right] \Big/ \left[\sin \pi \, \gamma \right] \qquad (2.7)$$

where $\gamma = \left[R/(\hbar\omega - E_g) \right]^{\frac{1}{2}}$. For large values of $\hbar\omega$, $\gamma \rightarrow 0$ and the Coulomb interaction is negligible. A schematic diagram of exciton levels in relation to the conduction band edge is given in Fig 2.6. Cadmium sulphide, zinc oxide and zinc sulphide show very strong exciton absorption. Fig 2.7 shows a series of lines in cuprous oxide at 77 K.

The magnitude and spectral width of the discrete lines are influenced predominantly by thermal broadening. Scattering of defects or impurities may also reduce the exciton lifetime and contribute to further broadening of the peak.

2.2.4 Exponential Absorption Edge

Some materials such as the alkali halides, exhibit an exponential increase in absorption coefficient with photon energy. Urbach (10) first proposed an empirical relationship to describe this type of absorption edge. This so called 'Urbach spectral rule' includes a temperature dependence of

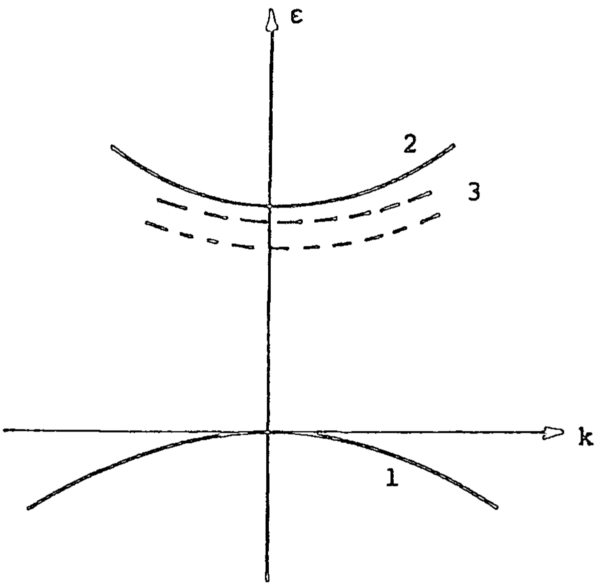

Fig 2.6 Exciton levels for a direct transition

(1) valence band, (2) conduction band, and

(3) exciton levels.

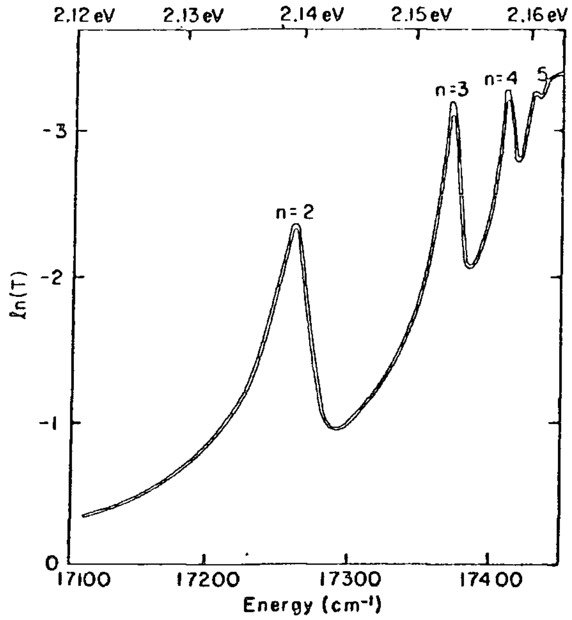

Fig 2.7 The logarithm of the transmission as a function of photon energy of a Cu_2O sample at 77 K showing the details of the exciton lines.

the exponential slope such that

$$\alpha = \text{const.} \exp\left[\frac{\gamma(\hbar\omega - E_g)}{kT}\right] \tag{2.8}$$

where γ is a constant, T is the absolute temperature down to a critical value T_o related to the zero point energy.

The exponential dependence of absorption coefficient on energy is thought to be due either to the existence of impurity band tails or internal microfields within the specimen. In the first case, a shallow impurity level with high concentration may lead to an exponential density of states tails which extends from the conduction or valence band into the forbidden gap (11). Assuming that the transition matrix element is independent of photon energy and that transitions are allowed from momentum considerations, it may be shown that

$$\alpha(\hbar\omega) = \left[A(E_o)\right]^{3/2} \exp(\hbar\omega/E_o).\ \text{const.} \tag{2.9}$$

giving the observed exponential energy dependence where E_o is an empirical parameter.

Redfield (12), however, attributed the broadening of the absorption edge to the electric fields of charged defects such as impurities and dislocations. The internal field produces an exponential shift of the absorption edge to lower energies due to a finite probability of tunneling of the band Bloch states into the energy gap. Dexter (13) postulated that the electric field arises from vibrating atoms in the material which can also explain the temperature dependence of the edge.

The most satisfactory explanation of the Urbach rule is that given by Dow and Redfield (14) who suggested that virtually all exponential absorption edges are probably due to electric field ionization of excitons. These authors carried out a numerical study of the shape of the absorption for direct excitonic transitions in a uniform electric field and their results are summarised in Fig 2.8 where the parameter f provides a measure of the electric field strength. Since excitons are known to exist in materials which exhibit as exponential absorption edge, this explanation seems most plausible.

The optical band gap of a crystalline material exhibiting Urbach's rule is usually determined by locating the focal point of a family of edges obtained as a function of temperature. By taking $E_g(T) = E_g(0)-\beta T$,

$$\alpha = \text{const.}\exp\left[-\frac{\gamma\,|E_g(0)-\hbar\omega-\beta T|}{kT}\right] \qquad (2.10)$$

The absorption coefficient is thus independent of temperature when $\hbar\omega = E_g(0)$ and this is the focal point. Trigonal selenium (15) displays the Urbach spectral rule for quite a large range of photon energies as shown in Fig 2.9.

2.3 OPTICAL ABSORPTION IN NON-CRYSTALLINE SOLIDS

Densities of electron states and band gaps remain valid concepts for non-crystalline as well as crystalline solids. Furthermore, non-crystalline materials are thought to contain imperfections such as impurities or dangling bonds at point defects or microvoids, and these, as in crystals, may lead to levels within the energy gap. In fact it is believed that the lack of long range order determined by bond lengths, bond angle and local coordination can lead to tails of states extending from the conduction and valence band. These localized states are separated from the extended states by an energy level E_{CM} known as 'the mobility edge'. The difference in energy between the mobility edges in the valence and conduction bands is called 'the mobility gap'. This picture is illustrated in Fig 2.10.

Mott (16) has also suggested that states due to defect centres such as dangling bonds, may lie near the mid-gap of an amorphous material. They could act both as deep donors (E_y) and acceptors (E_x) separated by an

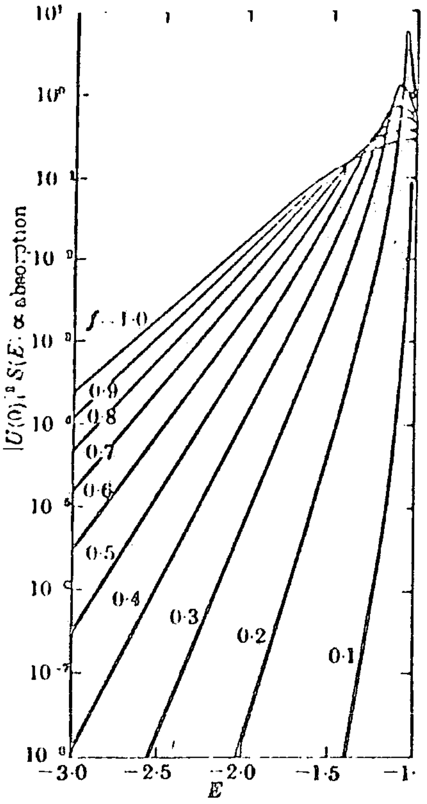

Fig 2.8 Dow and Redfield's theory for optical absorption in the presence of an electric field with exciton effect included.

(14)

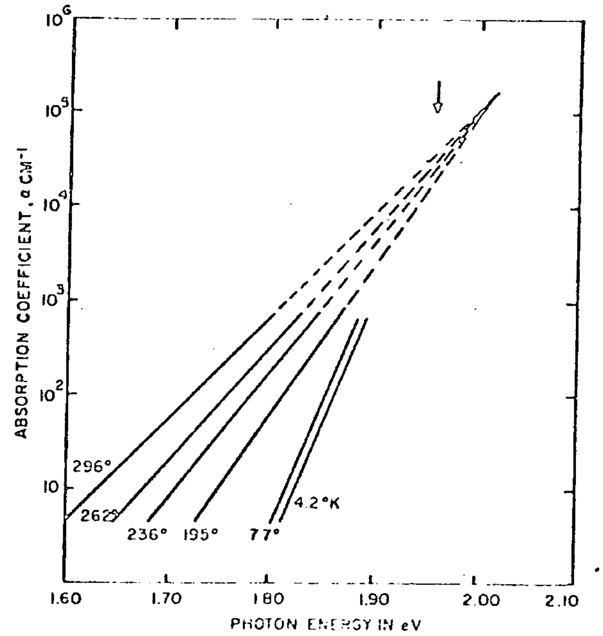

Fig 2.9 Absorption coefficient of trigonal Se as a function of photon energy for light polarized with the E vector perpendicular to the c axis. The arrow denotes the position of the exciton peak at 20° K.

(15)

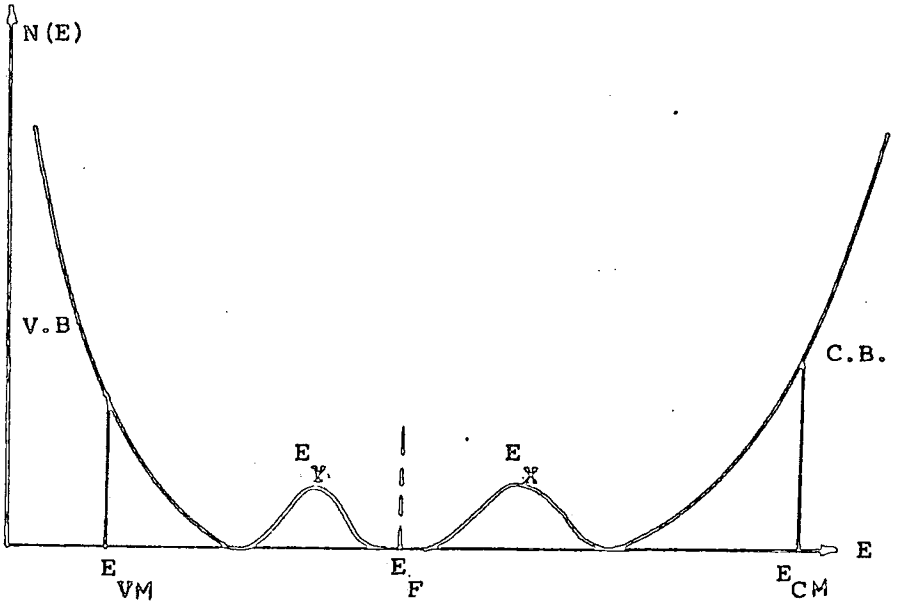

Fig 2.10 Schematic diagram of the density of states of amorphous material. $(E_{CM}-E_{VM})$ is the mobility gap with E_F as the Fermi energy level.

appropriate correlation energy. The Fermi level, E_F, should lie between the two bands if they do not overlap or be pinned within them if they do. These localized states and their distribution within the gap frequently determine the transport properties of amorphous materials.

The fact that the optical excitation of an electron may involve localized states as well as extended states, complicates the absorption edge of an amorphous material. In the low energy règime, the absorption edge is normally exponential. It then increases more rapidlyat higher energies where the absorption edge can be expressed by a simple power law. These two regions require separate discussions.

2.3.1 Exponential Absorption Edge

This kind of absorption edge is observed in most non-crystalline materials with the exception of certain thin films such as InSb. Fig 2.11 shows the room temperature absorption edges of a few amorphous semiconductors. Tauc (11) and Lanyon(17) attributed this effect to electronic transitions between localized states in the band edge tails, the densities of which are assumed to fall off exponentially. However, according to Mott and Davis (18), this is not likely since the gradient of the observed exponential absorption edges are very much the same in a variety of materials.

In contrast, the field broadening of an exciton line theory by Dow and Redfield (14) may offer some explanation. The model, however, requires the existence of excitons in amorphous semiconductors. Excitons do indeed exist in such materials although sharp exciton lines are hardly to be expected. The possible source of electric fields in amorphous semiconductors is longitudinal optical phonons or static spatial fluctuations in potential arising from the lack of long range order, variation in density or charged defect centres.

The exponential edges in amorphous semiconductors are, however, only slightly temperature dependent. The temperatures where the focal point predicted by Urbach's empirical rule occur, are relatively higher than those for crystalline materials. Street et al (19)'s analysis based on As_2S_3 suggested that the exponential slope in amorphous semiconductors is determined by two types of broadening namely static disorder and phonons. They estimate the former which is insensitive to temperature, to be about three times the latter.

2.3.2 Simple Power Law

For energies above the exponential behaviour, the absorption edge can be expressed in terms of a simple power law. This can be explained if it is assumed that the matrix elements of the electronic transitions are constant over the range of photon energies of interest and if the κ-conservation selection rule is relaxed. The conductivity can then be written as (16)

$$\sigma(\omega) = \frac{2\pi e^2 \hbar^3 \Omega}{m^2} \int \frac{N(E)\ N\ (E + \hbar\omega)\ |D|^2}{\hbar\omega}\ dE \qquad (2.11)$$

where Ω is the volume of the specimen and D is the matrix elements such that

$$D = \pi(a/\Omega)^{\frac{1}{2}} \qquad (2.12)$$

with a the average lattice spacing. D is assumed to be the same whether or not the initial or final states, or both, are localized (16,20). The absorption coefficient is related to conductivity by the equation

$$\alpha = \frac{4\pi}{n_o c}\, \sigma(\omega) \qquad (2.13)$$

where n_o is the refractive index. This leads to the following expression for interband transitions

$$\alpha(\omega) = \frac{8\pi\ e^4 \hbar a}{n_o c\ m^2} \int \frac{N_v(E)\ N_c(E + \hbar\omega)}{\hbar\omega}\ dE \qquad (2.14)$$

It can be shown that for a parabolic band

$$\alpha(\omega) = \text{const.} \frac{(\hbar\omega - E_o)^2}{\hbar\omega} \qquad (2.15)$$

The above quadratic relation has also been derived by Davis and Mott(18) using the assumption that the densities of states of the band edge are linear functions of energy. Examples of materials obeying this rule are shown in Fig 2.12. However, this quadratic dependence is not a characteristic phenomenon of amorphous materials. Some materials, in their amorphous form such as selenium, obey a relation of the form

$$\alpha(\omega)\hbar\omega = \text{const} (\hbar\omega - E_o) \qquad (2.16)$$

Others such as the example shown in Fig 2.13 satisfy the following rule

$$\alpha(\omega)\hbar\omega = \text{const} (\hbar\omega - E_o)^3 \qquad (2.17)$$

It therefore appears that the absorption edge of many amorphous materials can be described by a simple power law, at least over a limited range of absorption coefficient. In most cases, E_o is taken as the optical band gap. It, however, requires an independent knowledge of the density of states and matrix elements as a function of energy to help confirm that it is a real gap in the density of states.

2.4 OPTICAL ABSORPTION IN ORGANIC MOLECULAR SOLIDS

Molecules can remain bound in excited states as well as in the ground state. The emission and absorption spectra of molecules are due to transitions between allowed energy states. The charge distribution in a diatomic molecule for example is symmetrical about an axis connecting the nuclei which can move relative to each other. The nuclei can vibrate

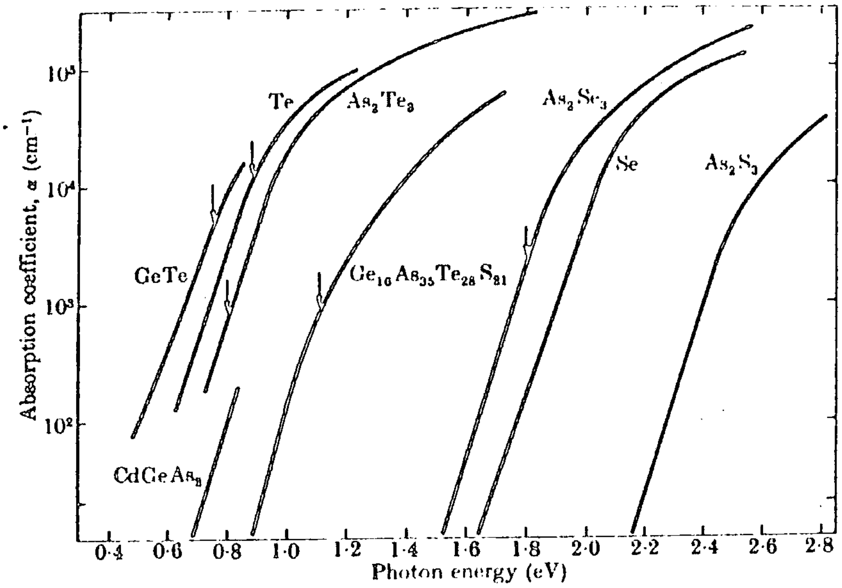

Fig 2.11 Exponential absorption edges in amorphous semiconductors at room temperature (16)

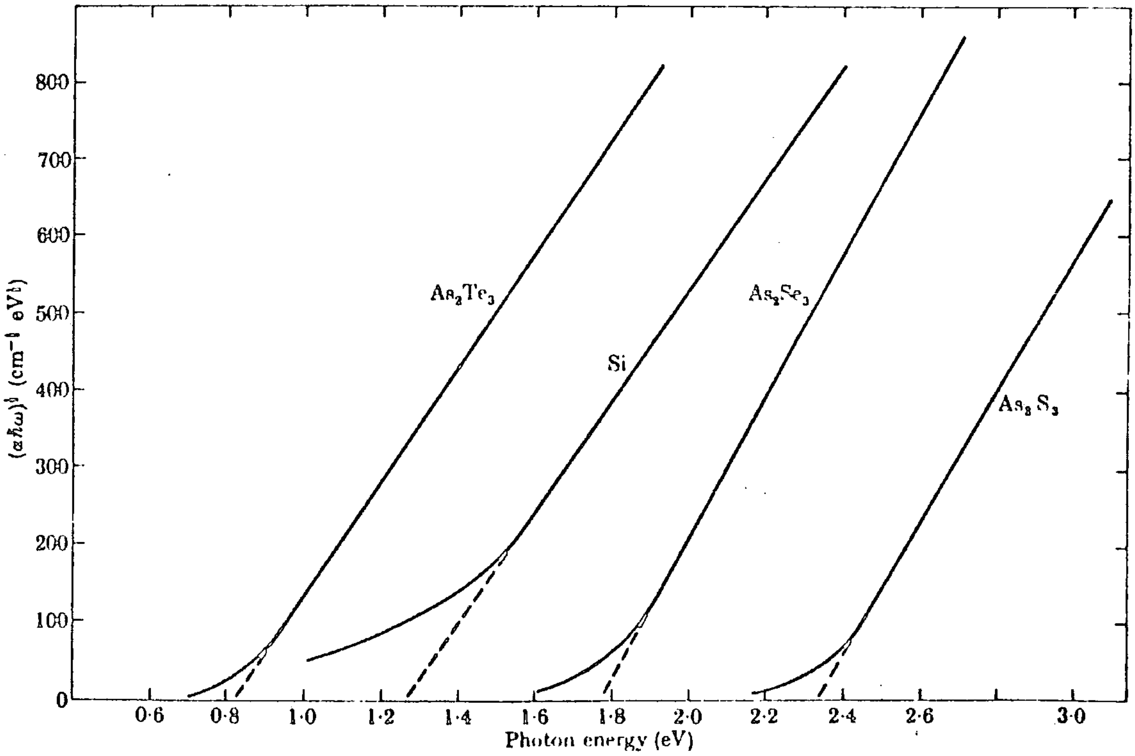

Fig 2.12 Examples of absorption edges whose functional dependence of photon energy is given by $\alpha\hbar\omega = \beta(\hbar\omega - E_o)^2$. (16)

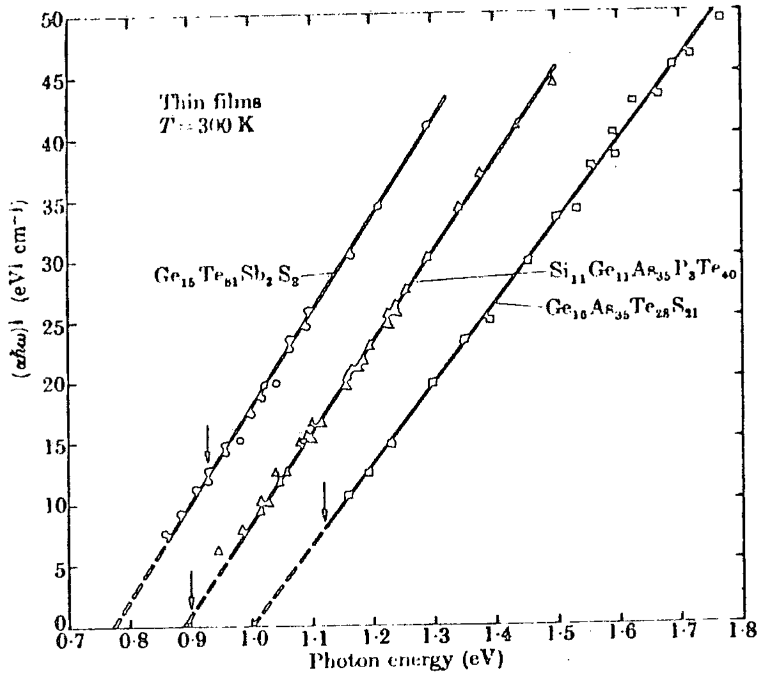

Fig 2.13 Absorption edges in three multi-component glasses which obey the relationship of $\alpha\hbar\omega \sim (\hbar\omega - E_o)^3$. (1.6)

about an equilibrium separation, and in addition the whole system can rotate about its centre of mass. The energy in each of these motions, vibrational and rotational, are quantized so that many more energy levels exist in a molecule than in an atom.

The spectrum can be divided into three spectral ranges corresponding to the different types of transition between the molecular quantum states. In the far infrared, rotational spectra are observed indicating transitions between rotational states of a molecule having an electric dipole moment. In the near infrared vibrational-rotational spectra are expected corresponding to transitions between vibrational states within which there are changes in rotational states. In the visible and ultra-violet regions, electronic spectra associated with electronic transitions are observed. These electronic vibrations undergo many cycles in the time required for the nuclear configuration to change, producing electronic spectra containing fine structure determined by the rotational and vibrational states of the nuclei.

2.4.1 Vibration - Rotation Spectra

The nuclei do not maintain a fixed separation so that a molecule is not like a rotating rigid body except to a first approximation. Also the nuclei vibrate about some equilibrium separation and thus the vibrational motion is quantized. For a given configuration, the minimum potential energy is at an equilibrium separation at which the energy-separation curve is a parabola, so that small oscillations are simple harmonic. Accordingly the energy of such oscillations are quantized and satisfy the equation

$$E_\nu = (\nu + \frac{1}{2})h\nu_o \tag{2.18}$$

where ν_o is the classical vibration frequency and $\nu = 0,1,2,.....$ is the vibrational quantum number. If the molecule has a permanent dipole moment at an inter-nuclear separation equilibrium, it will exhibit vibrational emission, and also absorption spectra due to the oscillations in the nuclear separation. The selection rule for an electric dipole moment transition is $\Delta\nu = \pm 1$, so that $\Delta E_n \simeq h\nu_o$. The resulting spectra for most materials lie in the infrared.

2.4.2 Electronic Spectra

There can also be electronic excited states corresponding to different electron configurations. For each electronic state with energy E_e, there are many bound vibrational states of energy E_v and to each vibrational state there are many bound rotational states of energy E_r. Neglecting the interaction between these modes, the total energy can be written as

$$E = E_e + E_v + E_r \tag{2.19}$$

The energies of all three modes may change in an electronic transition so that in general

$$\Delta E = \Delta E_e + (E_v' - E_v) + (E_r' - E_r) \ldots \tag{2.20}$$

where the prime indicates the final vibrational and rotational states.

Consider a molecule in which only one vibrational mode is dominant with the energy of the fundamental vibrational mode in the ground state E_v.

Then,
$$E = E_e + (\nu + \frac{1}{2})\ E_\nu \tag{2.21}$$

If the energy of the fundamental vibrational mode in the excited state is E_ν'

$$E' = E_e' + (\nu' + \frac{1}{2})\ E_\nu' \tag{2.22}$$

with $\nu' = 0, 1, 2, \ldots$.

The transition constituting the main electronic absorption spectra is

$$\Delta E = E' - E$$

$$\approx (E_e' - E_e) + \Delta\nu E_\nu' \qquad (2.23)$$

since $E_\nu' \approx E_\nu$ and $\Delta\nu = \nu' - \nu$. The selection rule for an electric dipole transition is that $\Delta\nu = \pm 1$ in the case of a simple harmonic oscillator. If however the potential is anharmonic, transitions with $\Delta\nu = 2,3,4,\ldots$ are also allowed.

A transition from a ground state to the ν'th vibrational level is the $(0-\nu')$ vibronic transition and is illustrated in Fig 2.14. If spin is considered, transitions from a ground singlet state to the first or higher excited states are allowed. Transitions from a ground singlet state to the first or higher triplet state are however forbidden and may only be observed with intense light sources. Fig 2.15 shows the electronic absorption spectra of a particular organic molecule, namely Mg-phthalocyanine(21).

2.5 ELECTROABSORPTION THEORY

The effect of an external electric field on the fundamental absorption edge of some solids will now be reviewed. In all cases the electric field shifts the absorption spectrum towards lower energies. There are two basic mechanisms which can account for the effect. The first is the so called Franz-Keldysh effect, normally observed if an optical transition from the valence band to conduction band is perturbed by a large electric field. The second is an electric field induced shift of the spectral lines produced by transitions between narrow energy levels or between quantized states such as those in organic molecular solids. This so called Stark effect is the electrical equivalent of the Zeeman effect. Both mechanisms will now be presented in this section. This section ends with an account of the complications introduced by disordered materials.

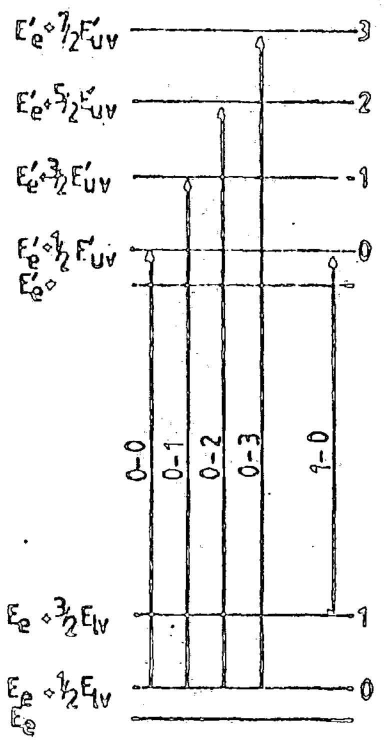

Fig 2.14 Vibronic Absorption levels.

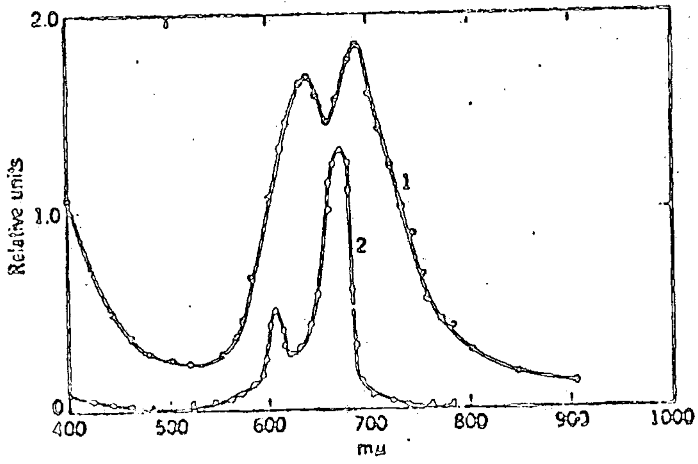

Fig 2.15 Optical absorption spectra of Mg-phthalocyanine

(1) sublimed film

(2) solution in acetone.

2.5.1 The Franz-Keldysh Effect

The perturbation by an electric field of the fundamental absorption edge of a semiconductor, was first considered theoretically by Franz(22) and Keldysh (23). Their calculations showed that in the presence of a high electric field, the absorption edge broadens and shifts towards lower energies. This phenomenon is widely referred to as the Franz-Keldysh effect.

The physical picture of this effect is as follows :
The presence of a high electric field will tilt the conduction and valence bands in real space. The band edges, however, remain parallel and separated vertically by the energy gap E_g as shown in Fig 2.16 The wavefunctions of the conduction band and valence band states will now have exponentially decaying tails extending into the forbidden gap. Thus an electron in the valence band has a finite probability of tunneling a distance Δx into the forbidden gap. Then, by absorbing a photon with energy $\hbar\omega<E_g$, the electron can be excited into the conduction band, giving rise to a finite absorption for $\hbar\omega<E_g$. This is regarded as photon assisted tunneling, an equivalent process to Zener tunneling(24).

A detail calculation of this process was made by Keldysh(23) and may be summarized as follows. The total probability of absorption of a photon $\hbar\omega$ per unit time per unit volume is

$$W(\omega) = \frac{e}{m}^{2} \frac{2\pi\hbar}{\omega} \int \left| \vec{e}\,\vec{\mu}_{vc}(\vec{p}) \right|^{2} \delta\left[\varepsilon_c(\vec{p})-\varepsilon_v(\vec{p})-\hbar\omega\right] \frac{d^3p}{(2\pi\hbar)}3. \qquad (2.24)$$

where

$$\vec{\mu}_{vc}(\vec{p}) = \int \psi_c^{*}\ (\vec{p},\vec{r})\ \nabla\ \psi_v(\vec{p},\vec{r})\ d\tau \qquad (2.25)$$

and the other symbols have their usual meanings.

For direct allowed transitions this simplifies to

$$W(\omega) = \frac{1}{\pi}\frac{e^2}{\hbar c}\frac{c}{\omega}\left[\frac{m_1 m_2 m_3}{m^3}\;\frac{q(\hbar\omega-\varepsilon_o)}{m}\right]^{\frac{1}{2}} \left|\,\vec{e}\;\vec{\mu}_{vc}(\vec{p}_m)\,\right|^2 \qquad (2{\circ}26)$$

where m_i^{-1} is the principal value of the tensor m_{ik}^{-1} . In the presence of an electric field the expression (2.24) no longer contains a delta function and therefore the probability of absorbing a quantum of frequency less than ω_o is not zero. In this case,

$$W(\omega) = \frac{a^2}{\hbar c}\frac{c}{\omega}\left[\frac{m_1 m_2 m_3}{m^3}\;\frac{2(\varepsilon_o-\hbar\omega)}{m}\right]^{\frac{1}{2}} \frac{(ehF)^2}{m_{11}(\varepsilon_o-\hbar\omega)^3}$$

$$\mathrm{X}\left|\vec{e}\;\mu_{vc}(\vec{p}_m)\right|^2 \exp\left[-\frac{4\sqrt{2m_{11}}}{3e\hbar F}(\varepsilon_o-\hbar\omega)^{3/2}\right] \qquad (2{\circ}27)$$

$$\text{with } m_{11}^{-1} = \sum_i \cos^2\gamma_i/\mu_i \qquad (2.28)$$

The above equation indicates that an exponential tail in the long wavelength region is formed due to application of an electric field. By comparing equations (2.26) and (2.27) it can be shown that in the presence of an electric field F, the absorption edge shifts towards the red such that

$$\Delta\omega_F = \frac{1}{\hbar}\left[(e\,Ed)^2\;\frac{\hbar^2}{m_{11}d^2}\right]^{1/3} \qquad (2{\circ}29)$$

For a direct allowed transition, the field dependence of the absorption coefficient change is thus given by

$$\Delta\alpha = \text{const}\;\; F^{1/3}$$

Later workers found theoretically that the change in absorption coefficient is proportional to F and $F^{4/3}$ for direct forbidden (25) and indirect (26) transitions respectively. An example of an electroabsorption spectrum for a direct transition is shown in Fig 2.17 .

In some materials, however, the absorption edge is already exponential in the absence of an external electric field as already mentioned in section (2.2.4). Equation (2.8) can then be written as

$$\alpha = \alpha_o \exp\left[\beta(\hbar\omega - E_g)\right] \tag{2.30}$$

Assuming that the edge retains its original exponential slope β in the presence of an external electric field F, Franz (22) showed that for low values of α, the change in absorption coefficient Δα can be expressed as

$$\frac{\Delta\alpha}{\alpha} = \frac{\beta^3\hbar^2F^2}{24m^*e} \tag{2.31}$$

where m^* is the reduced effective mass. It is evident from equation (2.31) that for solids which exhibit an exponential absorption edge, electroabsorption can provide a means of measuring the reduced effective mass. Since it is extremely difficult to measure the reduced effective mass of doped or undoped semi-insulating materials, this represents an important use of the electroabsorption technique.

2.5.2 Development of One-Electron Theory

The theories mentioned up to the present have been formulated within the context of a one-electron model ; that is without electron-hole interaction. Several extensions to the simple theories now exist. For example, Callaway (27) has used experimental data to calculate the mixing of Bloch states as a consequence of the application of an electric field. A different approach was used by Tharmalingham (28) who solved the effective mass Schrodinger equation by considering the effect of a uniform electric field on the probability of producing an electron-hole pair. If Coulomb

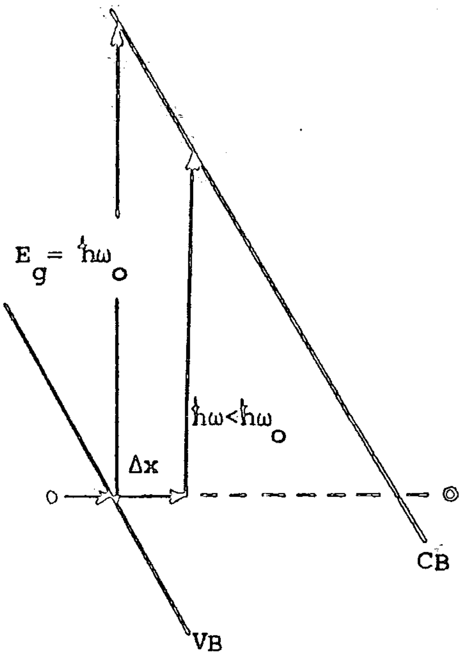

Fig 2.16 Schematic diagram of a photon assisted tunneling process.

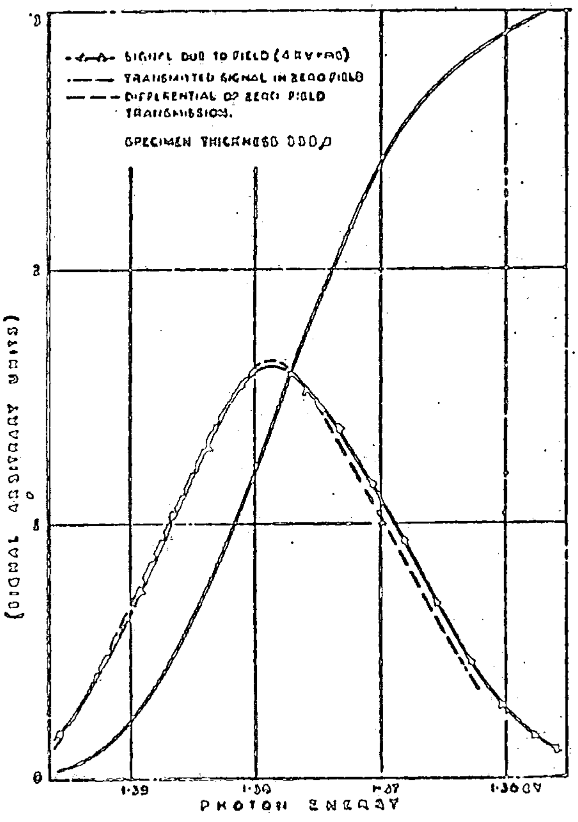

Fig 2.17 Electroabsorption in GaAs at room temperature for a field of 4×10^3 V.cm^{-1}.

interaction is neglected, the solution can be expressed in terms of a well known Airy function, Ai. For a direct allowed transition under the influence of an electric field F, the absorption coefficient α can be written

$$\alpha = R\Theta_F^{\frac{1}{2}} \int_{(\omega_o-\omega)/\Theta_F}^{\infty} |Ai(t)|^2 \, dt \tag{2.32}$$

with

$$\Theta_F^3 = (e^2F^2)/(2m^*\hbar) \quad ; \quad \hbar\omega_o = E_g$$

and

$$R = \frac{2e^2C_o^2}{\hbar\omega c n m^2} \left[\frac{2m^*}{\hbar}\right]^{3/2}$$

where C_o is a constant in the transition matrix element expression.

Two limiting cases can be considered :

(1) For $\omega \ll \omega_o$; equation (2.32) simplifies to

$$\alpha \simeq R \frac{\Theta_p^{3/2}}{8(\omega-\omega_o)} \exp\left[-\frac{4}{3}\left(\frac{\omega_o-\omega}{\Theta_F}\right)^{3/2}\right] \tag{2.33}$$

thus giving an exponential-type tail in the long wavelength region as predicted by the Keldysh theory.

(2) For $\omega > \omega_o$ and near the edge,

$$\alpha \simeq R\Theta_F^{\frac{1}{2}} \left[\left(\frac{\omega-\omega_o}{\Theta_F}\right)^{1/2} + \int_0^{\infty} \left| Ai(t) \right|^2 dt\right] \tag{2.34}$$

In this case $\alpha \to R(\omega-\omega_o)^{\frac{1}{2}}$ as $F \to 0$ and leads to the familiar $F^{1/3}$ dependence for the change in absorption coefficient induced by the electric field. Tharmalingham also proved the linear field dependence of the change in absorption for a direct forbidden transition. The presence of an Airy function, i.e. equation (2.34) indicates an oscillatory nature to the absorption coefficient. Such oscillations were also evident in an improved theory by Callaway (29) .

In a further extension of the theory Aspnes (30,31) and Philips(32) took into account all types of critical points as well as the fundamental absorption edge. A critical point is defined as a region of the energy band structure in k-space which satisfies the equation

$$\nabla_k \ (E_c - E_v) \ = \ 0 \qquad (2.35)$$

Aspnes calculated an expression for the change in the imaginary part of the dielectric constant $\Delta\varepsilon_2$ in the presence of an electric field [$\Delta\varepsilon_2$ is related to the change in absorption coefficient $\Delta\alpha$ such that

$$\Delta\varepsilon_2 \ = \text{const.}\ ^{\Delta\alpha}/_{(\hbar\omega)} \quad \Big] \qquad (2.36)$$

Aspnes, Hadler and Blossey (33) in an attempt to unify the electroabsorption theory demonstrated that the method of Callaway and of Tharmalingham come to the same conclusion. Their theory was used by Hamakawa, Germano and Hadler (34) to analyse the data obtained for germanium. In the presence of an electric field, ε_2 for a fundamental absorption edge can be expressed as

$$\varepsilon_2(h\omega, F) \ = \ \frac{B}{\omega^2} \int_{E_g}^{\infty} \left(\frac{E-E_g}{\hbar}\right)^{\frac{1}{2}} \left(\frac{1}{\hbar\Omega}\right) \mathrm{Ai} \left(\frac{E-\hbar\omega}{\hbar\Omega}\right) dE \qquad (2.37)$$

where $\Omega^3 = e^2F^2/_{(8m^*\hbar)}$ and B is a constant which contains the dipole matrix element and ω is the frequency of the incident photon. In the limit of zero electric field $F \rightarrow 0$, $\Omega \rightarrow 0$ and

$$\lim_{F \rightarrow 0} \varepsilon_2 (\hbar\omega, F) = \frac{B}{\omega^2} \left(\frac{\hbar\omega - E_g}{\hbar} \right)^{\frac{1}{2}} \quad ; \; \hbar\omega \geq E_g \qquad (2.38)$$

By comparing equation (2.37) and (2.38), the change in ε_2 with field, $\Delta\varepsilon_2$ can be written as

$$\Delta\varepsilon_2 (\hbar\omega, F) = \frac{1}{(\hbar\omega)^2} \int_{E_g}^{\infty} E^2 \varepsilon_2 (E, 0)$$

$$\text{X} \left[\left(\frac{1}{\hbar\Omega} \right) A_i \left(\frac{E - \hbar\omega}{\hbar\Omega} \right) - \delta (E - \hbar\omega) \right] dE \qquad (2.39)$$

The functional form of $\Delta\varepsilon_2$ is plotted on an arbitrary scale in Fig. 2.18 as a function of a dimensionless variable

$$\eta = (\hbar\omega - E_g) / (\hbar\Omega) \qquad (2.40)$$

From this result it is evident that $\Delta\varepsilon_2$ oscillates for $\hbar\omega > E_g$. For energies below the gap where $\hbar\omega < E_g$, the asymptotic form for $\Delta\alpha$ becomes

$$\Delta\alpha \; (\omega, F) = \alpha \; (\omega, F) - \alpha \; (\omega, 0)$$

$$= \frac{Km^*}{\hbar\omega (E_g - \hbar\omega)} \exp \left[- \frac{4}{3} \frac{(2m^*)^{\frac{1}{2}}}{\hbar} \frac{(E_g - \hbar\omega)^{3/2}}{eF} \right] \qquad (2.41)$$

where K is a constant, producing the exponential tail of the spectrum.

In Fig. 2.18 $\Delta E_1, \Delta E_2$ and ΔE_3 are the energy difference of zeros of the

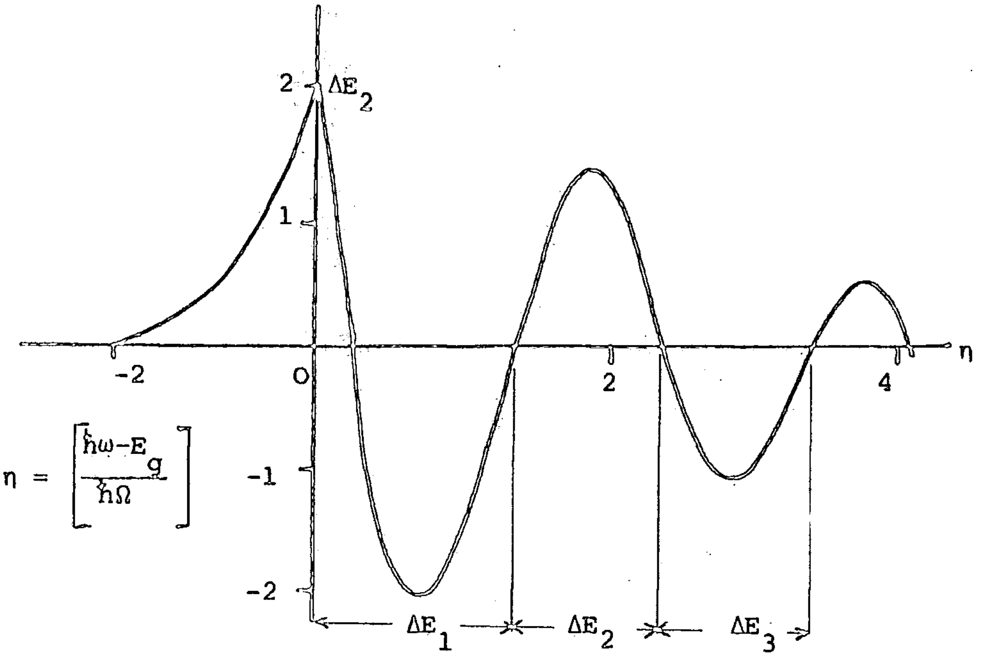

Fig 2.18 The change in imaginary part of the dielectric constant as a function of η. (34)

Type of transition	m	n	Absorption edge
Direct allowed	½	1/3	$\alpha\hbar\omega = \alpha_o(\hbar\omega - E_o)^m$
Direct forbidden	3/2	1	$\Delta\alpha \propto F^n$; $3n = 2m$
Exponential	-	2	$\alpha = \alpha_o \exp\left[\beta(\hbar\omega - E_o)\right]$ $\frac{\Delta\alpha}{\alpha} = \frac{\beta^3\hbar^2F^2}{24m^* e}$

Table 2.1 The main conclusions of the one-electron electroabsorption theories.

observed $\Delta\varepsilon_2$. If η_n in equation (2.40) is the zero of $\Delta\varepsilon_n$ then

$$\eta_n - \eta_n' = \frac{2(m^*)^{1/3}}{(e\hbar)^{2/3}} \left[\frac{\hbar\omega_n - \hbar\omega_n'}{F^{2/3}} \right] \qquad (2.42)$$

$$\Delta E_n = \hbar\omega_n - \hbar\omega_n'$$

$$= \left(\eta_n - \eta_n'\right) \left[\frac{(e\hbar)^{2/3}}{2(m^*)^{1/3}} \right] F^{2/3} \qquad (2.43)$$

indicating that the distance between the two peaks should depend on $F^{2/3}$.

2.5.3 Summary of the 'One-Electron' Theories

The main predictions of the one-electron-theories mentioned in the previous subsection are :

(1) The field dependence of the change in absorption coefficient is governed by the zero-field absorption mechanism. Table 2.1 summarizes this relationship for various types with the exception of the exponential edge. The change in the absorption coefficient is proportional to F^n where n is determined by the simple relation $3n = 2m$; m is the exponent in the spectral dependence of the zero field absorption mechanism. For an exponential absorption edge $n = 2$.

(2) The energy gap should occur very close to the first positive peak where $\eta = \frac{\hbar\omega - E_O}{\hbar\Omega} = 0$ as illustrated in Fig 2.18.

(3) The relative amplitudes of the various peaks should increase in a fixed ratio but the magnitude of the peaks above E_g should decrease slowly with energy.

(4) The distance between peak heights should depend on $F^{2/3}$.

2.6 EXCITONIC ELECTROABSORPTION THEORY

Earlier in this chapter it was assumed that excitons could readily be ionized by small electric fields or temperature and it was therefore reasonable to completely ignore their effect. This assumption is evidently not true for some materials where there is strong exciton absorption. The ionization fieldof an exciton F_i ; the field required to ionize the ground state of an exciton ; is normally very high in these materials. It may be written

$$F_i = R/_{ea} \qquad (2.44)$$

where R is the effective Rydberg and a is the effective Bohr radius. Table 2.2 provides values of F_i for some semiconductors.

The first calculation of the effect of an electric field on Wannier excitons was performed for hydrogen(35). Due to the large ionization field of this molecule ($\sim 10^9$ V.cm^{-1}), the external electric field only slightly modifies the energy levels of the system. It is therefore valid to use first and second order perturbation theory in the calculation of the Stark effect. In 1966, Duke and Alferieff (36) studied the optical absorption by excitons in an external electric field. Their simplified model was based on the assumption that the Coulomb potential has zero effect outside a certain critical radius. The external field in contrast has negligible effect inside this potential well. This picture is illustrated in Fig.2.19. This reasonable assumption however did not correctly predict the magnitude of the Stark shift.

This approach was subsequently improved by Ralph (37) and Dow and Redfield (38) who numerically integrated the effective mass differential equation. However, their calculations unfortunately did not show the electric field induced oscillations in the continuum density of states. An attempt was also made by Enderlein (39) to solve the problem using a Green's function method. His result however was restricted to only weakly bound

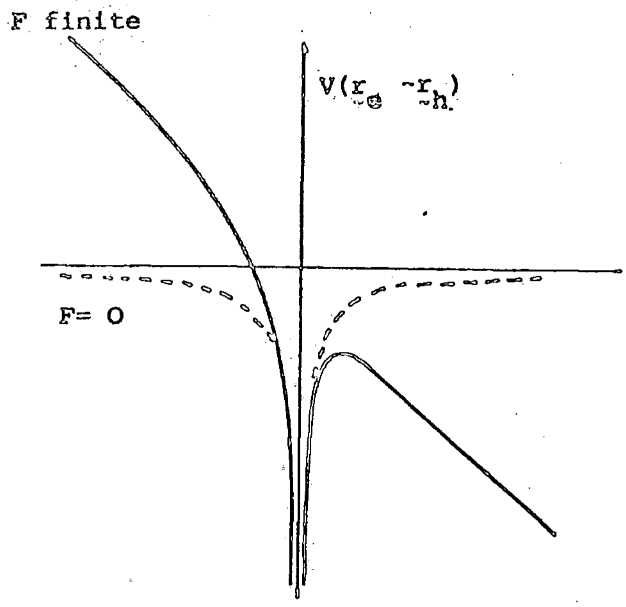

Fig 2.19 Coulomb potential for zero- and finite-electric fields.

Table 2.2: ENERGY GAPS, RYDBERG ENERGIES, AND IONIZATION FIELDS FOR SELECTED SEMICONDUCTORS

Material	Energy gap (eV) E_0	Effective Rydberg energy (eV) R^a	Ionization field R/ea (V/cm) $\mathscr{E}_i$
PbI_2	2.55	0.073	4.6×10^5
Ge	0.80	0.0014	5.5×10^2
GaAs	1.41	0.0051	5.7×10^3
GaSb	0.813	0.0018	1.0×10^3
InP	1.29	0.0065	7.8×10^3
InAs	0.360	0.0018	7.0×10^2
InSb	0.2357	0.0005	7.6×10^1
AlSb	1.6	0.0075	1.2×10^4
CdS	2.5831	0.0294	1.4×10^5
CdSe	1.8415	0.0157	6.0×10^4
CdTe	1.606	0.0100	3.1×10^4
ZnS	3.9115	0.0401	2.0×10^5
ZnSe	2.818	0.0190	7.5×10^4
ZnTe	2.301	0.0130	4.7×10^4

[a] Exciton from highest energy split-off valence band.

excitons. Blossey (40,41) was the first to calculate the effect of an electric field on the higher bound exciton levels. His numerical computation produced an expression for the imaginary part of the dielectric constant and included the electric field induced oscillations in the continuum density of states. His theory represents the most detailed computation to date and is summarized in the next section.

2.6.1 Summary of Numerical Calculations

The main conclusions of the numerical calculations are as follows :

(1) In the low energy règime, below the absorption edge, the logarithm of the absorption coefficient should be linearly dependent on photon energy.

(2) The shift in energy position of the exciton ground state is shown in Fig 2.20. For fields less than 0.85 F_i, the ground state shifts towards lower energies in agreement with perturbation theory. However for $F \geq 0.85 F_i$ the ground state begins to tunnel out the potential well and thus shifts towards higher energies.

(3) The exciton bound states are split and broadened according to their degeneracies as predicted by perturbation theory. It becomes a continuum at very high fields.

(4) Quenching and broadening produces peaks as shown in Fig 2.21. The magnitude of peak A and C may increase or decrease depending on whether it is quenched or broadened. The peak B however never decreases with field since it is related to the degree of ionization of the exciton.

(5) For low fields, i.e. $F < 0.5 F_i$, the energy position of peak B should occur at $E_g - R$.

(6) The separation ΔE_2 in Fig 2.21 should increase as $(F/F_i)^{2/3}$ and be independent of temperature.

(7) For $F \gg F_i$ the external field dominates the Coulomb potential.

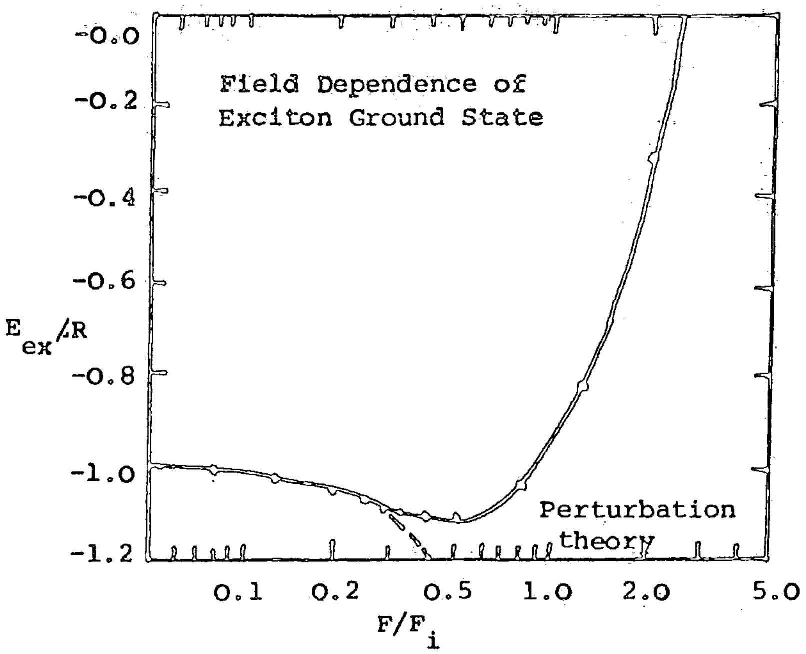

Fig 2.20 Electric field dependence of an exciton ground state energy for a hydrogenic model. The position is measured in units of the exciton Rydberg from the continuum. The electric field is unit of the ionization field F_i.

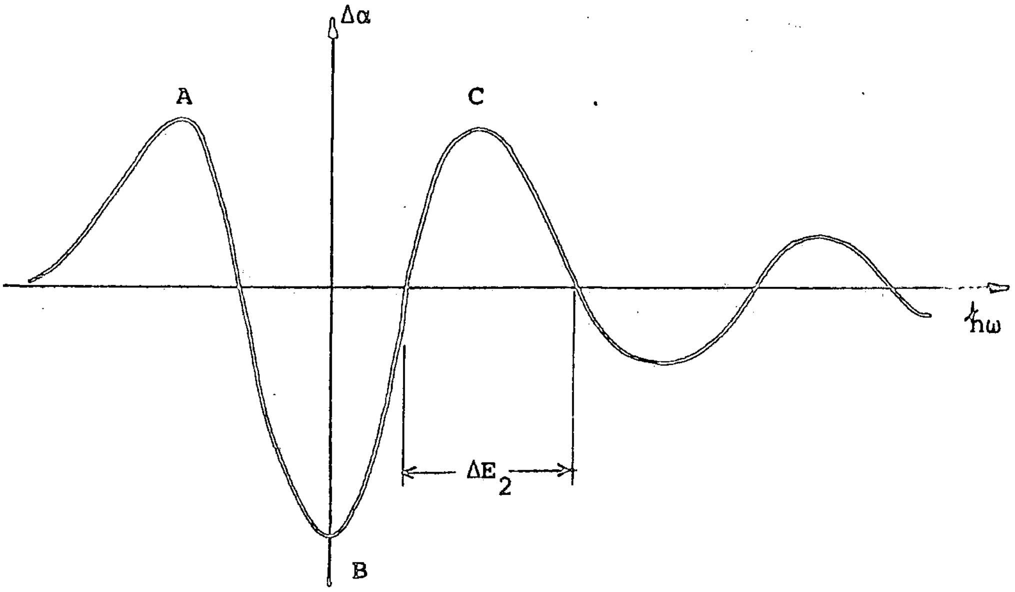

Fig 2.21 Schematic diagram of an excitonic electroabsorption spectrum. Oscillations are due to quenching and broadening of exciton states.

2.7 THE STARK EFFECT

Spectral lines corresponding to transitions between narrow quantized states are normally observed in many materials including organic molecular solids. This subject was discussed in section 2.4, the effect being termed the 'Stark effect' following Stark's observation (42) in 1919. The analysis of the Stark effect can lead to information concerning molecular dipole and higher moments of charge distribution, polarizability of the excited electronic states and parameters describing the inter-molecular interaction in a crystal.

A quantum mechanical treatment of the effect of an electric field on the spectral lines of the hydrogen molecule was performed by Pauling et al (43) and Schiff (44). By using first and second order perturbation theory, it is possible to approximate the first and second order Stark effect. In the case of the hydrogen molecule, only the second order effect has a non-zero solution. The first order effect is normally only observed in molecules which possess a permanent dipole moment. It corresponds to a symmetrical splitting of an energy level about the field free position. By contrast a unidirectional shift in the energy level producing the second order Stark effect is expected for a molecule which exhibits a polarizability. These two effects will be discussed separately.

2.7.1 The First Order Stark Effect

The change in potential energy of a polarizable molecule due to a uniform electric field F_i ; directed in a space-fixed 1-direction which could for example be one of three principal crystal axes ; is the work done on the dipole by changing the field from 0 to F_1 such that

$$V(F_1) = - \int_0^{F_1} m_1 dF_1$$

$$= - \mu F_1 \cos\Theta - \frac{1}{2} \alpha_{11} F_1^2 + \ldots \qquad (2.45)$$

where m_1 is 1-component of the dipole moment in the presence of an electric field defined as

$$m_1 \quad = \quad \mu \cos\Theta \quad + \alpha_{11}F_1 \qquad (2.46)$$

where μ is the permanent dipole moment and α_{11} is one of the six independent components of the polarizability. The definition of the field and dipole moment and their relative orientation are also shown in Fig 2.22 ; it may be seen that the potential energy is lowered when Θ lies between 0 and $\approx \pi/2$.

It is useful to consider an idealized crystal having one molecule as the crystal asymmetric unit and n non-interacting molecules per unit cell. Each molecule in the unit cell is identical in the sense that a charge exploring one molecule would be unable to distinguish it in form from the others.

The approximation of non-interacting molecules is partly realized in practice by using dilute mixed crystals which contain molecules of interest ; the guest, dispersed randomly throughout the host of known structure. The various possible orientations for the case of two molecules per unit cell is shown in Fig 2.23. Two interpenetrating translational sub-lattices A and B are shown and each hoat molecule is assumed to be centro-symmetric. The four possible equivalent guest dipole orientations A_α, A_β, B_α and B_β are also shown. The change in energy per molecule upon application of an electric field F_1, neglecting the polarizability for the present, is given by $-\mu_o F_1 \cos\Theta$ where the ground state dipole moment μ_o makes an angle Θ with the field. Accordingly, the molecules of type A_α and B_α have thier energy lowered (attractive interaction with the field) while A_β and B_β have their energy increased by the field.

The effect on the ground state Γ_o of the whole system can be represented as the splitting shown in Fig 2.24. Similarly the excited states' orientational degeneracy will be split by $2\ \mu_e F_1 |\cos\Theta|$ where μ_e is the dipole moment of the excited state Γ_e. A spectrum of the mixed crystal with

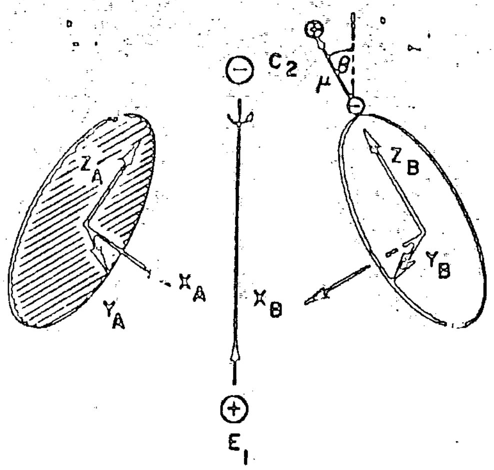

Fig 2.22 Conventions for axes, dipoles, and fields. Note that the dipole vector is positive along the direction from minus to plus.

(45)

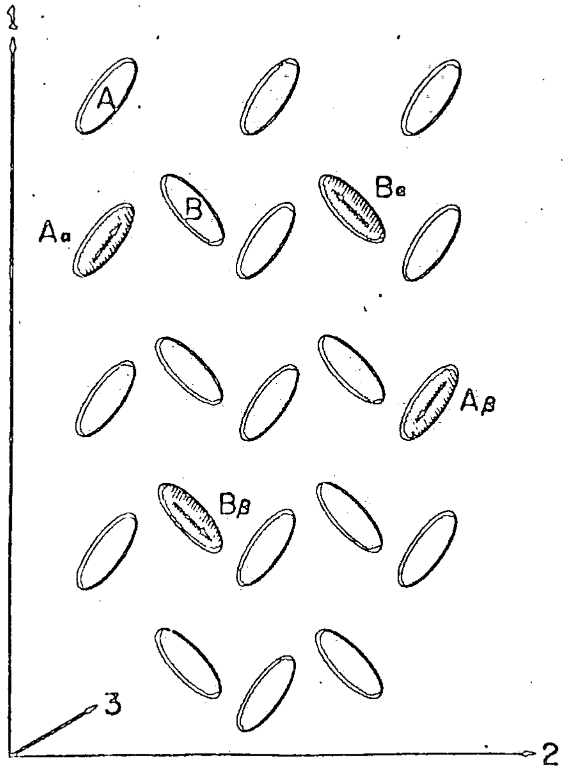

Fig 2.23 Orientation of molecules in a model molecular crystal.

(45)

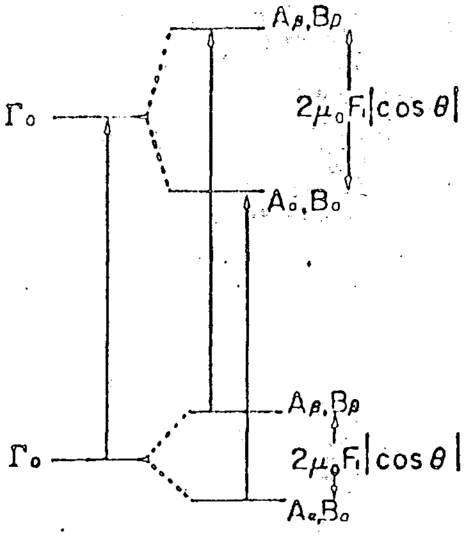

Fig 2.24 Model energy level diagram for oriented polar molecules of a crystal in an electric field assuming a non-polarizable lattice.

$F = 0$ would consist of a single line $(E_e - E_o)$; however in the presence of the field, two transitions will be observed ; one from α and the other from β molecules with

$$\Delta E = E_\beta - E_\alpha = 2F_1(\mu_e - \mu_o) |\cos\theta| \tag{2.47}$$

Note that the Stark splitting predicted here is expected for a transition between any two states that have

$$\Delta\mu = (\mu_e - \mu_o) \neq 0 \tag{2.48}$$

2.7.2 Lorentz Field Correction

The magnitude of $\Delta\mu$ can only be obtained if F_1 which can be more complex than simply the applied field, is known. It is normally assumed that the field is uniform over each molecule and that the fluctuations in field due to the non-uniformity of the electronic distribution around a given molecule can be neglected. Furthermore each polar molecule may be treated as a point dipole and each polarizable molecule as a point induced dipole. Accordingly the average field in the crystal can be used to describe the effective field F. Due to the field produced by the induced dipole moment on the host molecule, the effective field acting on a molecule is different from the applied field. In general, however, we may write

$$F_1 = L_1 E_1 \tag{2.49}$$

2.7.3 The Stark Effect in a Non-Polar Molecule

Some crystals exhibit a resonance interaction between molecules ; the observed spectroscopic transitions then no longer indicate the state of an isolated molecule. Dipolar molecules commonly form centrosymmetric crystals so that the dipole moment of a crystal state may vanish even if the component molecules are strongly polar. In general, for crystals having non-polar space groups, there is no first order Stark effect, but an electric field may mix states and produce the second order Stark effect. In this case the energy shift is proportional to the square of the field.

Liptay et al (46) developed a relationship between the observed change in absorbance ΔA and the difference in static polarizability namely,

$$\Delta A = \left(\frac{1}{2}\,\delta a_x + \delta a_y + \delta a_z \right) L E^2 A'/5 \qquad (2.50)$$

where L is the Lorentz correction, δa_x is the difference in static polarizability along the direction of transient moment and A' is the first derivative of the absorbance with respect to energy.

The second order Stark effect results in a unidirectional shift of an electronic level, producing the first derivative curve of the field free spectrum. In terms of the change in transmission, $\Delta I/I$, for the quadratic case (46)

$$\frac{\Delta I}{I} = \frac{1.15}{hc} \left[\frac{V}{d\sqrt{2}} \right]^2 \left[\frac{\varepsilon + 2}{3} \right]^2 \Delta\alpha \left[D + \frac{\lambda dD}{d\lambda} \right] \qquad (2.51)$$

where V is the applied field, d being the thickness of the sample, ε the static dielectric constant and D the optical density. The term

$\left[\frac{\varepsilon + 2}{3}\right]$ is the Lorentz field approximation in this case.

2.7.4 Summary of Electroabsorption in Molecular Crystals

The main features of the Stark effect in molecular crystals may be summarized as follows :

(1) The first order Stark effect is normally recognised in the electroabsorption spectra as a second derivative of the zero-field absorption curve. The effect indicates the presence of polar space groups in the crystal, leading to a symmetrical splitting of a crystal state.

(2) Crystals having non-polar space groups may exhibit a second order Stark effect. The field induced dipole moment leads to a unidirectional shift of an absorption line. The effect is normally recognized in electro-absorption spectra as a first derivative of the zero-field absorption curve.

(3) Information on crystal symmetry may be obtained by varying the direction of the applied field across the crystal.

2.8 ELECTROABSORPTION IN AMORPHOUS MATERIALS

The magnitude and spectral dependence of an electroabsorption spectrum are governed by the zero-field absorption mechanism. In most amorphous materials, an exponential absorption is observed in the low energy règime of the spectrum followed by a more rapid increase in absorption coefficient satisfying the equation

$$\alpha\hbar\omega = C\,(\hbar\omega - \hbar\omega_o)^m \qquad (2.52)$$

where C is a constant and the value of m observed experimentally range from 1 to 3. Electroabsorption theories have been developed for crystals which exhibit an exponential absorption edge as well as those obeying the power law expressed in equation (2.52). It is therefore reasonable to assume that the various electroabsorption models put forward for crystalline solids may also be relevant to non-crystalline solids. Due allowance must however be taken of transitions into and from localized states.

The effect of an electric field on an exponential type of edge has been studied by Franz (22). In this case the change in absorption coefficient $\Delta\alpha$, is predicted to follow a quadratic field dependence such that

$$\frac{\Delta\alpha}{\alpha} = \frac{\beta^3\hbar^2F^2}{24m^*e} \,. \qquad (2.53)$$

This theory however requires the assumption that the exponential slope β remains unchanged following the application of an external electric field.

Being a free electron theory, it is valid for only materials with small reduced effective mass m^* ($\sim m_o$) which experimentally would display a relatively large value of $\Delta\alpha$.

In the high energy régime where the absorption edge satisfies the simple power law, the field dependence of the change in absorption coefficient, $\Delta\alpha$, is such that

$$\Delta\alpha \quad = \quad BF^n \qquad (2.54)$$

where B is a constant. In this case the value of n is determined by a simple relation namely $3n = 2m$ where m is defined by equation (2.52).

2.8.1 Localized State Transitions

The above models describe the Franz-Keldysh effect. The optical transitions in an amorphous material however, involve both localized and delocalized states, but respond differently to an external electric field. The variation of the local potential described for instance by a distribution of a deformation potential$^{(47, 48)}$, will mainly vary the local distribution of energy states generating the tail of the density of states into the gap region. These states are localized and large transition matrix elements are probable if both the initial and the final states do not overlap. The influence of an external electric field on these types of transitions is to produce the Stark effect which leads to a red shift in the absorption spectrum. Since most amorphous materials exhibit no permanent dipole momentr, then the quadratic Stark effect is most likely to be observed. The electric field may also reduce the degree of localization of those states which should alter the transition matrix elements between localized and delocalized states. These type of transitions are expected to gain strength in an external electric field.

Experiments on the delocalized band states in crystals reveal that an electroabsorption signal decreases rapidly as the lifetime of an electron in a given state is reduced by scattering or defect or phonon-induced perturbation of the periodic lattice. The random potential in a disordered solid should scatter the electrons in delocalized states much more than phonons do in a crystal. In such conditions the electroabsorption response will vanish for energies corresponding to transitions between delocalized states.

The model described above could thus provide a means of locating the position of the mobility edge in an amorphous material and also of determining whether the change from localized to extended states is an abrupt or a gradual process.

2.8.2 Summary

The possibility of observing the Franz-Keldysh effect in disordered solids has been considered. However, the exponential tail normally observed in these materials is attributed to transitions involving localized states. The Stark effect is therefore most likely to be the electroabsorption mechanism in disordered solids. In addition, the external electric field could slightly reduce the degree of localization of these states and should alter the transition matrix elements between localized and delocalized states. These transitions are expected to gain strength in an external field.

CHAPTER 3

EXPERIMENTAL TECHNIQUES

3.1 INTRODUCTION

In the previous chapter, the theory of electroabsorption which is relevant to the present work was reviewed. It is a particular branch of an experimental method known as modulation spectroscopy. The technique involves the application of large electric fields to a specimen and the measurement of a small resultant change in transmission, and thus the consequent change in the optical absorption. The experimental technique and equipment used during the course of this work will now be described.

The chapter is divided into five sections. Those describing the zero-field absorption, and the electroabsorption measurement techniques receive most emphasis. However, supporting experiments were also performed. These included d.c. conductivity, a.c. conductivity and capacitance measurements and photoconductivity. Therefore, brief descriptions are also given of these methods.

3.2 ZERO-FIELD ABSORPTION

The magnitude of $\Delta\alpha$, the change in the optical absorption coefficient induced by the electric field and its spectral dependence, are governed by the zero-field absorption mechanism. Hence, a vital part of the experimentation was equipment to accurately measure the absorption coefficient at a variety of temperatures and over a wide spectral range.

3.2.1 The Optical System

The optical system was based on the Hilger/Watts D331 double monochromator equipped with either 1.0 μm or 0.5 μm gratings. This instrument is capable of resolving the 3610.5 - 3612.8 Å cadmium doublet. The optical source was an Atlas 24V, 250 W projector bulb. It has a nominal lifetime of 50 hours. However, this could be greatly extended by operating at slightly less than 24V and by cooling with compressed air. The lamp was powered from a stabilized mains supply, stepped down with a Variac. A period of stabilization of about ninety minutes was allowed before measurements commenced.

Radiation of a suitable wavelength was focussed onto the input slit of the monochromator by means of two converging quartz lenses. The input and the output slits widths could be adjusted between 0.004 mm and 3.00 mm. The grating, and thus the wavelength of the radiation, could be varied manually or by using small electric motors which have a number of different scanning rates from 250 Å in two hours to 250 Å per minute.

These gratings were capable of producing second order effects which could be eliminated by means of a set of Optics Technology band pass filters. Even though most of these filters transmitted less than 0.05% below their cut-off, unwanted orders could still be detected due to the very high sensitivity of the detector running at maximum power. A series of filters was thus used to obtain the correct spectral purity.

Two types of detectors were employed to monitor the transmitted light depending on the spectral area of interest. For wavelengths less than 1.0 μm, an EMI 9659B photomultiplier with an extended S20 response was normally used. An RCA C31034 photomultiplier tube was also employed. The cut-off wavelength of both photomultipliers is approximately 9300 Å The quantum efficiency of the extended S20 type photomultiplier tube is illustrated in figure 3.1. The response between 8000 Å and 10,000 Å is extremely small, decreasing to less than 1% for the area above 8500 Å However, by operating the tube at maximum permitted power, it was found possible to detect the transmitted light up to 1 μm region. The extremely

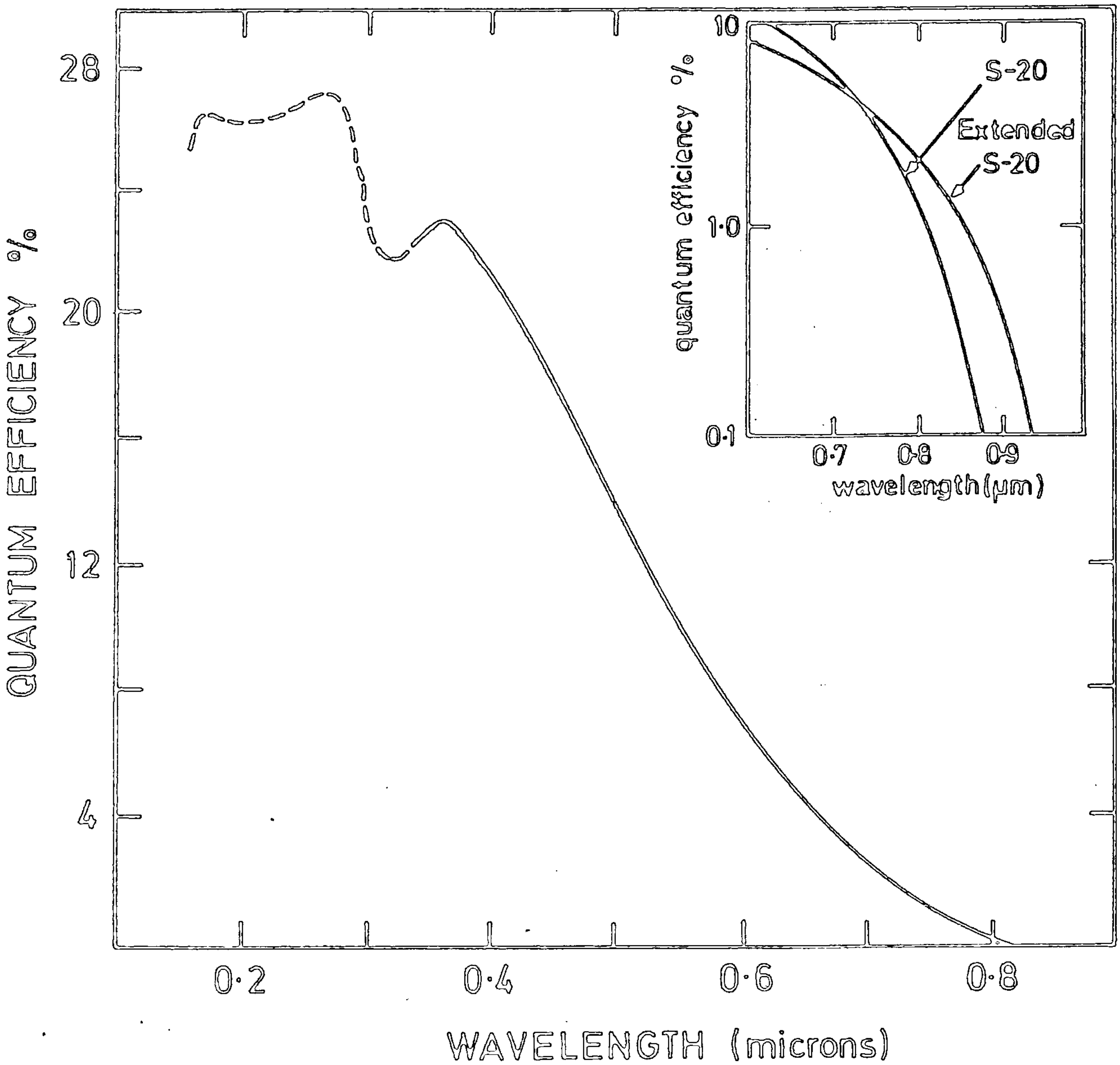

Figure 3.1 : Quantum efficiency of an S-20 photomultiplier tube.

low detector sensitivity resulted in very noisy signals. This will be discussed in section 3.3.3. The signal from the photomultiplier was taken to a load resistor and thence to the detection system.

Within the infrared region, namely 1-5 μm, a Mullard FPY 35 Indium Antimonide infrared detector was used. The detector operated at 77K, and was cooled by using liquid nitrogen transferred by means of a Rank automatic cooling head, type ZX6481. It was only used however to look for the absorption in the region of 1-2 μm. The signal from the detector was taken to the detection system as shown in figure 3.2.

3.2.2 The Sample Chamber

The samples were mounted in an Oxford Instruments CF 104 continuous flow cryostat. The cryostat consisted of a centrally positioned cold finger attached to a heat exchange copper block which could be rotated about its vertical axis to face any direction as shown in figure 3.3. It was covered by a radiation shield which in turn was surrounded by the outer wall of the cryostat. The optical points of the cryostat were equipped with Spectrosil windows, and attached directly to the monochromator on one side, and to the photomultiplier on the other side to prevent any stray light entering the chamber.

Liquid nitrogen could be pumped in through the heat exchange block from an outside dewar. A 30W heater was also fixed in such a way that it had a good thermal contact with the heat exchange block and cold finger. The temperature of the sample was determined by the flow rate of the liquid nitrogen and the voltage applied to the heater. This could be done either manually or automatically by means of an Oxford Instruments DTC2 digital temperature controller. This instrument

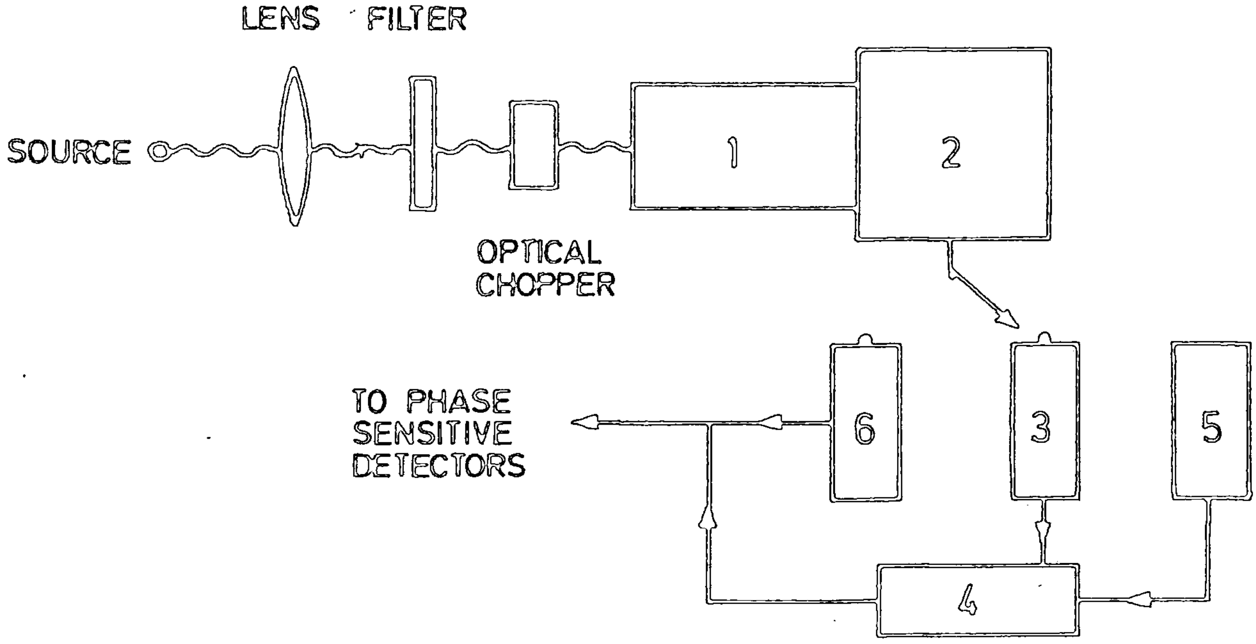

1 – MONOCHROMATOR
2 – CRYOSTAT
3 – LOAD RESISTOR
4 – PHOTOMULTIPLIER
5 – P.M. POWER SUPPLY
6 – INFRA-RED CELL

Figure 3.2 : The optical system block diagram.

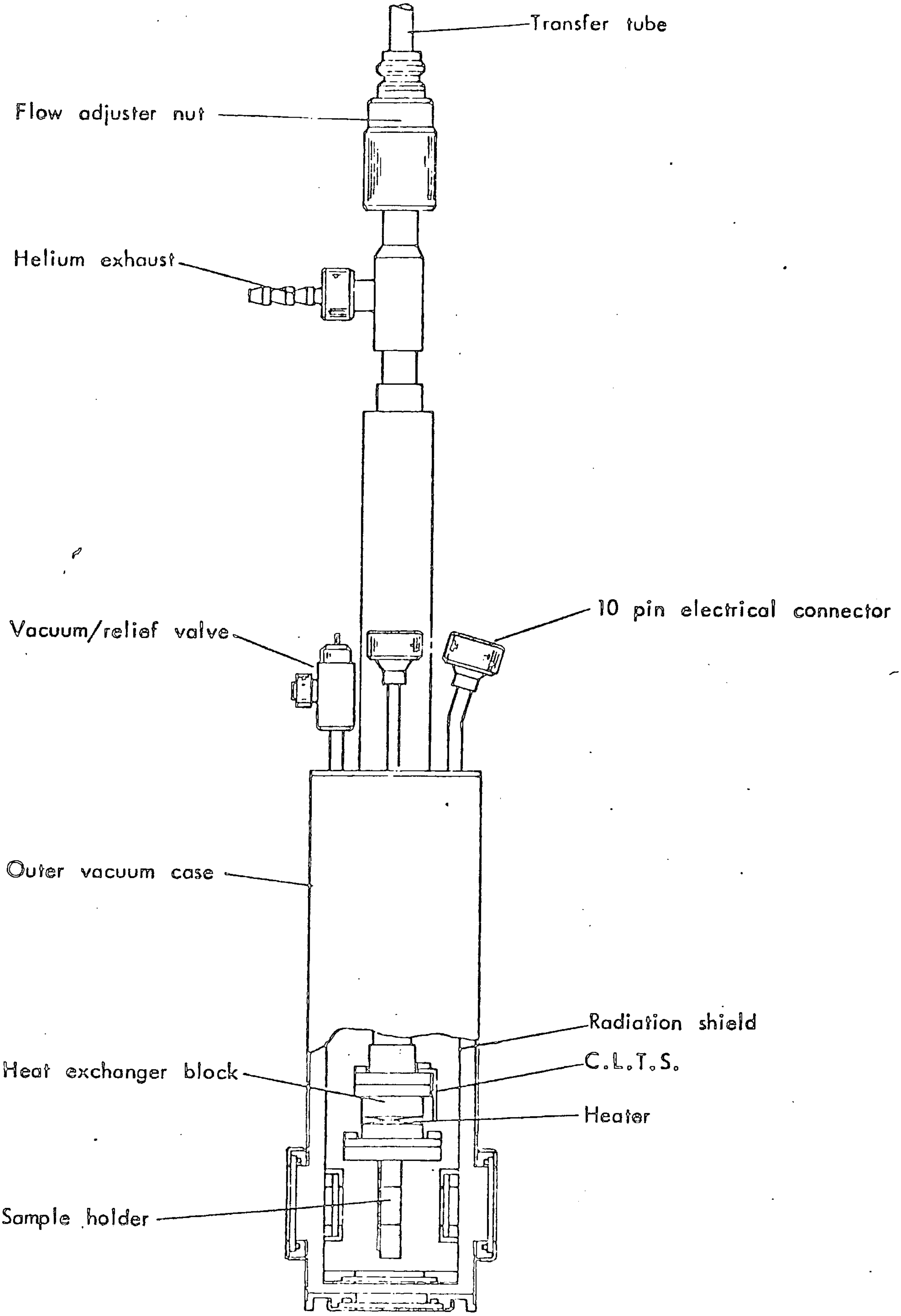

Fig 3.3 : CF104 Continuous flow cryostat.

controlled the output of the heater depending on the difference between the measured and the set temperatures. A temperature of an accuracy of ± 0.1K could be achieved by this method.

A carbon linear temperature sensor was used as the temperature detector. It was mounted on the cold finger, in close proximity to the sample. Good thermal contact was ensured by using G.E. varnish to mount the sample.

It was necessary to evacuate the cryostat to provide a good thermal insulation and to prevent water vapour condensing on the sample. This was achieved using an Edwards 3" diffusion pump capable of pumping down to 10^{-6} torr.

3.2.3 Experimental Procedure

The incident light was modulated at 400 c.p.s. by an optical chopper. The transmitted light, I, was detected by a photomultiplier and the subsequent signal fed into a Brookdeal lock-in amplifier, Model 9501, after first passing through a load resistor. Maximum signal was measured at the same frequency as the modulated light. This could be achieved by adjusting the reference phase angle.

The sample was then moved out of the light beam by rotating the sample holder 90° about its vertical axis. This enabled the incident light, I_o, to be measured. The light in this case passed through an aperture identical in size to that over which the sample was mounted, and travelled exactly the same path length before detection. The incident light measurements were done subsequent to the measurements of transmitted light because the equipment was a single beam instrument.

The two recorded signals I and I_o are related to each other by the equation

$$I = \left[I_o e^{-\alpha d} (1-R)^2 \right] \Big/ \left[1-R^2 e^{-2\alpha d} \right] \qquad (3.1)$$

where α and R are the absorption and the reflectance coefficients respectively. The value of R was taken from published data and small changes in R over the energy range of interest were neglected. It was found in our measurements that the value of the term $R^2 e^{-2\alpha d}$ was always negligible. This reduced the above equation to

$$I = I_o e^{-\alpha d} (1-R)^2 \qquad (3.2)$$

from which values of α were deduced. Absorption coefficients at various wavelengths were plotted for several temperatures, typically 295K, 150K and 77K.

3.3 ELECTROABSORPTION

The optical system already discussed in section 3.2.1 was also used in electroabsorption measurements. It could provide as high transmitted light as required. The 'red shift' of the absorption edge of crystalline and non-crystalline solids upon application of a very large external electric field as predicted by theory, normally requires an a.c. technique detection system. This is due to the fact that the fine structure has a separation of about 10^{-3} eV when electric fields of the order of 10^4V/cm are applied across a crystal with an effective mass less than the free electron mass. The Stark effect also involves very small changes in α ; typically one has to apply 10^5-10^6 V/cm to observe a change of the same magnitude. The technique offers an extremely sensitive detection system with very high signal-to-noise ratio and is thus capable of resolving the structure. Since a large a.c. field must necessarily be applied across the sample, a section of this chapter describes the pulse generation system.

3.3.1 The Pulse Generation System

An electric field was applied across the sample in the direction of light propagation. It is accepted in electroabsorption theories that a positive going pulse is equivalent to a negative going pulse in so far as the effects produced should be the same. For this reason a square wave such as illustrated in figure 3.4a(1) was used. In addition, it was found more convenient to have a small rest period(1) between positive and negative going pulse as shown in figure 3.4a(2). However, distortion in the high voltage square waves were normally observed at frequencies above 2.0 kHz. Since it was necessary to work at frequencies greater than 2.0 kHz, a sinusoidal waveform, such as illustrated in figure 3.4a(3), was also sometimes used. In this case each half of the cycle has an equivalent effect.

The difficulties with the sinusoidal waveforms is that the observed electroabsorption signal is a composite of changes produced by the various magnitudes of voltage in the sinusoidal pulses dominated by the peak. It is difficult therefore to estimate the average voltage applied to the sample, since the transmission changes are, in general, a non-linear function of voltage.

Unidirectional waveforms of the type shown in figure 3.4a(4) were sometimes employed in our experiments. This was particularly useful if large electric fields were required in producing observable signal.

The above mentioned waveform generation system was based on an Advance Pulse Generator Model PG511, on a Keithley 240A high voltage power

Figure 3.4a : Pulse shapes with the respective voltage and frequency ranges.

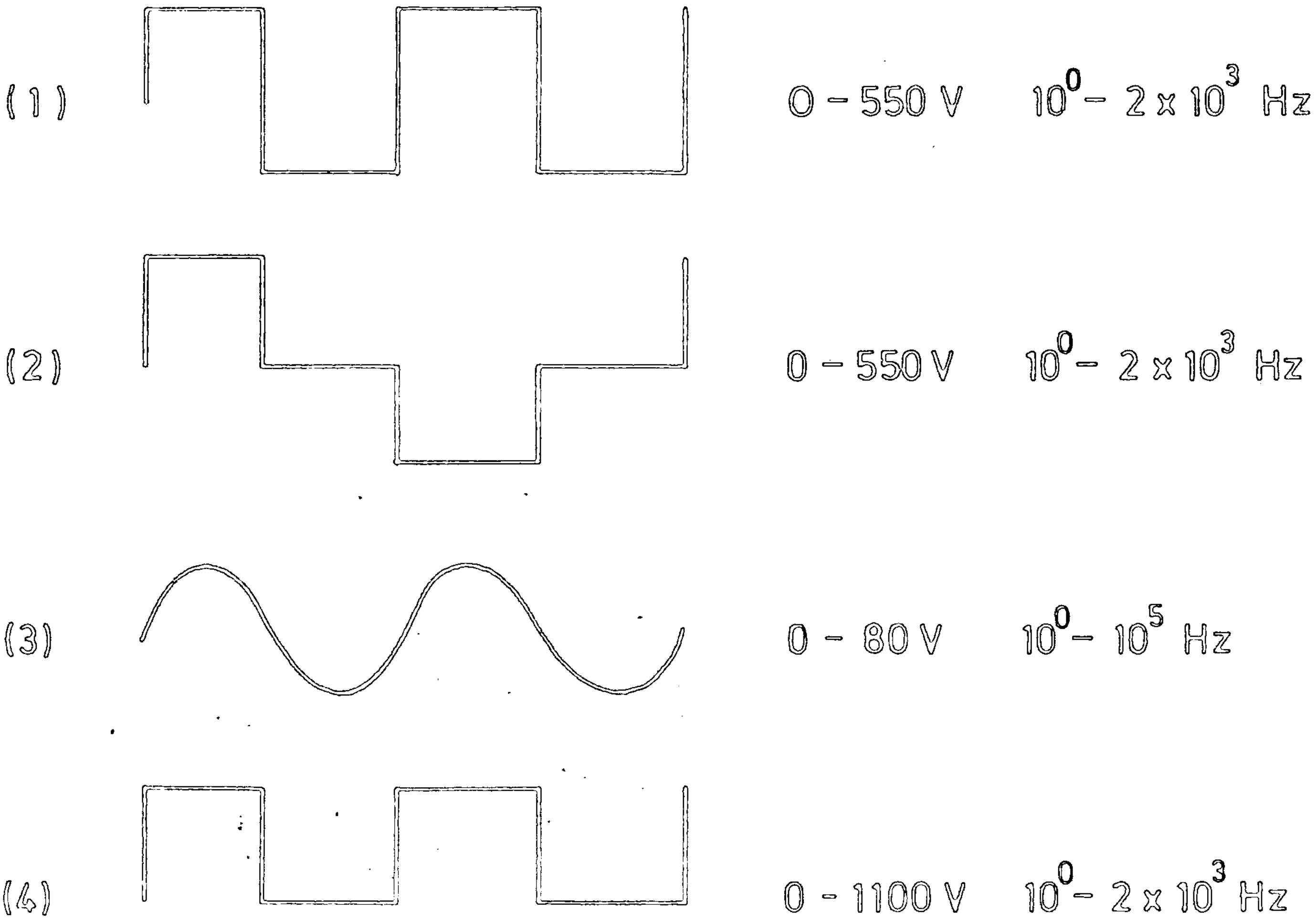

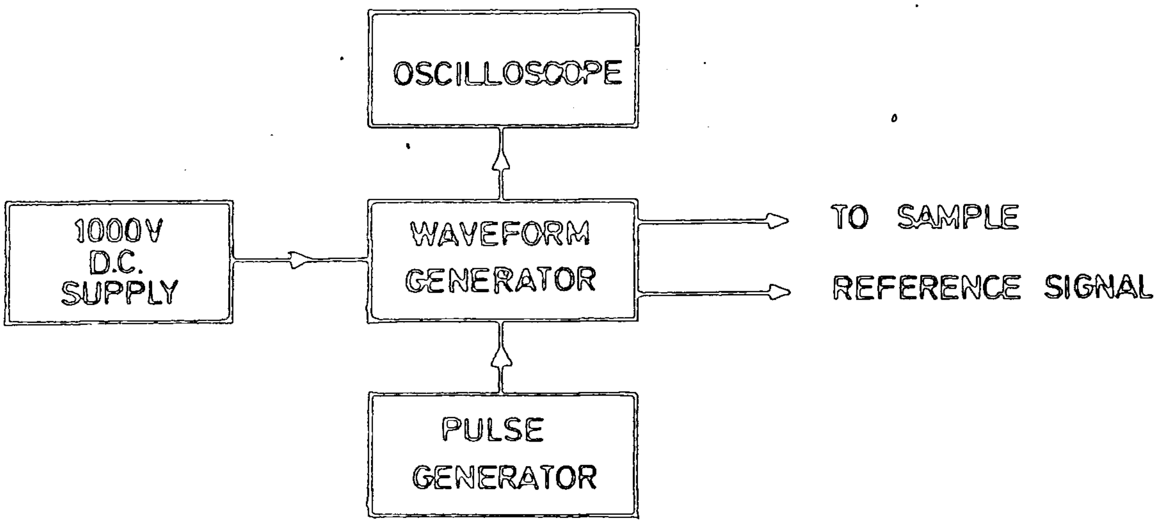

Figure 3.4b : The pulse generation system block diagram.

supply. A high voltage from the power supply was applied between the cathode and the anode of a high voltage triode valve with low voltage pulses from the pulse generator being fed to its grid. The high voltage output from the valve was thus modulated by the low voltage pulses applied to the grid. By capacitively coupling the valve to the sample, positive and negative transgression voltages were obtained, while the unidirectional positive pulses were made available by using d.c. coupling. A delay between the positive going pulse and negative going pulse could be obtained by inserting a delay unit between a pulse generator and the triode. A schematic diagram of the pulse generation system together with the respective voltage and frequency ranges is shown in figure 3.4.

To ensure that the full electric field appeared across the sample, the capacitor formed by the cell had to be charged fairly rapidly and consequently the unit was built to sustain currents up to 10 mA. The square pulses employed also had extremely fast rise and fall times. The frequency and the mark-space ratio of the generated pulses could be varied at the pulse generator. The frequency range of the system was between 1.0 kHz and 10.0 kHz. In practice, however, distortion of the pulse shape was noticed at approximately 2.0 kHz and became serious at 5.0 kHz. Accordingly, square wave modulation was not used above 3.5 kHz to prevent introducing error into the numerical results.

An Advance low frequency oscillator model HIE was used to generate sinusoidal waves. It had a maximum output of 80V peak-to-peak and could be operated at frequencies up to 50 kHz.

The a.c. voltage could be made to oscillate about a negative or positive level by superimposing a d.c. voltage on the above mentioned waveforms. This was made possible by incorporating an extra 0-200V power supply in the system.

3.3.2 The Detection System

The signal recovery of the change in transmission was achieved using a couple of Brookdeal lock-in amplifiers, Model 9501. A schematic diagram of the equipment is shown in figure 3.5. The Brookdeal 9501 phase sensitive detector contains a facility for reference frequency doubling. The photomultiplier output contains two types of signal in this measurement, a large signal resulting from the modulation of the incident light beam by an optical chopper at 400 c.p.s. and a much smaller signal due to the small periodic change in transmission upon the application of the electric field. The signals were fed into two Brookdeal 9501 lock-in amplifiers. The first was referenced at the frequency of the optical chopper, namely 400 c.p.s. and thus was used to measure the transmitted light. Since the change in transmission due to the electric field is independent of the sign of the field, the second phase sensitive detector was referenced at twice the frequency of the modulating field. However, a signal was also observed at the fundamental frequency. This deviation from the idealized case will be discussed later.

Interference between the two signals could be observed if the frequency of the electric field was very close to the frequency of the optical chopper. In this case the zero-field transmission must be determined subsequently or if the transmitted light is large, the d.c. signal from the photomultiplier (with the optical chopper off) can be connected directly to the chart recorder.

The second lock-in amplifier system also incorporated a Brookdeal 5004 preamplifier and a Brookdeal 5011F active filter. The first was capable of amplifying the small signal due to the electric field while the filter was used to improve the signal-to-noise ratio and thus reduce the noise which was also amplified by the amplifier. The filter could be operated in either notch mode, in order to exclude a particular noise frequency, or in band pass in which case a narrow band of frequencies centred on the reference frequency was passed. The two units were plug-in accessories to the 9501 lock-in amplifier system. Maximum signals were

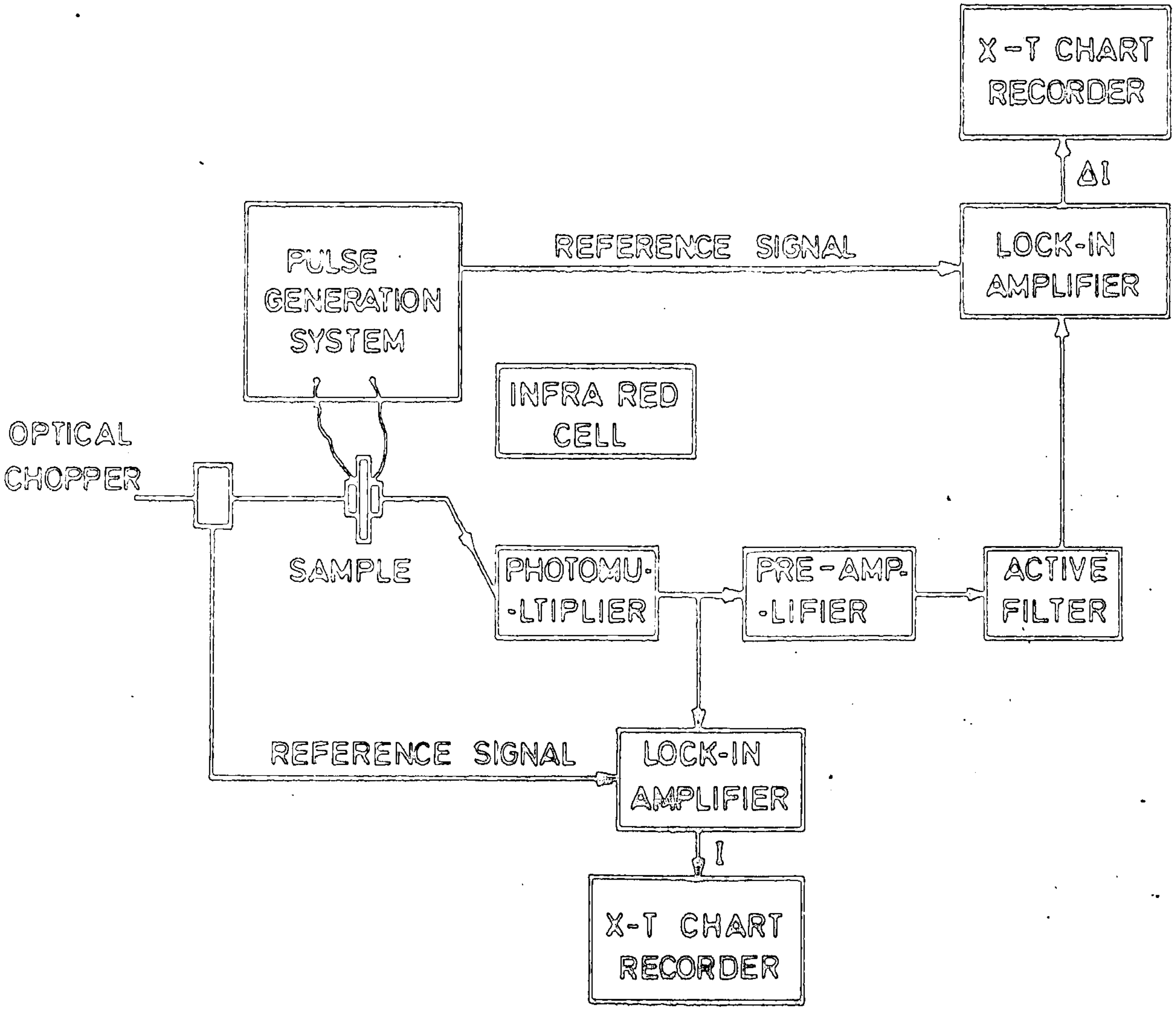

Figure 3.5 : Schematic diagram of the detection system.

produced by adjusting the reference phase angle and the output was taken to a Bryans 28000 X/T chart recorder. A complete arrangement of equipment used in this experiment is shown in figure 3.6.

The two quantities namely, Δ I, the change in transmission due to the field, and I the zero field transmission can thus be measured as a function of wavelength, thereby producing an electroabsorption spectrum. In practice, because of electrical noise, the procedure was achieved by scanning at a very slow rate utilising a large time constant up to 100 seconds. If the scanning facility was used, one had to ensure that the phase angle required to maximise the signal was independent of wavelength. Otherwise a point by point measurement was required with the phase angle being adjusted at each point.

It can be shown that ΔI and I are related to each other by the equation

$$\Delta\alpha = -\frac{1}{d}\left(\frac{\Delta I}{I}\right)\left[1 - R^2 e^{-2\alpha d}\right] \Big/ \left[1 + R^2 e^{-2\alpha d}\right] \qquad (3.3)$$

where d and R are the thickness and reflection coefficient of the sample, respectively and $\Delta\alpha$ is the change in absorption coefficient. For the sample studied, it was found that the term $R^2 e^{-2\alpha d}$ was negligible and thus reduced the equation to

$$\Delta\alpha = -\frac{1}{d}\left({}^{\Delta I}/_{I}\right) \qquad (3.4)$$

3.3.3 Electrical Noise

The change in transmission is in general extremely small, typically one part in 10^4, leading to signals buried in noise. Steps had been taken to reduce the noise level. Short low noise cables and filters were used. Photon shot noise was predominated in the photomultipler. This noise

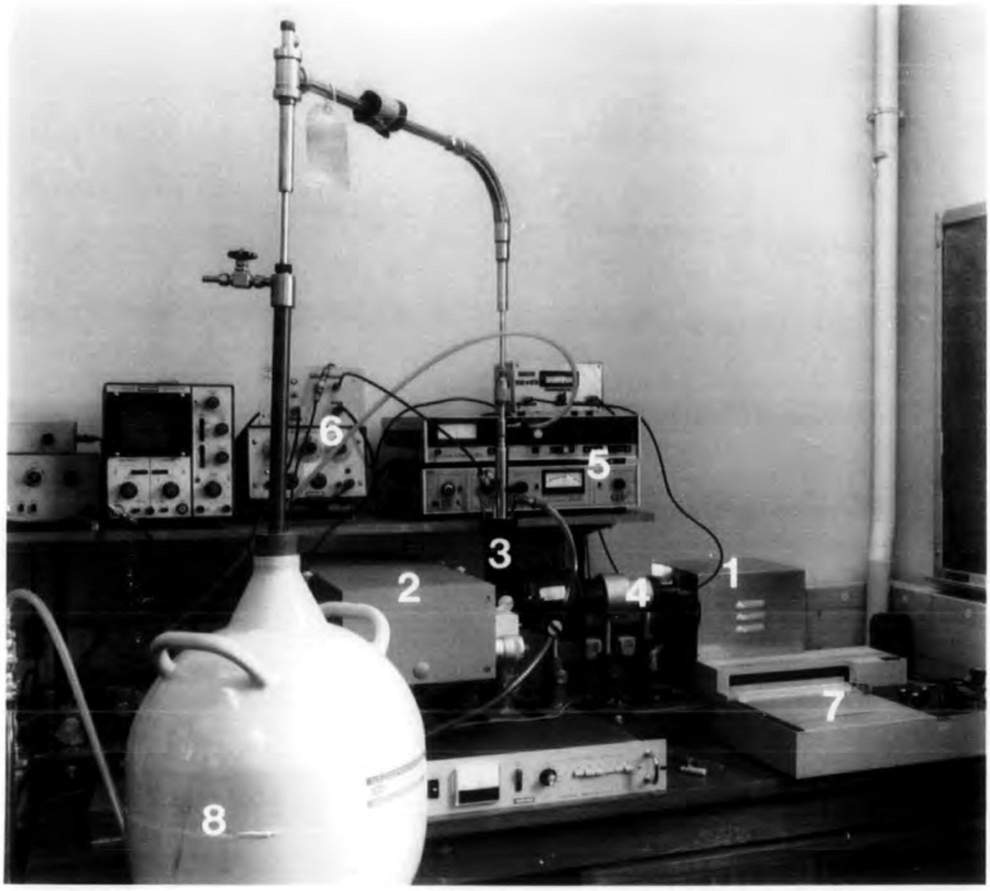

1 - LIGHT SOURCE
2 - MONOCHROMATOR
3 - CRYOSTAT
4 - PHOTOMULTIPLIER
5 - DETECTION SYSTEM [LOCK-IN AMPLIFIERS]
6 - PULSE GENERATION SYSTEM
7 - CHART RECORDER
8 - LIQUID NITROGEN DEWAR

FIG. 3·6 Photograph of electroabsorbtion equipment.

however goes roughly as the square root of the signal and thus a strong light source is suggested. There is, however, a practical limit to the intensity of the source that can be used.

3.4 D.C. CONDUCTIVITY MEASUREMENTS

Prior to electroabsorption experiments, d.c. conductivity measurements were performed for amorphous and crystalline samples in the temperature range 300K to 77K.

The d.c. conduction measurement equipment for high resitivity material is shown in figure 3.7. A stainless steel gas exchange cryostat mounted firmly on a metal rack was used. It was evacuated by using an Edwards ES 330 rotary pump to a pressure as low as 10^{-3} torr to prevent water vapour condensing on the samples. The cryostat was placed in a glass dewar which could be raised or lowered as required and could be filled with liquid nitrogen. A 150 W circular heater surrounded the area in which the sample was positioned. Dry helium exchange gas was allowed to pass through the cryostat at a controlled rate. This was done accurately using a needle valve. The heater and the cooling jacket of liquid nitrogen provided an equilibrium temperature which could be varied by changing the flow rate of helium gas. The dewar had two walls with adjoining space evacuated to provide a good thermal insulation. For safety reasons and ease of handling, it was assembled in a box.

A Eurotherm temperature controller was used to supply power to the heater using a feedback system. A copper-constantant thermocouple was used to measure the temperature of the sample. It was placed very near to the sample in order to obtain accurate temperature readings. Since a room temperature reference was used, a relevant compensation circuit was contained in the Eurotherm. The voltage supplied to the heater was varied automatically by the controller depending on the difference between the set and the measured temperatures. An accuracy of ± 1 K was possible in the range 400 K to 100 K.

The sample was mounted within the circular heater which could be moved upward or downward along three hollow pillars. A PTFE block with an adjustable clamp was positioned at the bottom of the heater as shown in figure 3.8. The sample was normally mounted on a PTFE disc which was then clamped on the PTFE block. This helped eliminate leakage currents. Highly insulated wire was used to make any electrical connections ; this was passed along the centre of two earthed pillars to ensure good screening and minimize electrical noise. The cryostat was earthed and no earth loop was allowed to occur.

A Keithley 241 high stabilized voltage with a range of 0.01 V to 1000 V in unit steps was used as a power supply. The potential was applied to the sample in the cryostat. The currents produced were measured by means of a Keithley 410 A picoammeter, with a range of 10^{-14} A to 10^{-2} A. The meter had an input impedance of less than 3×10^{9} ohms on the 3×10^{-13} A scale decreasing to 1 ohm on the 10^{-3} A scale ; it was thus quite suitable for our purpose. The picoammeter produced a full scale deflection output of 1 V and was connected to a Bryans 28000 X/T recorder.

3.4.1 Experimental Procedure

Several precautions were taken to ensure reproducible d.c.conductivity measurements.

(1) A large voltage was applied across the sample to obtain a good contact between the metal electrodes and the sample.

(2) The sample was heated to a high temperature at low voltage to remove any space charge introduced by the above procedure.

(3) The sample was subsequently cooled to the desired temperature and current-voltage plots were taken for increasing voltage.
Current values were only recorded when the plot on the Bryans 28000 X/T recorder showed a constant value with time, for a particular constant voltage and temperature.
The same procedures were followed when measurements were done with

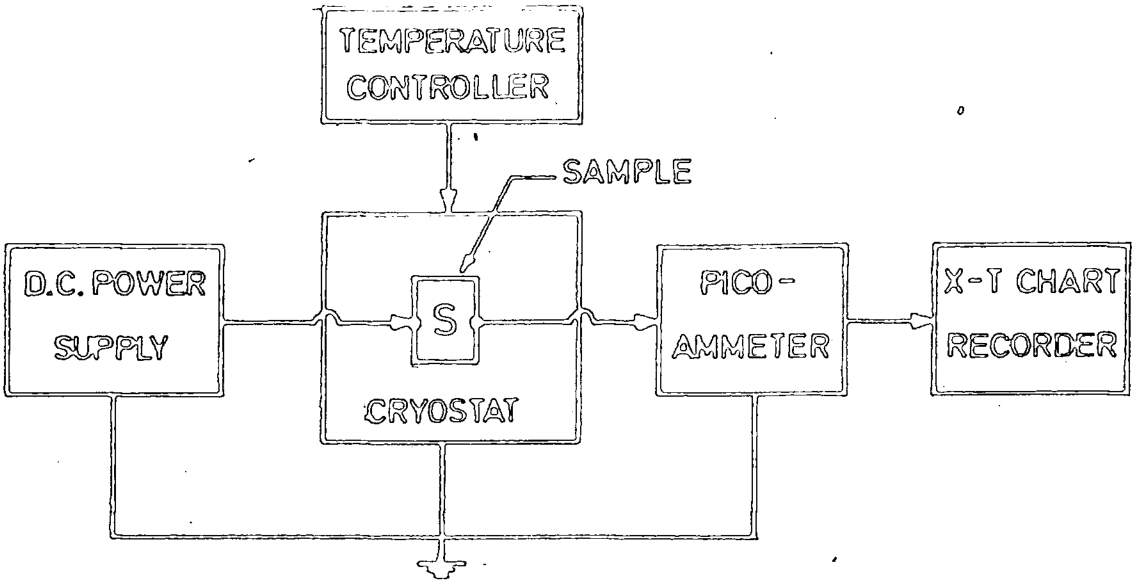

Figure 3.7 : The d.c. conductivity measurement system block diagram.

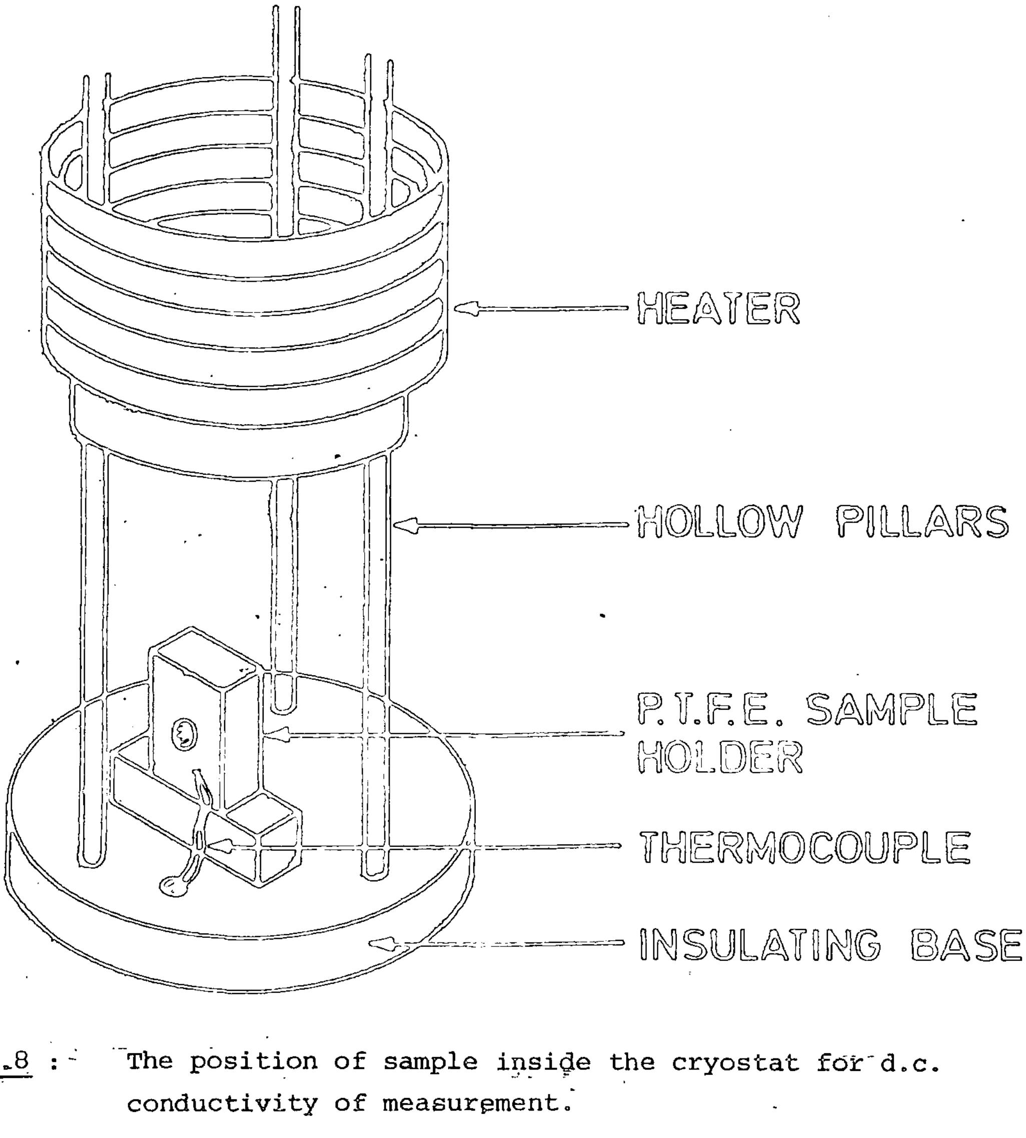

Figure 3.8 : The position of sample inside the cryostat for d.c. conductivity of measurement.

reverse voltage. Several I-V measurements were performed at different temperatures. This enabled activation energy values to be measured. Care was taken to ensure the current did not change from Ohmic to space charge limited region during a run. The activation energy measurements were always done for decreasing temperature.

Special precautions were taken before commencing conductivity measurement. For example, a small voltage was applied to the sample at room temperature and currents recorded. On each subsequent occasion when measurements were to be taken, the same voltage was applied and the currents checked. Any space charge injected in to the sample can be noticed in this way and steps taken to remove it. It also enabled any permanent change in characteristic, due to degradation of the contact to be detected.

3.5 A.C. CONDUCTIVITY MEASUREMENTS

A.C. conductivity and capacitance measurements were also performed on the semi-insulating crystalline and amorphous materials before the corresponding electroabsorption studies. In these materials the conductance component dominated that due to capacitance so that standard bridge techniques could no longer be used. To cope with the large phase angle, a phase sensitive detection system similar to that used by Polanco et at$^{(2)}$ was employed. The narrow band properties of such a system give an enhanced signal/noise ratio over a wide range of frequencies. A schematic diagram of the apparatus is shown in figure 3.9. The device may be regarded as a capacitance, C_x, in series with a resistor R_x. At frequency ω, the total impedance is equal to

$$Z_x = \left[G_x + i\, G_x \omega \right]^{-1} \tag{3.5}$$

where $G_x = R_x^{-1}$. If a small a.c. voltage, V_1, at frequency ω is applied to the sample, in series with a standard capacitance, C_o ; the output voltage V_o across C_o may be considered to have two components, one in phase with V_1

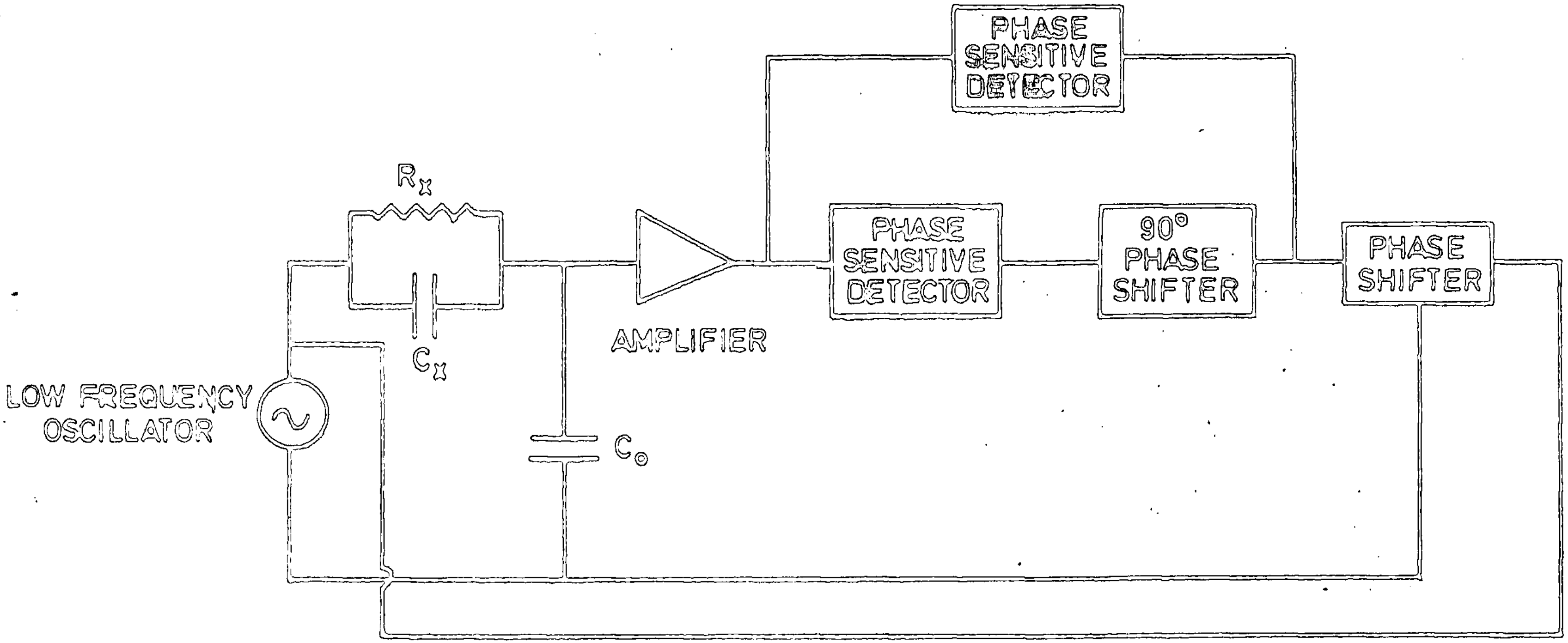

Figure 3.9 : The a.c. conductivity measurements circuit diagram.

and the other in quadrature with V_1. Using simple a.c. theory it may be shown that the two are related to each other by the equation

$$\frac{V_o \text{ (in phase)}}{V_o \text{ (out of phase)}} = \frac{\omega^2 C_x (C_o + C_x) R_x^2 + 1}{\omega C_o R_x} \qquad (3.6)$$

if C_o is chosen so that $C_o >> C_x$ but maintaining $G_x << C_o \omega$, the above equation then reduces to

$$\left[V_o \text{(in phase)} \right] \Big/ \left[V_o \text{(out of phase)} \right] = C_x R_x \omega \qquad (3.7)$$

Equation (3.7) has been used to evaluate G_x and C_x over a wide range of frequencies between 10 Hz and 10^6 Hz.

In the actual measurements, the voltage V_1 applied to the device was extracted from an Advance SG 67A low frequency oscillator. The voltage is required to be as low as possible to avoid any non-linear effect and was normally less than 100 mV. The output voltage V_o across the capacitor C_o was fed into a Brookdeal 450 low noise amplifier from which the output voltage was taken to two Brookdeal 411 phase sensitive detectors. The reference signals, which were taken to a Brookdeal 421 reference unit, were derived from the low frequency oscillator. The reference unit provided two subsidiary reference outputs with a phase difference of 90^o and served as the reference inputs of the phase sensitive detectors. The phase of the reference unit inputs could be shifted with respect to its input and hence used to compensate for any stray sources of phase shift, such as the resistive input of the low noise amplifier lead capacitance, etc.

The outputs of the detectors referenced with a 90^o difference between them could thus be used to detect the 'in phase' and 'out of phase' component of V_o. The capacitance C_x, and the conductance G_x are in direct proportion to the 'in phase' and 'out of phase' components, respectively.

Since the conductance term was usually very small, a digital voltmeter was employed for greater accuracy.

3.5.1 Experimental Procedure

To set up the system a standard capacitor of known value C_x, very close to the value of the sample capacitor C_s was placed in the test condition. The phase-shifter was then adjusted so that no output was observed from the conductance indicating phase sensitive detector. The output of the capacitance indicating phase sensitive detector was recorded for this known capacitance. The same procedure was employed to calibrate the conductance indicating phase sensitive detector with a known R_x. The sample was then inserted to replace the standard capacitor and resistor, and its capacitance was calculated by direct comparison with C_x, while its conductance was deduced from equation (3.7). Care was always taken to ensure that C_o was at least ten times greater than C_s and a large number of resistors and capacitors were available for calibration purposes.

3.6 PHOTOCONDUCTIVITY MEASUREMENTS

When studying the photoconductive properties of materials, the samples were normally mounted in the Oxford Instrument CF104 cryostat linked to the Oxford Instrument DTC 2 digital temperature controller described in section 3.2.2. Monochromatic light was obtained from a Hilger/Watts double monochromator with an Atlas 250W projector bulb as an optical source. Spurious harmonics were eliminated using the Optics and Technology band pass filters mentioned previously.

Photoconductive response curves were obtained by applying a constant voltage across the sample and measuring the currents flowing through a sensitive Keithley 410 A picoammeter as the wavelength of the radiation falling on the sample was scanned from high to low wavelengths. The scanning rate used was very slow to ensure that measurements were taken under steady state conditions. The output of the picoammeter was connected to a Bryans 28000 X/T chart recorder. Any d.c. voltage applied to the sample was derived directly from a Keithley 240 stabilized power supply.

All curves required a correction for the energy distribution of the light source, and thus the spectral response of the source-filter-grating combination was calibrated using either a Gamma Scientific digital photometer, model 2400 or a United Technology Inc. photodiode. The latter was especially used for the spectral range between 350 nm and 1160 nm. However, it was found more convenient to use the Gamma Scientific photometer for the region between 400 nm and 700 nm. The calibrated responses are shown in figure 3.10.

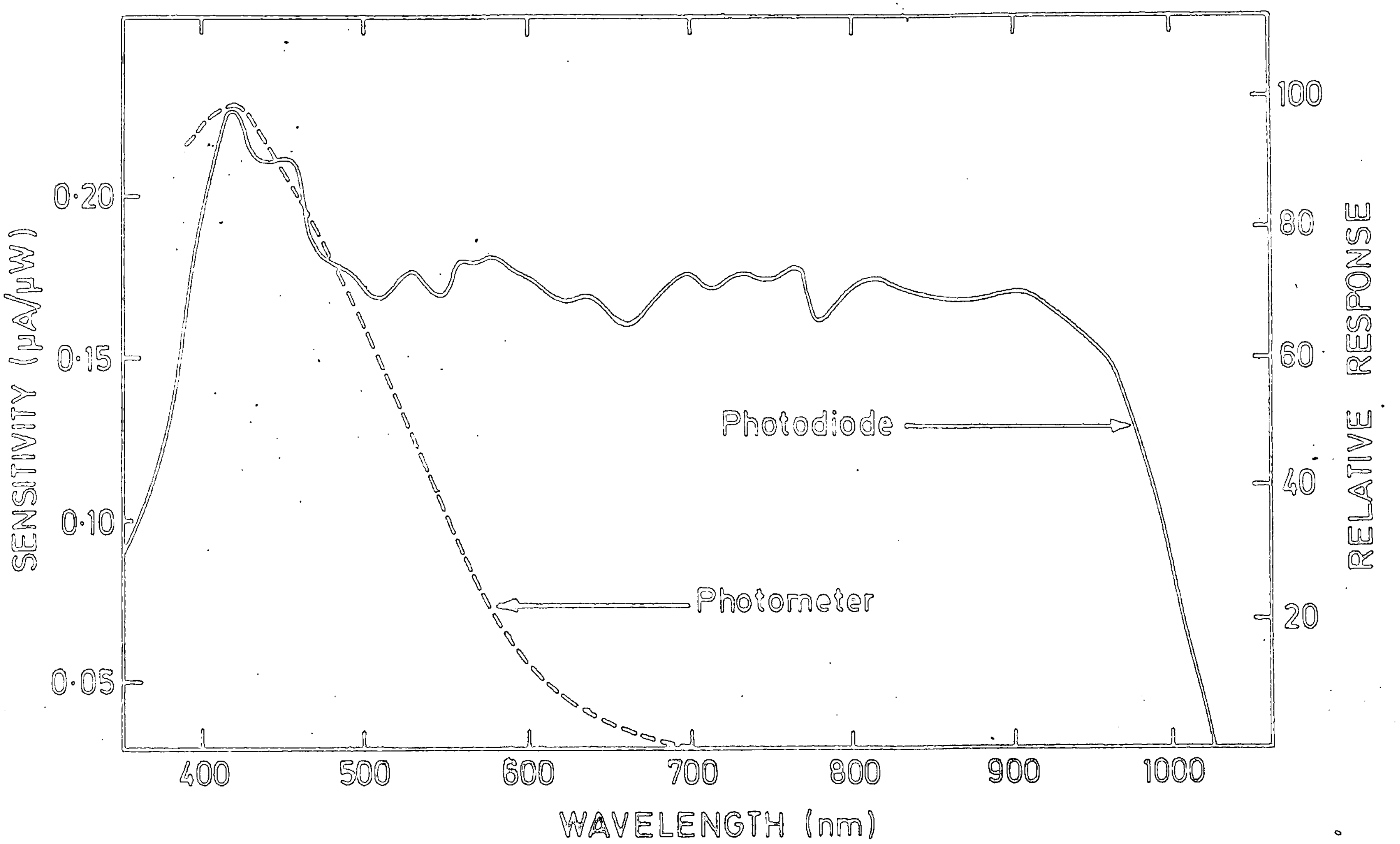

<u>Figure 3.10</u> : Spectral responses of the Gamma Scientific photodetector and the United Detector photodiode.

CHAPTER 4

ELECTROABSORPTION IN CADMIUM TELLURIDE

4.1 INTRODUCTION TO CADMIUM TELLURIDE

Cadmium telluride is a semiconducting material which crystallizes with a 1:1 atomic ratio between cadmium of group II and tellurium of group VI in the periodic table. It is therefore known as one of the II-VI compound semiconductors. Both elements are located in the fourth row of the table with atomic numbers of 48 and 52, respectively. The average atomic number of 50 is the highest for any semiconducting compound in the II-VI series.

There is considerable interest in the potential applications of single crystal CdTe. For example, it is known that the material is sensitive to many types of radiations. The combination of large band gap, high average atomic number and reasonable mobility-lifetime product for both electrons and holes makes CdTe an attractive material for use in gamma radiation detectors. Semi-insulating CdTe offers the additional advantage that devices based on this material can be operated at room temperature. This high resistivity material may also be useful as a substrate on which to grow epilayers of CdTe and $Cd_xHg_{1-x}Te$. Alloys of $Cd_xHg_{1-x}Te$ have direct band gaps in the range zero to 1.5 eV and, because of their low recombination efficiency, are important as infrared detectors.

The ability to control the conductivity from n- to p-type, means that semiconductor devices such as diodes or transistors can also be fabricated using this material. CdTe has important advantages as a material for photovoltaic solar cells, namely its appropriate value of direct energy gap and the ability to produce thin films using inexpensive techniques. In addition, CdTe has a high optical absorption coefficient ; less than 2μ of CdTe would be capable of absorbing all the usable energy from the solar spectrum.

Difficulties arise however in producing films with controlled properties. For example, the films produced are normally of high resistivity and are n-type ; CdTe homojunction cannot therefore be prepared using thin film techniques.

In spite of the large literature on CdTe, little has been done to explore the effect of a large electric field on the optical absorption edge of the material. This is the main subject discussed in this chapter which begins with a general description of CdTe and the device preparation details relevant to our electroabsorption experiments.

4.1.1 Crystal Growth

Three principal approaches have been used to grow single crystal CdTe namely : growth from a congruent or near congruent melt, growth from a Te-or Cd-rich solution and growth from the vapour.

All single crystals used in this work were grown from solution where a temperature gradient was imposed on a Cd-Te melt containing excess Cd. The technique is known as the solvent evaporation technique (SET) because the Cd excess is removed from the Cd rich solution by evaporation(1). The system is allowed to remain in the molten condition for sometime to ensure complete dissolution during which time any excess Cd distills into a reservoir and provides a Cd pressure. This equilibrium is then disturbed by continuously reducing the temperature of the reservoir thus permitting the growth of single crystal CdTe.

In common with other semiconductors, single crystal CdTe can be doped with certain amounts of impurity. This process will introduce localized levels within the band gap of CdTe, and can thus define whether the material is n- or p-type. For example De Nobel(2) has reported that acceptor levels are created by doping CdTe with elements from group 1B namely Cu, Ag and Au, and thus producing p-type material. The most popular method of doping involves the zone-levelling procedure developed by Pfann(3). In this method a known amount of foreign element is placed at one end of a boat filled with pure CdTe and a molten zone is allowed to pass the CdTe bar in both directions. After about ten passes the whole bar is homogeneously doped except that section of the bar where the molten zone ends up. Direct doping of the molten CdTe before crystallization is also possible. For example, a known amount of $CdCl_2$ can be added to the melt in order to obtain chlorine doped CdTe(4).

4.1.2 Band Structure

The stable form of CdTe single crystal at atmospheric pressure is the zinc blende structure shown in Fig 4.1. The structure belongs to the cubic space group $F\bar{4}3\,m(F_d^2)$ (5) and consists of two interpenetrating face centre cubic lattices offset from one another by one-fourth of a body diagonal. The best value for the cubic lattice parameter at room temperature is 6.481 Å (6) with a density of 5.855 $gm.cm^{-3}$. There are four molecules per unit cell. The zinc blende structure is an immediate result of electron sharing and the bonding in CdTe is predominantly homopolar(7). However the ionic and metallic contributions are both significant and are reflected in its physical properties.

The band structure of CdTe was ill-understood before Marple in 1966(8) studied the relative position of valence and conduction bands extrema in k-space. However by utilizing high speed computer techniques and using the pseudopotential method developed Cohen and Bergstresser(9), the problem has been solved. The band structure calculated by Chelikowsky and Cohen(10) using a nonlocal empirical pseudopotential model (EPM) is shown in Fig 4.2. The most important symmetry points in the Brillouin zone are those at the centre of the zone (Γ), the (111)-axes (Λ) and their intersection with zone edge (L), and the (100)-axes (Δ) and their intersection (X). The (110)-axes (Σ) and points (U,K) along the intersection planes are also defined.

The valence band is associated with the 5s and 5p atomic orbitals of Cd and Te. The valence band is composed of four sub-bands if spin is

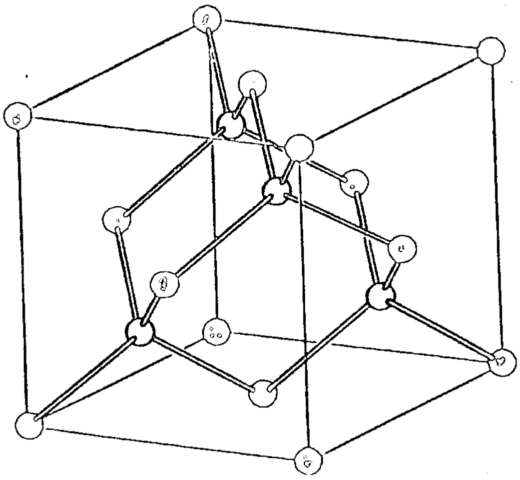

Fig 4.1: The two equivalent interpenetrating face centre cubic lattices of the zinc blende structure.

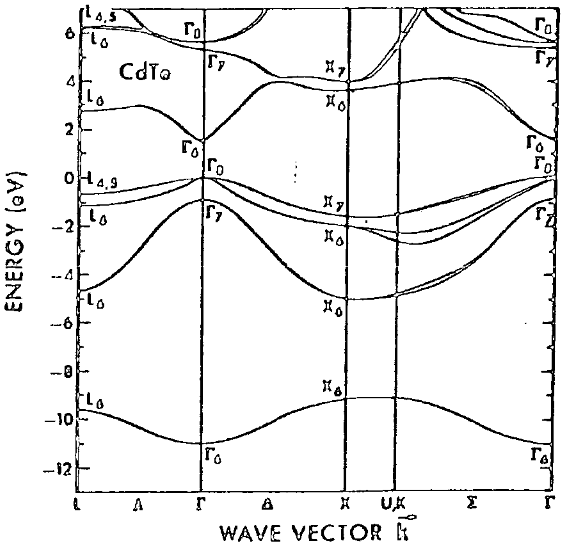

Fig 4.2 : Electronic band structure of CdTe in the principal symmetry directions using the nonlocal empirical pseudopotential method, after (10).

neglected. The lowest is primarily associated with the S-orbitals of Te. The three upper bands are degenerate at k = 0 and form the upper edge of the band. The higher band states consist largely of the p-electron state of Te and a small admixture of the S electron states of Cd.

The low lying conduction band states are also associated with s and p orbitals which are heavily concentrated about the cations. The lowest conduction band and the highest valence band both occur at k = 0 so that the energy gap is direct. At liquid helium temperature, the energy gap is 1.606 eV.

4.1.3 Optical Properties

A theoretical study of the optical absorption edge in CdTe was made by Segall in 1966(11) who suggested that the material is a direct gap crystal. He also showed that the agreement between the calculated result and the experimental data extends up to the temperature range at which the absorption coefficient begins to exhibit Urbach rule behaviour. These facts were supported by Marple(8) who completed an experimental study of the optical absorption edge of CdTe. He showed that the absorption curve, especially near the band edge, was extremely sensitive to surface preparation and the quality of the crystal. His results for a chemically polished crystal differed from those measured previously for mechanically polished samples ; the contrasting data are shown in Fig 4.3. The effect probably explains why early workers interpreted their CdTe data in terms of an indirect gap. The absorption constant at room temperature shows a steep exponential rise up to $\sim$ 300 cm^{-1} with a slope of about 110 eV^{-1}.

The reflectance results (12,13) show that as the temperature is increased from liquid helium temperature, the band gap E_g decreases very slowly up to 20 K, then begins to decrease more rapidly, and between 30 K to 150 K decreases linearly at the rate of $- 3.5 \times 10^{-4}$ eV. K^{-1}. Extrapolation to 300 K gives E_g = 1.520 eV. This energy gap is very close to the optimum value required for the conversion of solar radiation to

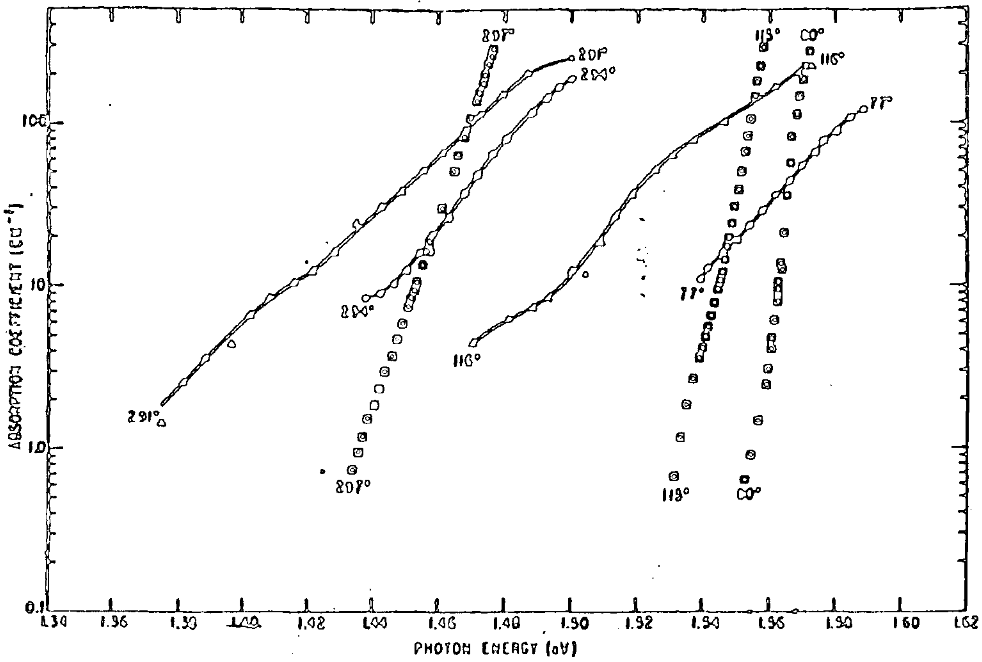

Fig 4.3 : Comparison of results from chemically polished samples (▣) of Marple (8) with those obtained in earlier studies. Δ-C.Konak, Phys. Status Solidi 3,1274 (1963) ; O-P.W.Davis and T.S.Shilladay,Phys.Rev.118,1020 (1960).

TABLE 4.1 : Some Optical Properties of CdTe at 300 K.

Parameter	Reported Value
Refractive index n_o, at 10.6 μm	2.672 (14)
Reflectivity at 10.6 μm	0.207
Optical dielectric constant ε_x	7.15 ± 0.05 (15)
Static dielectric constant ε_o	10.3 ± 0.1 (15)
Optical band gap at 2 K	1.606 eV (13)
Theoretical $(dE_g/_{dT})$	-4.2×10^{-4} eV.K^{-1} (38)
Experimental $(dE_g/_{dT})$	-3.5×10^{-4} eV.K^{-1} (13)

electric power by means of a semiconductor photovoltaic solar cell. Some optical properties of CdTe at 300 K are shown in Table 4.1.

4.1.4 Electrical Properties

The charge transport properties of II-VI compounds are largely determined by their band structure and scattering mechanism. In the case of CdTe, Hall effect experiments indicate that the dominant scattering results from the interaction of electrons with optical phonons(17). Segall(18) concluded that electron scattering was dominated by longitudinal optical phonons and discussed deformation potential scattering as being insignificant. Rode(19) however developed an iterative solution of the Boltzmann equation for lattice scattering which included both polar optical mode scattering and acoustic deformation potential scattering ; he concluded that the latter mechanism was more important than previously expected. The electron mobility measured for the purest sample at 300 K is 1100 $cm^2/V.sec$; the highest reported for CdTe is by Triboulet and Marfaing(20).

Different values of hole mobility have been reported depending on the method of preparation and the type of impurities present. The lowest is $\simeq$ 8.2 $cm^2/V.sec$(21,22), and the highest is $\simeq$ 200 $cm^2/V.sec$(22).

(a) Impurities and Native Defects

The intrinsic carrier concentration of a semiconductor is determined by its energy gap and the effective masses of the electrons and holes. With the experimentally observed values of the above parameters, the intrinsic carrier concentration in CdTe is calculated to be about 1.0×10^6 cm^{-3} (23). This value is too low to account for room temperature conduction in this material. The lowest room temperature carrier concentration observed experimentally is 8.3×10^7 cm^{-3}, is reported by Alekseenko et al(24) for a p-type sample. The current carriers responsible for conduction at room temperature and below must therefore be generated by the ionization of impurities, native defects, or complexes between them.

Impurity atoms in the columns adjacent to Cd in the periodic table can substitute for Cd atoms in the lattice and those adjacent to Te can substitute for Te to act as donors or acceptors depending on whether they have more or less electrons than the atom they replace. Since these elements differ only by one valence electron, all impurities considered here should be singly ionized acceptors or donors. Doping CdTe with elements from group V, namely P, As and Sb for example, introduce acceptor levels(25), presumably by substituting for Te, and have ionization energies in the range from 0.036 to 0.060 eV. These crystals have hole mobilities of 24 to 39 $cm^2/V.sec$ and hole concentrations in the range 5.0×10^6 to 6.0×10^{17} cm^{-3}.

It is known that electrically active native point defects are formed in II-VI compounds. This is due to deviations from the stoichiometric composition or due to the presence of one element in excess which will act as donors or acceptors, depending on whether the excess element is the metal or non-metal component of the compound. Measurements on the purest samples of CdTe by Triboulet and Marfaing(20) show that the room temperature carrier concentrations are between 1 and 5×10^{13} cm^{-3} and resistivities lie in the range 100-400 Ω cm. It has been estimated that the total concentration of electrically active centres in these crystals is about 10^{14} cm^{-3}.

When both donors and acceptor atoms are present simultaneously, electrons from donor impurities can fill up acceptor-like native defects ; and the electronic conduction in this case is determined by the difference between the donor and acceptor concentrations. When $N_a \simeq N_d$, the crystal is said to be compensated. Furthermore if the concentration of a deep donor level become large enough to exceed $(N_a - N_d)$, the Fermi level will rise abruptly from the vicinity of the shallow acceptor level to the vicinity of the deep donor level, where it remains pinned producing semi-insulating material over a wide range of deep donor concentration. This mechanism is termed auto-compensation and has been extensively employed to obtain CdTe samples with carrier concentrations low enough to give the high electrical resistivity needed for γ-ray detectors. Compensation in Cl doped CdTe has been reported by Petty et al (26). The Cd vacancies behave as acceptors in CdTe grown from tellurium rich solution. Doping with chlorine, which creates shallow donor levels in CdTe, compensates these acceptors and produces high resistivity single crystals.

4.1.5 Previous Electroabsorption Studies of Cadmium Telluride

The first published electroabsorption data for CdTe was by Kareev et al (27) in 1965. A constant electric field was applied to a film of CdTe at room temperature. Even though a red shift of the intrinsic absorption edge was observed, the data showed a lack of agreement with what is predicted by the Franz-Keldysh theory. The authors attributed the discrepancy to poor film quality. Further measurements were subsequently carried out (28) in 1967, on both films and single crystal CdTe at 77 K. These data are shown in Fig 4.4 and were successfully interpreted in terms of the Franz-Keldysh effect. The value of reduced effective mass of the charge carriers was calculated to be 0.09 m_0. Later in this chapter we shall be demonstrating how careful one must be in carrying out electroabsorption studies of wide band gap semiconductors. For example, the specimen quality, pulse shape, electric field frequency and magnitude etc, all have a critical bearing on the final result. The Russian authors, however, failed to mention the conditions under which their data were taken. They encountered difficulties in obtaining the appropriate value of absorption coefficient which seemed to be specimen dependent. It is worth noting that the value of β; the gradient of the exponential absorption edge with photon energy, is between 40 eV^{-1} and 60 eV^{-1} in their samples indicating poor quality single crystals.

Oscillations of the electroabsorption signal in the vicinity of the fundamental absorption edge of CdTe films has also been reported(29). Small discrepancies with results predicted for an ideal direct gap crystal were attributed to the existence of internal microfields. This work stimulated further investigations in this area(30-32). The change of absorption constant in an alternating electric field should contain only even harmonics of the modulating field. However, odd harmonics signals were also observed. Their magnitudes were found to be greatly dependent on the size and direction of a small d.c. field superimposed on the much larger alternating field. These effects were also believed to be due to the existence of internal microfields.

While serious attention was given to the existence of these odd harmonics signals in CdTe, no detailed studies were reported on the even harmonic electroabsorption signal. The purpose of this chapter is to demonstrate the various pitfalls that must be avoided if a correct effective mass value is to be deduced using such data.

Electroabsorption studies of impurity levels in CdTe have also been reported(33); and these data are reproduced in Fig 4.5 for Cl doped CdTe. The Cl level in these specimens was about 2.0×10^{17} cm^{-3}. Two types of transitions were observed at 77 K for undoped CdTe. Peak D_2 in Fig 4.5 corresponds to an optical transition from the valence band to a donor level located 30 meV below the conduction band at 77 K while peak A_2 is assigned to a transition from acceptor levels localized at about 55 meV above the valence band to the conduction band. Doping with Cl resulted in an extra peak C_2 which was attributed to a transition from an acceptor complex which consists of a cadmium vacancy and a chlorine atom on the nearest tellurium site, to the shallow donor state. These two levels were believed to dominate the auto-compensation mechanism in Cl doped CdTe.

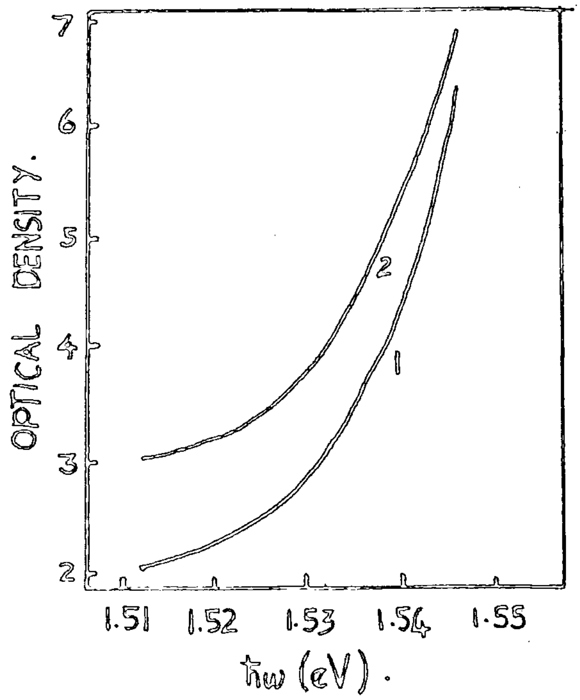

Fig 4.4 : Absorption spectra of CdTe single crystal

(1) F = 0 ; (2) F = 4.84×10^{4} V/cm, T = 77 K,

after (28).

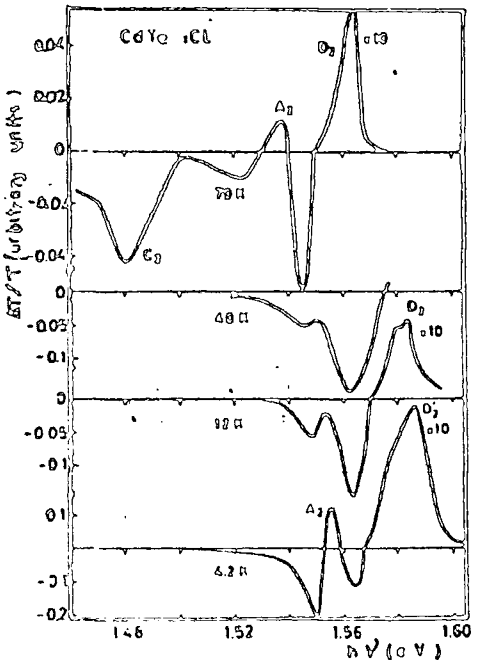

Fig 4.5 : Dependence of the E.A. spectra on temperature for chlorine doped CdTe (E = 1000 V/cm), after (33).

4.2 DEVICE PREPARATION

Electroabsorption experiments were performed on semi-insulating Cl doped CdTe crystals grown by the solvent evaporation technique at RSRE, Malvern. The crystals were cut in <111> orientation from boules with thickness between 200 μm and 500 μm. The surface area of each sample was about 1.0 cm^2. During any electroabsorption experiment, an external electric field was applied across a sandwich structure formed by depositing semi-transparent metal electrodes on both sides of the parallel surface of the slice.

Knowledge of the magnitude and distribution of the applied field are important in the analysis of electroabsorption spectra. This is most conveniently achieved by producing a good Ohmic electrical contact which ensures the uniformity of the field across the sample. The production of a good Ohmic contact, however, depends on the surface preparation. Accordingly, this section includes a discussion of the surface treatment prior to metal deposition. This is followed by a description of the electrical, both d.c. and a.c., properties of the resulting structures.

4.2.1 Production of Ohmic Contact

Each sample investigated was prepared in a systematic manner as follows : it was first mechanically polished to a finish of 0.25 μm using diamond paste and then degreased by refluxing in isopropanol (BDH-analar). This was followed by a chemically etch in a fresh solution 1% (by volume) bromine in methanol (BDH-analar). Then the sample was washed in methanol and de-ionized water. Immediately before metal deposition, the sample was etched in 40% hydrofluoric acid solution for about one minute to remove any oxide layer present. On removal it was again washed in de-ionized water and then immersed in methanol.

Metal contacts were prepared by evaporating Au-Sb(1% by weight) alloy from a molybdenum boat at a pressure of about 10^{-6} torr. The electrode was typically about 100 Å thick evaporated at a rate of about

40 Å/minute. A.c and d.c. conductivity experiments were performed to investigate the quality of the contact prior to the electroabsorption experiments.

For optical absorption purposes, samples were prepared without electrodes. Even so it was found necessary to follow the above surface treatment. This is due to the fact that the absorption curve near the band edge is extremely sensitive to the surface condition of the crystal.

4.2.2 D.C. and A.C. Conductivity Measurements

D.c. and a.c. conductivity measurements were performed prior to the electroabsorption experiments. Fig 4.6 shows an example of a d.c. conductivity curve for Cl doped CdTe at room temperature. Good Ohmic behaviour is observed below a field of about 3.25×10^{3} V.cm^{-1}. The resistivity deduced from this region is 8.84×10^{9} Ω cm. Above this value of field the current increases quadratically with field. Since the power dissipated in this sample is only about 2.0×10^{-8} W, the rapid increase in current is certainly not due to Joule heating. Space charge limited currents are the most likely explanation.

Fig 4.7 shows the variation of current density with temperature for CdTe : Cl. In the temperature range investigated there is one activation energy (0.61 eV) for the space charge limited current (SCLC), whereas the Ohmic current shows two distinct energies (0.61 eV, 0.80 eV) with a transition at 248 K. These different activation energies were interpreted using a theorem proposed by Roberts and Schmidlin(34) which states :

'The existence of different (or identical) activation energies for Ohmic and SCL conduction is both a necessary and a sufficient condition for Ohmic conduction to be non-extrinsic (or extrinsic)'. The conductivity of a material is referred to as non-extrinsic (or pseudointrinsic) when it is dominated by two localized levels within the band gap. From Fig 4.7, the Ohmic conduction in CdTe:Cl sample is extrinsic at temperatures up to 248 K and non-extrinsic above this. Using the above theorem, it can be

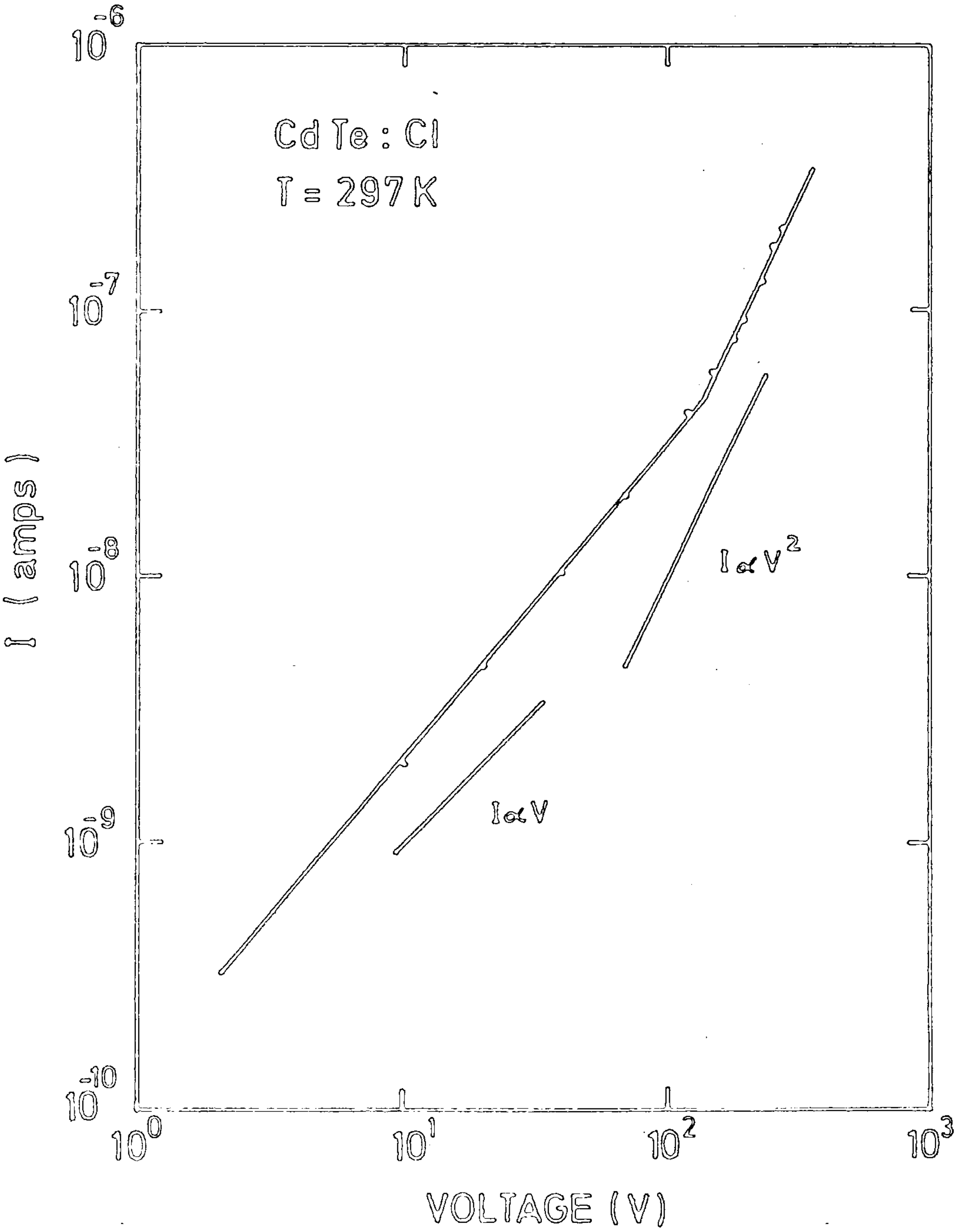

Fig 4.6 : Current voltage curve for CdTe:Cl at room temperature.

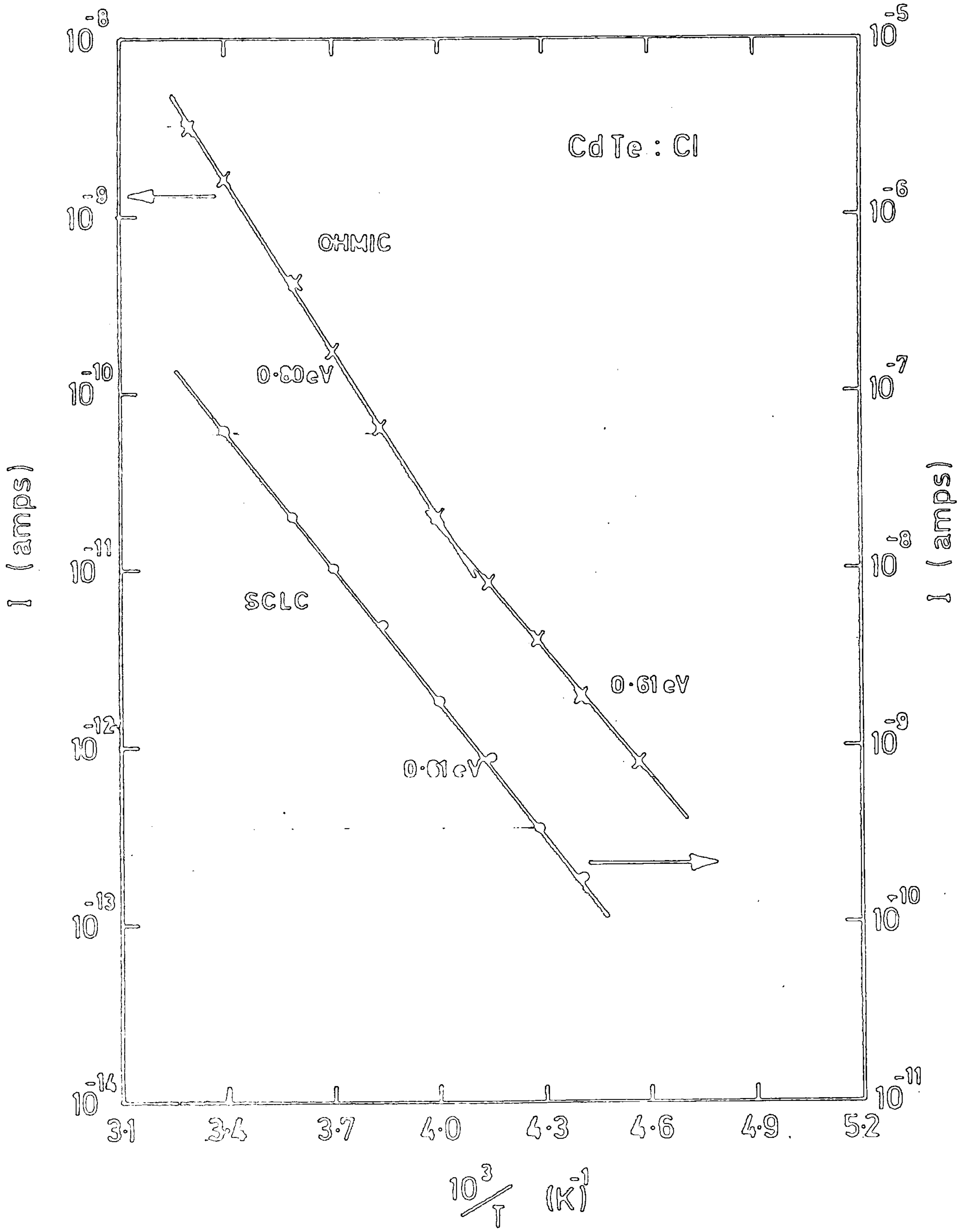

Figure 4.7 : Current versus reciprocal temperature in the Ohmic and space-charge-limited regions for a CdTe : Cl sample. Electrode area = 0.07 cm^2. Thickness = 400 μm.

shown that the Ohmic conduction of the sample is governed by two levels ; 0.61 eV and 0.99 eV above the valence band. At temperatures below 248 K, the conduction is extrinsic and the activation energy is simply 0.61 eV. Above 248 K, the conduction becomes non-extrinsic with an activation energy of 0.99-0.5(0.99-0.61) = 0.80 eV.

Space charge injection leads to non-uniform fields in a sample and must therefore be avoided if possible by performing electroabsorption experiments in the Ohmic region. However, some materials display space charge effect at relatively low fields, and therefore experiments in the SCL region cannot be avoided. For this reason we carried out a systematic investigation of electroabsorption within the SCLC region in CdTe:Cl. The results can be compared with those obtained from data in the Ohmic region and are discussed in section 4.6.

Further investigations of the quality of electrical contact have been carried out using the a.c. conductivity technique. This involves the measurement of capacitance and conductance at different frequencies. A crystal with one good Ohmic contact on each side should exhibit a frequency independent capacitance, the magnitude of which is equal to the geometric capacitance of the bulk of the semiconductor. This has been observed in our CdTe:Cl samples. If ε is the static dielectric constant, the geometric capacitance is given by

$$C = \frac{\varepsilon\varepsilon_o A}{d}$$

where A and d are the area and thickness of the capacitor, respectively. An example of data obtained by this type of measurement is shown in Fig 4.8 where the a.c. capacitance and conductance are plotted against frequency. Constant values of capacitance and conductance in the frequency range between 10^2-10^4 Hz help confirm the evidence of a good Ohmic contact.

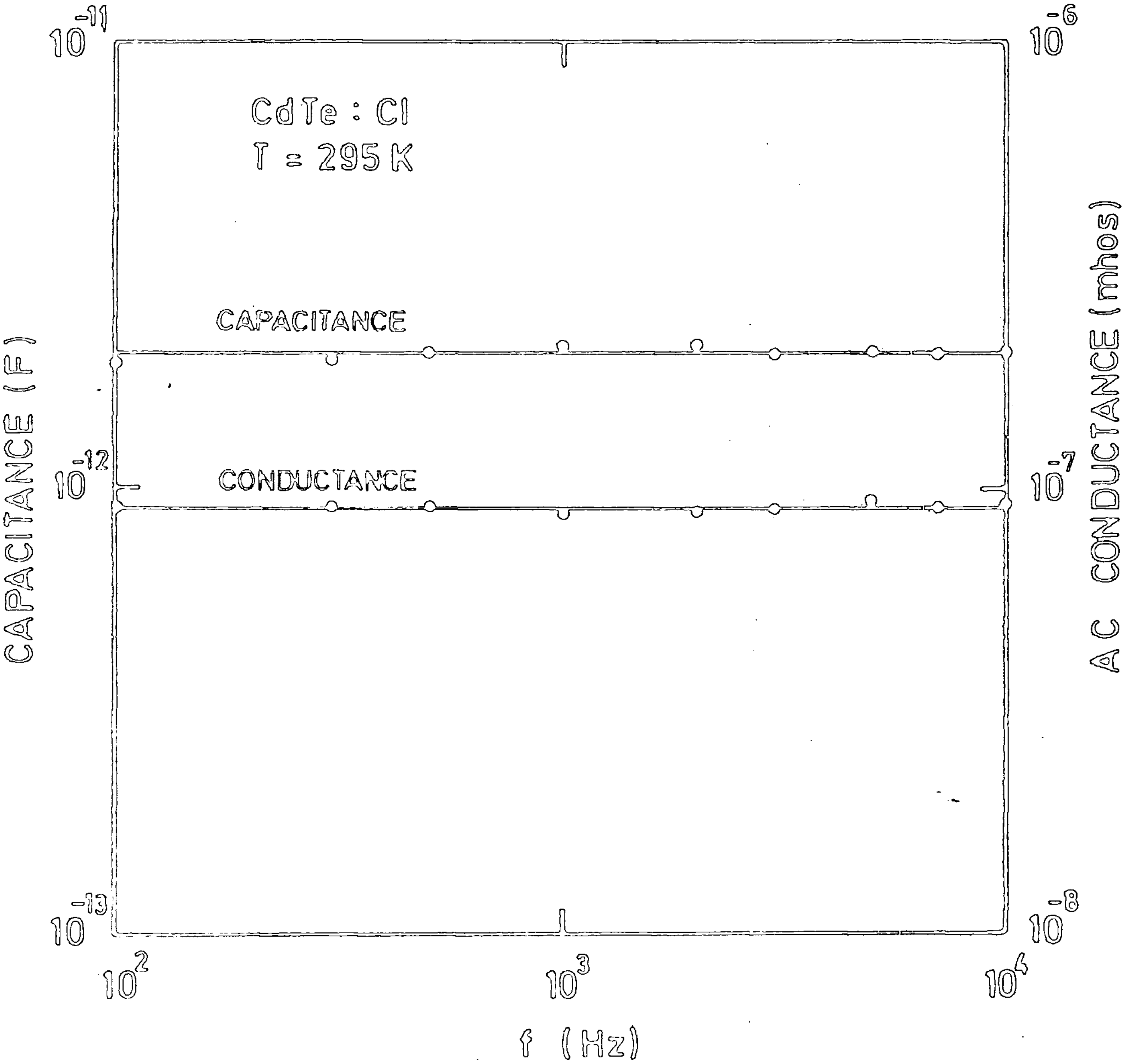

Figure 4.8 : Capacitance and conductance data as a function of frequency for a CdTe : Cl sample.

4.3 RESULTS OF ELECTROABSORPTION STUDIES IN THE OHMIC REGION

The results of our absorption measurements on CdTe:Cl are now described. Fig 4.9 shows the absorption coefficient, α , over a wide range of temperature. In most cases, samples with a thickness in excess of 250 μm were used giving accurate values of $\alpha < 300$ cm^{-1}. This was found to be sufficient since this work concentrated only on the longer wavelength area of the absorption edge. Good quality crystals together with proper surface treatments appeared to produce a sharp absorption edge with the band gap energy, E_g equalling 1.48 eV at room temperature ; a temperature shift of -4.0×10^{-4} eV.K^{-1} was observed in the range 300 K to 150 K. These curves are very similar to those reported by Marple$^{(8)}$ for chemically polished single crystals and reproduced in Fig 4.3. The exponential slope of the absorption edge at room temperature, in both cases, is about 110 eV^{-1}.

The reflectance data of Thomas$^{(13)}$, however, show that as the temperature is increased from liquid helium temperature, E_g decreases very slowly up to about 20 K, then begins to decrease more rapidly, and between 30 K and 150 K, decreases linearly at the rate of -3.5×10^{-4} eV.K^{-1} the extrapolation of which gives $E_g = 1.520$ eV at 300 K.

The results of our electroabsorption experiments on CdTe:Cl samples are now presented. We first describe those taken in the Ohmic region where space charge complications can be ignored. A field induced absorption change, $\Delta\alpha$, at room temperature ($E = 2.5 \times 10^3$ V.cm^{-1}) is plotted against photon energy in Fig 4.10. This figure is typical of data obtained for CdTe:Cl. The zero-field absorption coefficient, α , is plotted alongside. The exponential slopes of α and $\Delta\alpha$ with photon energy are equal, an indication that the Franz-Keldysh effect is observed. The peak of the electroabsorption spectrum is at about the band gap of CdTe.

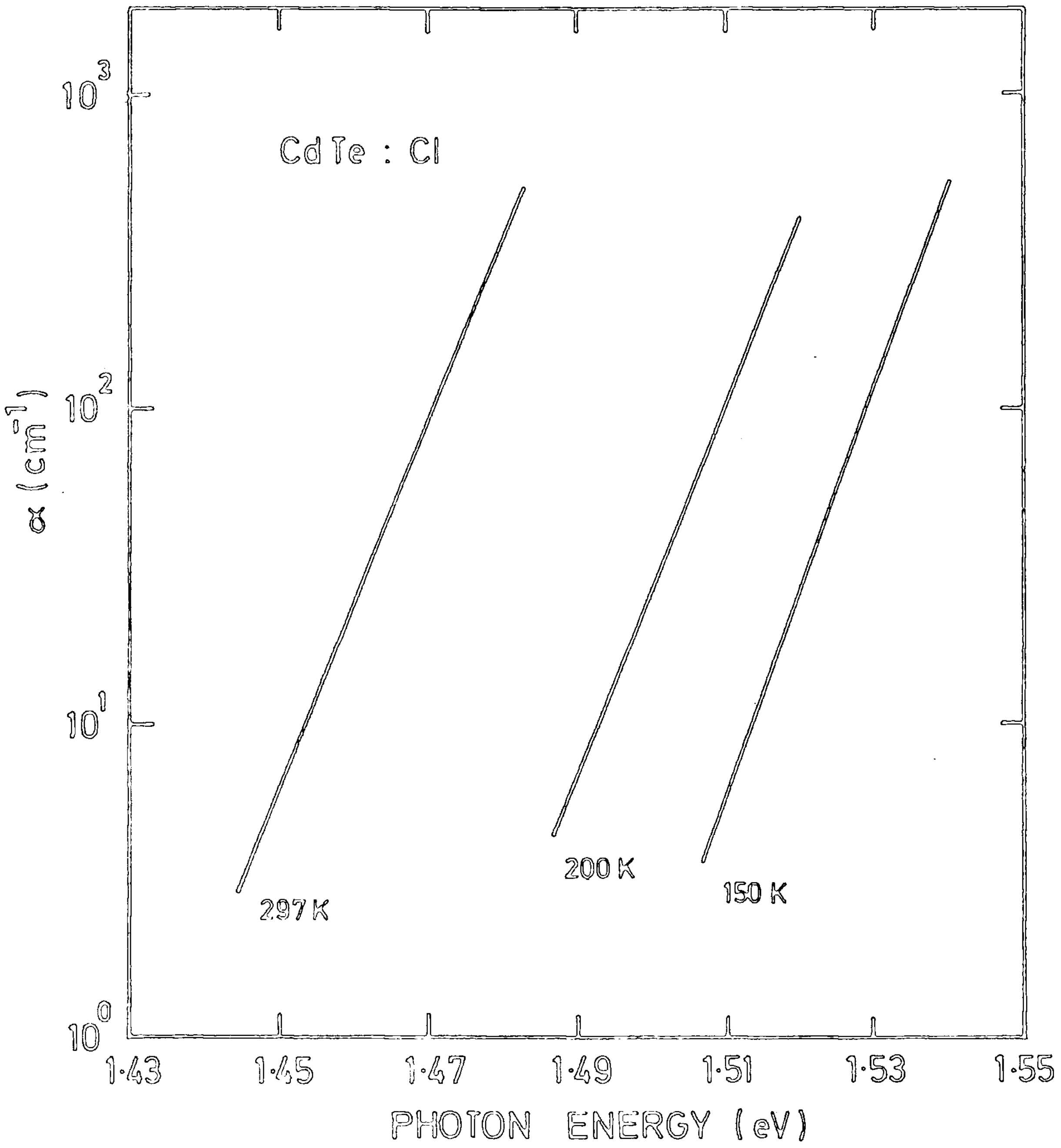

Fig 4.9 : Optical absorption coefficient of CdTe:Cl as a function of photon energy at 297 K, 200 K, and 150 K.

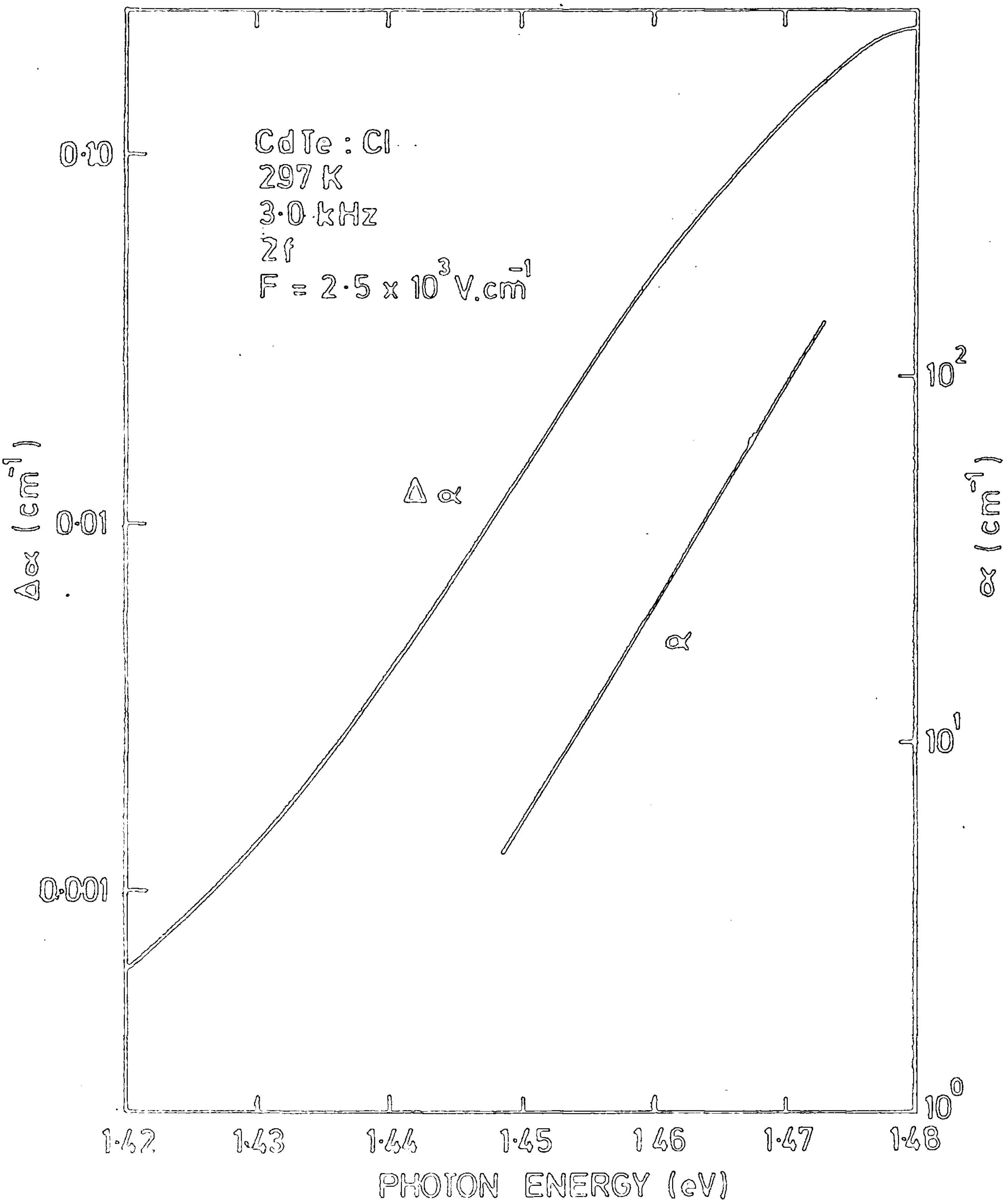

Figure 4.10 : Graph of the absorption change, Δα, due to an applied field of 2.5 x 10^3 V.cm^{-1} for a CdTe : Cl crystal at room temperature. The zero field absorption curve is also shown.

Measurements were also taken at different temperatures. Fig 4.11 shows the electroabsorption spectra of CdTe:Cl at 150 K. Most features of the room temperature spectra are retained at this lower temperature. However, the 150 K curves are steeper with an exponential slope of 150 eV^{-1}. The position of the peak at this temperature is shifted to a higher photon energy at the rate of -4.0×10^{-4} $eV.K^{-1}$. This displacement is in accordance with the band gap widening with decreasing temperature.

4.4 ELECTRIC FIELD DEPENDENCE OF THE ELECTROABSORPTION RESPONSE

It has been mentioned in Chapter 2 that the field dependence of the electroabsorption spectrum may provide knowledge about the optical transition mechanism involved. The field dependence of the electroabsorption responses described in the previous section are shown in Figs 4.12 and 4.13. All measurements were taken in the region where the exponential gradients of the $\Delta\alpha$ and α curves against photon energy are equal. A good straight line is obtained over a wide range of voltage indicating that the absorption change is proportional to the square of the field. This result has been confirmed by us for various samples of CdTe at different temperatures. The fact that the graph extrapolates to the origin is a good indication of the absence of any space charge injection effects in our sandwich structures.

4.5 FREQUENCY DEPENDENCE OF THE ELECTROABSORPTION RESPONSE

The early electroabsorption theory by Franz and Keldysh predicted that the electroabsorption spectrum should not depend on the frequency of the modulating field. That is the positive going pulse has an equivalent effect to the negative going pulse as far as the electroabsorption response is concerned. In the case of a sinusoidal field, each half of the cycle is equivalent and therefore the electroabsorption signal should be detected at twice the frequency of the modulating field; that is the second harmonic response. However, deviations from this idealized case are often encountered. The second harmonic signal usually depends on the frequency, and a signal is also observed at the fundamental frequency ; that is the first harmonic

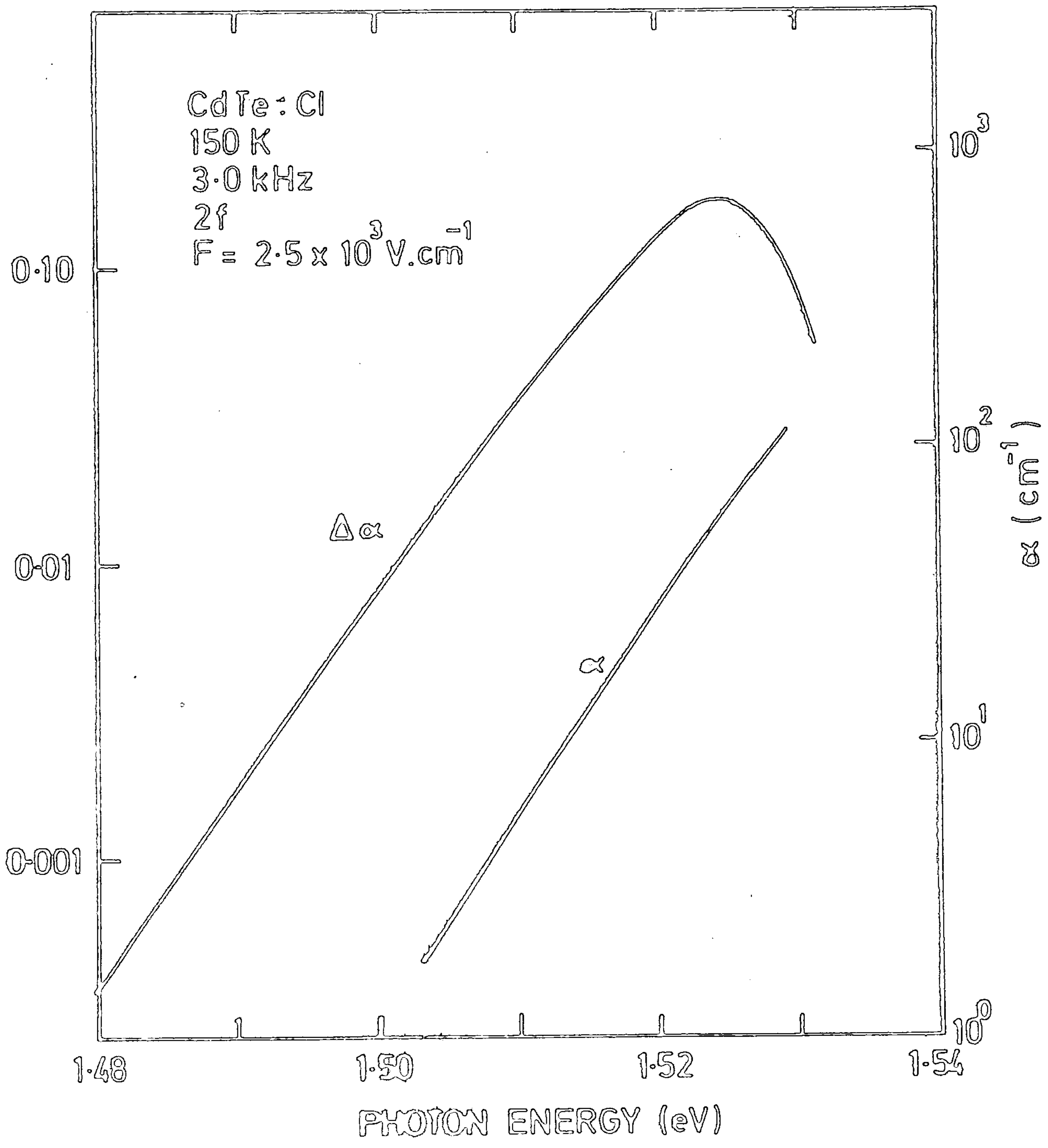

Figure 4.11 : The absorption and electroabsorption (F = 2.5 x 10^3 V.cm^{-1}) spectra of a CdTe: Cl crystal at 150 K.

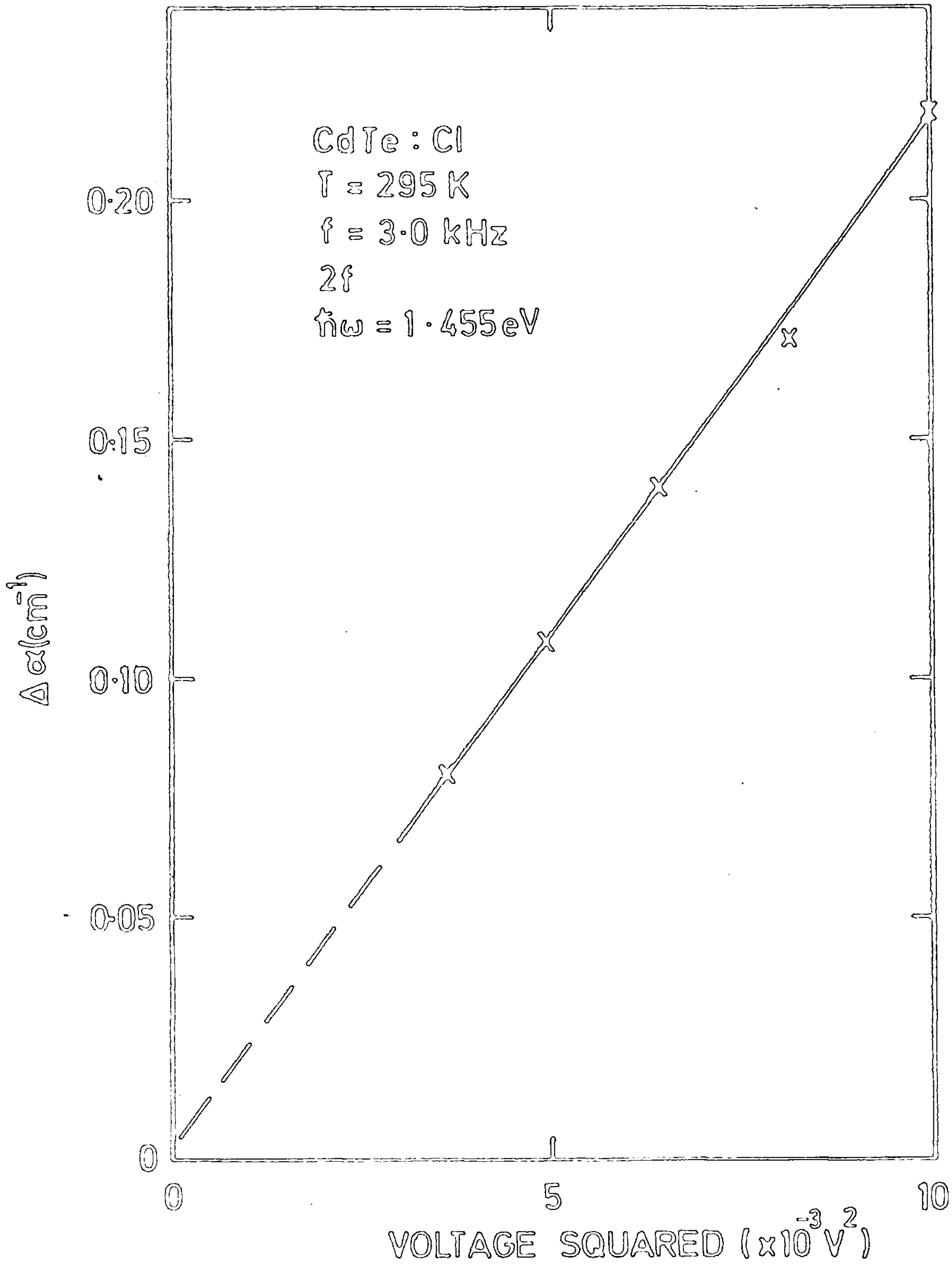

Figure 4.12 : Dependence of the absorption change of a CdTe : Cl crystal on the magnitude of the applied field at room temperature.

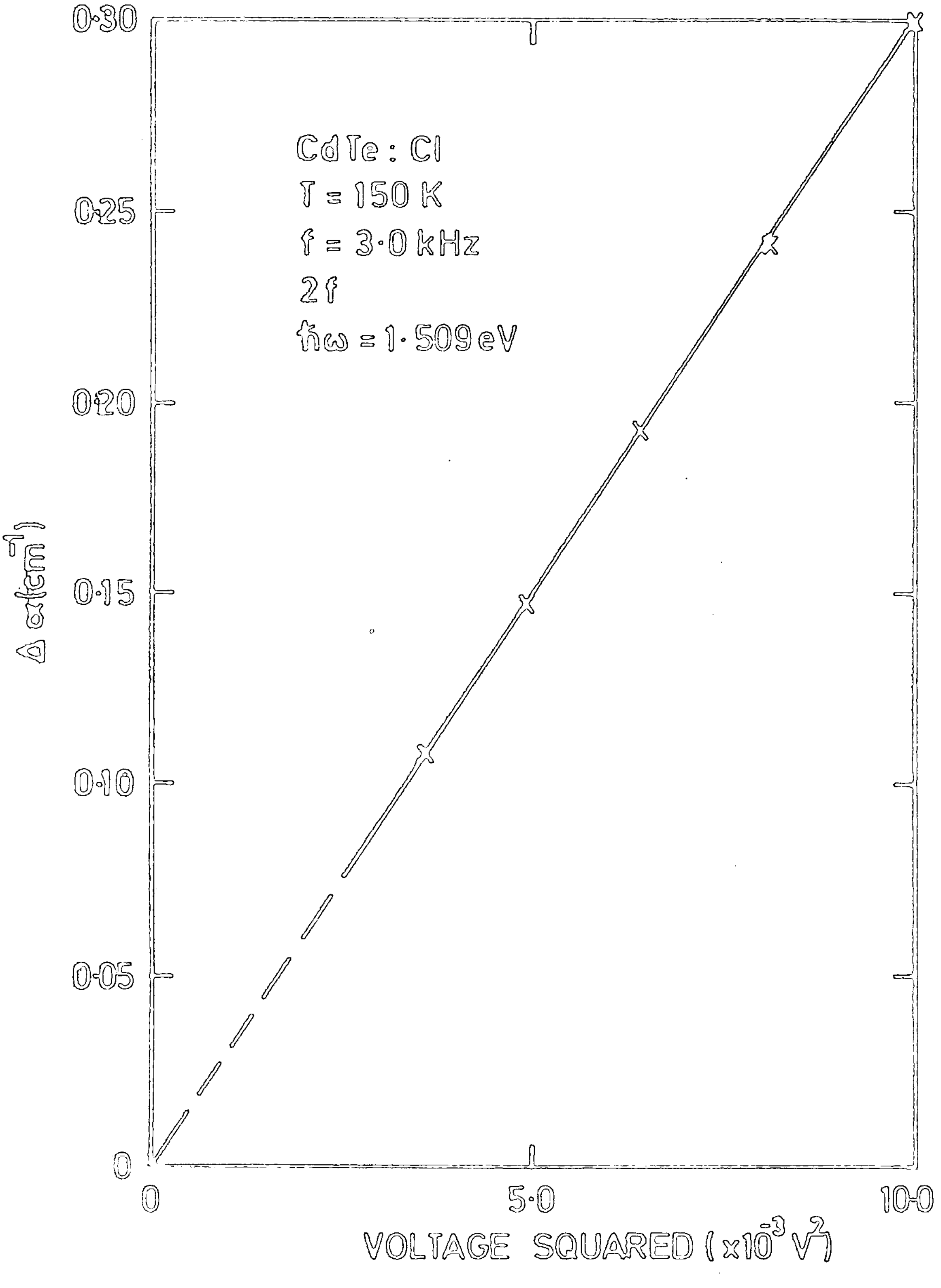

Figure 4.13 : The quadratic field dependence of the absorption change of a CdTe : Cl crystal at 150 K.

response. These points will be discussed in the following subsections.

4.5.1 Frequency Dependence of the First Harmonic Response

Fig 4.14 shows the frequency dependence of the first harmonic response at a particular photon energy for CdTe:Cl. The large value of $\Delta\alpha$ at very low frequencies is seen to decrease rapidly with increasing frequency and vanishes at approximately 4.5 kHz. The effect was first thought to be due to the non-Ohmicity of the electrical contact which in turn could lead to a non-uniformity of the electric field distribution in the sample. Variation of the frequency would then alter the field distribution producing a resultant change in the electroabsorption signal. This explanation is, however, extremely unlikely due to the fact that extensive precautions, as already mentioned in section 4.3.1 were conducted to ensure a good Ohmic contact to the specimen.

It was suspected that the effect was due to photo-generated carriers since it was discovered that a large photocurrent flowed at energies near the band gap. Fig 4.15 shows the normalized photocurrent (photocurrent divided by spectral response) for the CdTe:Cl whose electroabsorption spectrum is shown in Fig 4.10. Confirmation that the first harmonic electroabsorption signal arises due to the photoconductive effect is obtained by noticing that the magnitude of $\Delta\alpha$ is strongly dependent on light intensity at low modulating frequencies. This is demonstrated in Fig 4.16 where $\Delta\alpha$ is plotted against light intensity. The magnitude of $\Delta\alpha$ increases rapidly with intensity before it saturates at about 90% intensity (arbitrary units).

The effect can be attributed to polarization effects in the crystal under illumination. For example, in the presence of an alternating field, a space charge build-up may occur at one electrode due to trapping effects. The favoured interpretation, however, is that the photoconductivity effect at the surface of the specimen produces a region which is electrically less resistive than the bulk. This will result in a larger drop of electrical potential across the remainder of the crystal and a larger electroabsorption

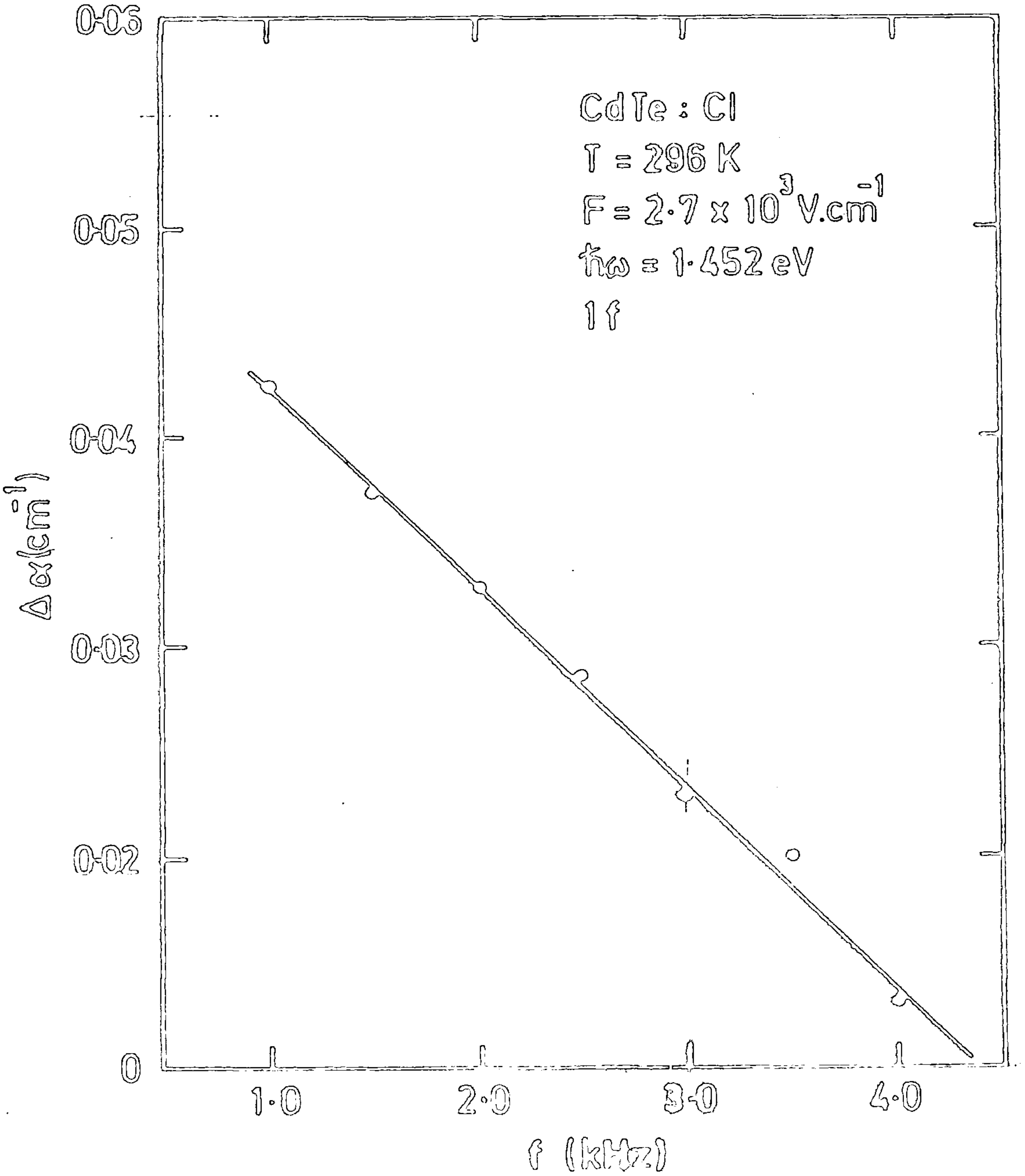

Figure 4.14 : Effect of a variation of the frequency of the applied electric field upon the first harmonic electroabsorption signal for a CdTe : Cl crystal at room temperature.

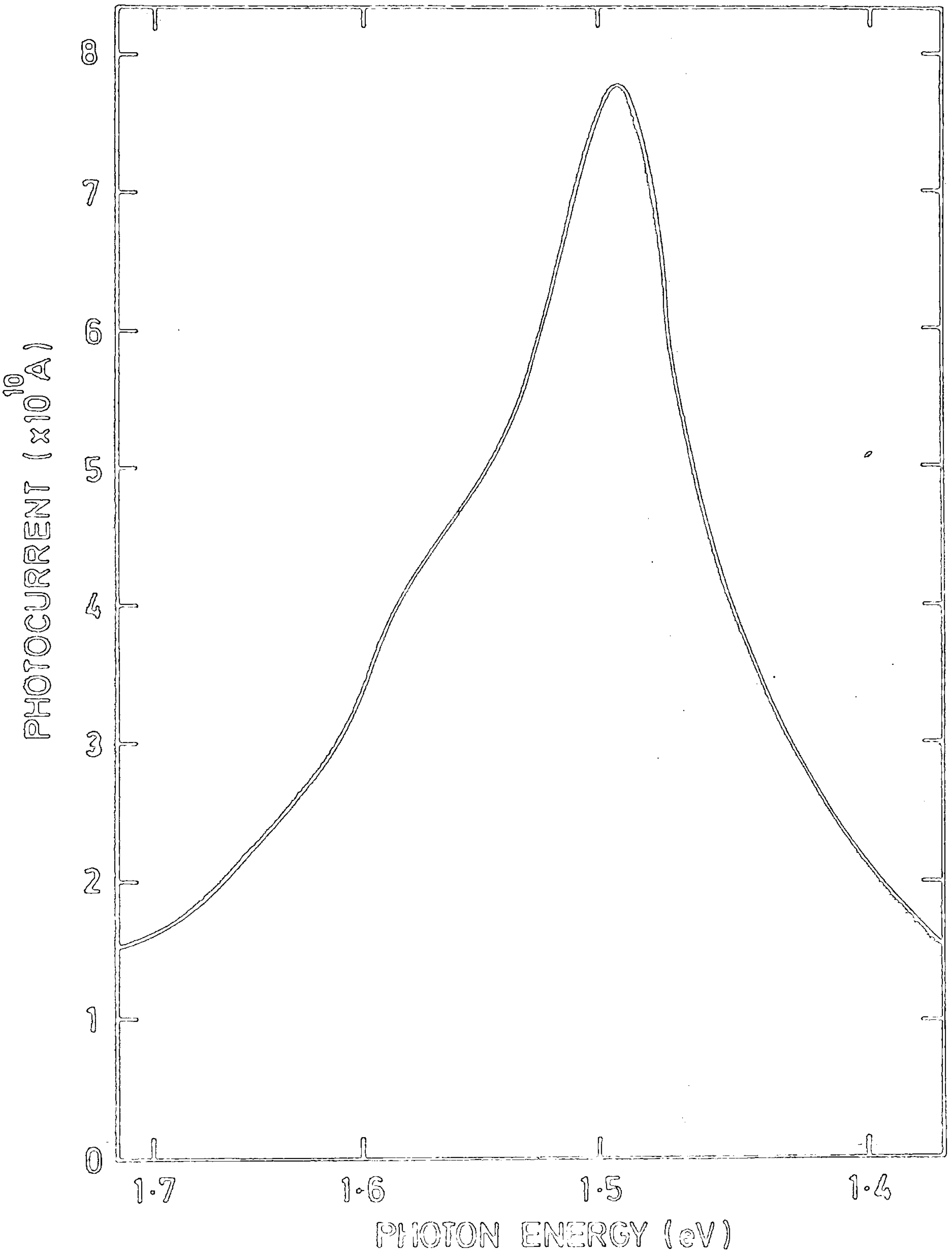

Figure 4.15 : Photocurrent as a function of photon energy at room temperature for a CdTe : Cl specimen.

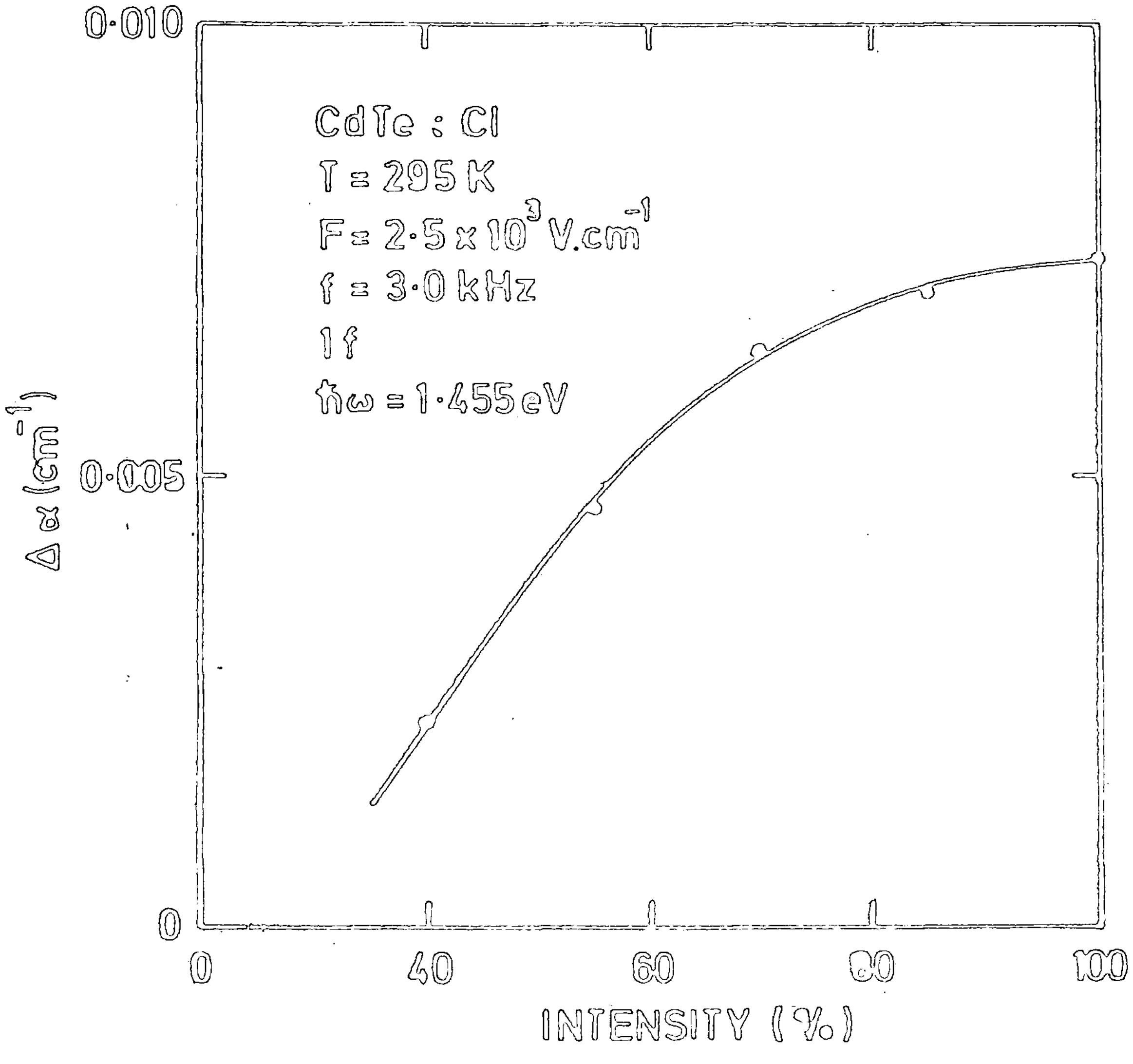

Figure 4.16 : Effect of a variation in the incident light intensity on the 1f electroabsorption signal at a frequency of 3 kHz for a CdTe : Cl crystal.

change. However, every photoconductive process has a particular time constant associated with it. At a frequency larger than the inverse of this time constant, the effect would be expected to reduce since the charge carriers in the sample could not respond fast enough. That is, the electric field induced absorption change at higher frequencies should vanish. This is exactly what is observed. This interpretation would lead to our predicting that the photocurrent should decrease in a similar fashion to $\Delta\alpha$ as the frequency is increased in the low frequency region. Fig 4.17 confirms this view ; a large photocurrent is observed at low frequency, but this decreases to virtually zero at 5 kHz, the frequency at which $\Delta\alpha$ vanishes.

This interpretation is further strengthened by the fact that if the photovoltage does exist, any external static field superimposed on an alternating field will reduce or increase the magnitude of $\Delta\alpha$. Fig 4.18 displays the results of such an experiment on CdTe:Cl. The first harmonic response was measured for an electric field of the form $E_1 + E_o\cos(\omega t)$ where E_1 is an external d.c. field. In this experiment E_1 takes the values of + 3.0 V, 0.0V and -10.0V. The curves show that $\Delta\alpha$ is strongly dependent on the magnitude and polarity of the static field. In addition, the magnitude of $\Delta\alpha$ is linearly dependent on the d.c. bias. This is demonstrated in Fig 4.19 which shows that $\Delta\alpha = 0$ at 5.25 V. for this particular sample. Beyond this point, negative absorption changes are recorded. This involves a 180^o reversal of the phase at which the signal is measured on the phase sensitive detector.

An important consideration is whether the built in field is an inherent property of the crystal. Fig 4.20 provides an answer to this question. The upper straight line is for the sample oriented with a particular face towards the incident light, the other for the sample with the same face rotated through 180^o. Both lines have very similar gradients with positive d.c. voltages required to null the electroabsorption signal. This observation implies that even though the sample has been rotated through

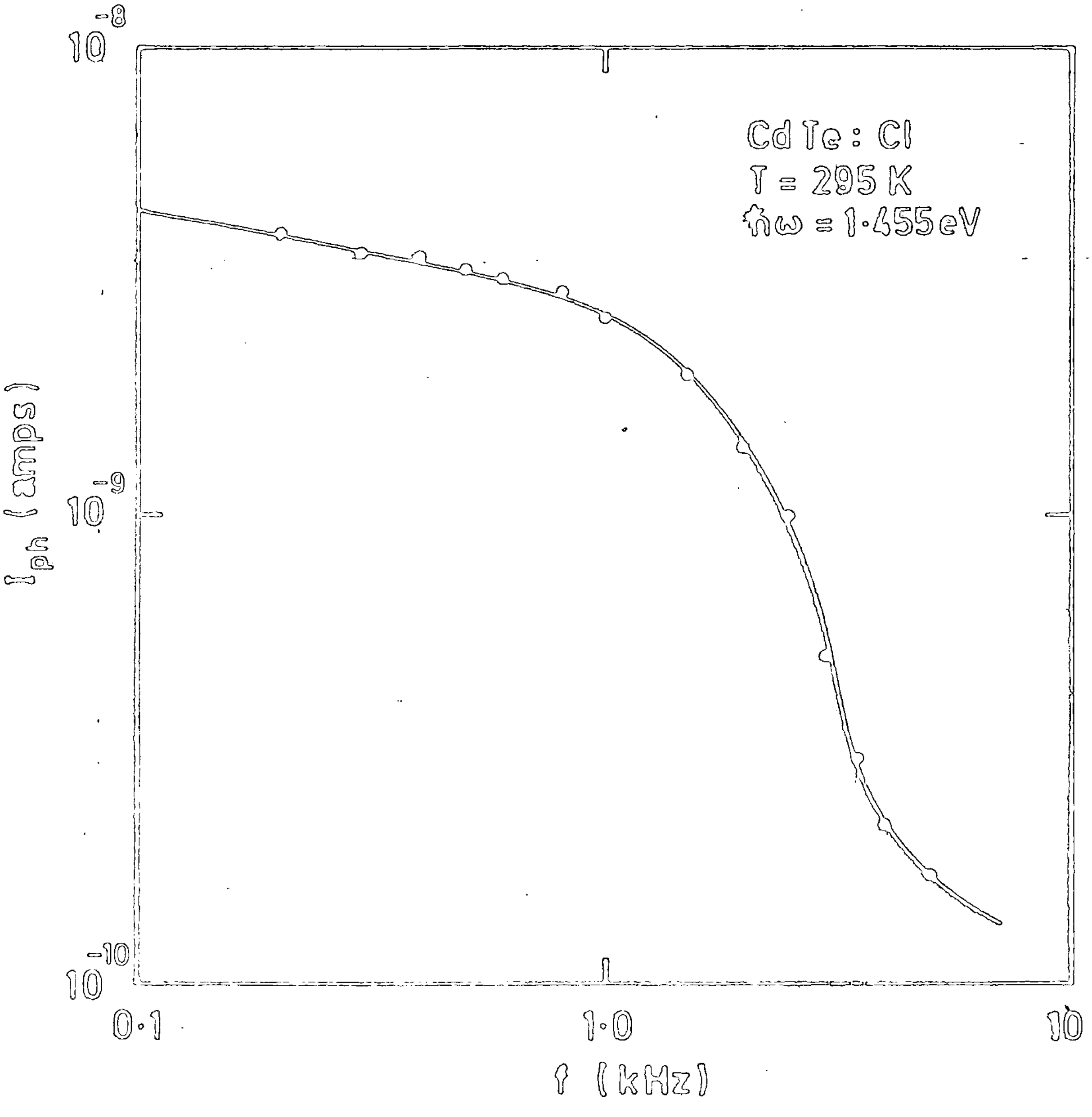

Figure 4.17 : Photoconductivity of a CdTe : Cl crystal as a function of the electric field frequency at room temperature.

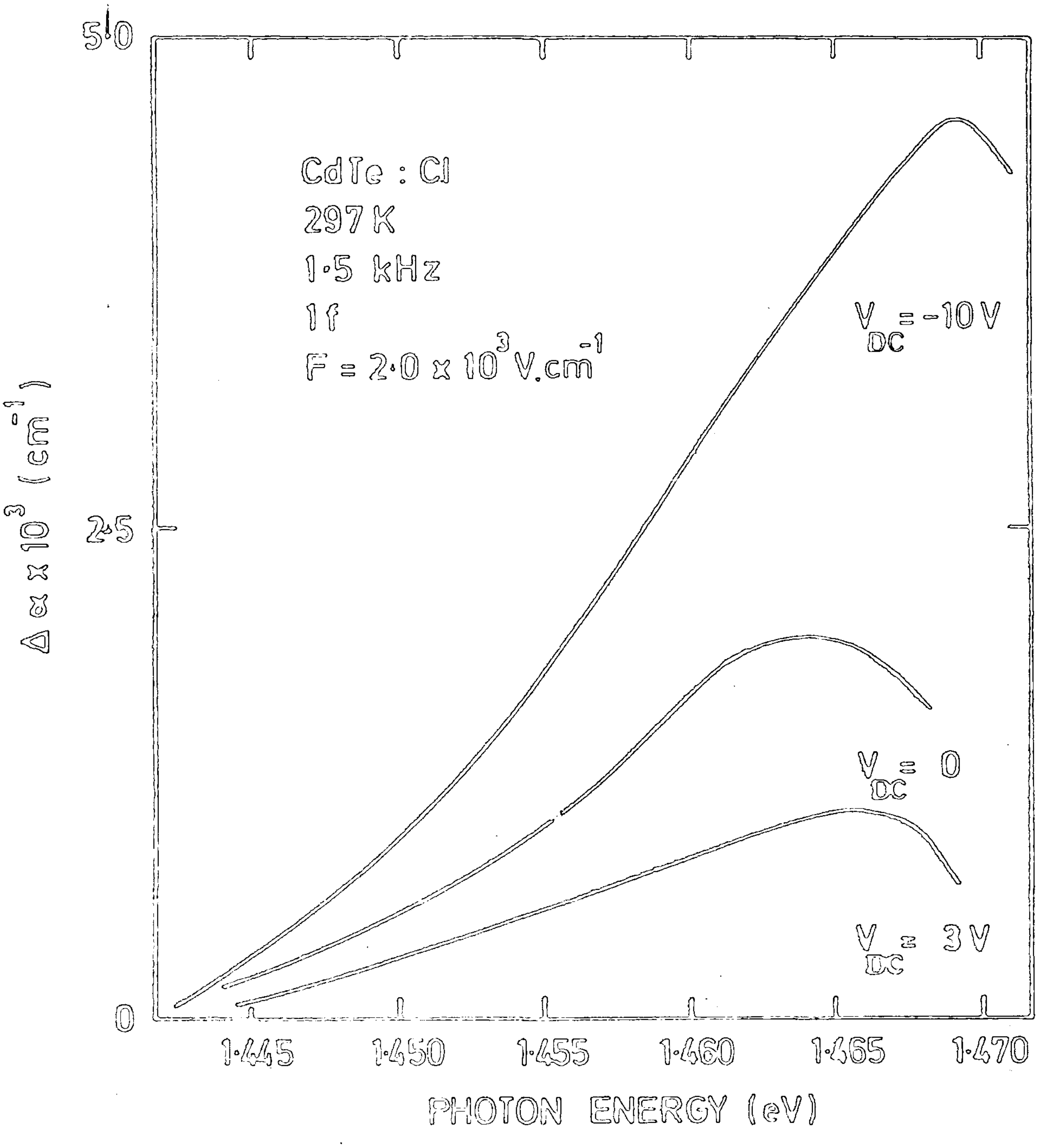

Figure 4.18 : Electroabsorption spectra of a CdTe : Cl crystal with a small d.c. field superimposed on a large a.c. field. Sample thickness is 400 μm.

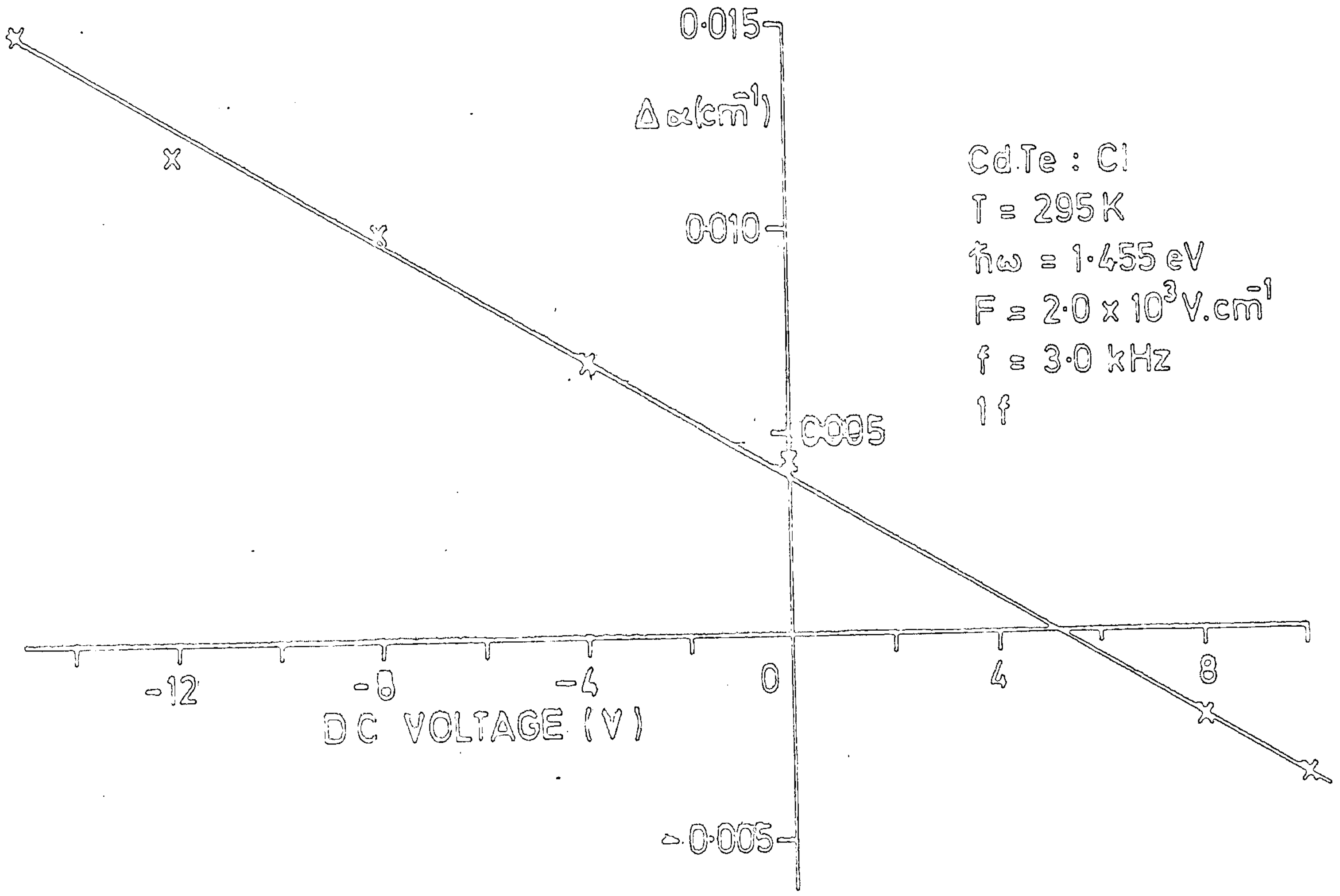

Figure 4.19 : Variation of the absorption change of a CdTe : Cl sample as a function of the superimposed d.c. bias.

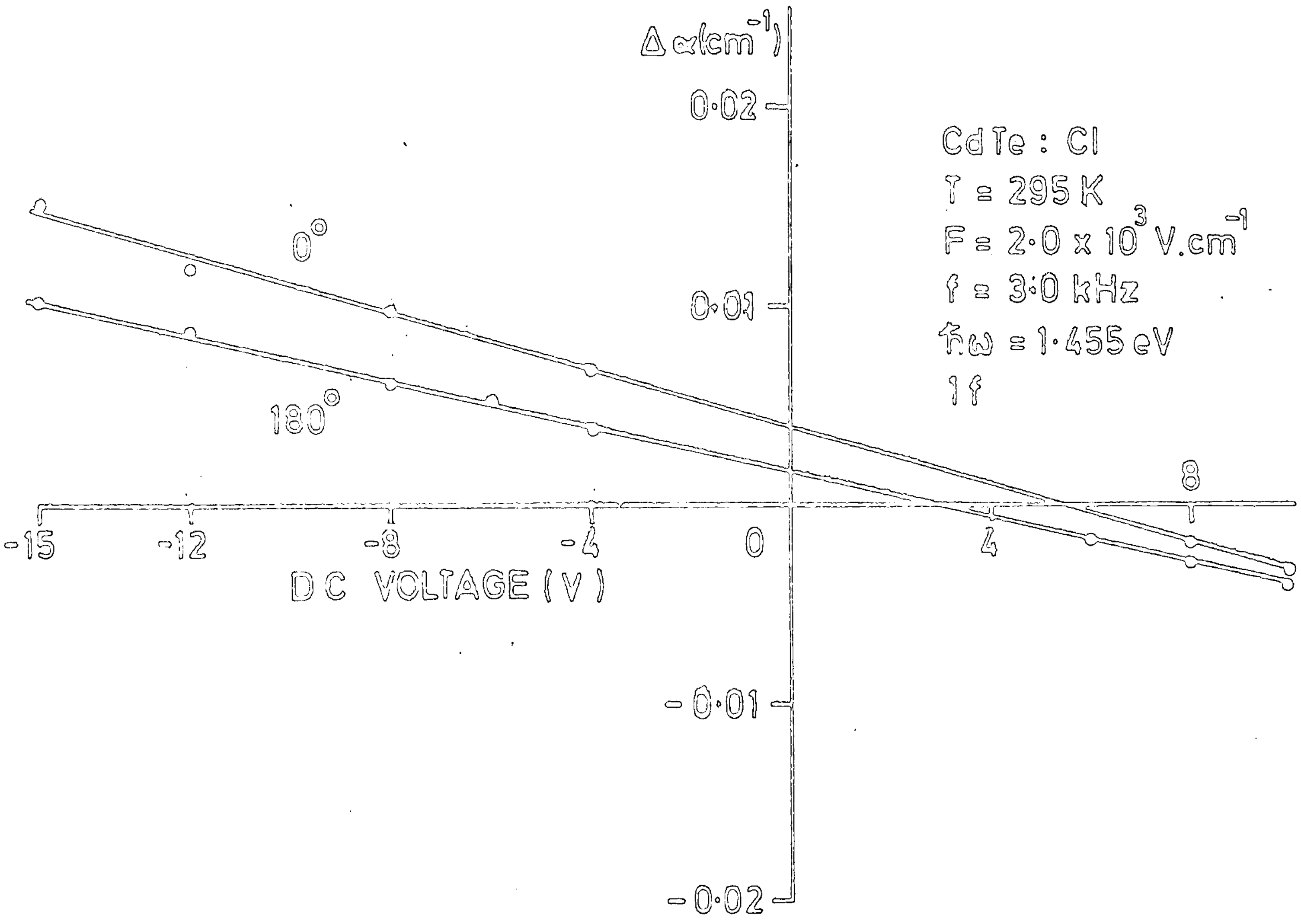

Figure 4.20 : Absorption change of a CdTe : Cl sample as a function of the d.c. component of the electric field, for a particular face of the crystal both towards and then away from the incident light.

180°, the field has not changed direction. This leads us to conclude that the apparent static internal field is not an inherent property of the sample but is externally generated.

4.5.2 Frequency Dependence of the Second Harmonic Response

It has been mentioned previously that for an idealized case, the absorption change induced by any external alternating electric field can only be detected at twice the modulating frequency ; the second harmonic response. However, our results indicate that this response depends on the modulating frequency as illustrated in Fig 4.21. In this case the magnitude of $\Delta\alpha$ decreases rapidly at low frequency and saturates at 4.0 kHz. The fact that the magnitude of $\Delta\alpha$ at low frequency is also a function of light intensity as shown in Fig 4.22, raises the possibility that this is also due to the photoconductive effect discussed in the previous subsection. This view is supported by the observation of a constant value of $\Delta\alpha$ above 4.5 kHz, the frequency at which this effect is expected to vanish. If so, one would predict that the second harmonic response at high frequency should not depend on the light intensity. In fact this is exactly what is observed and the data from such an experiment are shown in Fig 4.23. In this case, as expected, a negligible effect was observed by superimposing a small d.c. field on an alternating electric field such as shown in Fig 4.24. The above experiments make us reasonably confident that the second harmonic response measured at high frequency is a genuine electroabsorption signal and can be used to obtain meaningful data.

4.5.3 Discussion of Results

As mentioned in Chapter 2, there are several models relevant to the effect of an electric field on the inter-band optical absorption of a crystal. The earliest, put forward by Franz and independently by Keldysh, was based on photon-assisted Zener tunneling of electrons across the energy gap. This theory predicted a 'red shift' of the absorption edge

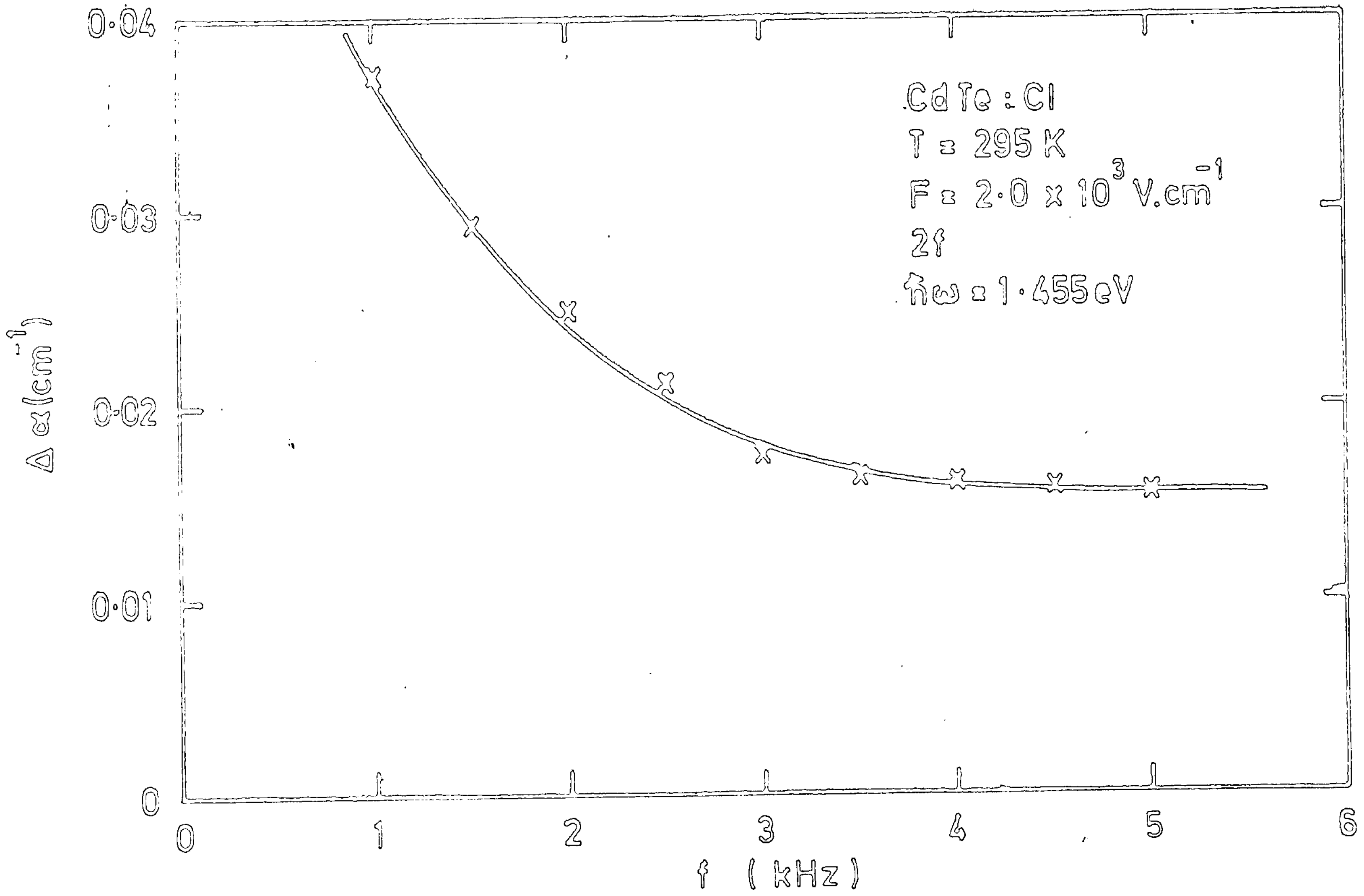

Figure 4.21 : Absorption change of a CdTe : Cl crystal as a function of the frequency of the applied electric field.

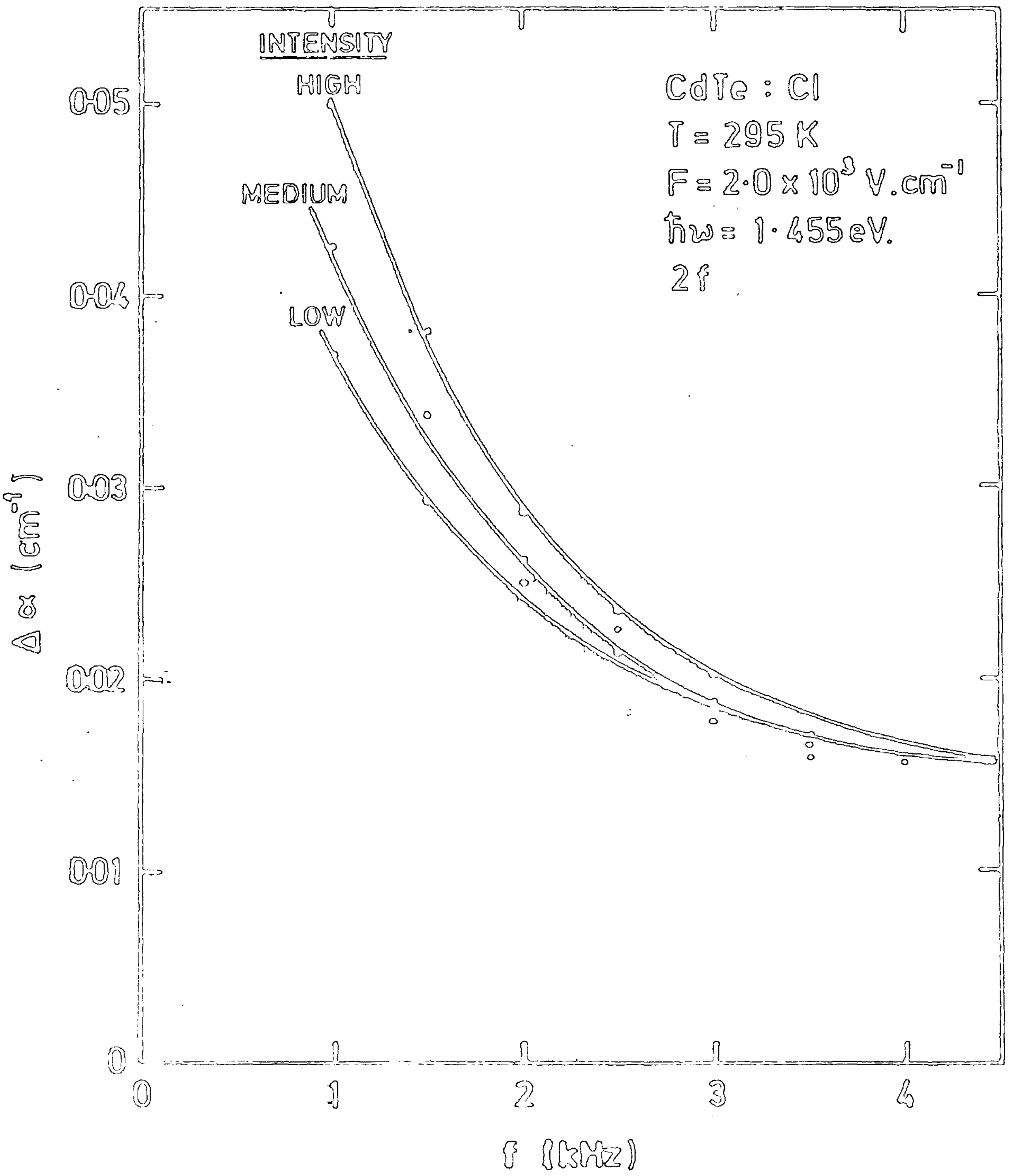

Figure 4.22 : Absorption change of a CdTe : Cl crystal as a function of the frequency of the applied electric field, for three different incident light intensities.

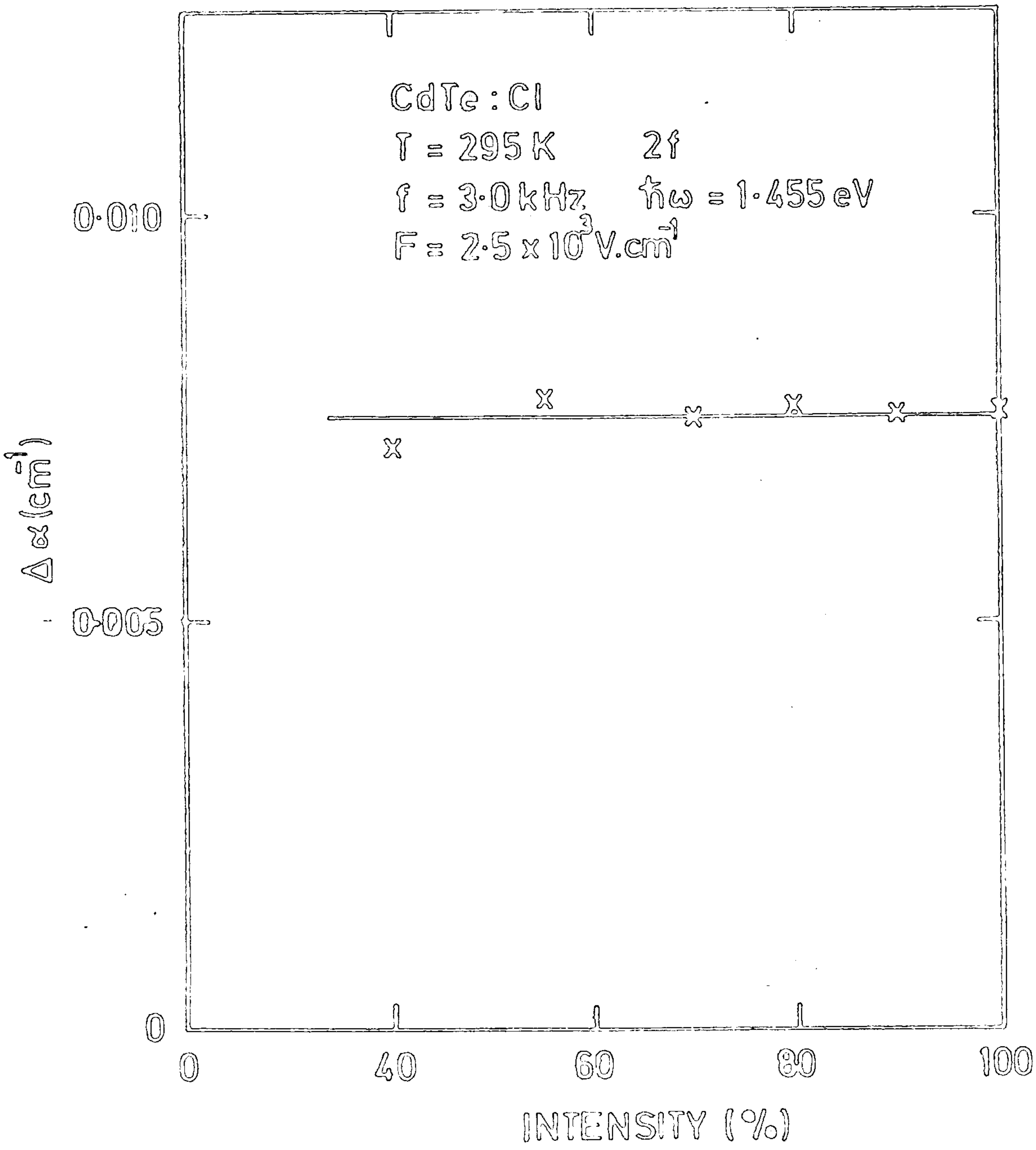

Figure 4.23 : Incident light intensity dependence of the absorption change of a CdTe : Cl crystal at 3.0 kHz.

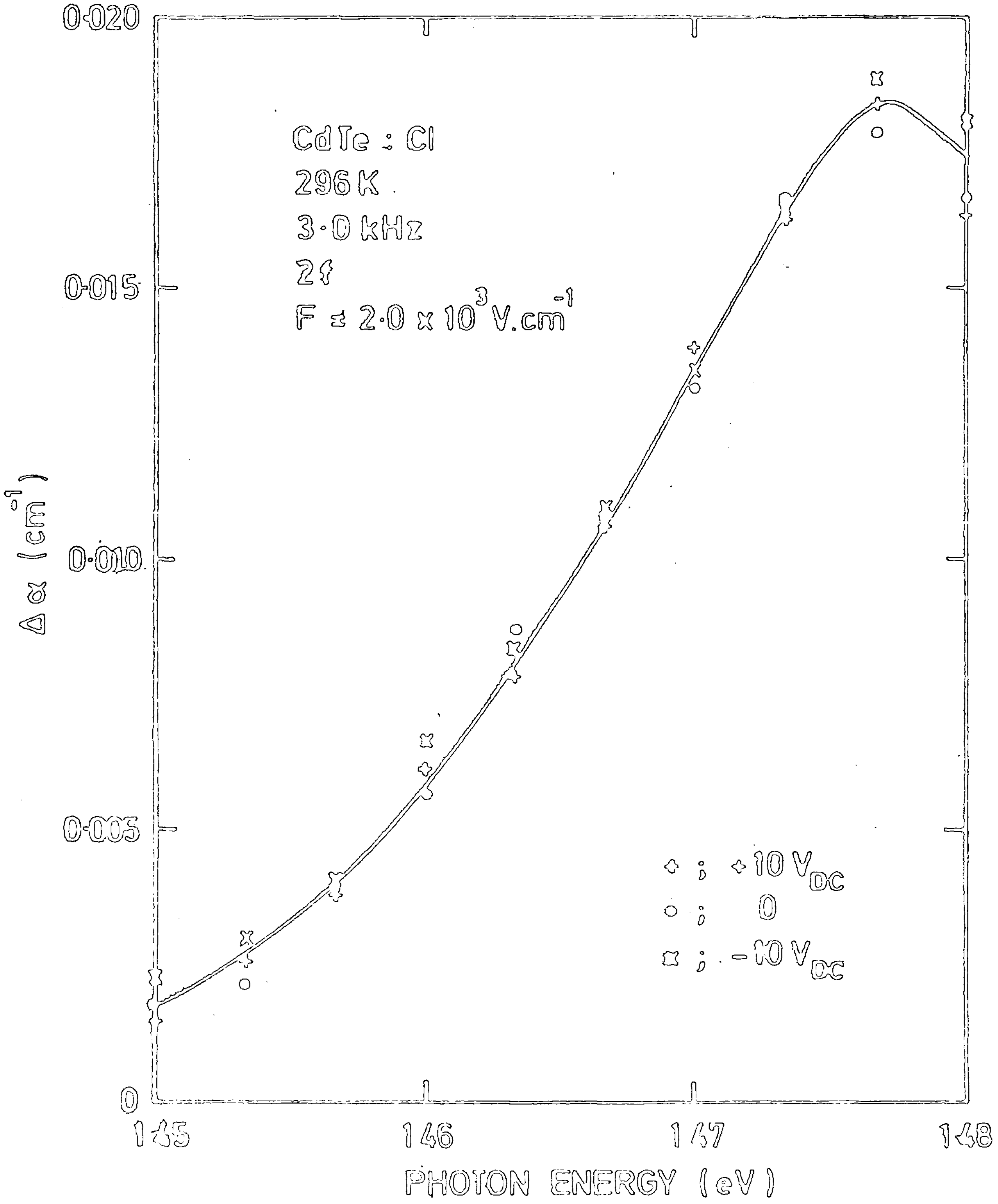

Figure 4.24 : Electroabsorption spectrum of a CdTe : Cl crystal with a small d.c. field superimposed on a large a.c. electric field.

with applied external field. The Franz-Keldysh theory was extended by Callaway and Tharmalingham, among others, who expressed the solution of Schrodinger's equation for an electron in an external electric field in terms of Airy functions which, when incorporated into the band gap optical absorption problem, produce spectral oscillations. These oscillations depended upon the nature of the band gap absorption process. The transitions involved are not always band edge transitions. Instead they may arise due to excitations from the valence band to exciton states lying just below the conduction band. This leads to a second group of theories which necessarily includes the Coulomb binding of the electron and hole pair.

The electroabsorption results presented in this chapter refer exclusively to the low absorption region, namely for $\alpha < 200$ cm^{-1}. This is an area where the Franz-Keldysh theory is most likely to be applicable. A careful analysis does indeed indicate that our results can be best fitted to this 'one-electron' theory of electroabsorption. That is, in the presence of an external electric field, the exponential absorption edge of CdTe:Cl is shifted towards lower photon energies, the magnitude of which is proportional to the square of the electric field strength. Quadratic field dependences are shown clearly in Figs 4.11 and 4.12. As predicted by theory the slope of the α and $\Delta\alpha$ versus photon energy curves are equal. Accordingly, the data should fit equation (2.31) namely,

$$\frac{\Delta\alpha}{\alpha} = \frac{\beta^3 \hbar^2 E^2}{24 m^* e}$$

from which the reduced effective mass of the carriers in CdTe:Cl can be calculated. A total of four samples were used and the average results of the calculation at two different temperatures are shown in Table 4.2.

Table 4.2: Values of the reduced effective mass of CdTe:Cl calculated from electroabsorption in the Ohmic region.

Temperature	Calculated m^*/m_o	Published Value for pure material
297 K	.105	0.10 (2)
150 K	.097	

Despite the complexity of the technique, satisfactory results have been obtained. The factor limiting the accuracy was the difficulty in obtaining a reproducible value of the absorption coefficient, α . This is because only a single beam monochromator was available for the spectral area concerned. Overall accuracy of the effective mass calculation is about ± 10%. However, in view of the quality of the data obtained and the reproducibility from one sample to another, an accuracy as good as ± 5% is thought possible.

It might be argued that the photocarrier effect could give rise to anomalous electroabsorption results. It has been shown, however, that the photoconductive effect disappears if measurements of the second harmonic signal were done above 3.5 kHz for CdTe:Cl. Furthermore a small d.c. voltage superimposed on a large a.c. field has virtually zero effect if measurements are taken at twice the modulating frequency. Thus, it seems reasonable to conclude that second harmonic data taken above 3.5 kHz are due to the true Franz-Keldysh effect.

4.6 ELECTROABSORPTION IN THE SPACE CHARGE LIMITED CURRENT REGION

Knowledge of the distribution of electric field across the bulk of the material is important in analyzing electroabsorption data. Within the Ohmic region, the electric field across the sample is uniform and it is straightforward to calculate the effective electric field which produces the field induced absorption change. The electroabsorption signal must however, in some samples, be detected at very large electric fields where charge carriers injection may occur. In this section we indicate how meaningful measurements can be made in such circumstances.

4.6.1 Space Charge Limited Currents (SCLC)

Charge carriers injection in solids can be observed only if the thermally generated carrier density is negligible. The general scaling law for bulk space charge currents, J, in a homogeneous medium is given by

$$J \propto L \left(\frac{V}{L^2} \right)^n \qquad (4.1)$$

where n is not necessarily an integer. L is the thickness of the sample and V is the applied potential. For the trap-free insulator n = 2, for double injection n = 3, and for recombination space charge injection $n = \frac{1}{2}$.

The existence of space charge will significantly alter the field distribution of the electric field across the sample. For example, a sample of 1.0 x 1.0 x 0.2 cm^3 dimension with a dielectric constant of 2.5 represents a capacitance of 1.0 pF. An opposite surface charge of 5.0 nC on each side produces a potential difference between the surface of 5.0 kV or an electric field of 25.0 $kV.cm^{-1}$, comparable to the field of 10^4-10^5 $V.cm^{-1}$ used in our experiments. Most of the high resistivity CdTe samples studied showed space charge limited conduction(26,35,36,37) due to the low density of thermally generated charge carriers. For this reason, a systematic study of electroabsorption experiments in the SCLC region was performed and the results were compared to the accurate measurements obtained in the linear I-V region.

A quadratic field dependence of the current density in CdTe:Cl in accordance with equation 4.1 with n = 2 is shown in Fig 4.6. At field strengths above 4 x 10^3V.cm^{-1}, the field distribution in the crystal is distorted due to the injected charge. The following section describes the effect of this injection on the electroabsorption properties of CdTe:Cl.

4.6.2 Electroabsorption Results

Typical room temperature electroabsorption data for CdTe:Cl taken in the SCLC region are shown in Fig 4.25 ; the zero field absorption curve is plotted alongside. No new structure is seen and the data appear to mirror closely those shown in Fig 4.10. A careful inspection of the results does, however, reveal an interesting trend when the electric field dependence is plotted as a function of frequency. In Fig 4.26, the change in absorption, $\Delta\alpha$, is plotted versus the square of the applied voltage for the specimen whose electroabsorption spectrum is shown in Fig 4.25. At the selected frequency of 3.5 kHz, a good straight line is obtained over a wide range of voltage and this extrapolates to the origin. If, however, measurements are taken at a lower frequency, the quadratic dependence is still satisfied but it is found that the straight line does not extrapolate to the origin. Fig 4.27 shows this effect for data detected at 1.0 kHz. The intercept on the abscissa at voltage V_o is an indicative of a built in field.

Fig 4.28 collects together data obtained at a variety of frequencies. All straight lines display the characteristics mentioned above up to a maximum frequency of about 3.3 kHz. Beyond this value, the magnitude of $\Delta\alpha$ at a particular field strength is independent of frequency. The frequency dependence of this second harmonic response is very similar to that observed in the Ohmic region. In the SCLC region, however, the field distribution in the sample is distorted by charge injection. As a result a large voltage is developed in the vicinity of the injecting electrodes which causes a larger potential drop across the remainder of the bulk and thus a larger electroabsorption signal. This effect is however reduced with increasing frequency and at 3.5 kHz or higher when the space charge cannot respond fast

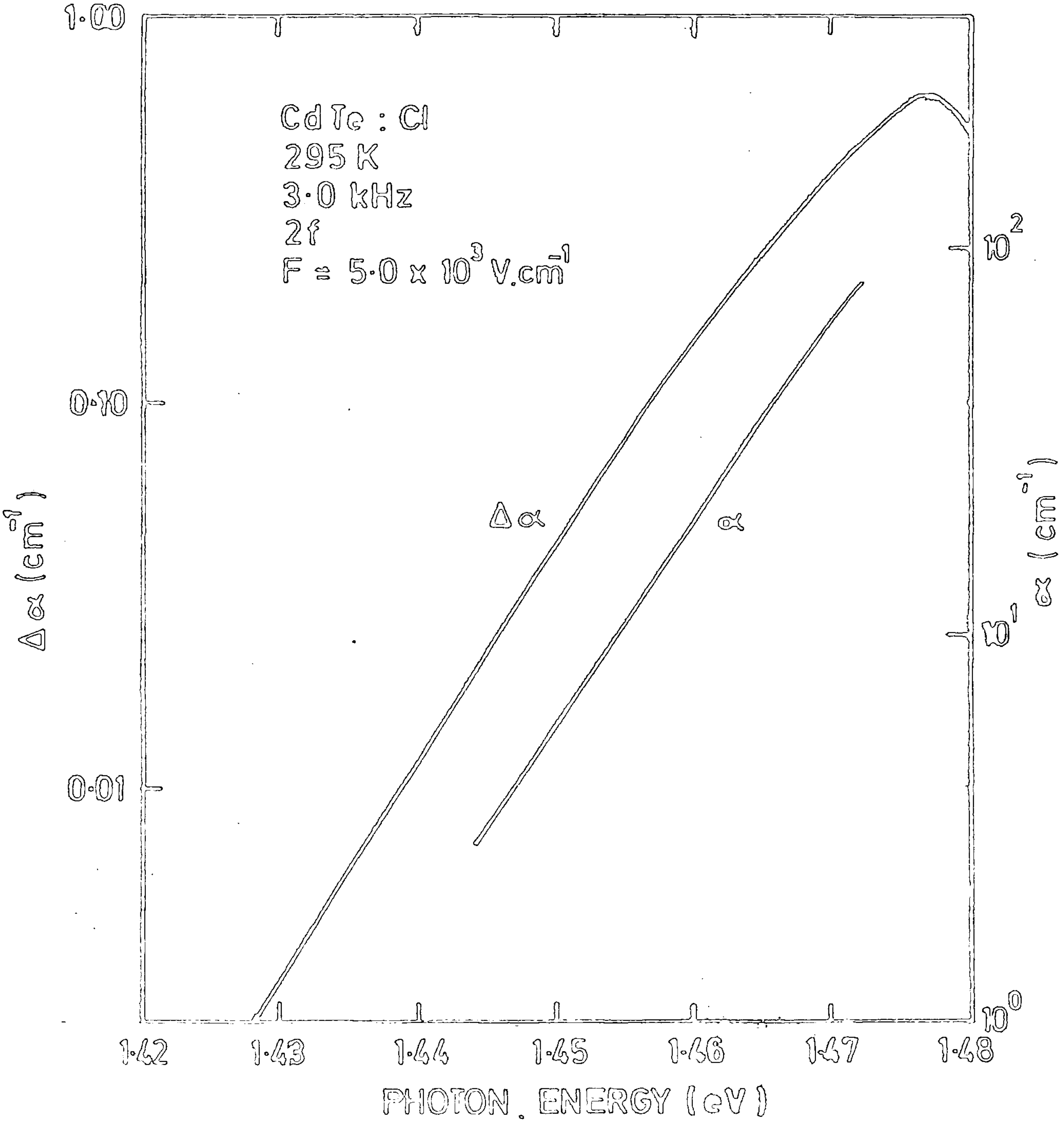

Figure 4.25 : Electroabsorption spectrum obtained from the space-charge-limited current region of a CdTe : Cl sample at room temperature. The absorption curve is also shown.

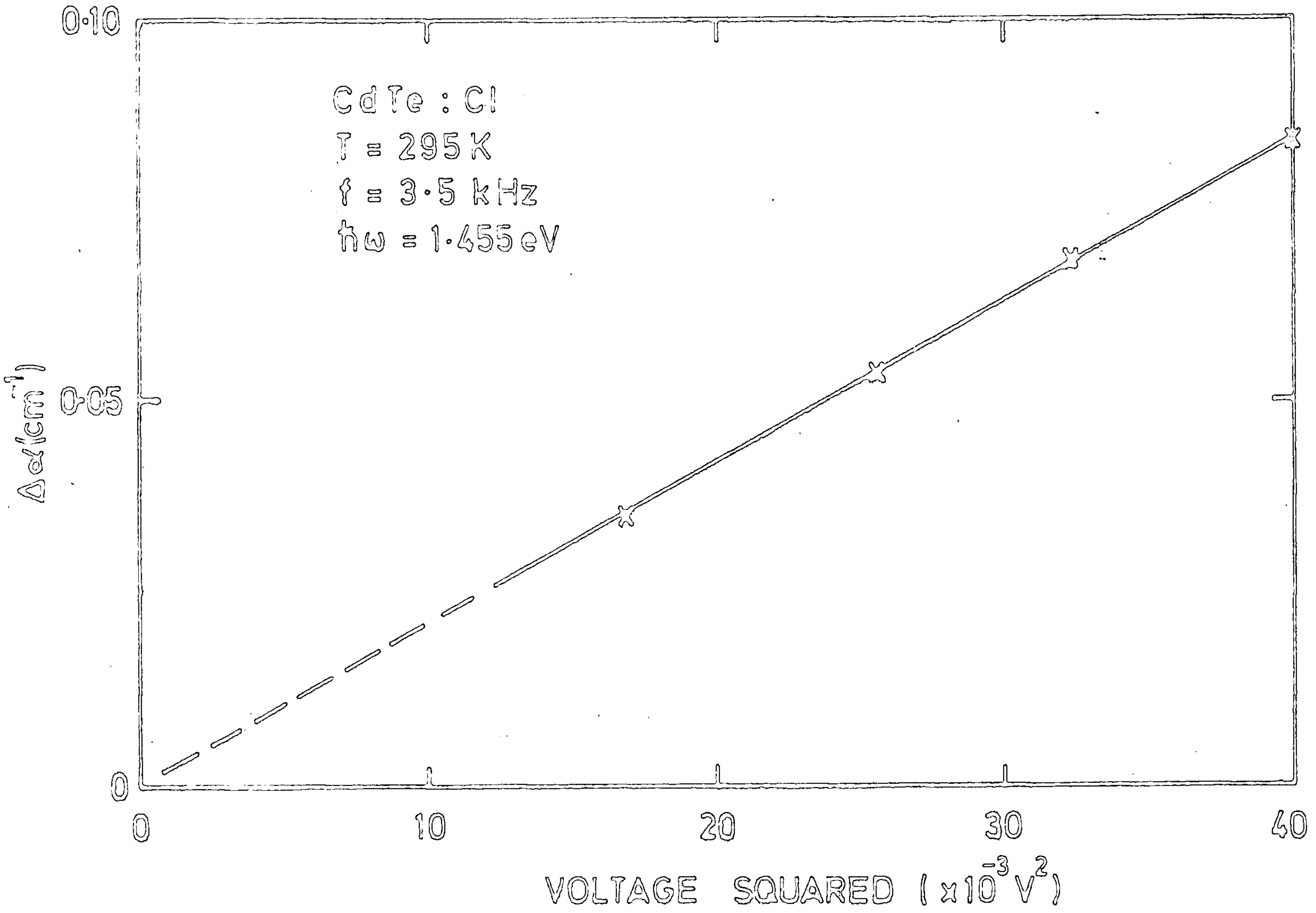

Figure 4.26 : Quadratic field dependence of the absorption change of a CdTe : Cl sample at 3.5 kHz.

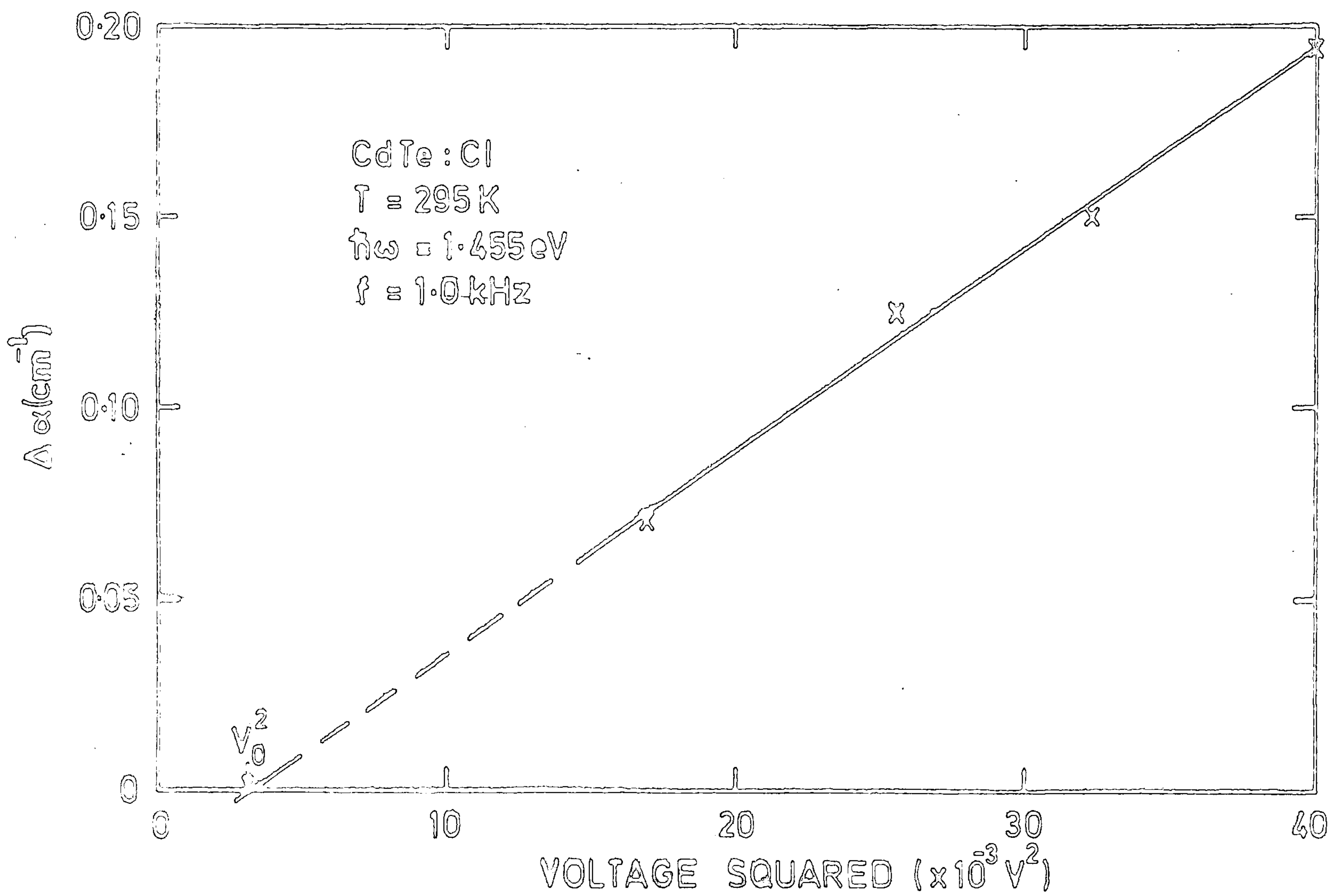

Figure 4.27 : Quadratic field dependence of the absorption change of a CdTe : Cl sample at 1.0 kHz.

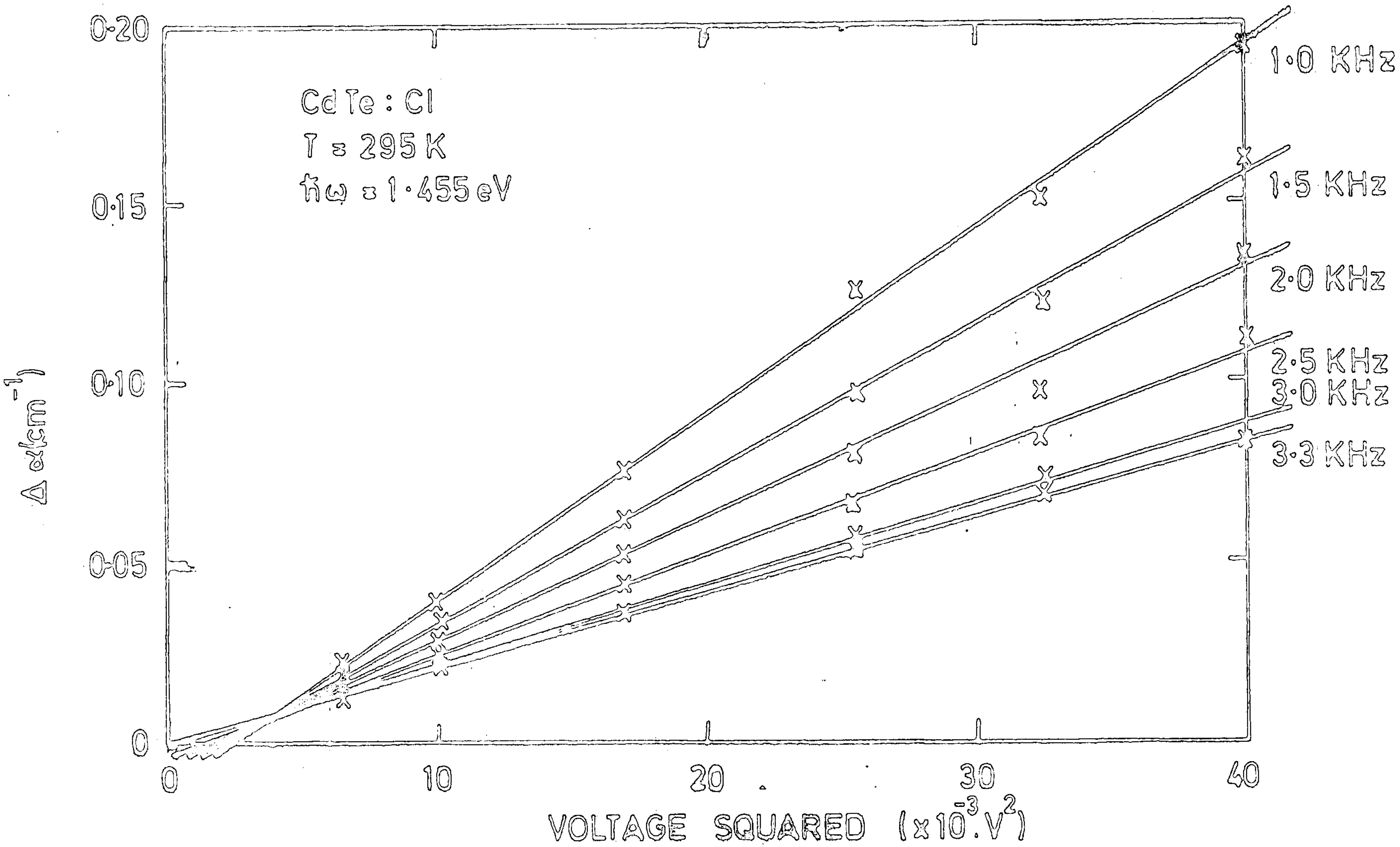

Figure 4.28 : Quadratic field dependence of the absorption change of a CdTe : Cl sample as a function of the frequency of the applied electric field.

enough, this effect is insignificant. This result lends support to our interpretation of the anomalous electroabsorption response (first harmonic and low frequency second harmonic responses) discussed in sections 4.5.1 and 4.5.2 ; that is, it helps confirm our belief that the field distribution in the sample can be different due to a photoconductive effect.

The purity of the second harmonic response taken above 3.5 kHz can be tested by substituting the data into the Franz formula and calculating the reduced effective mass. This is valid since the exponential slope of $\Delta\alpha$ and α with photon energy are equal, and a quadratic field dependence of $\Delta\alpha$ is obeyed. The result of the calculation is given in Table 4.3 and is compared to the value obtained using measurements in the Ohmic region. Good agreement is achieved indicating that the space charge effect can in fact be compensated by measuring the second harmonic response at frequencies above 3.5 kHz.

Table 4.3 : Value of m^* of CdTe:Cl deduced from electroabsorption in SCLC region.

Temperature	(m^*/m_o)	
	SCLC region	Ohmic region
297 K	0.107	0.105

It appears therefore that, provided certain precautions are taken, genuine electroabsorption responses can be detected in either the Ohmic or SCLC regions. Such experiments can thus be performed in certain types of semiconductor where charge injection is often present, e.g. in thin films.

4.6.3 Electroabsorption in Semiconductors other than the Cadmium Telluride

Having discovered how to compensate for the effects of photoconductivity and injected charge, we thought it useful to study other wide band gap semiconductors and compare results. We were particularly interested to explore the possibility of a pattern developing in the characteristic frequency f_o, required to avoid field distortion. Similar measurements to those performed for CdTe:Cl have been carried out for GaAs:Cr,CdS and ZnSe and the results are shown in Figs 4.29 to 4.31. It would appear that the values of f_o do not correlate well with the band gap energies of these materials. For example, only small differences in the values of f_o are observed between CdTe:Cl and CdS which have band gap energies of 1.45 and 2.37 eV, respectively. The properties of these materials are however controlled by the presence of impurity levels within the forbidden gap. For example, CdTe:Cl, CdS and ZnSe crystals all possess dominant levels at 0.8 eV below the conduction band as shown in Table 4.4; consequently, it is not surprising that they should be characterised by a similar value of f_o. The value of f_o is lower for GaAs: Cr and therefore we must assume that the trapping or recombination constants for this material are rather different to those in the II-VI compounds mentioned above.

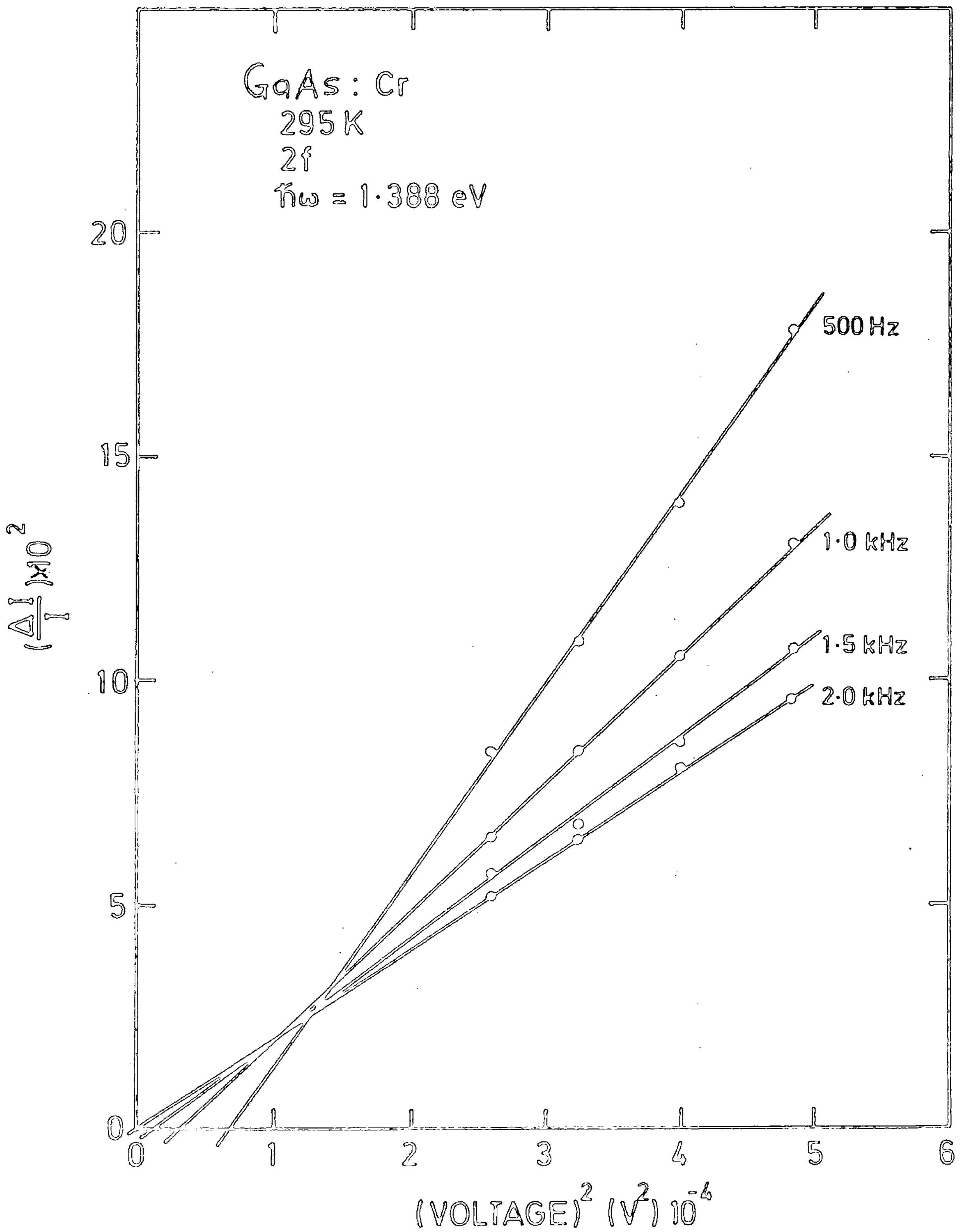

Figure 4.29 : Quadratic field dependence of the fractional change in transmission of an GaAs :Cr crystal at 295 K, as a function of the frequency of the modulating electric field.

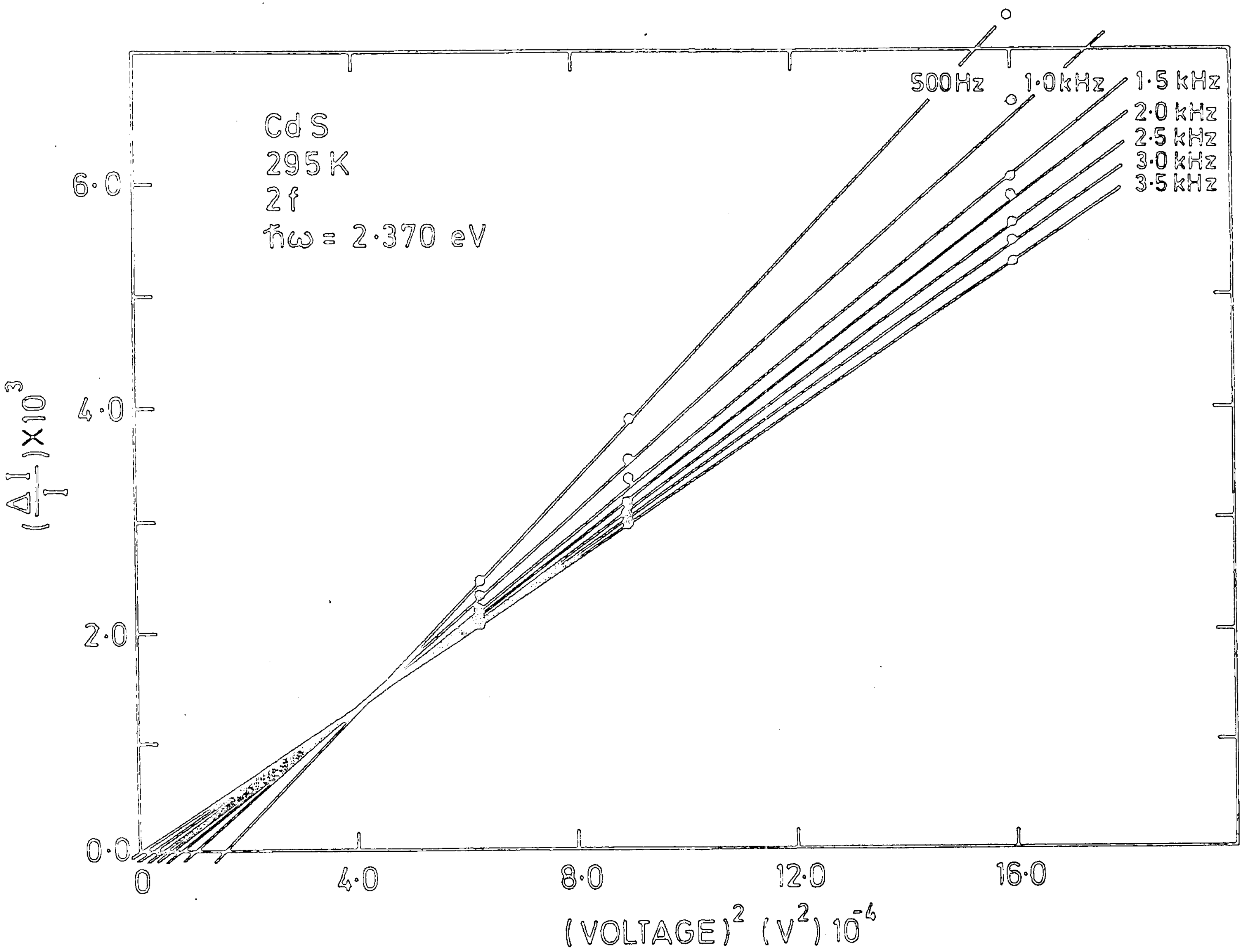

Figure 4.30 : Quadratic field dependence of the fractional change in transmission of a CdS crystal at 295 K as a function of the frequency of the modulating electric field.

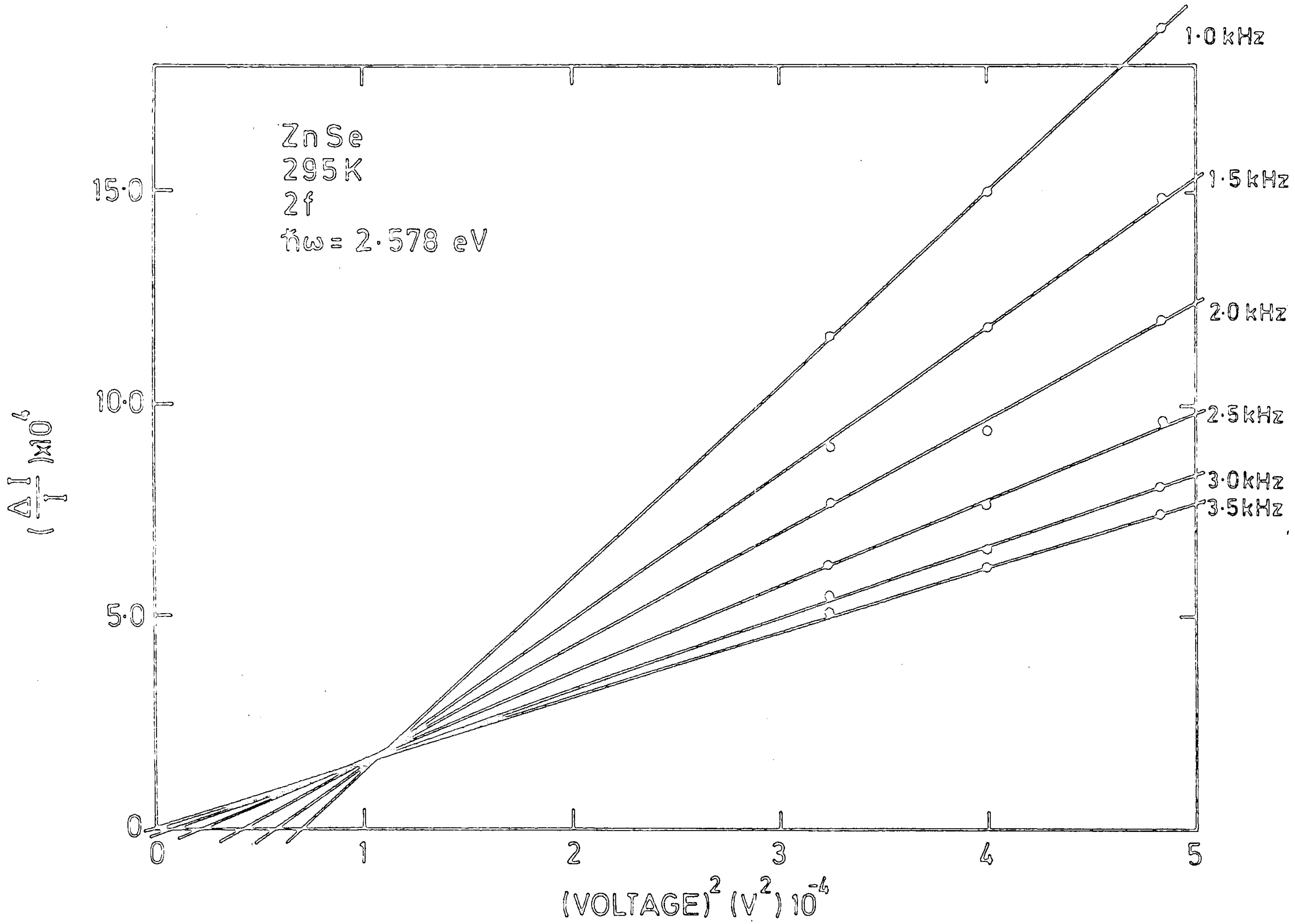

Figure 4.31 : Quadratic field dependence of the fractional change in transmission of a ZnSe crystal at 295 K, as a fraction of the modulating frequency.

Table 4.4 : Variation of f_o for different compounds.

Compound	E_g (eV)	f_o kHz	(E_c-E_r) eV
GaAs:Cr	1.38	2.0	0.4 - 0.68$^{(a)}$
CdTe:Cl	1.45	3.3	0.45, 0.84
CdS	2.37	3.5	0.70 - 0.80$^{(b)}$
ZnSe	2.56	3.5	0.80

(a) D.C.Look, J.App.Phys. 48 (1977) p 5141.

A. Ashby et al, Solid State Commun. 20 (1976) p 61.

(b) E.A. Niekisch, Proc. of the International Conf. on Semiconductor Physics, Prague (1960) Academic Press Publ. p 1064.

CHAPTER 5

ELECTROABSORPTION IN SOLID SOLUTIONS OF $Cd_xZn_{1-x}S$

5.1 INTRODUCTION TO $Cd_xZn_{1-x}S$

As we have already seen, the application of an electric field to a solid produces changes in the optical properties which can be related to the energy level structure of a material. The largest changes are expected to occur at energies corresponding to critical points in the energy band structure or at other singularities in the electronic density of states such as excitons(1). For energies corresponding to the band gap of a material, the electroabsorption data are generally interpreted in terms of optical transitions at critical points in the joint interband density of states. This was the case for the cadmium telluride data discussed in Chapter 4. However, it was suggested as already discussed in section 2.6, that exciton effects may play a significant role in the electroabsorption experiments and should be taken into consideration in the interpretation of such measurements.

The objective of this chapter is to describe results for a system where exciton effects are definitely of significance. The one we have chosen involves solid solutions of CdS and ZnS, both of which exhibit strong exciton absorption. In addition to demonstrating the sensitivity of this technique in examining excitonic effects in semiconductors, the experiments provide for the first time an indication of how the effective mass varies with alloy composition. That is, the excitonic electroabsorption theory discussed in Chapter 2 provides a means of locating the energy of the exciton levels, information which can then be used to calculate the reduced effective mass of the exciton for different contents of zinc in the $Cd_xZn_{1-x}S$

system where x is the mole fraction of CdS.

The crystals used in this work were grown in this department as photoconductors for photovoltaic solar cell applications$^{(2)}$. This follows the finding by Hill$^{(3)}$, that CdS : Cu_2S solar cell characteristics, which are determined by the interface densities and distributions at the junction due to the lattice mis-match between CdS and Cu_2S, can be considerably improved by employing $Cd_{0.8}Zn_{0.2}S$ instead of CdS. Solar cells have also been fabricated using mixed crystals with different zinc contents$^{(2)}$; here it was found that the open circuit voltage increased with increasing zinc content. The short circuit current, however, decreased resulting in no significant improvement in efficiency.

The chapter begins with an introduction to the $Cd_xZn_{1-x}S$ system which includes a review of the previous electroabsorption experiments carried out on the individual components of this alloy system.

5.1.1. Crystal Growth

The single crystals of $Cd_xZn_{1-x}S$ used in this work were grown by vapour phase sublimation down a temperature gradient as described in (4,5). This technique requires the simultaneous presence of both group II and group VI elements in the gaseous form. The origin of the elemental vapour species may be direct from the elements or indirect via the dissociation of the preformed compounds. In this particular case, a charge of CdS and ZnS, of the desired proportion, is held at a temperature of about 1150°C. It is contained in a silica growth capsule which is connected via a narrow orifice to a long tail extending to the lower temperature region of the furnace. The tail contains one of the elemental constituents of the binary system, and its temperature is adjusted to provide a vapour pressure over the evaporating charge required for crystallization. Crystal growth occurs at the upper part of the capsule where the temperature is slightly lower. In this technique, the capsule is sealed nominally at high vacuum. Crystals with high content of zinc are more difficult to grow due to higher melting point. This work is therefore restricted to only crystals with low zinc content.

The as-grown crystals normally have resistivities of less than 10 Ohm.cm. For the purpose of this work, the samples were annealed in sulphur vapour at 600°C for about 36 hours to produce semi-insulating material with a resistivity of about 10^9 Ohm.cm.

5.1.2 Band Structure

CdS and ZnS are II-VI compound semiconductors which crystallize with either the zinc blende or wurtzite structure and often with intermixtures of both structures. The wurtzite structure which is in the hexagonal crystal class, has the combination of tetrahedral sites. It consists of two interpenetrating close-packed hexagonal lattices as shown in Fig 5.1. The zinc blende structure which has already been described in Chapter 4 for CdTe, is in the cubic class but also has the combination of tetrahedral sites. The tetrahedral lattice sites which characterize the zinc blende and wurtzite structures suggest that homopolar bonding(7) ; bonding via electron spin pairing, is present. However, an exchange of electrons which results in an ionic electrostatic attraction and thus ionic bond is also possible. The ionic characteristic which increases with decreasing atomic weight has the effect of strengthening the lattice and thus raising the melting point and increasing the energy gap.

The majority of our knowledge of the band structure of the II-VI compounds has been derived from the semi-empirical pseudopotential method. For example, the band structure of CdS, as determined by Bergstresser and Cohen(7) is shown in Fig 5.2. Eckett(8) has obtained results for ZnS which show good agreement with those of Cohen and Bergstresser(9), and these are shown in Fig 5.3. In both cases, however, no account was taken of spin-orbit splitting effects. The minimum of the conduction band and the maximum of the valence band occur at a Γ point thus making both CdS and ZnS direct band gap materials.

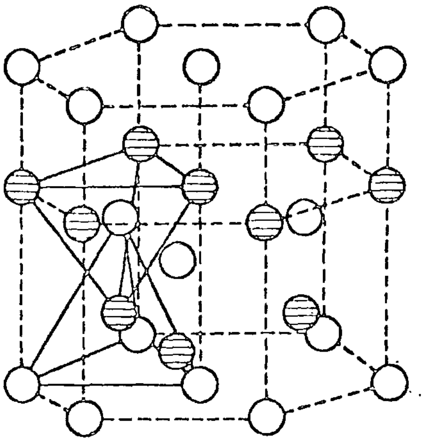

Fig 5.1 : Wurtzite Structure illustrating the tetrahedral site.

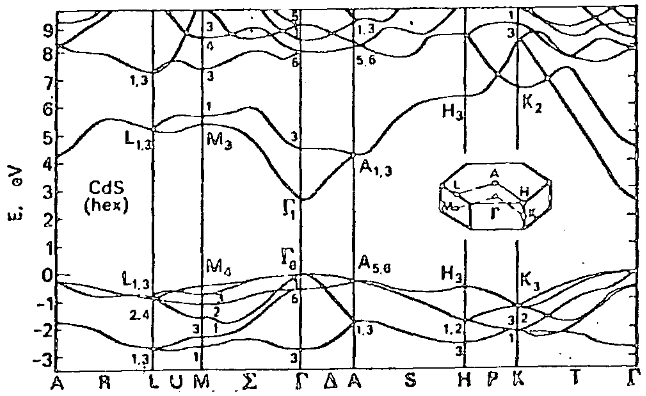

Fig 5.2 : Band structure of CdS (7).

It is however evident from the reflectance spectrum at low temperatures that two or three exciton peaks, depending upon whether the crystal is zinc blende or wurtzite, are observed(10). These peaks result from the splitting of the valence band through spin orbit interaction and crystalline field effects. These effects are illustrated in Fig 5.4. In the zinc blende structure for example, the valence band is composed of eight sub-bands. At k = 0 there are two bands forming the upper edge Γ_{25} which is threefold oribitally degenerate (p^3) or sixfold spin degenerate, and the lower edge Γ_1 which is twofold spin degenerate (s). The upper edge is split into a twofold spin degenerate term with Γ_8 symmetry. Γ_7 is lower in energy than Γ_8 by the spin-orbit interaction energy Δ_{so}. The conduction band at k = 0 has two minima Γ_2' and Γ_{15} which are two and sixfold spin degenerate, respectively. Γ_2' is associated with an s electron state and Γ_{15} with a p^3 electron state. If a non-perturbational approach is adopted, the Γ_2' term becomes the Γ_1 term.

Very little work has been performed on the band structure of intermediate crystals of the $Cd_xZn_{1-x}S$ system. Photoconductivity and transmission measurements, however, indicate that the band gap of the alloy increases with decreasing x,(11 to 13) and can be expressed(3) as $E_g(x) = 2.42 + 0.87x + 0.43\,x^2$ eV at room temperature, where $0 \leq x \leq 1$.

5.1.3 Optical Properties

The spectrum in the region of the fundamental absorption edge exhibits much useful information about the material under investigation. A particular feature in the studies of this alloy system is the presence of exciton states which appear as peaks on the longwavelength side of the absorption edge. Thomas and Hopfield(14) have studied in detail the exciton spectrum of CdS at temperature between 77 K and 4.2 K. The observation of exciton states and the polarization properties of excitons make possible the determination of the position of excitons A, B and C as shown in Fig 5.5. These correspond to the energy splittings of the

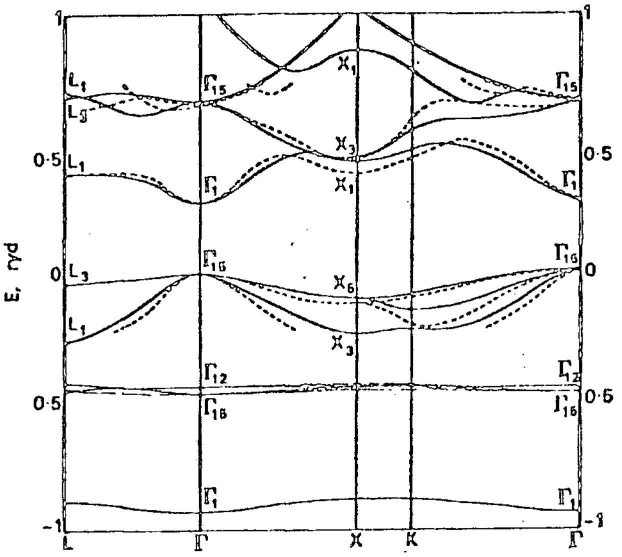

Fig 5.3 : Band structure of ZnS as calculated by Eckett et al (8) and the results of Cohen et al (9) (dashed lines).

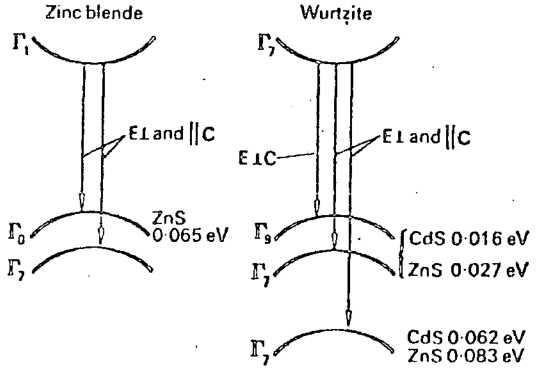

Fig 5.4 : Energy band structure of wrutzite and zinc blende in the region of the Γ point with crystalline field and spin-orbit splitting effects present in the valence band structure (6).

valence band into three sub-bands shown schematically in Fig 5.6.

Brodin et al$^{(13)}$ have also observed the exciton structure in CdS at 20.4 K. The magnitudes of the exciton peaks are however reduced as the content of ZnS in $Cd_xZn_{1-x}S$ is increased as shown in Fig 5.7, an effect which is attributed to the strong lattice distortion in the mixed crystal resulting in a deformation of energy bands and broadening of exciton bands. The variation of the band gap of the mixed crystals with composition has been measured by Davis and Lind $^{(12)}$ and is shown in Fig 5.8 ; these results are in substantial agreement with those determined from photoconductivity measurements. . Other optical parameters for CdS and ZnS are shown in Table 5.1 below.

Table 5.1: Optical constants for CdS and ZnS

Parameter	CdS	ZnS
Band gap, E_g, at 300 K	2.43 eV $^{(12)}$	3.72 eV $^{(12)}$
Temperature coefficient of E_g i.e. $dE_{g/dT}$.	-6.0×10^{-4} eV.K^{-1}. $^{(15)}$	-4.0×10^{-4} eV.K^{-1}. $^{(16)}$
Refractive index	2.3$^{(17)}$	2.27$^{(18)}$
Static dielectric constant	8.64 $^{(19)}$	8.1 $^{(20)}$

5.1.4 Electrical Properties

CdS and ZnS, both of the group II-VI family, exhibit properties intermediate between those of the covalent group IV elements and III-V compounds on the one hand, and the ionic I-VII compounds on the other.

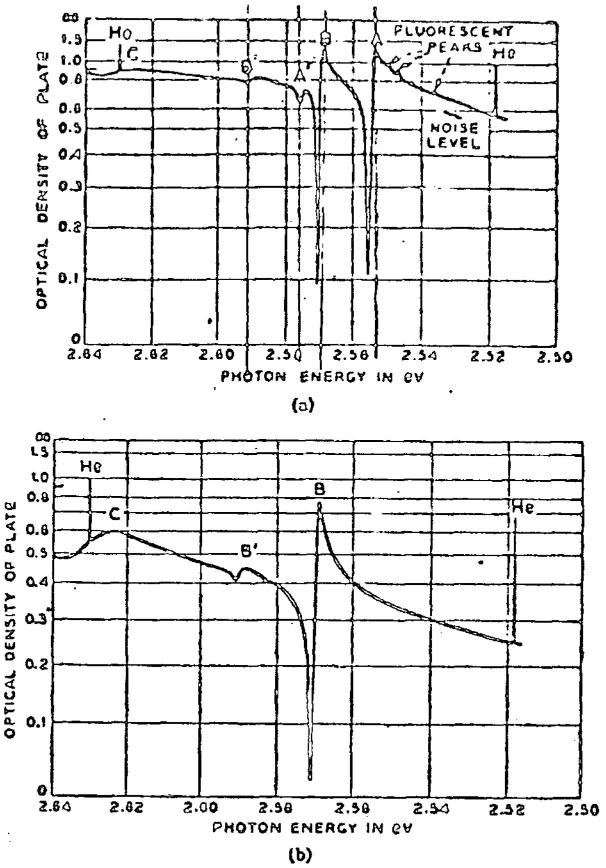

Fig 5.5 : Reflection of CdS at 4.2° K for light polarized with (a) E $\perp$ and (b) E $\parallel$ to c. These are traces taken from microphotometer recordings of Kodak 103-0 plates. The noise level is as indicated in Fig 2(a). The helium calibration lines indicate the resolution used. (14).

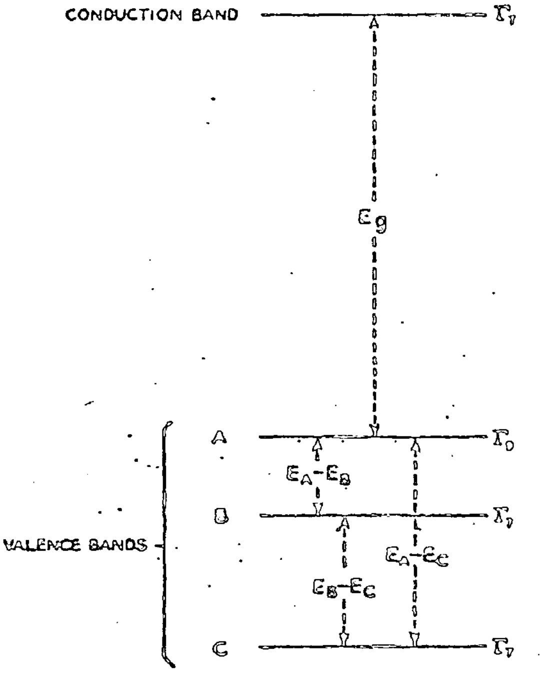

Fig 5.6 : Energy band structure of CdS at k = 0. The levels A, B and C refer to the hole bands from which excitons causing reflections A, B and C arise(14).

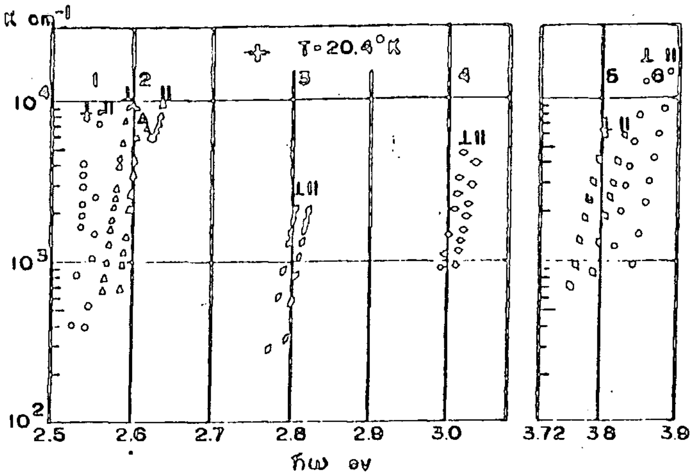

Fig 5.7 : Spectral dependence of the absorption coefficient for two light polarizations of ZnS-CdS crystals at 20.4°K. The curves 1-6 are for $x = 0; 0.06; 0.28; 0.49; 0.96; 1.0$, respectively$^{(13)}$.

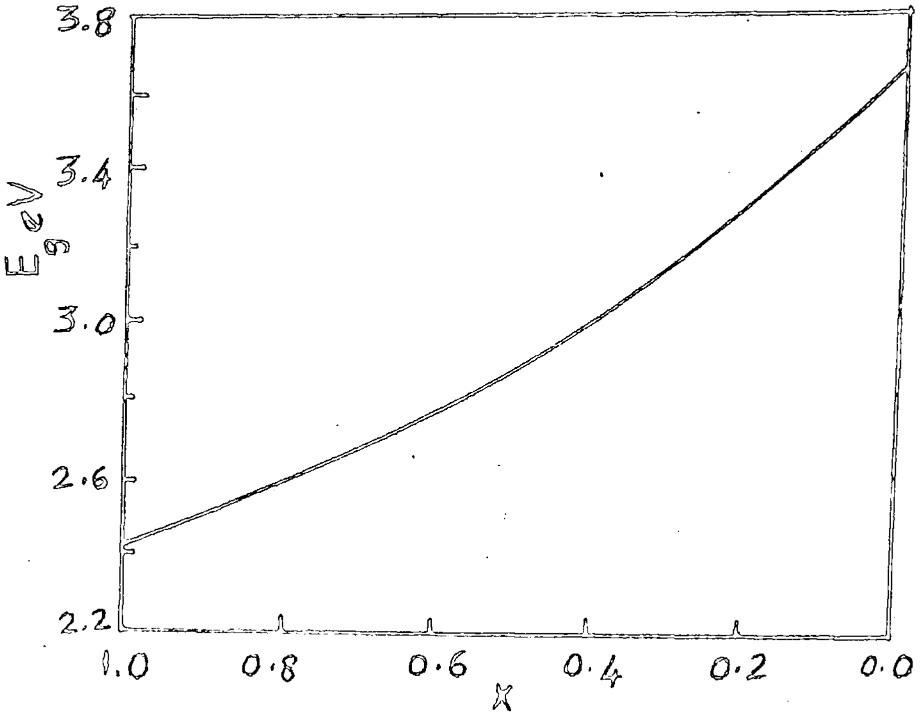

Fig 5.8: Variation of band gap, E_g, with composition in $Cd_xZn_{1-x}S$ crystal$^{(12)}$.

They are good phosphors exhibiting n-type photoconductivity with analogous edge emission and fluorescence(21). The photoconductivity of the mixed crystal decreases linearly with increasing content of zinc(12). The activation energy however increases by a factor of ten to about 0.32 eV when the content of zinc is about 20%.

The high photosensitivity in the crystal of $Cd_xZn_{1-x}S$ system is assumed to arise by the same mechanism as that known to operate in CdS(12), where electron-hole pairs are generated by light of energy greater than the band gap. The holes (with a lifetime $\sim 10^{-7}$ μs) are however rapidly trapped in centres lying approximately 1 eV above the valence band. These centres are cation vacancies (Zn or Cd) and are negatively charged even after capturing holes. The capture cross-section for electrons is very small in these materials ($\sim 10^{-22}$ cm^2 in CdS and $\sim 10^{-21}$ cm^2 in ZnS) with photoexcited electron lifetimes of the same order as those for the release of holes from the trapping centres.

The electron mobility observed at room temperature in the purest sample of CdS is 350 cm^2/V.sec(6) ; this increases by about two orders of magnitude at 1.8 K(23). Room temperature hole mobility as determined by Spear and Mort(22) ranges from 16.5 to 10 cm^2/V.sec. Because of its fast recombination and poorly conducting characteristics, the corresponding parameters for ZnS are not well established. Aven and Mead(24) have investigated systematically the conductivity and Hall mobility in low resistivity (1-10 Ohm.cm) ZnS crystals produced by doping with Aℓ and I. In these samples, the Hall mobility was found to be 140 cm^2/V.sec at 300 K increasing to a maximum value of 300 cm^2/V.sec at 180 K.

5.2 PREVIOUS ELECTROABSORPTION STUDIES IN CADMIUM SULPHIDE AND ZINC SULPHIDE

The majority of electroabsorption experiments performed to date have been on CdS. Boer et al(25-28) were the first to observe a red shift in the optical absorption edge of CdS when a large d.c. field was applied across the crystal. Their results were interpreted in terms of the Franz-Keldysh effect. Their experiments were followed by those of Williams(29) in 1960 who used a rectifying junction between a conducting CdS crystal and an electrolyte solution to sustain a large d.c. field. A linear shift of photon energy with electric field strength was noticed. Further analysis, however, indicated that most of the potential was dropped across the barrier.

More comprehensive studies were made in 1964 by Gutsche and Lange(30) who applied an a.c. field and observed a shift of about 100 Å at 2×10^5 V.cm^{-1}. A different displacement was observed for light polarized parallel and perpendicular to the c-axis of the crystal such that

$$\Delta(h\omega)_{\perp c} = -1.8 \times 10^{-12} F^2$$

and

$$\Delta(h\omega)_{//c} = -1.1 \times 10^{-12} F^2$$

where F is the electric field strength. The quadratic field dependence fits the Franz-Keldysh theory very well. These authors(31) were also able to deduce the reduced effective mass of CdS from their electroabsorption data.

Electroabsorption experiments in the exciton absorption region of semi-insulating CdS were performed by Snavely(32,33). A square voltage pulse at 8 kHz was applied across the crystal producing the electroabsorption spectra shown in Fig 5.9. Positive and negative peaks were observed, and were interpreted in terms of phonon-assisted transitions

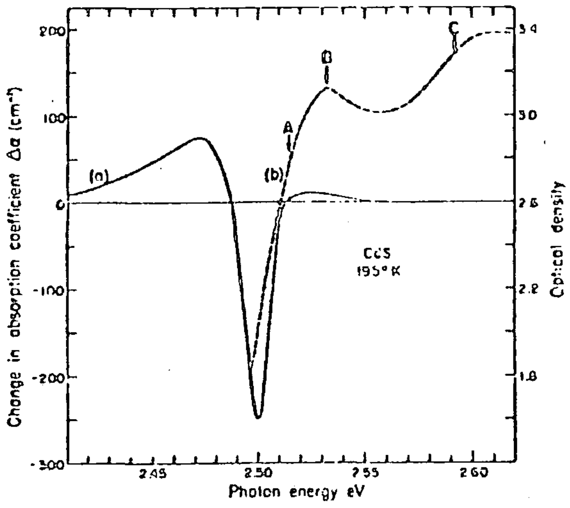

Fig 5.9a : Absorption (dashed line) and electroabsorption spectra of CdS at 195 K. $F = 4.4 \times 10^4$ V.cm^{-1}. (33).

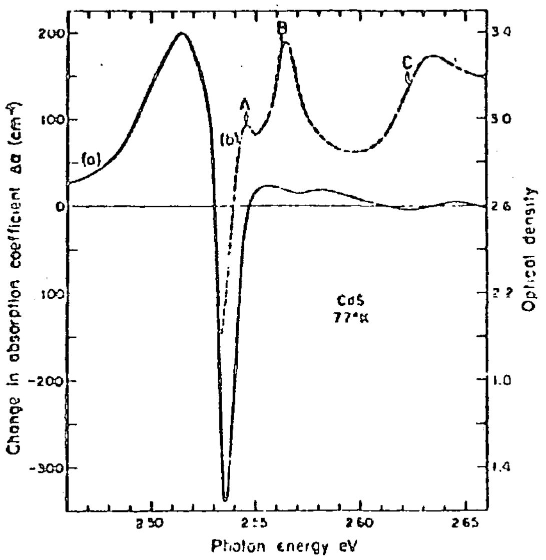

Fig 5.9b : Absorption (dashed line) and electroabsorption spectra of CdS at 77 K. $F = 4.4 \times 10^4$ V.cm^{-1}. (33).

involving exciton levels. A somewhat similar observation was made by Nobuyasu Hase et al(34) in 1970. Perhaps the most detailed studies were made by Gutsche and Lange(35) who were able to resolve the exciton spectrum in CdS using the electroabsorption technique. For small electric fields ($<10^4$ V.cm^{-1}), this showed that the change in absorption, $\Delta\alpha$ increases quadratically with electric field strength. Their results are reproduced in Fig 5.10 and have been interpreted in terms of the quadratic Stark effect. The exciton structure, however, broadens with increasing electric field or temperature.

The first electroabsorption measurements on ZnS were made by Damaskova et al(36) in 1961. In addition to a large electroabsorption signal which was also detected beyond the absorption edge, a long response time ($\sim$ 0.8 sec), was reported. This was believed by later workers(37) to be due to Joule heating instead of the Franz-Keldysh effect. The electroabsorption technique has also been used to investigate an anomalous photovoltaic effect(37,38) in this material. Measurement of the Franz-Keldysh effect on different types of ZnS crystal have been reported by Yacobi et al(39) and their results are reproduced in Fig 5.11. A 'red shift' was observed for different orientations of the electrical vector of the incident light with respect to the c-axis of the crystal. The energy shift was used to calculate the reduced effective mass of the crystal and was found to be 0.22 m_o, where m_o is the free mass of electron. The reduced effective mass of CdS deduced from electroabsorption data(34) at 300 K is 0.16 m_o. However, the variation of this parameter as a function of alloy composition has not yet been reported.

5.3 EXPERIMENTAL RESULTS

The crystals grown in this department using the vapour phase sublimation technique were cut into slices with surface areas of about 0.2 cm^2 before mechanically polishing them to a thickness between 200 and 400 μm. The crystals were then chemically etched prior to metal deposition

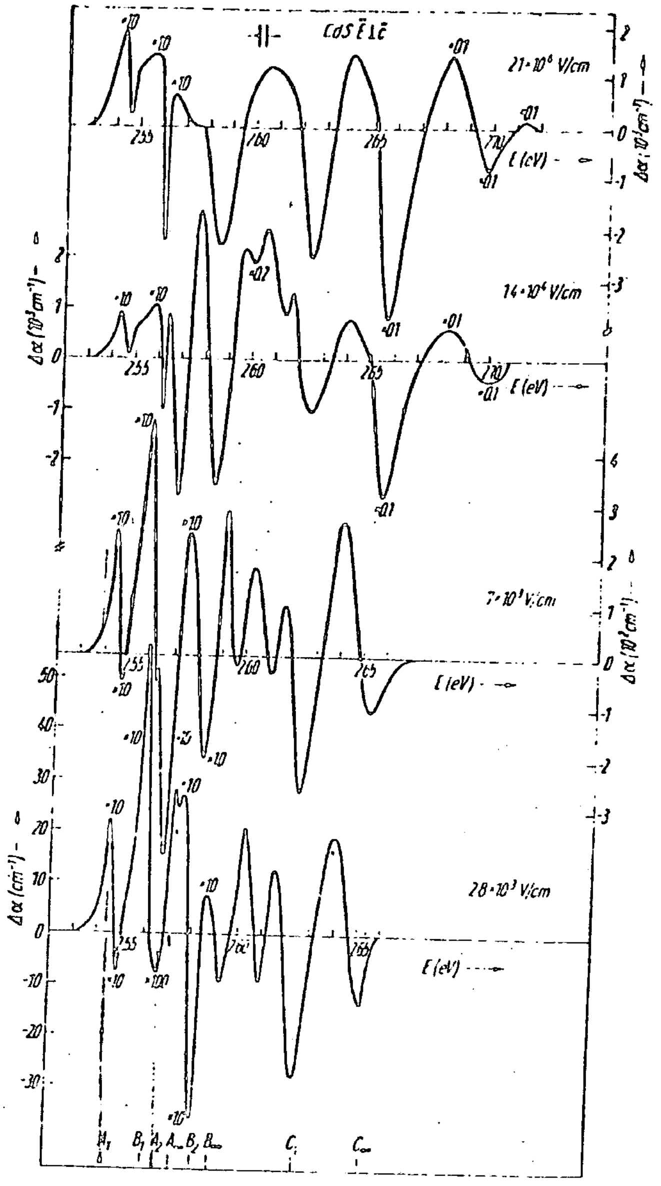

Fig 5.10 : Electroabsorption spectra of CdS single crystals at 77°K for several field strengths for E ⊥ c (35).

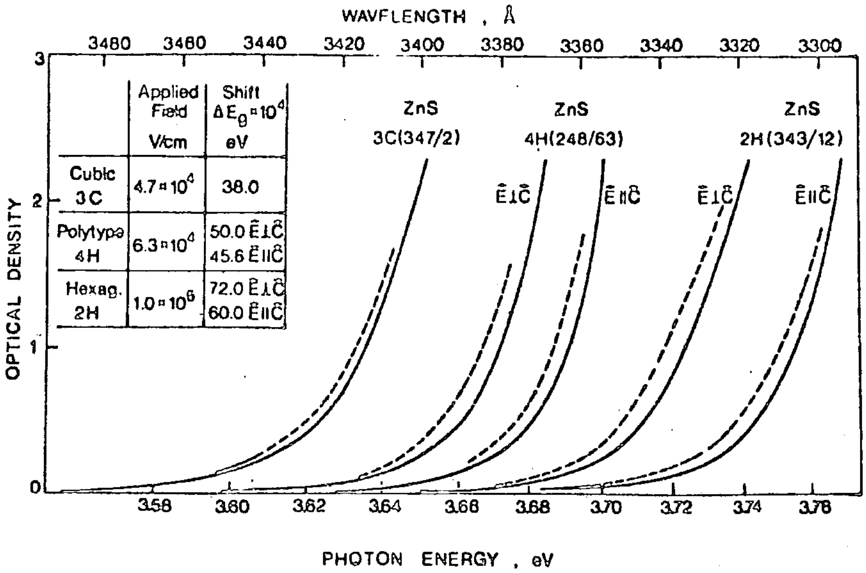

	Applied Field V/cm	Shift $\Delta E_g \times 10^4$ eV
Cubic 3C	4.7×10^4	38.0
Polytype 4H	6.3×10^4	50.0 $\hat{E}\perp\hat{C}$ 45.6 $\hat{E}\parallel\hat{C}$
Hexag. 2H	1.0×10^5	72.0 $\hat{E}\perp\hat{C}$ 60.0 $\hat{E}\parallel\hat{C}$

Fig 5.11 : Optical density of single crystals 347/2 (3C), 248/63 (4H), 343/12 (2H) at room temperature. Solid line, without electric fields ; dashed line, with electric fields. Evaporated semitransparent gold electrodes, external field perpendicular to the c axis. Electrical vector of incident light both parallel (||) and (⊥) to the c axis$^{(39)}$.

in the similar manner to the process used for CdTe:Cl (see section 4.2.1). Different etching solutions were, however, used for different materials, and these are summarized in Table 5.2.

Table 5.2 : Surface treatment of $Cd_xZn_{1-x}S$ crystals prior to metal deposition

Material	Etching Solution	Treatment after etching process
CdS	Fresh solution of bromine (1% by volume) in methanol	Wash in CS_2 solution to remove bromine remains on the surface. HF treatment
$Cd_{0.8}Zn_{0.2}S$ and $Cd_{0.7}Zn_{0.3}S$	Concentrated HCl (Etch for 10 to 15 sec)	HF treatment
ZnS	Concentrated HCl (Etch for 10 to 15 sec) or Fresh solution of HPC which consists of (1 part of a saturated solution of chromium trioxide in phosphoric acid + 2 parts of concentrated HCl) (40)	HF treatment

The crystal was washed with deionized water and then with methanol after etching process and HF treatment. The HF treatment was found to be necessary to remove any oxide layer formed on the surface of the crystal and was therefore done shortly before metal deposition. Al or In/Sn alloy was evaporated onto the crystal to form electrodes which were typically 100 Å thick, and deposited at the rate between 5-10 Å per second in a vacuum chamber of pressure about 10^{-6} torr. Good electrical contacts were ensured from d.c. conductivity measurements. Figs 5.12 and 5.13

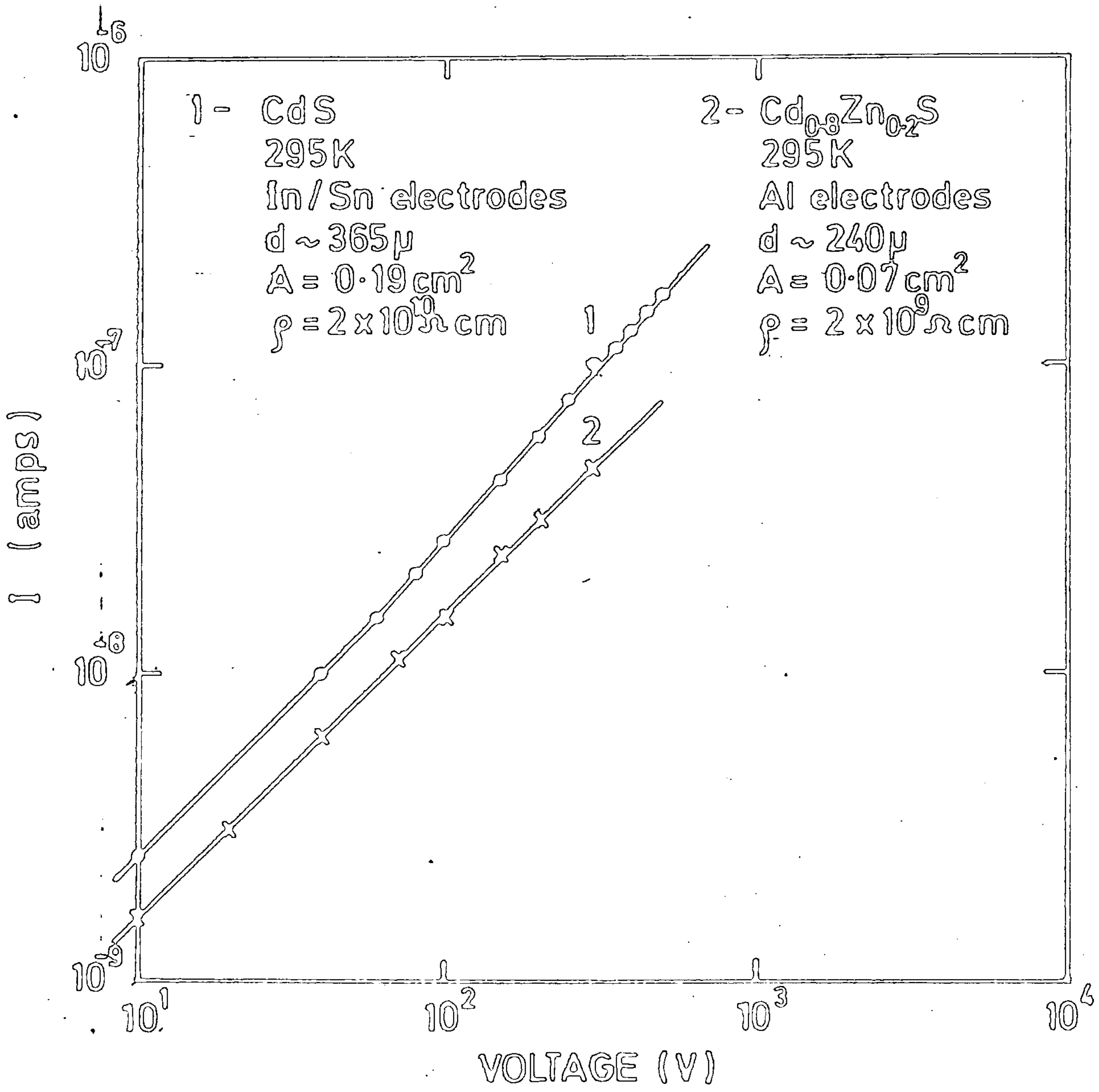

Fig 5.12 : Current voltage curves for CdS and $Cd_{0.8}Zn_{0.2}S$ samples at room temperature.

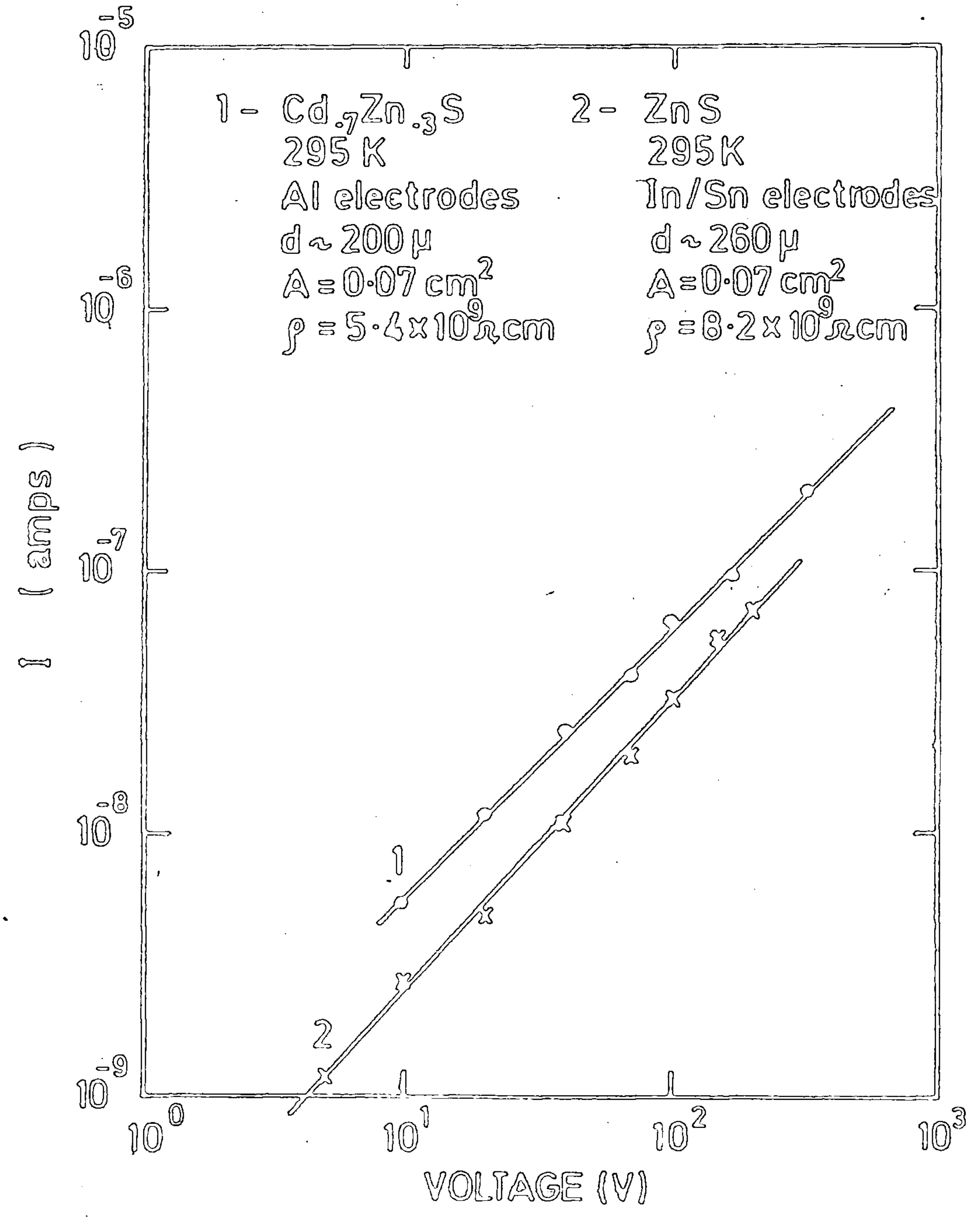

Fig 5.13 : Current voltage curves for $Cd_{0.7}Zn_{0.3}S$ and ZnS samples at room temperature.

demonstrate that Ohmic electrical contact can be formed using either Al or In/Sn. The resistivity of each sample is indicated in the diagram. In addition, a.c. conductivity measurements were also performed, as has already been described for CdTe : Cl in section 4.2.2, to confirm the Ohmicity of the electrical contact required for electroabsorption measurements.

5.3.1 Absorption Edge

The optical absorption spectra of the $Cd_xZn_{1-x}S$ system were measured with the crystalline c-axis parallel to the propagation vector of the incident light. Although the crystals were quite thick, the exciton peaks could still be observed at the measuring temperatures of 150 K and 77 K. Effects of thermal broadening were however clearly evident.

CdS

The absorption spectrum of CdS at 150 K showed a single broad peak as illustrated in Fig 5.14. Additional peaks emerged on cooling to 77 K, and these have been assigned the designations used by Thomas and Hopfield(14). The line A, B, and C as indicated in the diagram, are so called intrinsic, or free, exciton lines and the subscripts on these letters denote the principal quantum numbers of a hydrogen series. The whole spectrum was shifted towards higher energies on cooling to 77 K at a rate of -6.0×10^{-4} eV. K^{-1} ; in rather good agreement with values published in the literature(15).

ZnS

By contrast, the exciton effect is less pronounced in ZnS at both temperatures as illustrated in Fig 5.15, despite quite a large exciton energy of formation of 40 meV(41) in this material as compared to only 28 meV(14) in CdS. The absorption spectrum at 150 K does not indicate any exciton peak while only a shoulder is observed at 77 K. A temperature coefficient of -3.8×10^{-4} eV.K^{-1} was recorded when the ZnS sample was cooled to 77 K.

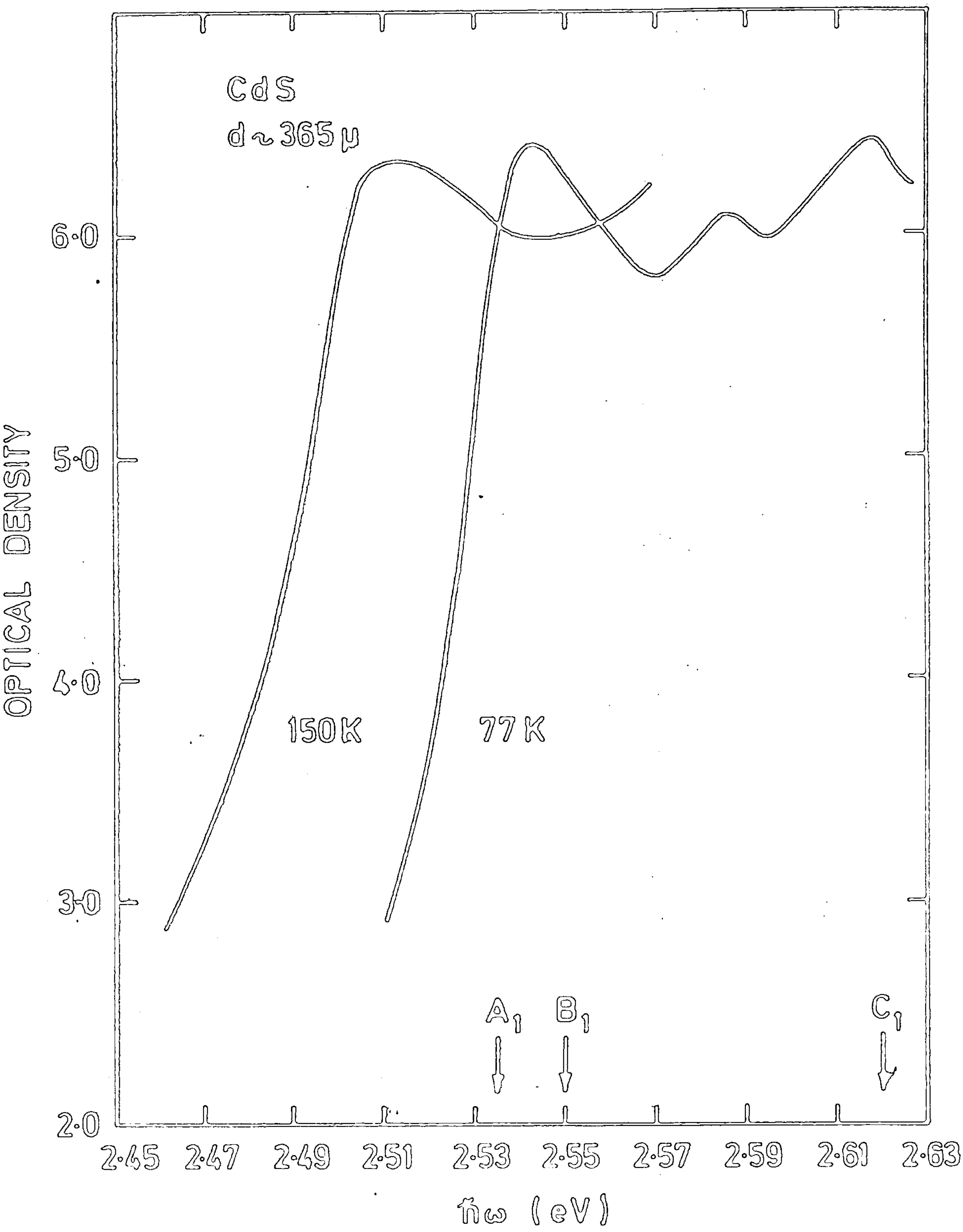

Fig 5.14 : Absorption edge of CdS at 150 K and 77 K.

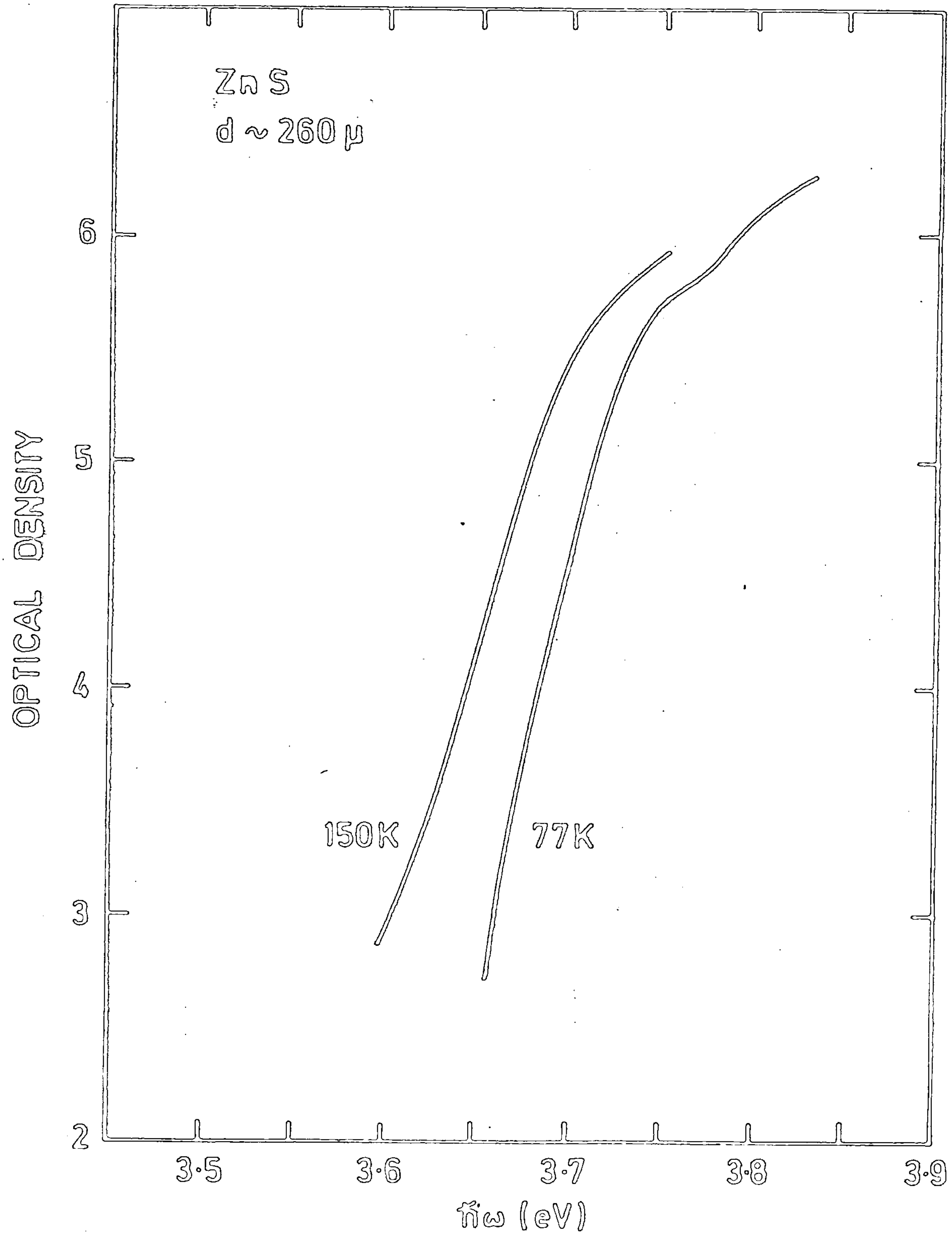

<u>Fig 5.15</u> :   Absorption edge of ZnS at 150 K and 77 K.

$Cd_{0.8}Zn_{0.2}S$ and $Cd_{0.7}Zn_{0.3}S$

The absorption edge of the crystal occurs at higher energies if the content of zinc in the alloy crystal is increased. This is demonstrated in Fig 5.16 where the spectrum for two components of the alloy system, namely for x = 0.8 and 0.7, are shown. At 150 K, a single broad peak for both components is observed. It was resolved into two peaks on cooling to 77 K. The widening of the band gap with decreasing temperature is also evident in both crystals; the degree of movement is summarized in Table 5.3. These data, together with the reported value of the energy gap E_g,(11,12), at room temperature, can be used to calculate the value of E_g at 77 K. When this is done, rather good agreement is obtained with those values reported in the literature(32,33).

Table 5.3: Parameters deduced from the absorption and electroabsorption spectra of the $Cd_xZn_{1-x}S$ system with $0 \leqslant x \leqslant 1$.

Parameter \ X	1.0	0.8	0.7	0.0
Temperature Shift of the absorption edge, $\frac{\Delta E}{\Delta T}$ (eV.K^{-1})	-6.0×10^{-4}	-5.0×10^{-4}	-4.7×10^{-4}	-3.8×10^{-4}
Band gap E_g at 77 K (eV)	2.564	2.660	2.760	3.802
The position of the first negative peak (eV)	2.535	2.630	2.727	3.760

5.3.2 Electroabsorption

A red shift of the absorption edge of each component of the system is observed upon application of an external electric field. In these measurements, the second harmonic signal (2f) was taken at a frequency

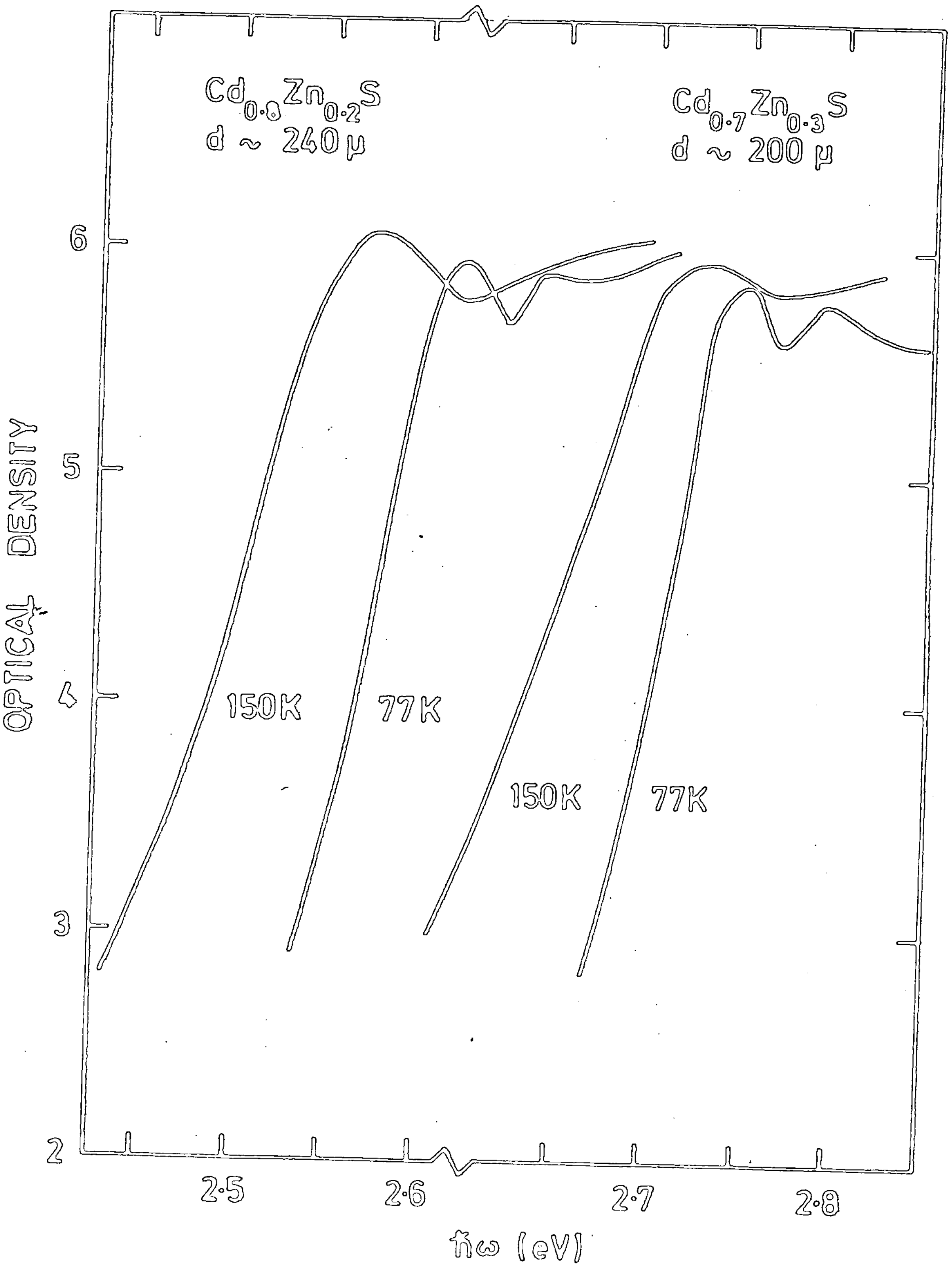

Fig 5.16 : Absorption edges of $Cd_{0.8}Zn_{0.2}S$ and $Cd_{0.7}Zn_{0.3}S$ samples.

$f > 3.0$ kHz to avoid the photoconductivity complications described in section 4.5.

CdS

The relative change in transmission, $\frac{\Delta I}{I}$ (which is proportional to the change in absorption $\Delta\alpha$) is plotted against photon energy for CdS at 150 and 77 K as shown in Fig 5.17. The temperature shift corresponds to the widening of the band gap as the temperature is decreased. Oscillations of positive and negative peaks were observed ; the first negative peak coincides with the lowest exciton peak in the absorption spectrum which presumably corresponds to the lowest exciton level. The position of this peak is considerably lower than the band gap at this temperature as indicated in Table 5.3. The field dependence of the electroabsorption spectrum was investigated at 77 K. The position of the first negative peak does not depend on the electric field (see Fig 5.17). Furthermore, the peak width does not exhibit field broadening. For electric fields $F << F_i$, the ionization field of exciton levels ($\sim 1.4 \times 10^5$ V.cm^{-1} in CdS$^{(41)}$), the magnitude of $\frac{\Delta I}{I}$ increased quadratically with electric field as illustrated in Fig 5.18a. The signal, however, increases more slowly as the electric field approaches the value F_i as shown in Fig 5.18b. This is a strong indication that the signal is due to transitions involving exciton states in this material.

ZnS

Even though the exciton lines of ZnS are not clearly observed in the absorption spectrum (see Fig 5.15) ; they are clearly visible in electroabsorption ; typical spectra are shown in Fig 5.19. As for CdS, they consist of positive and negative peaks, thus allowing us to accurately position the exciton peak in this material. This represents one of the advantages of this modulation technique. The field dependence of the electroabsorption signal in ZnS is very similar to that observed in CdS as shown in Fig 5.18. That is the position and the width of the first negative

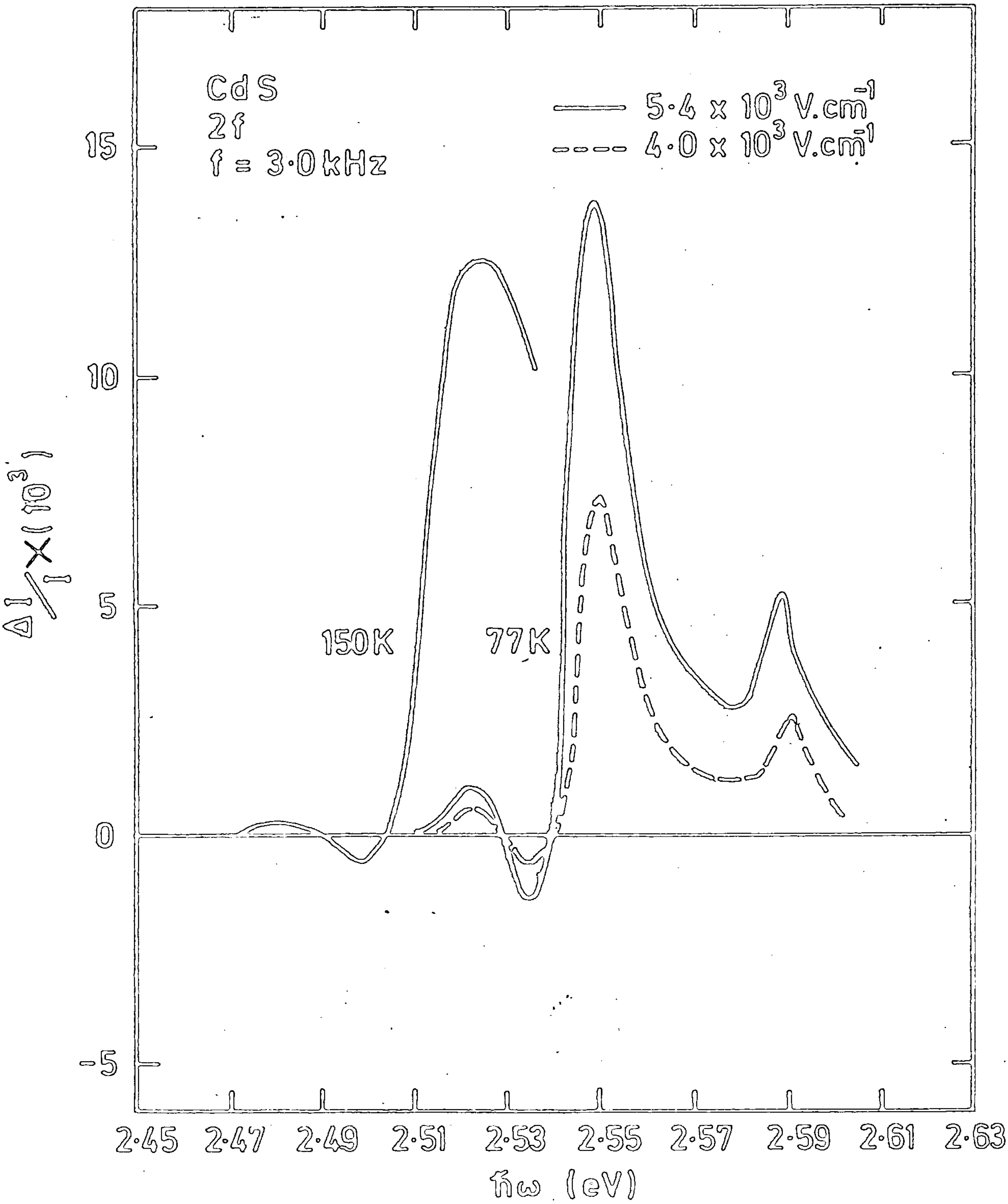

Fig 5.17 : Electroabsorption spectra of CdS sample at 150 K and 77 K.

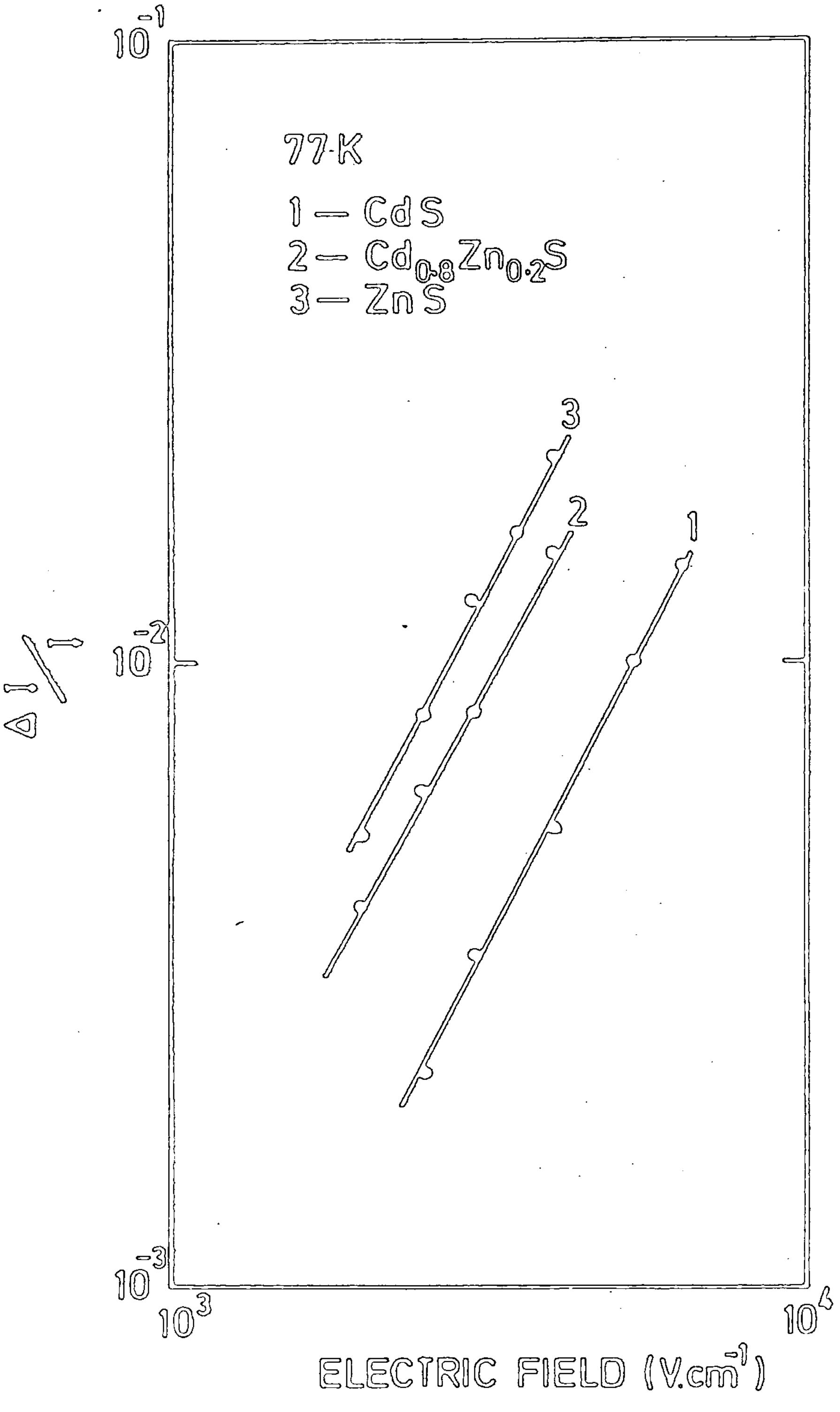

Fig 5.18a : Dependence of the electroabsorption response of CdS crystal on the magnitude of the applied electric field at 77 K.

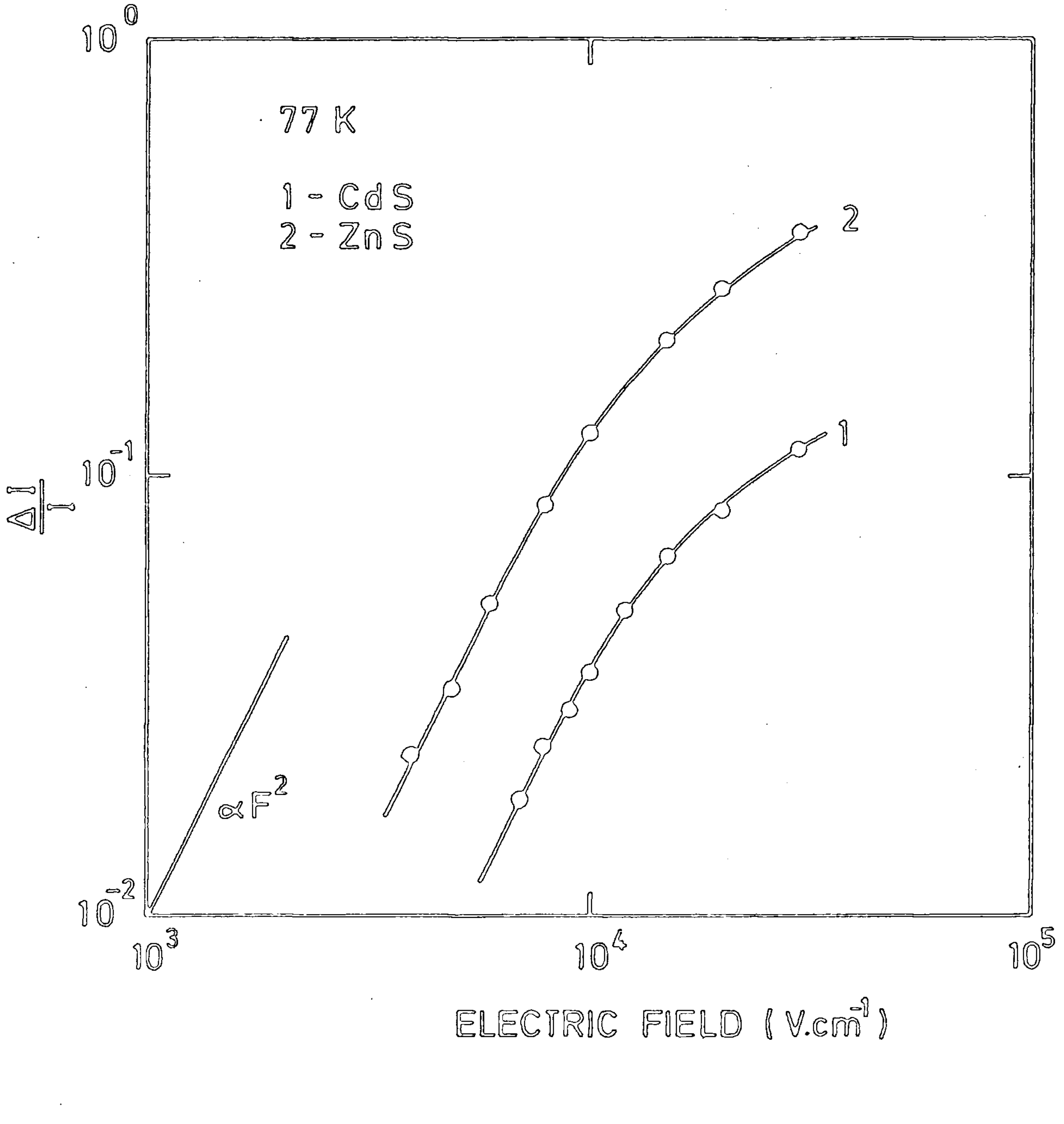

Figure 5.18b : Fractional change in transmission of the first negative peak of CdS and ZnS crystals at 77 K, as a function of the applied electric field.

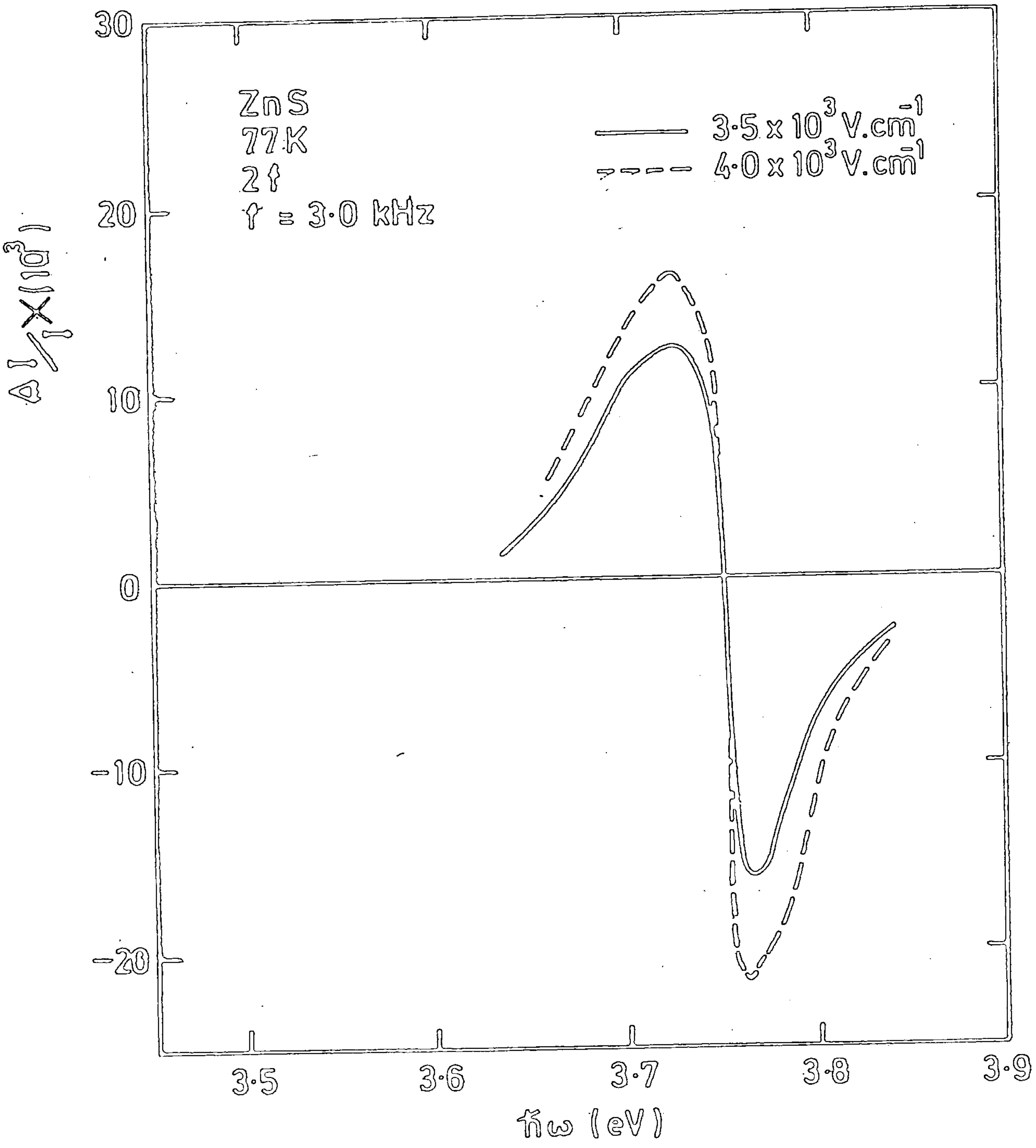

Fig 5.19 : Electroabsorption spectra of ZnS crystal at 77 K.

peak at 77 K are independent of the electric field (see Fig 5.19). However, in this case the ionization field of exciton levels in ZnS$^{(41)}$ is 2.0×10^5 V.cm^{-1}.

$\underline{Cd_{0.8}Zn_{0.2}S \text{ and } Cd_{0.7}Zn_{0.3}S}$

The dependence of the electroabsorption spectrum on the alloy composition is best described by reference to Figs 5.20 and 5.21 where the electroabsorption spectra of the components of the alloy system with x = 0.8 and 0.7 are shown. As in the case of CdS, the position and the width of the first negative peak do not depend on the electric field. In each component, the position of the first negative peak coincides with the first exciton line. The temperature coefficient of this peak was measured to be exactly the same as that for the absorption edge ; these data are summarized in Table 5.3.

5.3.3 Discussion of Results

The electroabsorption spectrum is very similar to that predicted by the one-electron theory for a direct allowed transition between parabolic energy bands, i.e. a type M_0 critical point in the joint density of states as described in section 2.5.2. A type M_0 critical point is a point in the energy band scheme that satisfies equation (2.35), namely $\nabla_k(E_c-E_v)=0$ with all the three components of the effective mass being positive. The theory also predicts that the position of the peaks in the electroabsorption spectrum should shift towards higher energies as the two-thirds power of the electric field. Furthermore the peak width is expected to exhibit field broadening for a type M_0 transition. On the basis of this model where photon-assisted tunneling of the band to band transition is considered, the position of the band gap should occur very close to the first negative peak as defined by equation (2.40), namely $\eta = \frac{\hbar\omega - E_g}{\hbar\Omega} = 0$.

The electroabsorption spectra of CdS and ZnS however do not satisfy the predictions of the one-electron theory. It is evident that the position and the width of the first negative peak do not depend on the

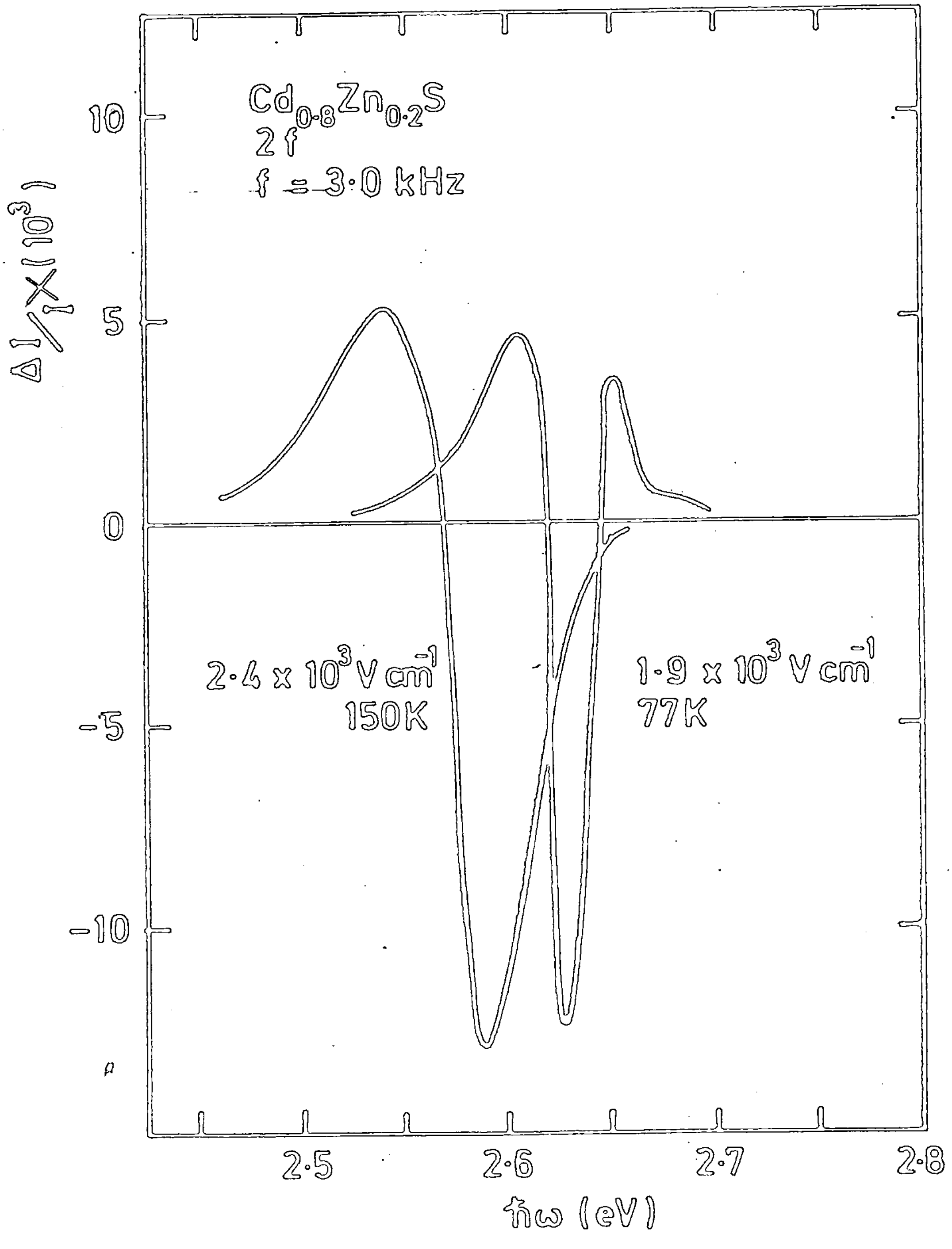

Fig 5.20 : Electroabsorption spectra of $Cd_{0.8}Zn_{0.2}S$ sample at 150 K and 77 K.

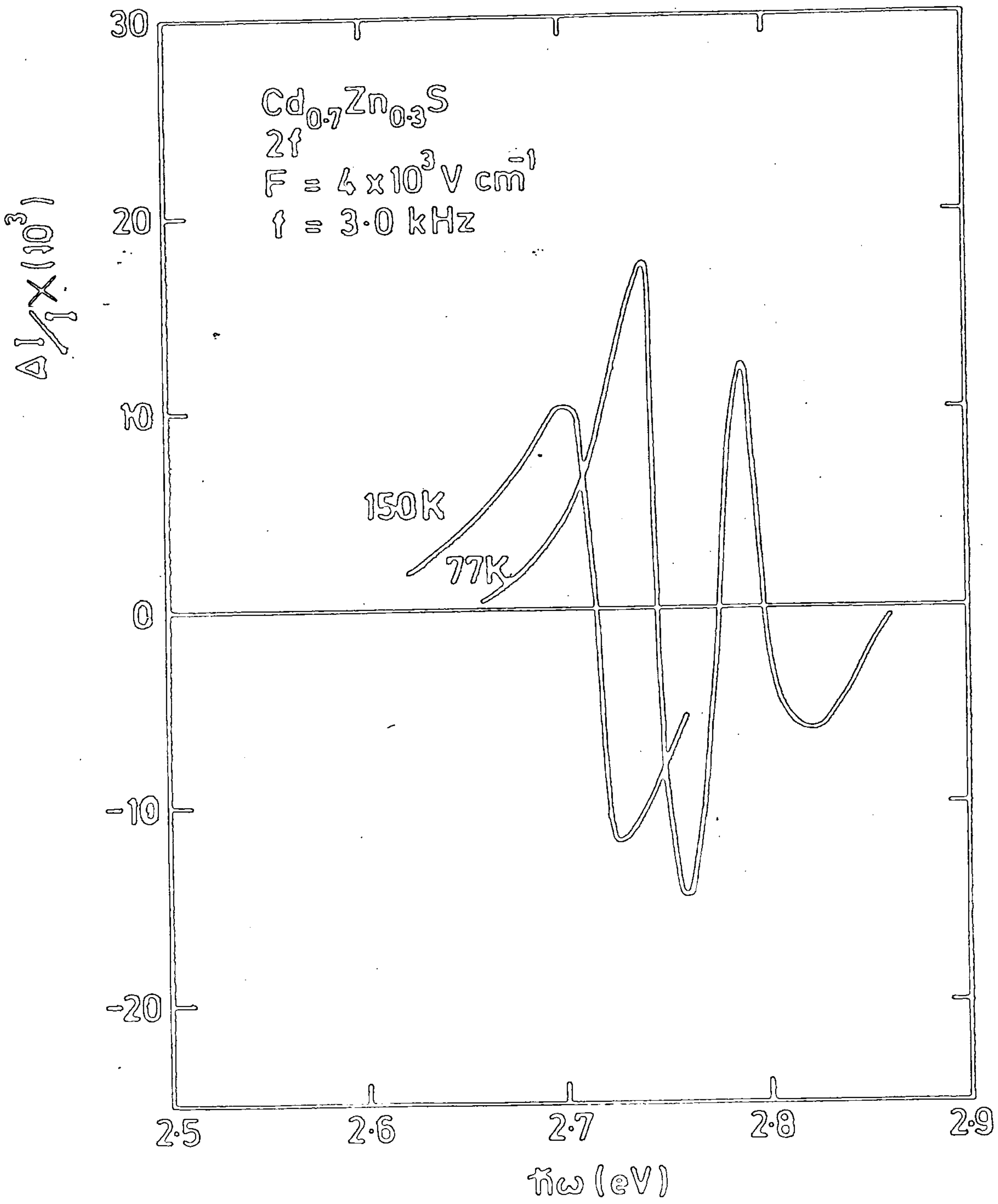

Fig 5.21 : Electroabsorption spectra of $Cd_{0.7}Zn_{0.3}S$ crystal at 150 K and 77 K.

electric field (see Figs 5.15 and 5.16). i.e. the first negative peak does not exhibit field broadening. In addition, the positions of these peaks are at significantly lower energies than the band gap deduced from the temperature shift of the absorption edge for these materials (see Table 5.3).

These observations have led us to conclude that the electroabsorption spectrum observed is not associated with band to band transitions at a type M_o critical point. A more suitable interpretation is in terms of exciton electroabsorption where the position and the width of the first negative peak are expected to be independent of the electric field as described in section 2.6. According to this theory, the first negative peak should occur at the lowest bound exciton states, i.e. at (E_g-R), where R is the binding energy of the exciton. A detailed study of the field dependence of the magnitude of the electroabsorption signal reveals that the relative change in transmission $\frac{\Delta I}{I}$ increases quadratically with electric field for $F << F_i$ but increases more slowly as F approaches F_i as illustrated in Fig 5.18. This change in the field dependence of the electroabsorption signal also provides a strong indication that the signal observed is due to transitions involving exciton states. The influence of a low electric field on the discrete level of an exciton is to produce the quadratic Stark effect. However, at high fields comparable to the ionization field of exciton, the exciton states are broadened, resulting in quenching of the Stark effect. The quenching process begins at a point where the transition occurs from the quadratic to a smaller field dependence of the electroabsorption signal.

The above characteristics have also been observed in the other two components of the alloy system, namely for x = 0.8 and 0.7. These spectra also provide further support that the Stark effect is the mechanism underlying the behaviour of the transition in an electric field. Apart from the spectral shift towards higher energies, which is in accordance with the shift of their absorption edges on cooling to 77 K ; additional structure is visible in the higher energy part of the spectrum ; these can probably be best explained as due to exciton transitions. The structure, in the form of oscillations comprising positive and negative peaks, is not observed at 150 K due to thermal broadening.

The position of the first negative peak at the lowest bound exciton states (E_g-R) can be used to calculate the reduced effective mass of the exciton, M^*. Using data given in Tables 5.1 and 5.3, and taking values of the static dielectric constant $\varepsilon_s = 8.55$ and $\varepsilon_s = 8.5$ for x = 0.8 and 0.7 respectively (from geometric capacitance measurements), the values of M^* have been calculated and are summarized in Table 5.4.

Table 5.4 : Calculated value of M^* at 77 K (m_o is the electron rest mass)

Material	Calculated M^*	Published value of M^*
CdS	0.16 m_o	0.16 m_o (34)
$Cd_{0.8}Zn_{0.2}S$	0.166 m_o	
$Cd_{0.7}Zn_{0.3}S$	0.17 m_o	
ZnS	0.21 m_o	0.22 m_o (39)

Good agreement with published values for CdS(34) and ZnS(39) was obtained. An accuracy of about 10% is estimated in this calculation; the error involved mainly arises due to an uncertainty in locating the point (E_g-R). The values of M^* are plotted against the composition of the crystal and are shown in Fig 5.22; the corresponding variation of E_g is plotted alongside. As expected M^* and E_g move together as the alloy composition is changed. Kurik(42) has shown that there is a good correlation between

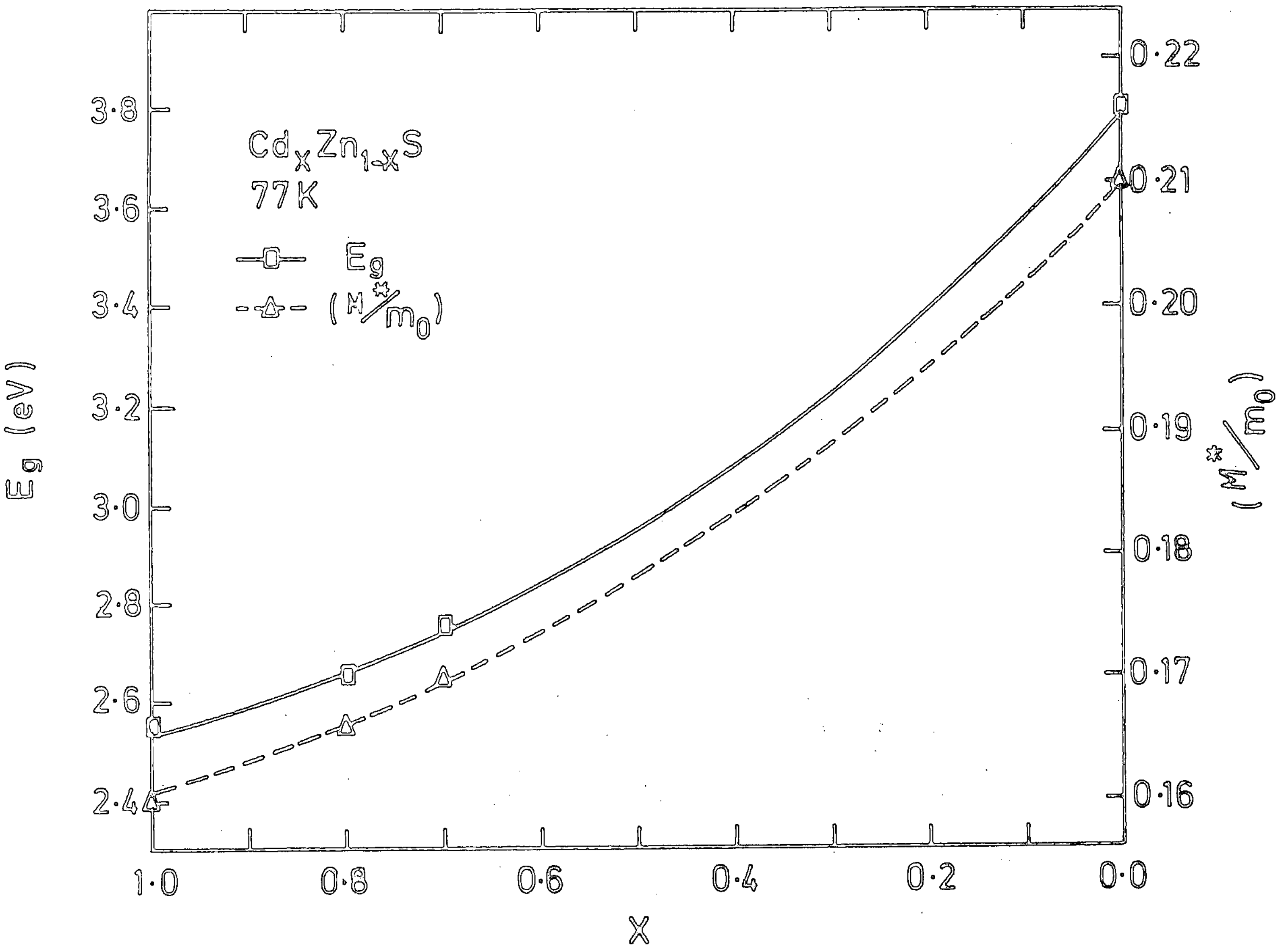

Figure 5.22 : Variation of the energy gap E_g and the reduced effective mass of exciton with composition x in the solid solutions of $Cd_xZn_{1-x}S$.

the band gap and the effective mass of II-VI compounds. Our results obtained for the solid solutions of $Cd_xZn_{1-x}S$ indicate that M^* increases linearly with E_g and agree well with this hypothesis.

This chapter demonstrates the importance of the exciton effects in the interpretation of the electroabsorption results for a system where exciton effects are definitely of significance. Early interpretations of the electroabsorption in CdS and ZnS were based on the Franz-Keldysh effect ; the reduced effective mass in this material was thus deduced by using the Franz's formula. Recent findings, however, indicate that the exciton effects are important, and therefore the results should be interpreted in terms of the Stark effect. The previous calculation of the reduced effective mass may not be valid. However, the excitonic electroabsorption theory provides a means of determining the exciton binding energy and thus the reduced effective mass of exciton. This parameter for the solid solution of $Cd_xZn_{1-x}S$ is believed to be reported for the first time in this thesis. It is evident that the high sensitivity of this modulation technique can be an advantage in the study of exciton effects.

CHAPTER 6

ELECTROABSORPTION STUDIES IN AMORPHOUS SILICON

6.1 INTRODUCTION TO AMORPHOUS SILICON

The properties of amorphous Si (α-Si) are very different to those of its crystalline form ; they also differ greatly from those of other amorphous materials such as the chalcogenide semiconductors. As well as being of fundamental interest, α-Si has tremendous potential in electronic devices. Most attention has been paid to glow discharge produced material rather than that produced using conventional sputtering techniques. The optical and electrical properties of α-Si are ideally suited for solar cell applications. The optical absorption coefficient is significantly larger than that of crystalline Si over the visible light range(1) and therefore most of the solar radiation with $\lambda < 0.7$ μm is absorbed in a film ∿ 1 μm thick. The carrier lifetime in glow discharge produced α-Si is significantly longer than in other amorphous semiconductors. This is due to the low density of gap states resulting from the discharge kinetics and compensation of dangling bonds by hydrogen. This property allows the Fermi level to be moved easily with respect to the band edges by means of an external field, substitutional doping, or a Schottky barrier. As a result, solar cells utilizing ∿ 1 μm of α-Si have been fabricated in heterojunction, p-i-n, MIS and Schottky barrier structures on low cost substrates such as glass and steel. Even though an efficiency of 5.5% has been reported for platinum Schottky barrier cells(2), work is in progress to produce solar cells with at least an 8% efficiency, the minimum acceptable value for large-scale terrestrial use. Another possible use of α-Si is as a large-area thin-film transistor for addressing purposes in display devices.

An improvement in device performance invariably depends on one's understanding of the basic properties of the material. Difficulties in interpreting α-Si data arise due to the presence of states in the gap, the mobility edge etc. Evidence for their existence in α-Si is based on electrical measurements, particularly conductivity, thermopower, Hall effect and drift mobility. One point of debate is whether the transition from localized to extended states is a gradual or an abrupt process. It was thought that a study of the effect of an electric field (at different temperatures) on the optical absorption edge of α-Si might provide some useful information concerning this transition. We shall find that the results of our electroabsorption experiments are very dependent on specimen preparation conditions. We begin this chapter therefore with a brief discussion of the α-Si preparation techniques. In section 6.2 a survey of previous electroabsorption studies in α-Si is given. Device preparation and results obtained during the course of this work are presented in section 6.3 and 6.4. The chapter concludes with an analysis of the electroabsorption results.

6.1.1 Preparation Techniques

The manner in which α-Si is prepared has a major effect on its optical and electrical properties. α-Si can be prepared using a variety of methods including evaporation from the crystalline phase(3), r.f. sputtering, and the decomposition of silane by means of r.f. and d.c. glow discharges. The last three methods are more popular and are therefore reviewed in the next subsections.

A. R.F.Sputtering

The technique of sputtering a silicon target in a partial pressure of argon has been described by Paul et al(4). The starting material is normally polycrystalline or compressed powder silicon. These sputtered films have atomic densities that increase with substrate temperature and are within a few percent of crystalline values. Early investigations on this type of film indicated that the density of states in the gap region was very high, of the order of 10^{20} states per cm.^{3}, this was considerably reduced by introducing hydrogen into the system during the sputtering process$^{(5)}$. The density of states could be reduced to about 10^{17} cm^{-3} following doping. This is achieved by incorporating hydrides of phosphorous or boron into the chamber during preparation to produce n- or p-type films. This method offers a great degree of control and allows deposition of metal contacts without having to break the vacuum, thereby reducing the oxide formation.

B. Glow Discharge Deposition

An alternative method of producing α-Si is by using an r.f. glow discharge system. This is normally achieved by operating a plasma in the low pressure region where the electron energy is limited by collision with any local surface of the reaction vessel. In order to maintain the plasma, the voltage must be increased to compensate for this energy loss. Thus, in this process, surface generated reactions are promoted, causing 'hydrogenated' α-Si to be deposited. The r.f. power is coupled into the system either capacitively or inductively. A complete description of this method is given by Chittick$^{(6)}$ and by Spear and his colleagues$^{(7)}$.

The r.f. glow discharge technique produces films that are several orders of magnitude more resistive than those produced by the sputtering method. This was thought to be due to the incorporation of hydrogen which was believed to neutralize the role of dangling bonds. Films deposited at low substrate temperature contain more hydrogen. Substitutional doping is also possible$^{(8)}$ and is achieved by glow discharge decomposition of SiH_4/PH_3 or SiH_4/B_2O_6 mixture to produce n- or p-type α-Si.

6.1.2 Density of State Distributions

The idealized model of the structure of α-Si is the random network structure of Polk et al$^{(9)}$ which has the same tetrahedral coordination as crystalline Si, but with little order extending beyond nearest neighbours. It is recognized that this picture must in reality be modified by the inclusion of defects which in more traditional forms of α-Si (e.g. evaporated films) involve dangling bonds in sufficient quantity to produce densities of states in the gap, thus pinning the Fermi level. The presence of hydrogen during the deposition process is however thought to prevent the formation of dangling bonds since these would provide favourable bonding sites for hydrogen atoms.

The density of states in the gap can be determined approximately by the field effect technique. The results deduced by Spear et al(10) for α-Si are reproduced in Fig 6.1. The density of states distribution N(E) for evaporated ($E_1.E_2.E_2'$) films and glow discharge films deposited at different substrate temperatures, T_d are shown. The localized state spectrum can be divided into two parts :

(a) States within about 0.2 eV of E_c (and probably also of E_v) are the so-called 'tail states' which arise through the lack of long range order.

(b) Structure deeper within the energy gap is most likely associated with localized states formed by structural defects.

The tail states are thought not to be affected by T_d and therefore do not arise from defects(11). The peak E_x is directly probed by field effect measurements . The E_y peak however can only be inferred by this technique ; its existence is confirmed by photoconductivity and luminescence.

Spear et al(10) has suggested that the E_x and E_y levels might correspond to the donor and acceptor levels of the divacancy very similar to those observed in crystalline Si. However the fact that E_y is more intense than E_x and that the spin signal ascribed to the dangling bond state is observed(12,13,14) after electron or ion bombardment in hydrogenated α-Si, indicate that the above interpretation is too simple and other types of defects should also be considered. According to Mott(11) a model which ascribes E_y to hole traps is required ; these could be due to stretched bonds or to twofold coordinated Si atoms as suggested by Adler(15).

With reference to Fig 6.1, the arrows indicate the position of the field-free Fermi level, E_F, which lies near a minimum in the density of states between two bands of defect levels E_x and E_y. The position of E_F depends on the deposition temperature ; n-type behaviour is obtained for films deposited at high temperature and p-type for those deposited at low temperature.

6.1.3 Electrical Properties

Early measurements by Beyer and Stuke(16) showed that sputtered films have high conductivity and small values of thermopower. Electrical transport normally occurs by hopping at the Fermi level as evident from a $T^{-1/4}$ dependence of the logarithm of the conductivity. Since the carrier lifetime in this material is very small, photoconductive properties can hardly be observed. Annealing was found to reduce the defect density resulting in an increase in the value of the thermopower and the activation energy for conduction.

Glow discharge films in contrast showed lower conductivity, higher values of thermopower and marked photoconductive properties. Measurements by Le Comber et al(17) of the electron drift mobility in glow discharge α-Si deposited at 500 K had shown an activation energy of 0.19 eV above a critical temperature T_c = 250 K and 0.09 eV below this temperature. This data is reproduced in Fig 6.2. Their results were interpreted in terms of transport in the extended states for $T > T_c$. The activation energy indicates that the injected pulse of excess electron drifts in the extended states just above E_c and during a transit time interacts through trapping and thermal release with states lying close to E_c in the rapidly decreasing edge of the tail states. The electron mobility in the extended states near E_c calculated from the drift mobility and field effect data is between 3 and 16 $cm^2\ V^{-1}.sec^{-1}$ (7) .

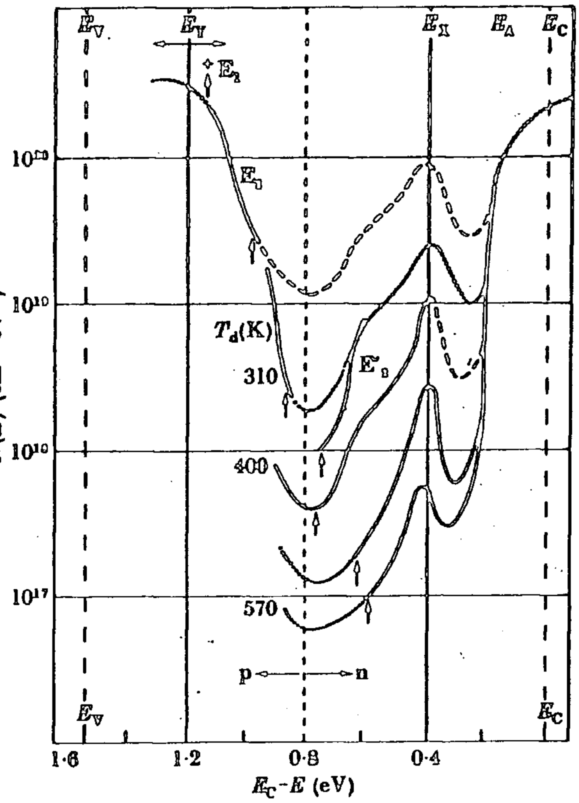

Fig 6.1 : Density of state distributions N(E) for evaporated (E_1, E_2, E'_2) and glow-discharge silicon films, the latter being deposited at the indicated temperatures. Solid curves, N(E) obtained from field-effect measurements ; broken curves, extrapolations. The arrows indicate the position of the field-free Fermi level. E'_2 was obtained after annealing E_2 at 540 K. (10)

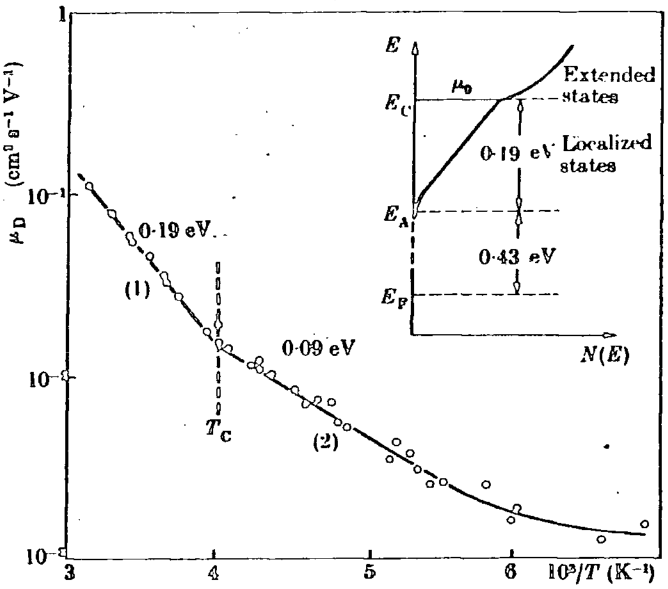

Fig 6.2 : Temperature dependence of the electron drift mobility μ_D, in a glow discharge film of silicon deposited at 500 K. (17)

With decreasing temperature the probability of thermal release from states near E_A becomes rapidly smaller and at $T \leq T_c$, hopping through states around this energy becomes the predominant transport mechanism and the activation energy of 0.09 eV gives the hopping energy directly. Similar measurements on samples prepared at different T_d show the temperature independent of those activation energies(7). The tail states are therefore not affected by T_d and do not arise from defects.

The study of the temperature dependence of photoconductivity(18) has given some interesting information concerning the role of localized states where electrons are trapped at E_A in the recombination process. The lifetime of electrons at E_C with respect to this process is about 10^{-5} sec, remarkably long for an amorphous material, providing an advantage for solar cell devices. Doping does not grossly change the density of states distribution, and appears to be mixed in the localized statea at the band edges ; quite likely having a similar spread of energies and preventing the activation energy for conduction from falling below ~ 0.2 eV(11).

6.1.4 Optical Properties

Preparation conditions greatly influence the position and the shape of the absorption edge of α-Si. Films deposited by glow discharge of silane have absorption edges positioned at higher energies than those produced by the sputtering process. The absorption edge shifts towards higher energies for films deposited at lower T_d. The incorporation of hydrogen during the sputtering process produces a similar effect. In general, however, an exponential absorption edge is observed in the low energy regime. The absorption coefficient α then increases more rapidly with energy satisfying equation

$$\alpha\hbar\omega_o = C\,(\hbar\omega - \hbar\omega_o)^m \tag{6.1}$$

where C is a constant and $\hbar\omega_o$ takes values between 1.5 and 1.9 eV for glow discharge films but smaller for sputtered films . In most cases, an absorption edge with m equal to 2 is observed. Fig 6.3 shows the spectral dependence of the absorption coefficient for a number of α-Si specimens prepared by different methods. The absorption edge is well within the visible spectrum with significantly larger values of absorption coefficient compared to crystalline Si. These properties are ideally suited to solar cell devices. In fact a theoretical efficiency of 18.8% has been estimated for α-Si solar cells, with only an 8% efficiency required for the economic use of a large-scale terrestrial solar cell.

The large value of α and ε, the refractive index, in the range of 1-3 eV as compared to crystalline Si, provides good evidence for a relaxation of the k-conservation selection rule. Glow discharge α-Si also exhibits strong photoconductive properties. One interesting feature of this material is that the structure seen in absorbance measurement is also evident in all photoconductivity curves and this has been explained by Spear et al(18). The onset of photoconduction in this material depends somewhat on T_d but is seen between ∿ 0.6 and 0.8 eV. This energy corresponds to excitation from states at the Fermi level, which shifts with T_d, to the mobility edge E_c in the conduction band or perhaps to tail states at E_A. The latter has a lower probability because of the small overlap between initial and final states (both being localized states).

Three peaks are observed in luminescence curves(20) namely at 1.25 eV, 1.10 eV and 0.92 eV corresponding to transitions (excitations) $E_A \rightarrow E_B$, $E_A \rightarrow E_y$, and $E_x \rightarrow E_B$, respectively. The luminescence decay time is about 20 nS, approximately 10^5 times faster than the photoconductivity decay time. This value is roughly what one would expect for an optical transition if the electron and hole orbitals are strongly localized. In this process the photogenerated electron-hole pairs recombine emitting

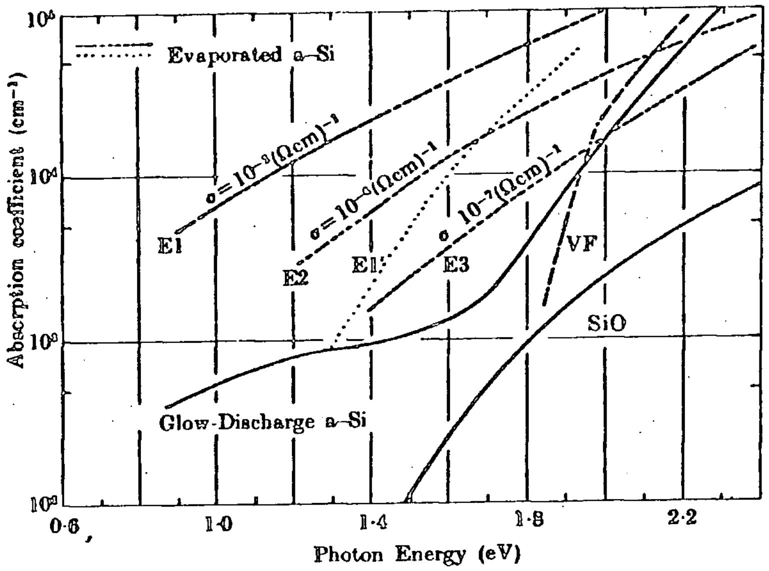

Fig 6.3 : Optical absorption edges of amorphous silicon. Curves E1, E2, and E3 refer to evaporated films with room-temperature conductivities as indicated. Curve E1' refers to specimen E1 measured after an anneal at 650 K. The glow-discharge film was deposited at 500 K (19).

radiation. The pairs might also be separated from their mutual Coulomb potential and lead to photoconductivity process.

6.2 PREVIOUS ELECTROABSORPTION AND ELECTROREFLECTANCE STUDIES IN AMORPHOUS SILICON

Despite the interest in α-Si, very little has been reported on the effect of an external electric field on the absorption edge or reflectance of this material. Freeman et al (21) in 1979 were the first to study the electroreflectance signal at room temperature. The effect was attributed to the change in the refractive index induced by an electric field. A study on samples deposited at different substrate temperatures in a plasma of argon and hydrogen indicates that the electroreflectance spectra, just like the absorption edges of α-Si, are shifted towards higher energies with decreasing T_d. However the electroreflectance spectrum is broader for films deposited at lower T_d. In most cases the structure of the electroreflectance spectrum is complicated by the presence of interference effects. Okamoto et al (22) were also able to determine the band gap energy of α-Si from electroreflectance data using a three point method developed by Aspnes (23). An energy gap $E_g = 1.74$ eV at 300 K was obtained for glow discharge α-Si deposited at 300° C.

The most detailed study on the effect of an external electric field on the absorption edge of α-Si was performed by Al-Jalali and Weiser (24). An electroabsorption signal was only observed in the fast rising part of the absorption spectrum (with $\alpha \sim 10^4$ cm^{-1}) and was attributed to transitions involving only localised states. Their data are shown in Fig 6.4a. These authors believed that two processes are responsible for the observed shift. The Stark effect is most likely to be observed in view of transitions involving localized states very similar to the one detected in α-Se (25). However a change in the transitional matrix element of localized to delocalized transitions by the electric field may also contribute to the observed shift. The peak of the electroabsorption spectrum shifts towards higher energies by about 0.1 eV on cooling from room temperature to 77 K ($\sim 4.5 \times 10^{-4}$ eV.K^{-1}) and corresponds to the similar shift of the absorption edge. The magnitude of the change in absorption coefficient $\Delta\alpha$, depends almost quadratically on the electric field strength. The electroabsorption spectrum obtained from films deposited at lower temperature shows a broader peak with smaller magnitude of $\Delta\alpha$. An electroreflectance spectrum was also deduced from the electroabsorption data and found to be about two orders of magnitude smaller than the electroabsorption signal as shown in Fig 6.4b.

6.3 SAMPLE PREPARATIONS

Our experiments were carried out on two different types of α-Si, namely glow discharge and sputtered films. The glow discharge samples were supplied by the Dundee group and were deposited onto thin conducting films of indium tin oxide(ITO). Sputtered films deposited on ITO were prepared at Xerox, Palo Alto. The thicknesses of these films were between 0.4 μm and 2.0 μm.

Experiments were performed on sandwich structures with ITO as the back contact. The top electrodes were either semitransparent aluminium or gold. Cleaning and degreasing the surface of the films were necessary prior to deposition of the top electrodes. The samples were normally placed in a soxhlet reflux unit to boil and recycle iso-propyl alcohol (BDH-Analar) for about one hour. In each case it was found advantageous to remove the samples from the reflux unit whilst the solvents were still hot. This ensured total evaporation of residual liquid from the sample, leaving the cleanest surface possible.

The sample was then mounted on a copper base in a vacuum chamber for electrode evaporation as described in section 4.4. For contacts to α-Si films, the chamber was pumped down to 10^{-6} torr, and the subsequent rate of evaporation used was about 1-5 Å sec^{-1}. depending upon electrode

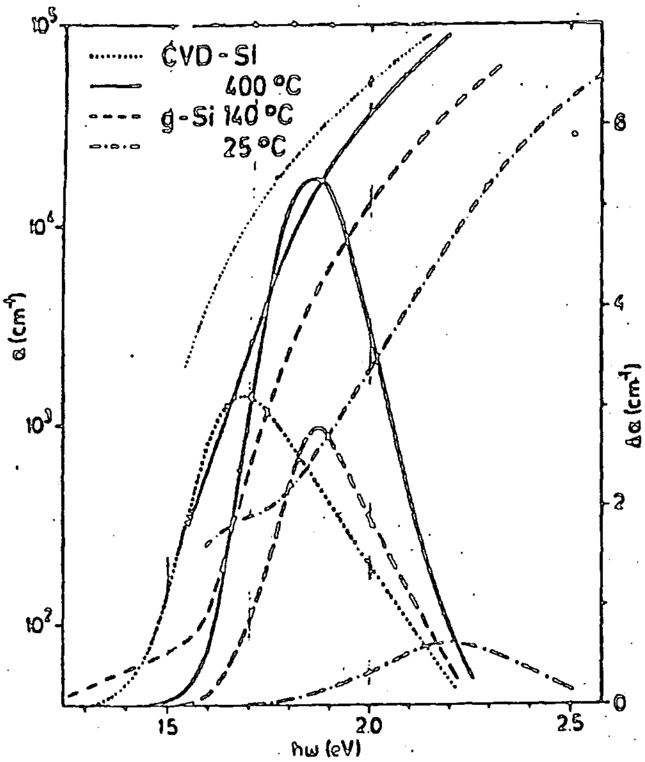

Fig 6.4a : Absorption and electroabsorption spectra (F = 5 x 10^4 V/cm) of silicon films deposited by chemical vapour deposition (CVD) or by plasma deposition (g) at various substrate temperatures.$^{(24)}$

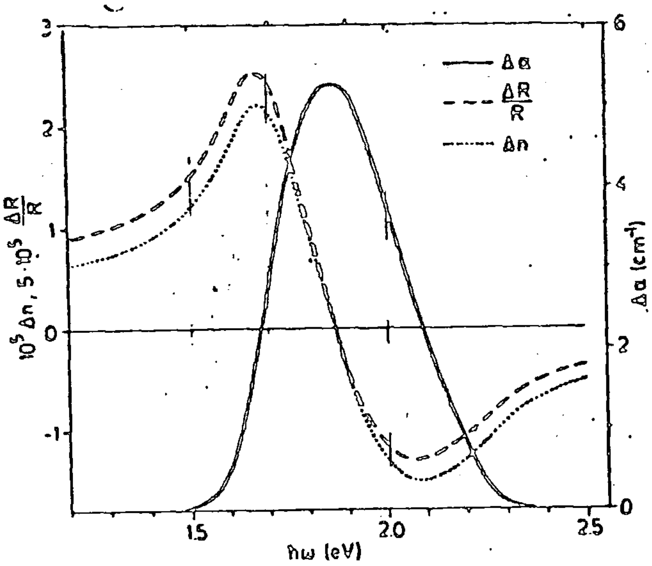

Fig 6.4b : Electroreflectance spectrum ΔR/R and the field induced change Δn of the refractive index calculated by Kramers-Kronig analysis of the electroabsorption spectrum Δα(g-Si), T_s = 400° C .$^{(24)}$

material.

6.3.1 Electrical Contact

The metal electrodes enable large electric fields to be applied across the films. One should ensure that no barrier has been formed at the metal-semiconductor interface. This was normally checked by performing d.c. conductivity measurements. Typical data are shown in Fig 6.5. The Ohmic characteristic from which the resistivity of the material was deduced, is evident at low voltage. For this particular sample, the room temperature resistivity is 1.1×10^{11} Ω.cm. The high value of resistivity allows large electric field effects to be studied with negligible dissipated power in the sample.

At high voltages the current increases more rapidly and is proportional to V^n with $n \sim 2$ in this particular case. In some samples however, values of $n > 2$ were also observed. Since the power dissipated is negligible the rapid increase in current has been attributed to space charge injection. Fig 6.6 illustrates d.c. conductivity data for a doped α-Si specimen at room temperature. If electroabsorption measurements were to be carried out in the V^n region where $n \geq 2$ as discussed in section 4.6, the modulating field must be operated at a high enough frequency such that space charge injection effects are eliminated. Good electrical contact can also be ensured by capacitance measurements. In all samples used during the course of this work, no detectable barrier was formed as evidenced by the fact that the capacitance of the structure equalled its geometric capacitance.

6.4 EXPERIMENTAL RESULTS

Optical absorption measurements were performed in the wavelength range between 5500 Å and 8500 Å using the grating monochromator already described in section 3.2. The absorption coefficient was calculated from the transmittance data using the standard formula (26) for absorption

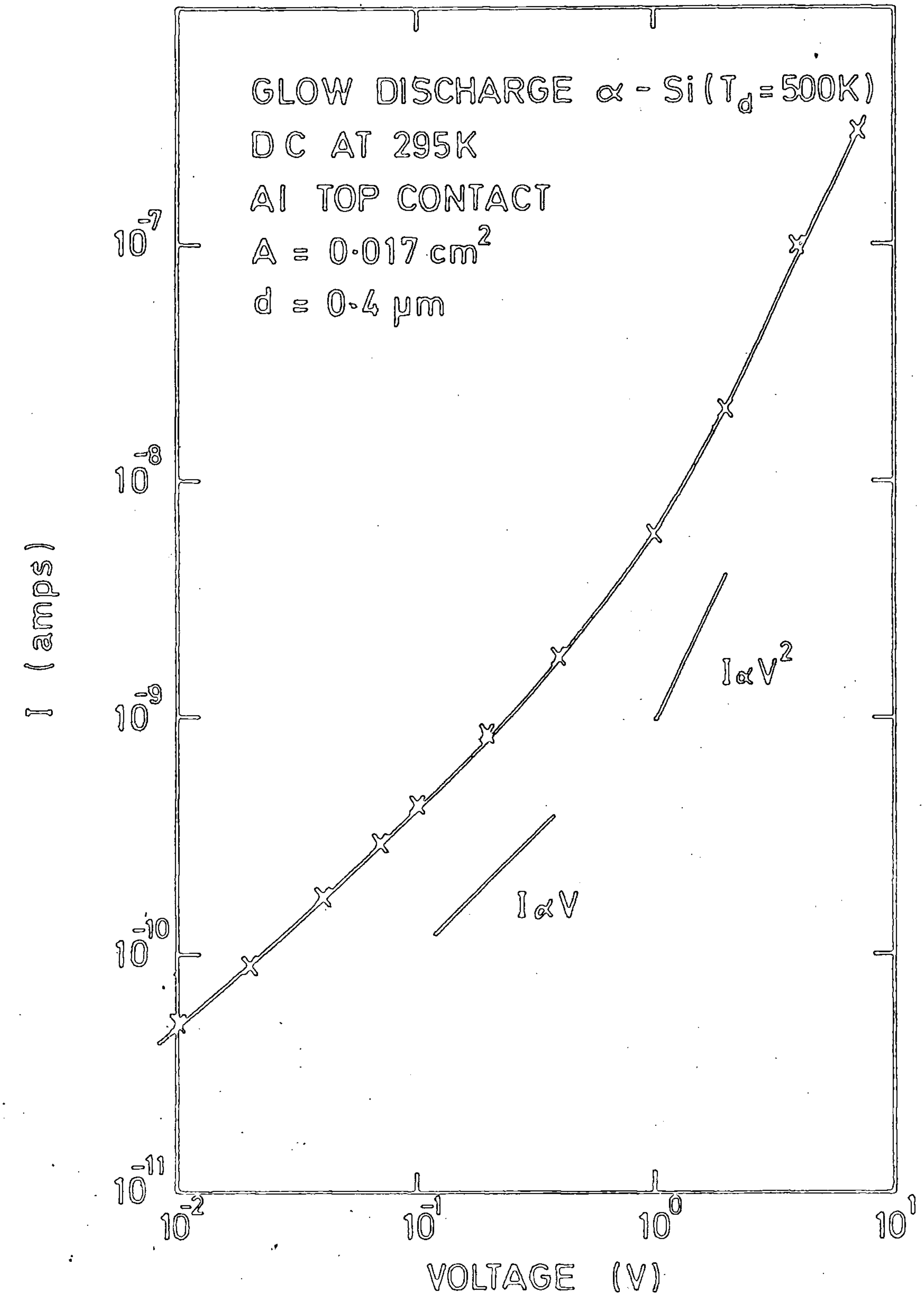

Figure 6.5 : Current-voltage characteristic of a glow discharge produced α-Si sample at room temperature.

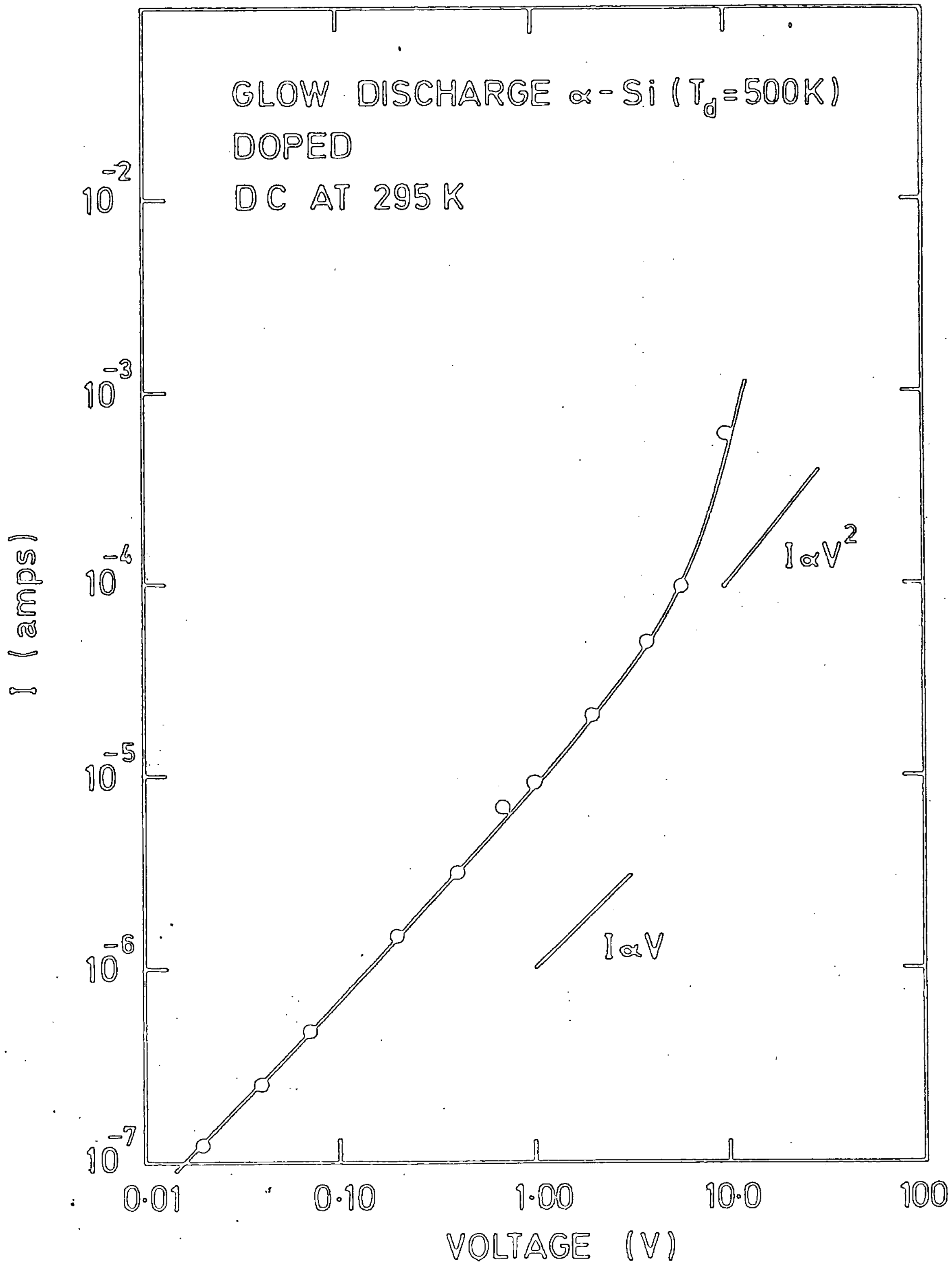

Figure 6.6 : Current-voltage characteristic of a glow discharge produced α-Si sample at room temperature.

in thin films. In this case

$$I/I_o = \left[(1 - R_1)(1 - R_o)\, e^{-\alpha d} \right] \Big/ \left[1 + R_o R_1\, e^{-2\alpha d} \right] \quad (6.2)$$

where I and I_o are the transmitted and the incident light intensity, respectively. d is the thickness of the film and R_o and R_1 are respectively the reflectivity of the film and of the film-substrate interface and are given by

$$R_o = \left(\frac{n - 1}{n + 1} \right)^2 \quad \text{and} \quad (6.3)$$

$$R_1 = \left(\frac{n - n_o}{n + n_o} \right)^2 \quad (6.4)$$

In this case, n and n_o are the refractive indices of the film and substrate, respectively. For our calculation $n = 3.4^{(27)}$ and $n_o = 1.5$ and hence $R_o = 0.29$ and $R_1 = 0.15$. It is evident that for $\alpha d > 0.2$, equation (6.2) can be reduced to

$$I/_{I_o} = (1 - R_1)(1 - R_o)e^{-\alpha d} \quad (6.5)$$

This condition therefore limits an accurate evaluation of absorption coefficient to values $> 10^3\ \mathrm{cm}^{-1}$.

Fig 6.7 shows typical absorption edges of glow discharge α-Si deposited at three different substrate temperatures. Studies of the absorption in the low energy règime are hampered by the high transparency of the thin films and require an accurate knowledge of the reflectivity. Since the thicknesses of the samples were between one and three times the wavelength of the corresponding photon energy in the absorption spectra, interference effects were normally encountered. These could easily be compensated for in the final analysis and are therefore not

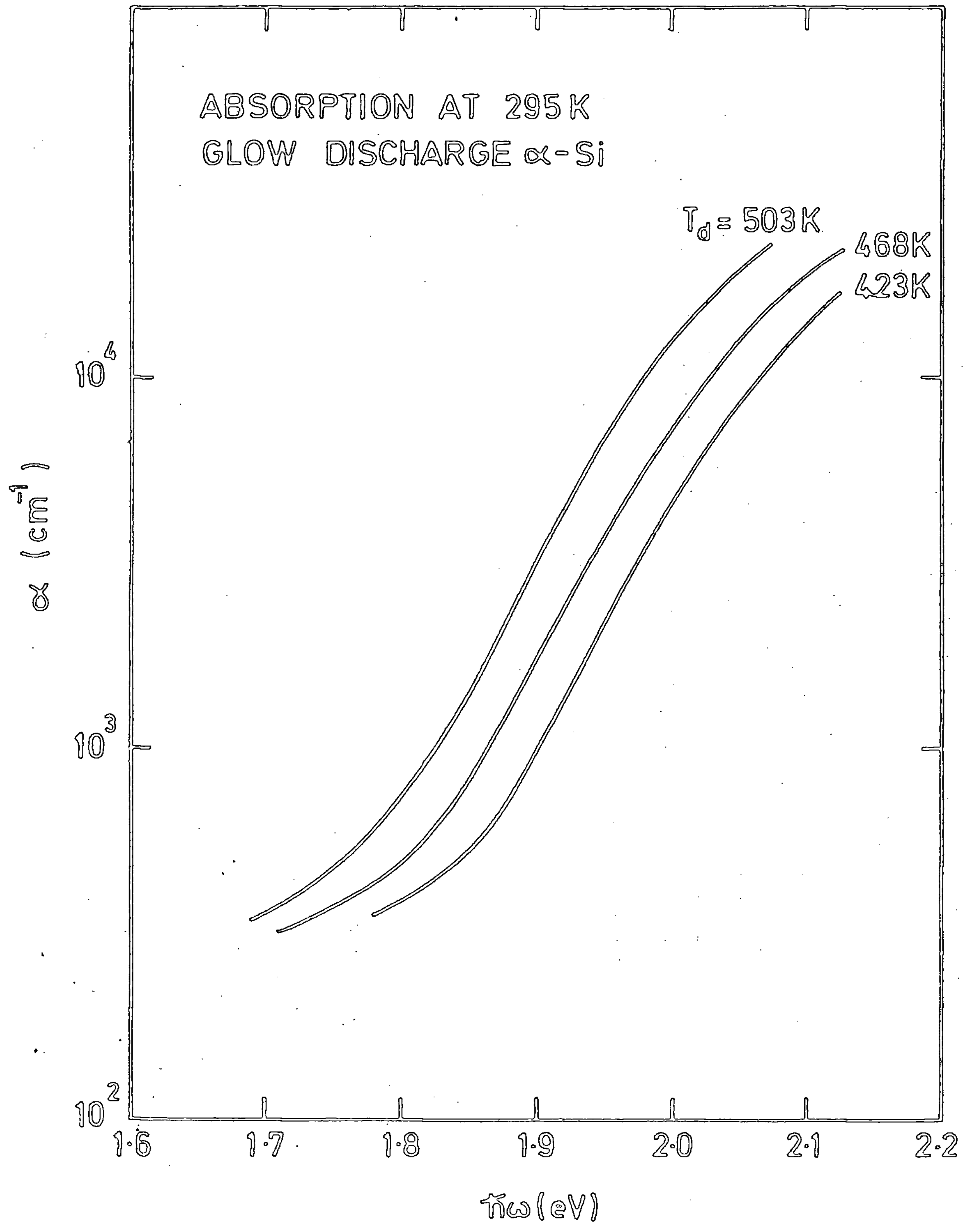

Figure 6.7 : Absorption coefficient of glow discharge produced α-Si samples deposited at 503, 468 and 423 K, as a function of photon energy.

necessarily indicated in all the absorption plots.

The absorption edges calculated from the transmittance data for glow discharge α-Si deposited at different substrate temperatures are shown in Fig 6.7. The absorption edge shifts towards higher energies for films prepared at lower substrate temperature. They have similar features to those reported in the literature(18,19). On cooling from room temperature to 77 K, the absorption edge shifts by about 0.07 eV towards higher energies as illustrated in Fig 6.8.

Sputtered α-Si has an absorption edge shifted to slightly lower photon energy than that for glow discharge α-Si as seen in Fig 6.9. The slope of the curve and its magnitude are also higher compared to those for glow discharge α-Si. Both absorption edges however increase as the quadratic of $\hbar\omega$ over a certain range of energy. This is shown in Fig 6.10. Extrapolation to the energy axis determines the value of $\hbar\omega_o$ which equals 1.755 eV and 1.785 eV for sputtered and glow discharge films respectively. Below the quadratic region, the absorption coefficient decreases exponentially with photon energy.

Electroabsorption measurements were performed on both sputtered and glow discharge α-Si grown at 500 K. The data obtained were used to compare the properties of films prepared by the different methods.

6.4.1 Electroabsorption

Typical electroabsorption spectra for undoped glow discharge α-Si are shown in Fig 6.11. The second harmonic response is that detected at 4.0 kHz. This is crucial in order to eliminate the photoconductivity effect present, a complication discussed in section 4.5. The magnitude of the change in absorption, Δα, induced by an electric field depends on the modulating frequency as shown in Fig 6.12. Δα decreases rapidly with frequency before it saturates at frequencies above 2.5 kHz where photoconductivity effects are eliminated. All data presented in this chapter were therefore taken at frequencies above 2.5 kHz.

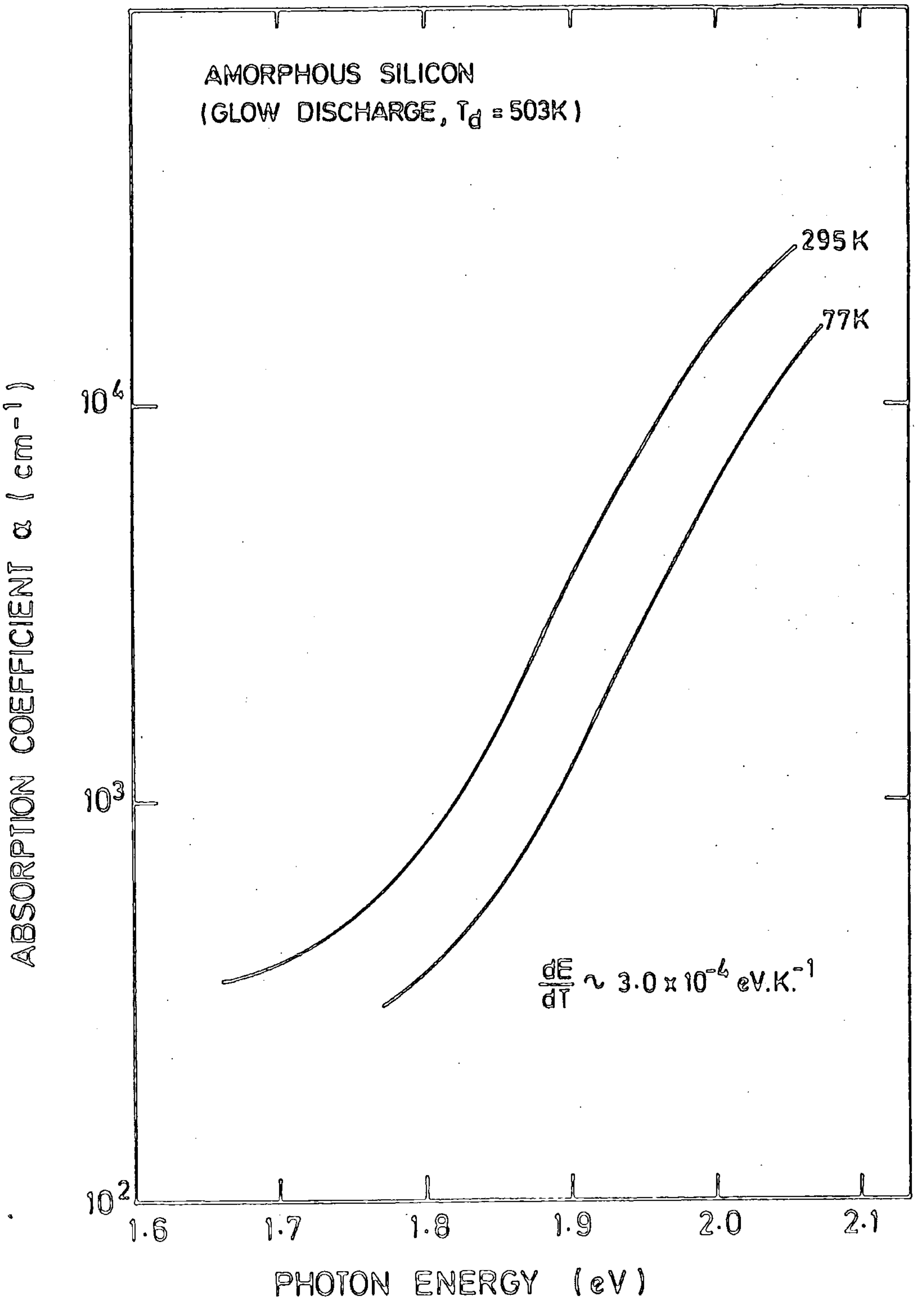

Fig 6.8 : Absorption edge of glow discharge produced α-Si deposited at 503 K.

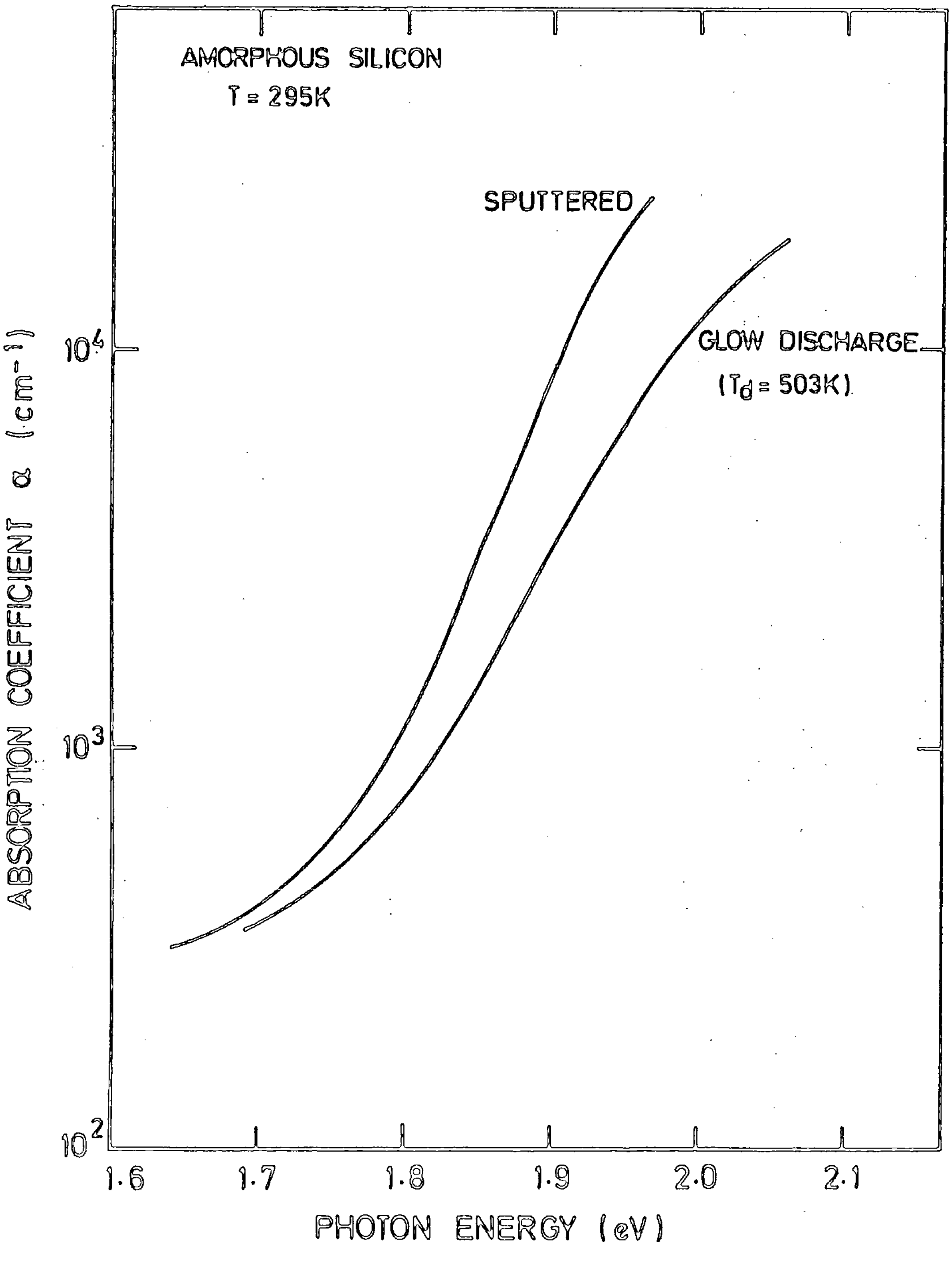

Fig 6.9 : Absorption edges of sputtered and glow discharge produced α-Si samples at room temperature.

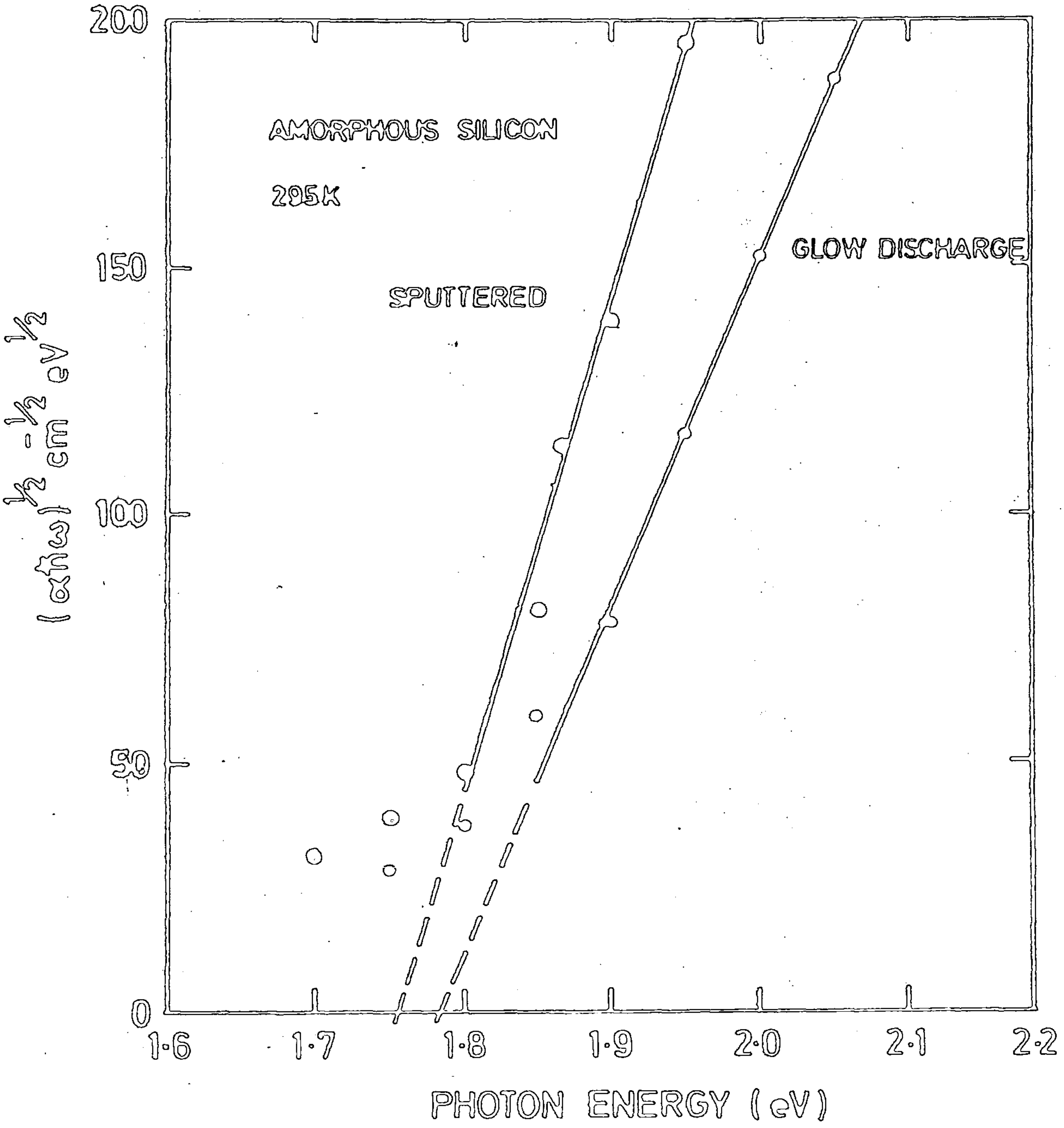

Figure 6.10 : Square root of absorption coefficient of sputtered and glow discharge α-Si samples as a function of photon energy.

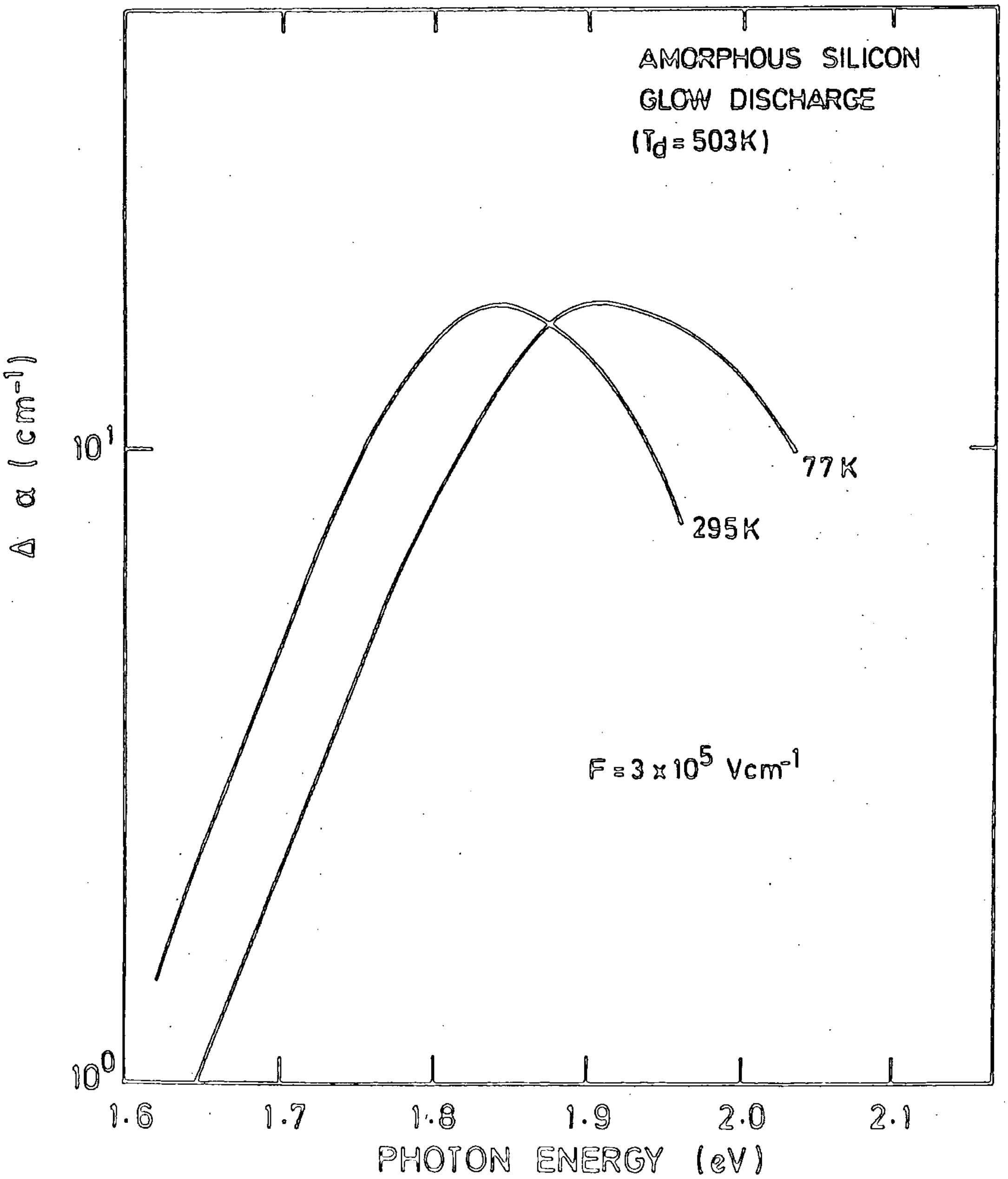

Figure 6.11 : Absorption change of an undoped glow discharge produced α-Si sample at 295 and 77 K, as a function of photon energy.

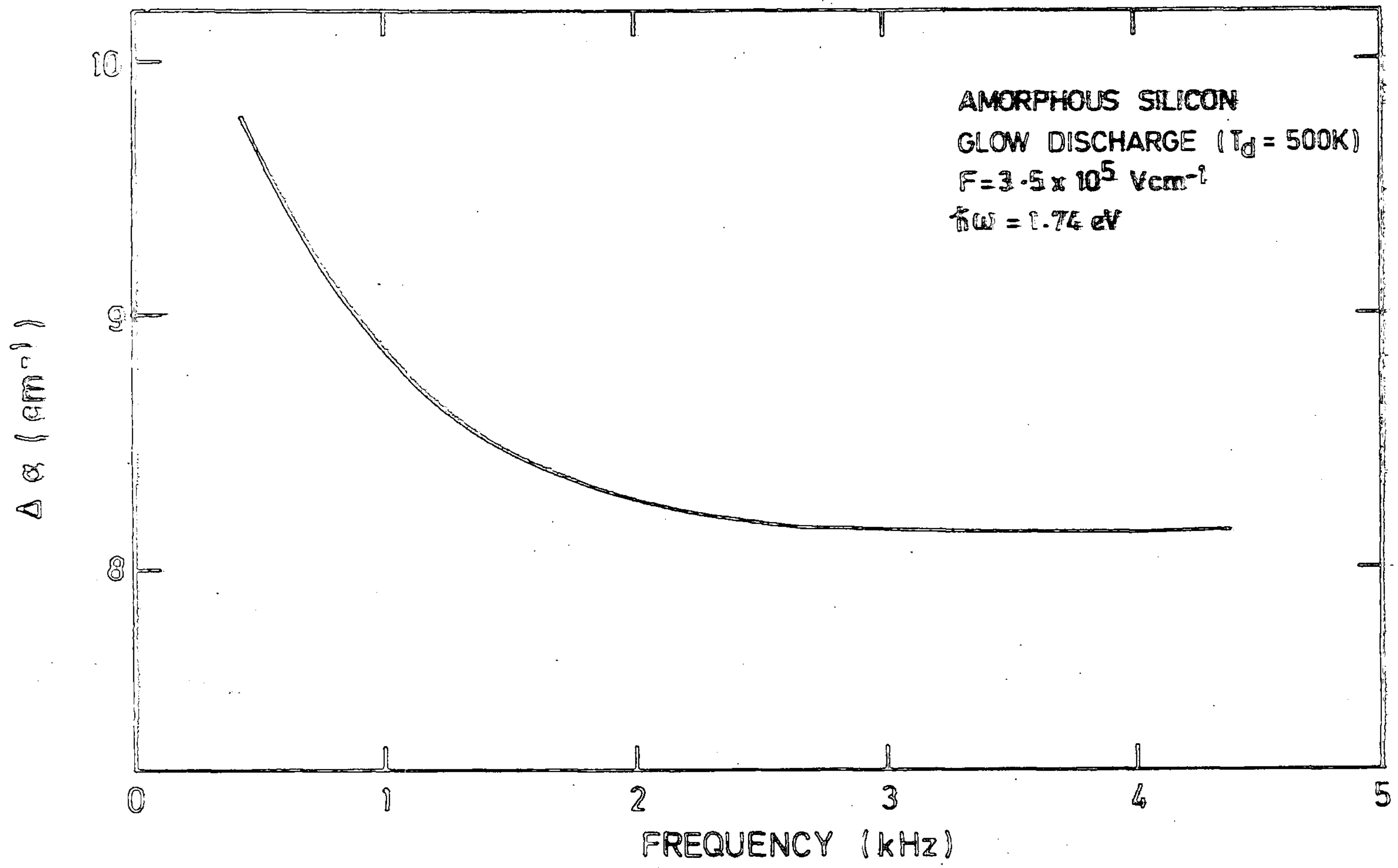

Fig 6.12 : Dependence of the change in absorption, $\Delta\alpha$, of glow discharge produced α-Si on the frequency of the modulating field at room temperature.

With reference to Fig 6.11, each spectrum is dominated by a single peak with a change in absorption of one part in 10^4 detected at field strengths of $\sim 10^5$ V.cm^{-1}. Below this peak $\Delta\alpha$ decreases exponentially with photon energies with a slope of about 16 eV^{-1} and becomes undetectable at energies less than 1.6 eV. On cooling from room temperature to 77 K, the whole spectrum shifts towards higher energies by about 0.07 eV ($\sim 3.2 \times 10^{-4}$ eV.K^{-1}) corresponding to the temperature shift in the absorption edge. The exponential slope is however virtually unchanged.

Figs 6.13 and 6.14 illustrate the electroabsorption spectra for doped glow discharge α-Si and for sputtered α-Si, respectively. These spectra have similar shape and structure to those obtained using undoped samples and shifts by about the same energy on cooling from room temperature to 77 K.

In all cases, the change in absorption coefficient beyond the peak decreases very rapidly with increasing photon energy and diminishes in the region where the absorption coefficient α, increases as the quadratic of the photon energy. This is shown in Fig 6.15 and Fig 6.16 where the absorption curves are plotted alongside the electroabsorption spectra for comparison. This behaviour provides a strong indication that only optical transitions involving localized states respond to the electric field modulation. The position of the peak coincides with $\hbar\omega_0$ for both glow discharge and sputtered α-Si films.

The magnitude of $\Delta\alpha$ for sputtered α-Si depends quadratically on the electric field strength. Fig 6.17 shows the room temperature variation of $\Delta\alpha$ with electric field at different photon energies. A straight line with a slope of 2 is obtained when $\ln \Delta I/_I$ is plotted against $\ln V(\Delta I/_I$ is the relative change in transmission which is proportional to $\Delta\alpha$ and V is the applied potential across the sample). Fig 6.18 shows a similar result at 77 K. The fact that the straight line extrapolates to the origin in (Fig 6.19) indicates the absence of space charge complications in these measurements.

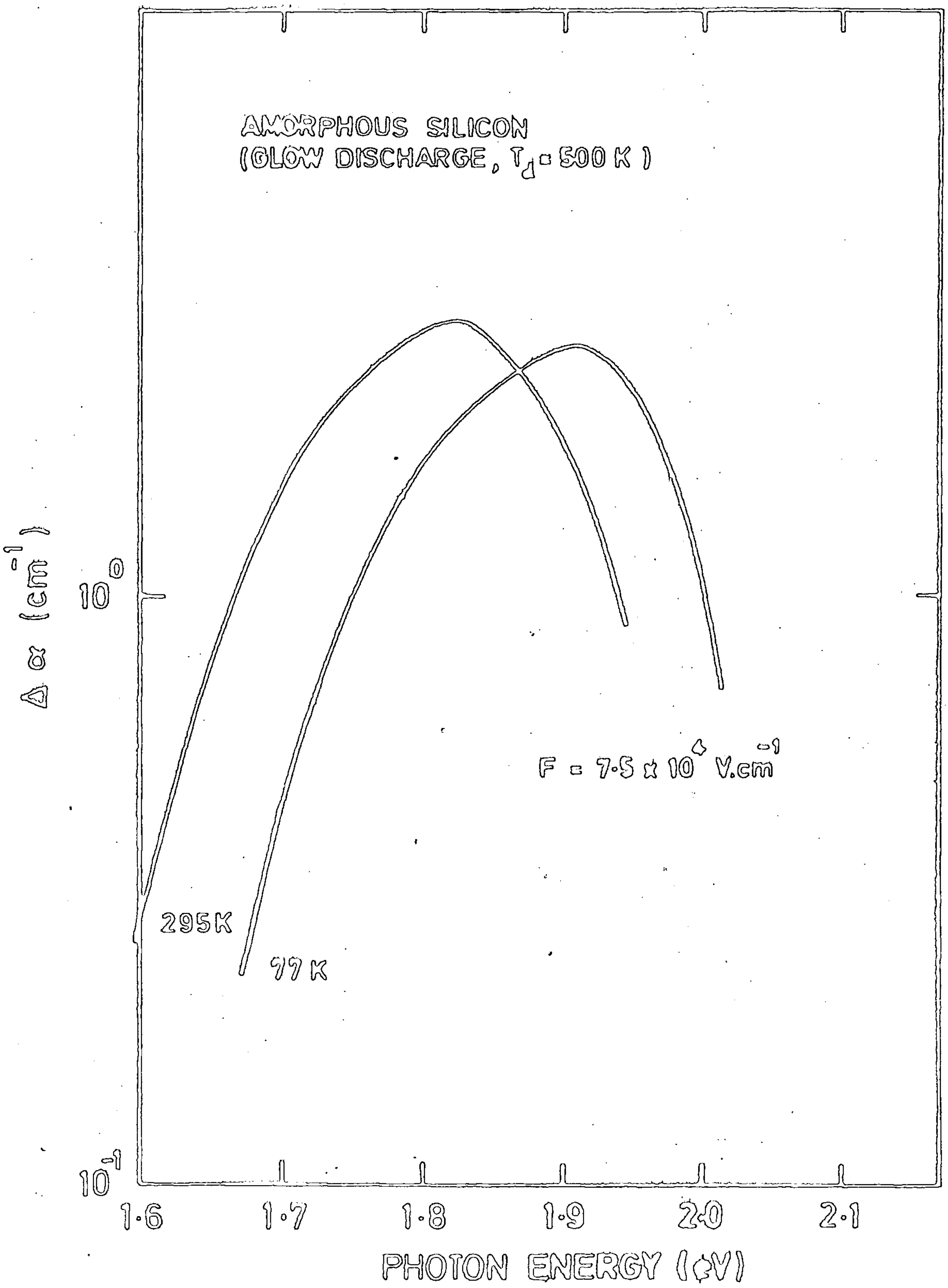

Figure 6.13 : Absorption change of a doped glow discharge produced α-Si sample at 295 and 77 K, as a function of photon energy.

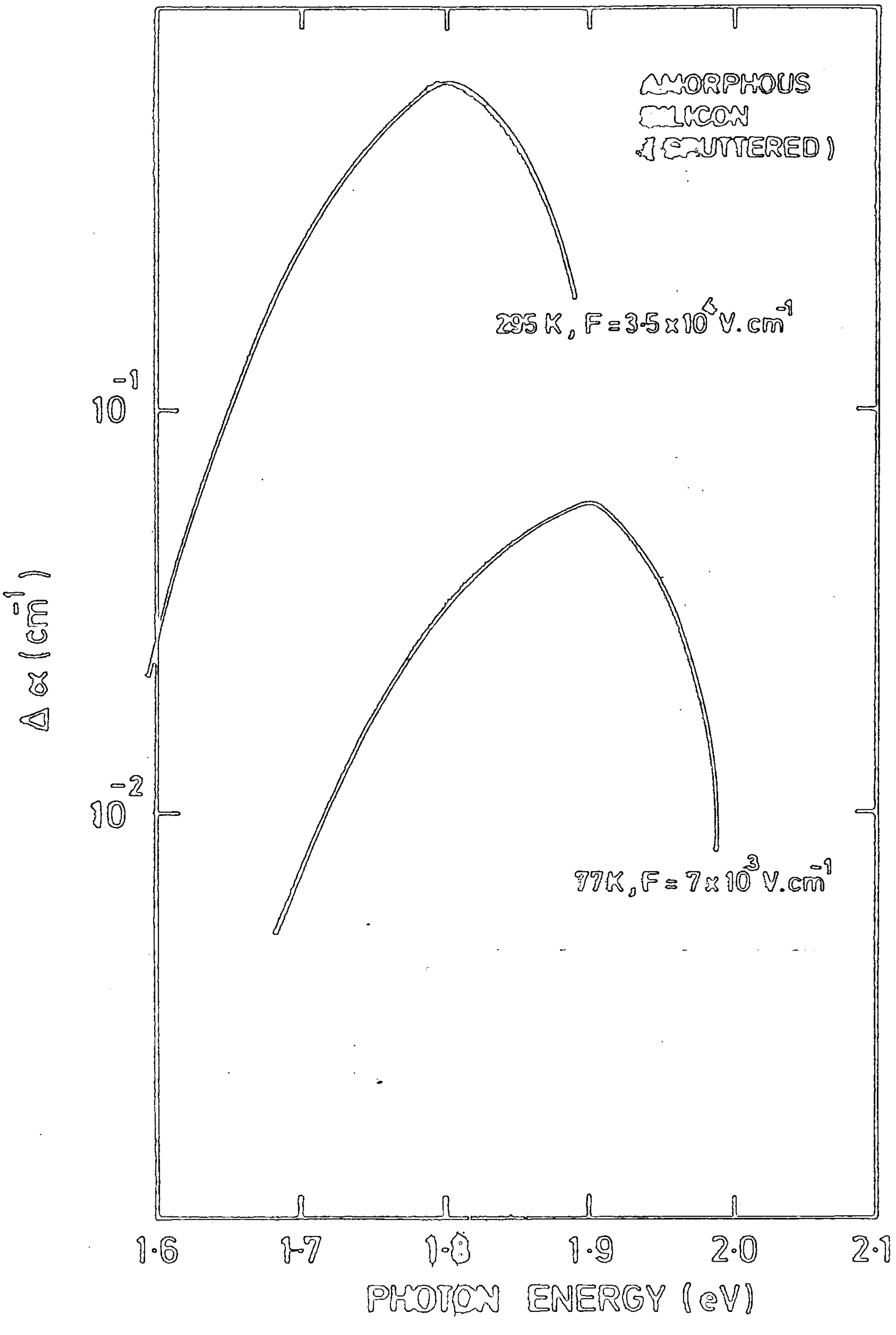

Figure 6.14 : Absorption change of a sputtered α-Si sample taken at 295 and 77 K, as a function of photon energy.

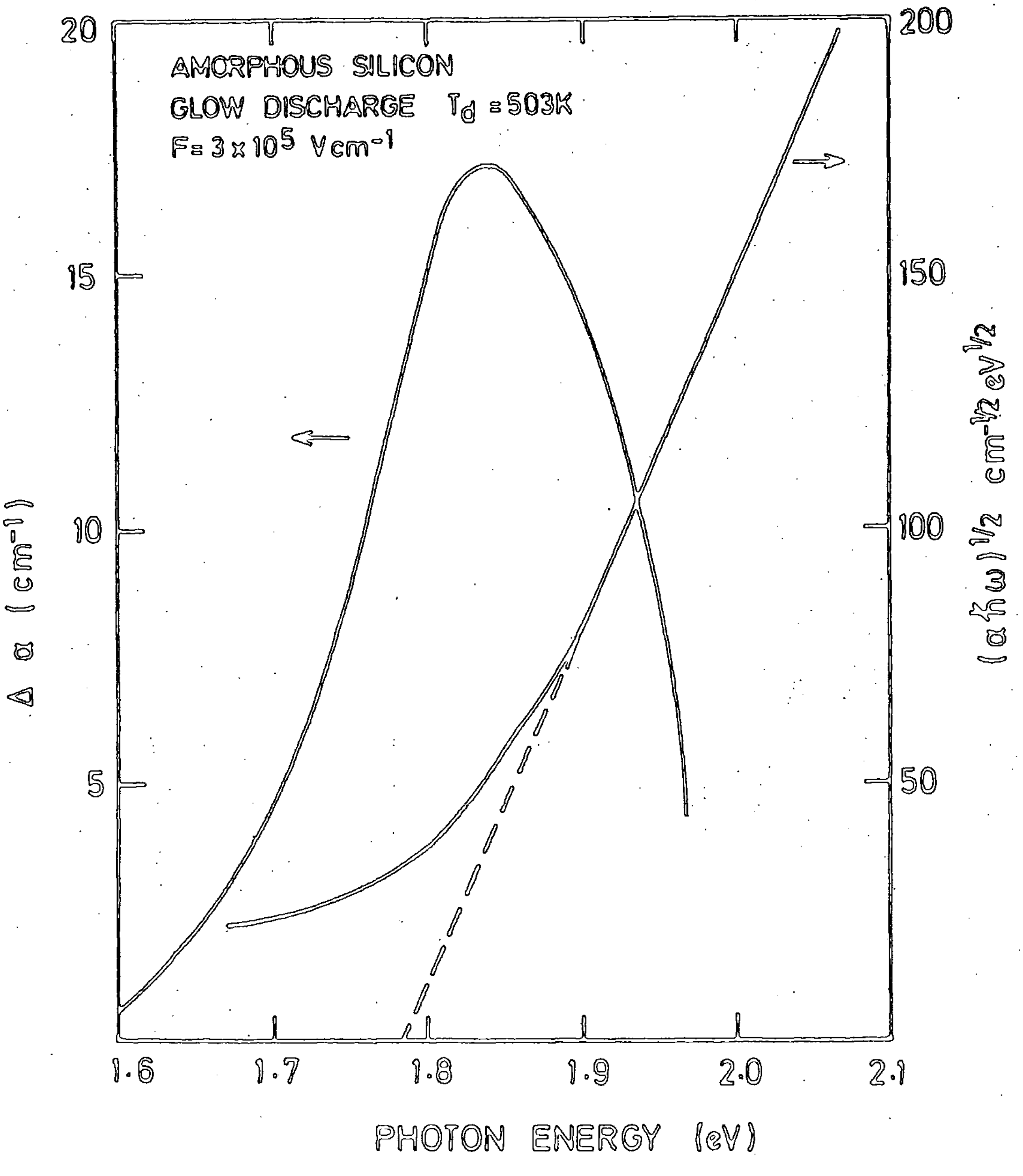

Figure 6.15 : Electroabsorption spectrum of a glow discharge α-Si film taken at room temperature. Square root of absorption coefficient is also plotted as a function of photon energy, indicating a quadratic dependence of α on photon energy at high energy regime.

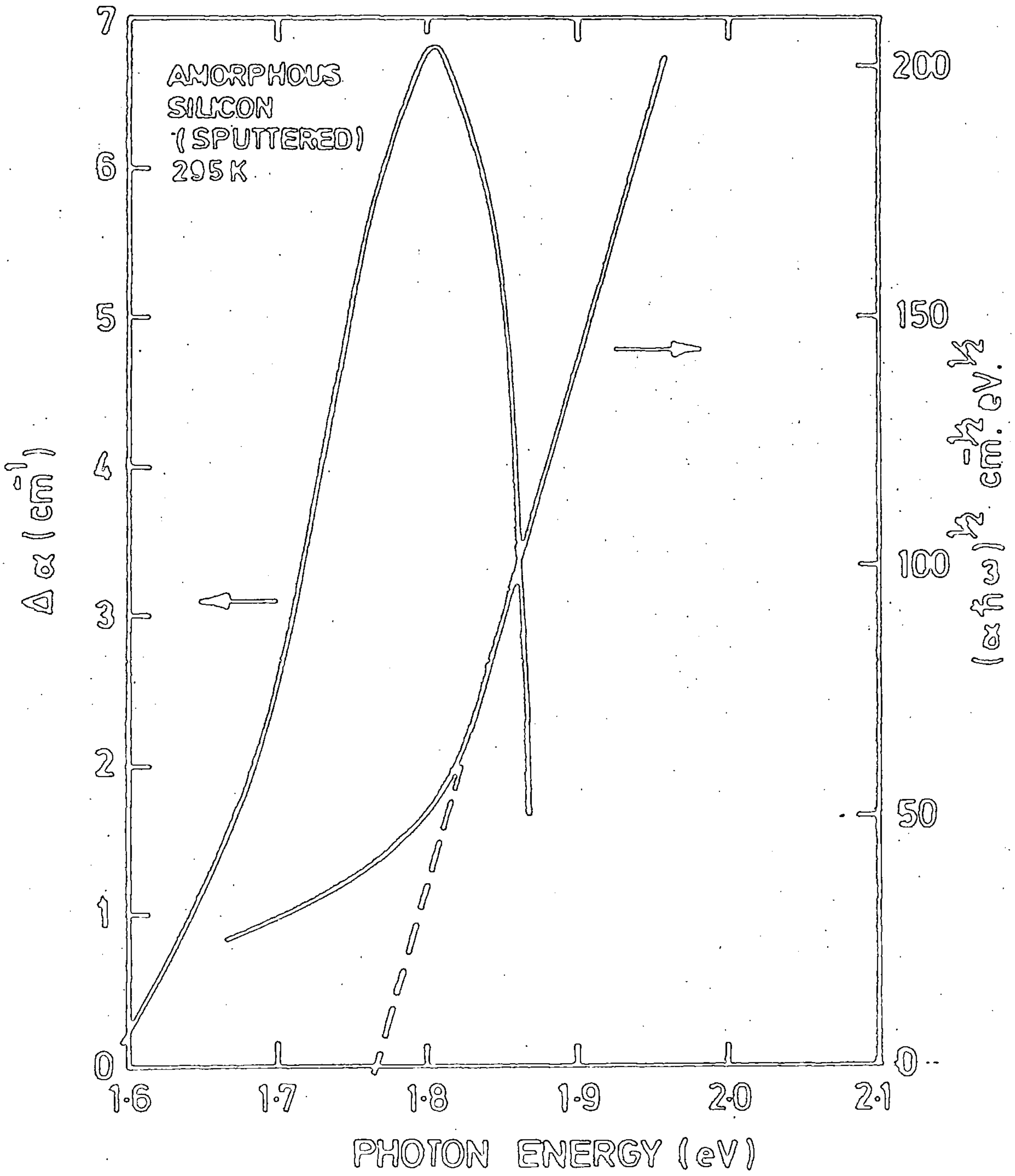

Figure 6.16 : Electroabsorption spectrum of a sputtered α-Si film at 295 K. For comparison, the quadratic dependence of α on photon energy at high energy règime is also shown.

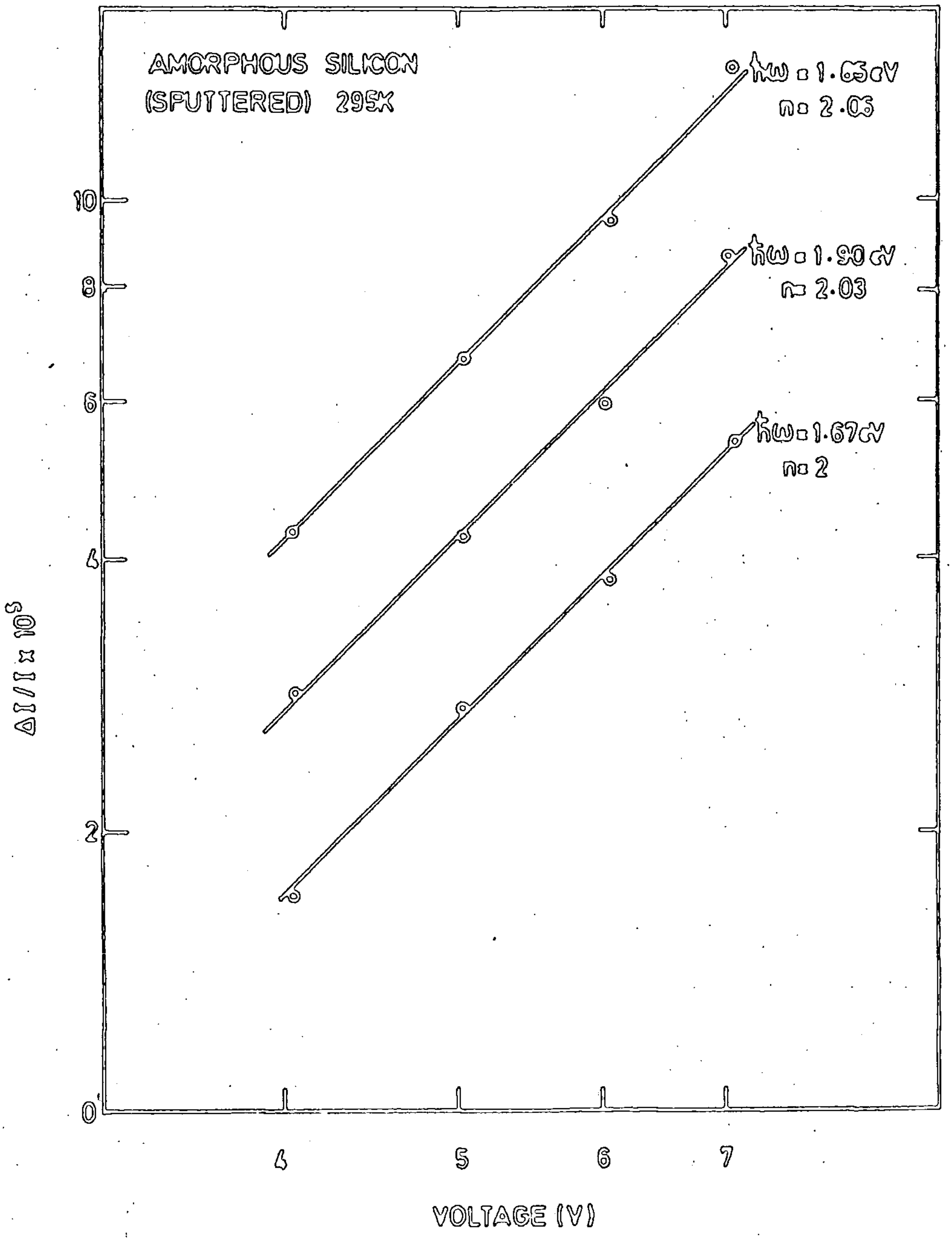

<u>Figure 6.17</u> : Dependence of the fractional change in transmission of a sputtered α-Si sample at 295 K on the magnitude of the applied voltage.

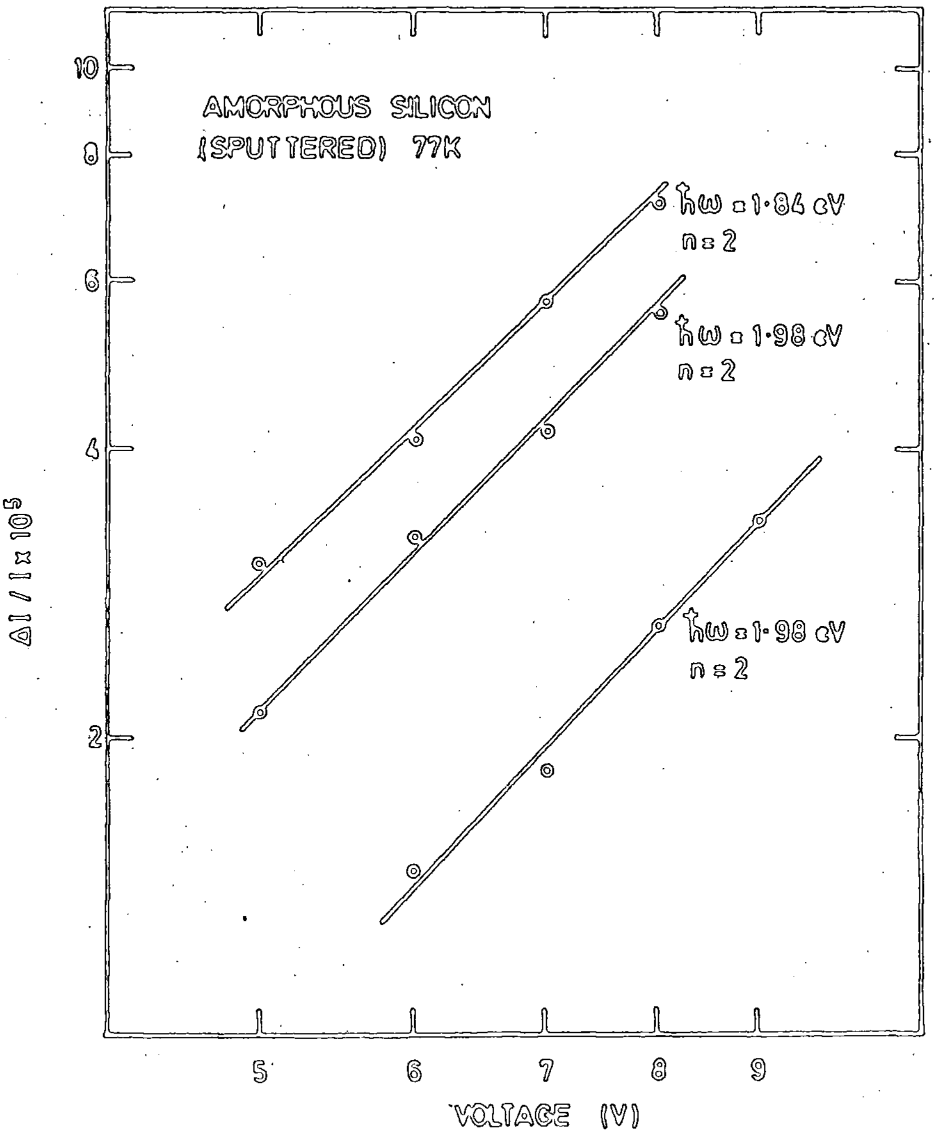

Figure 6.18 : Dependence of the fractional change in transmission of a sputtered a-Si sample at 77 K on the magnitude of the applied voltage.

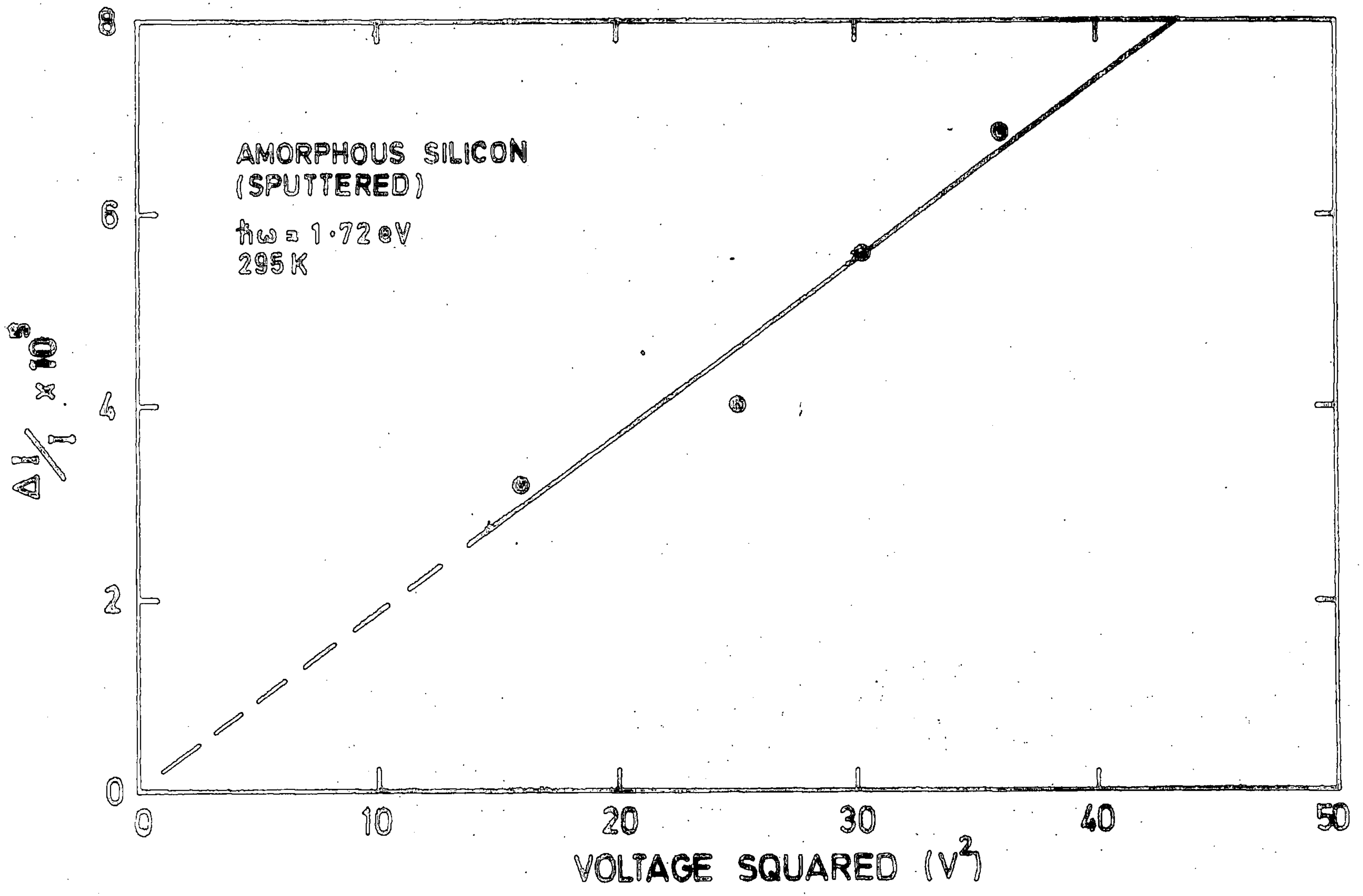

Figure 6.19 : Dependence of the fractional change in transmission of a sputtered α-Si sample at 295 K on the magnitude of the applied voltage.

Similar experiments on glow discharge films show totally different results. In this case the magnitude of $\Delta\alpha$ increases in proportion to F^n (F is the electric field strength) where $n \leq 2$ depending on the photon energy considered. This is shown in Fig 6.20 and 6.21 taken for two different temperatures namely 295 K and 77 K. Space charge complications are also absent in this sample as indicated in Fig.6.22. The following figure summarizes the field dependence of $\Delta\alpha$ at 295 K and 77 K for the undoped film whose electroabsorption spectra are shown in Fig 6.11. An interesting point here is that the temperature coefficient of the energy shift ($^{\Delta E}/_{\Delta T}$), seems to depend on the value of n. At the peak position where n takes the value 2, ($^{\Delta E}/_{\Delta T}$) $\sim 3.0 \times 10^{-4}$ eV.K^{-1} ; this is the value observed for the temperature shift of the absorption edge. However, below the peak, at $n = 1.7$ for example, ($^{\Delta E}/_{\Delta T}$) is significantly larger and reaches approximate 5.0×10^{-4} eV.K^{-1} . An identical effect is also observed in doped films as illustrated in Fig 6.24. These data are probably related to the observed temperature shift at the onset of the photoconduction in glow discharge α-Si$^{(18)}$.

6.5 DISCUSSION OF RESULTS

In an amorphous material, both localized and delocalized states contribute to the absorption but respond differently to an external electric field. An electroabsorption response in α-Si is obtained only in the absorption edge below the region where the absorption coefficient rises as the quadratic of the photon energy as shown in Figs 6.15 and 6.16. These regions include the exponential absorption edge and the fast rising part of the edge where the transition from the exponential to the quadratic region occurs. Optical transitions between delocalized states in α-Si thus are not altered to a detectable degree by an electric field of less than 10^5 V.cm^{-1} and do not contribute to the electroabsorption spectrum.

The exponential tail observed in most amorphous solids is thought to be due to the broadening of a band edge$^{(28,29)}$ or of exciton states$^{(30,31)}$

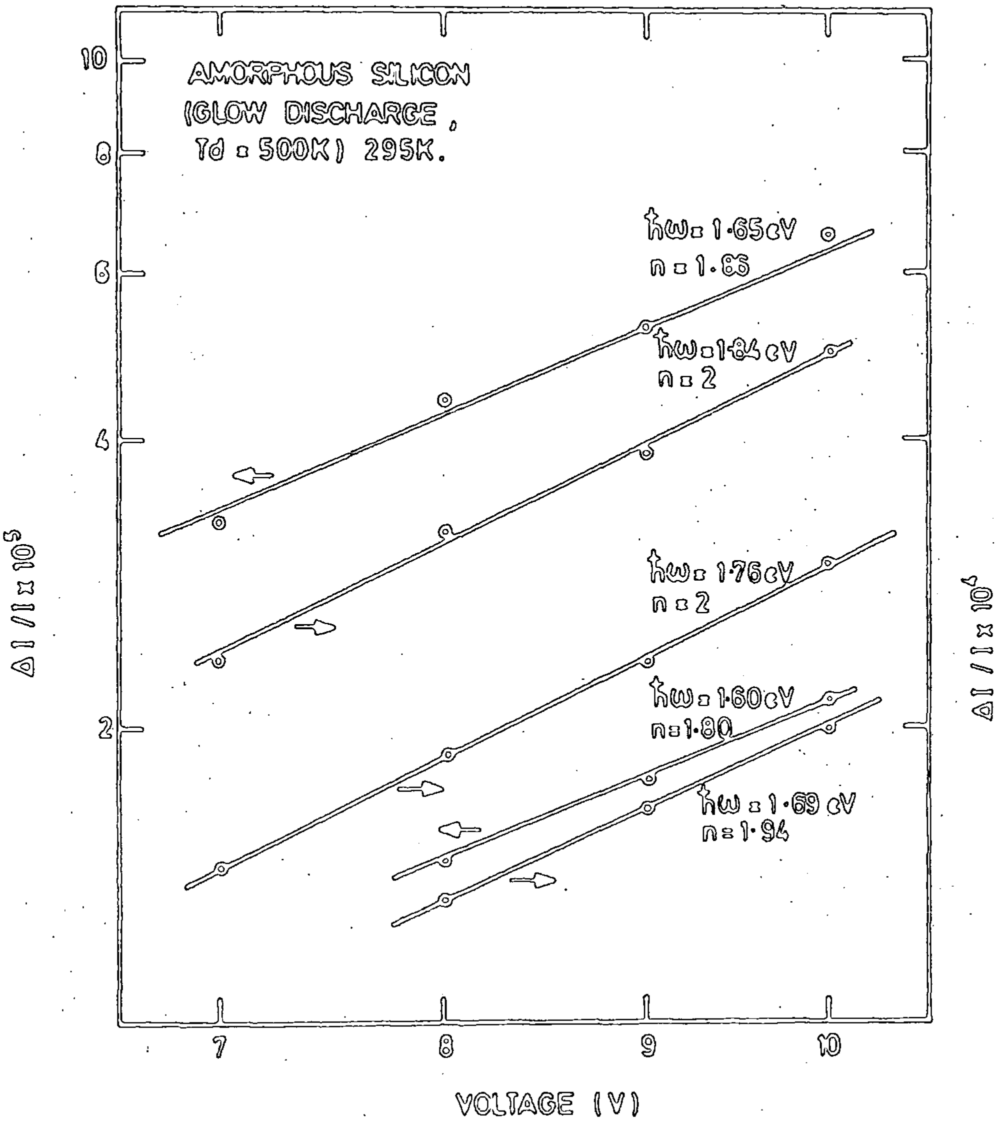

Figure 6.20 : Dependence of the fractional change in transmission of a glow discharge produced a-Si sample at 295 K on the magnitude of the applied voltage.

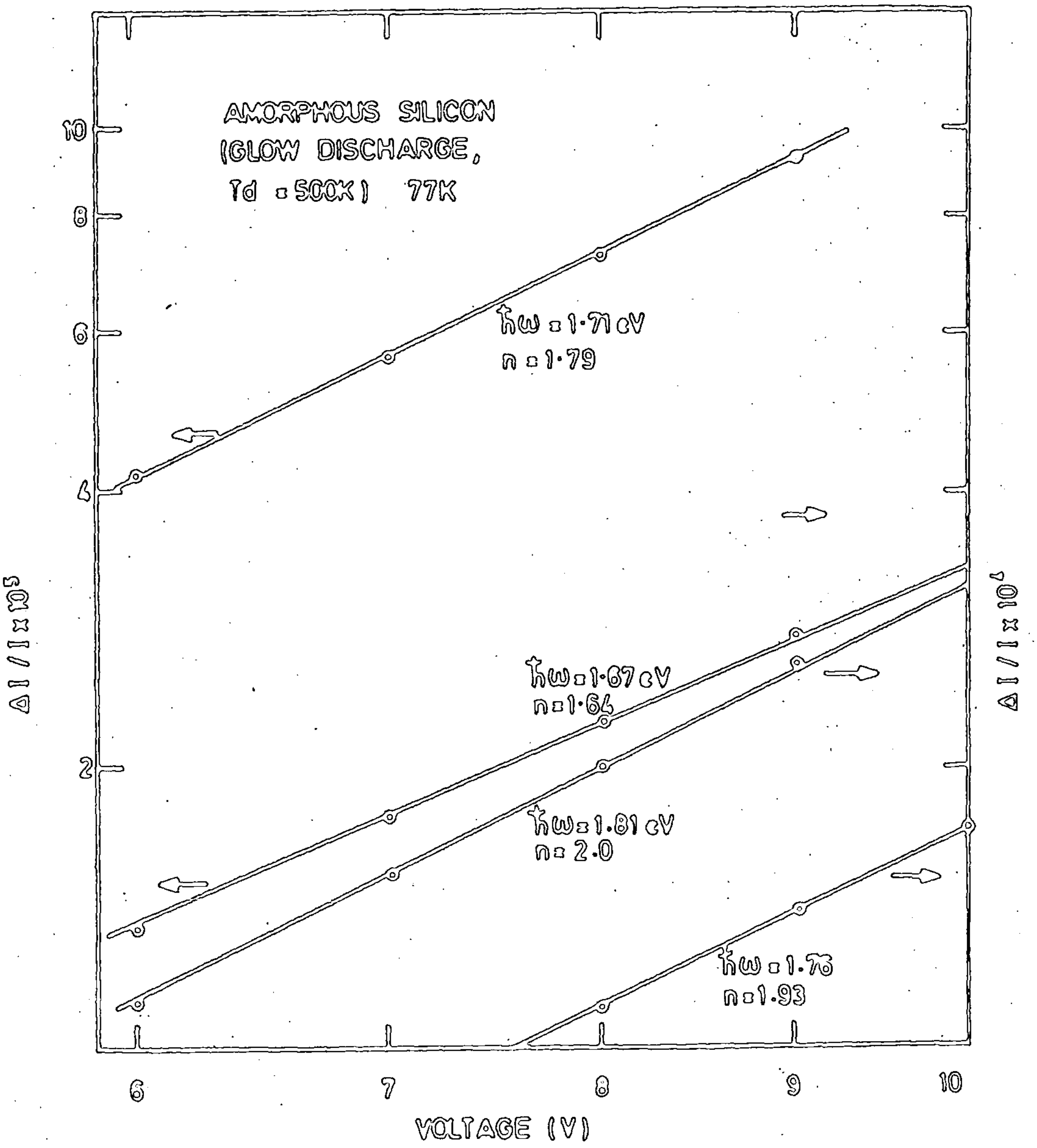

Figure 6.21 : Dependence of the fractional change in transmission of a glow discharge a-Si sample at 77 K on the magnitude of the applied voltage.

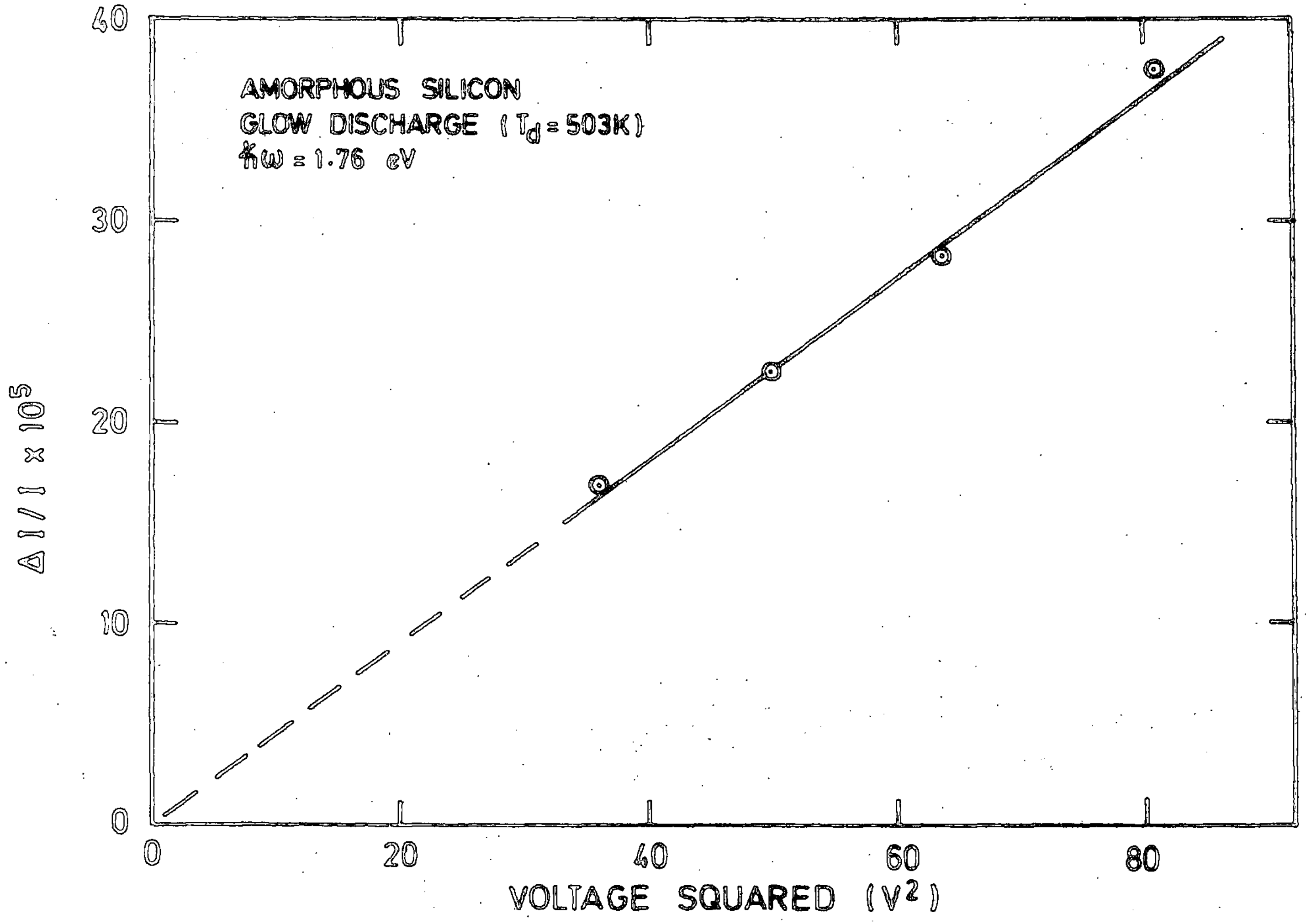

__Figure 6.22__ : Dependence of the fractional change in transmission of a glow discharge α-Si sample at 295 K on the magnitude of the applied voltage.

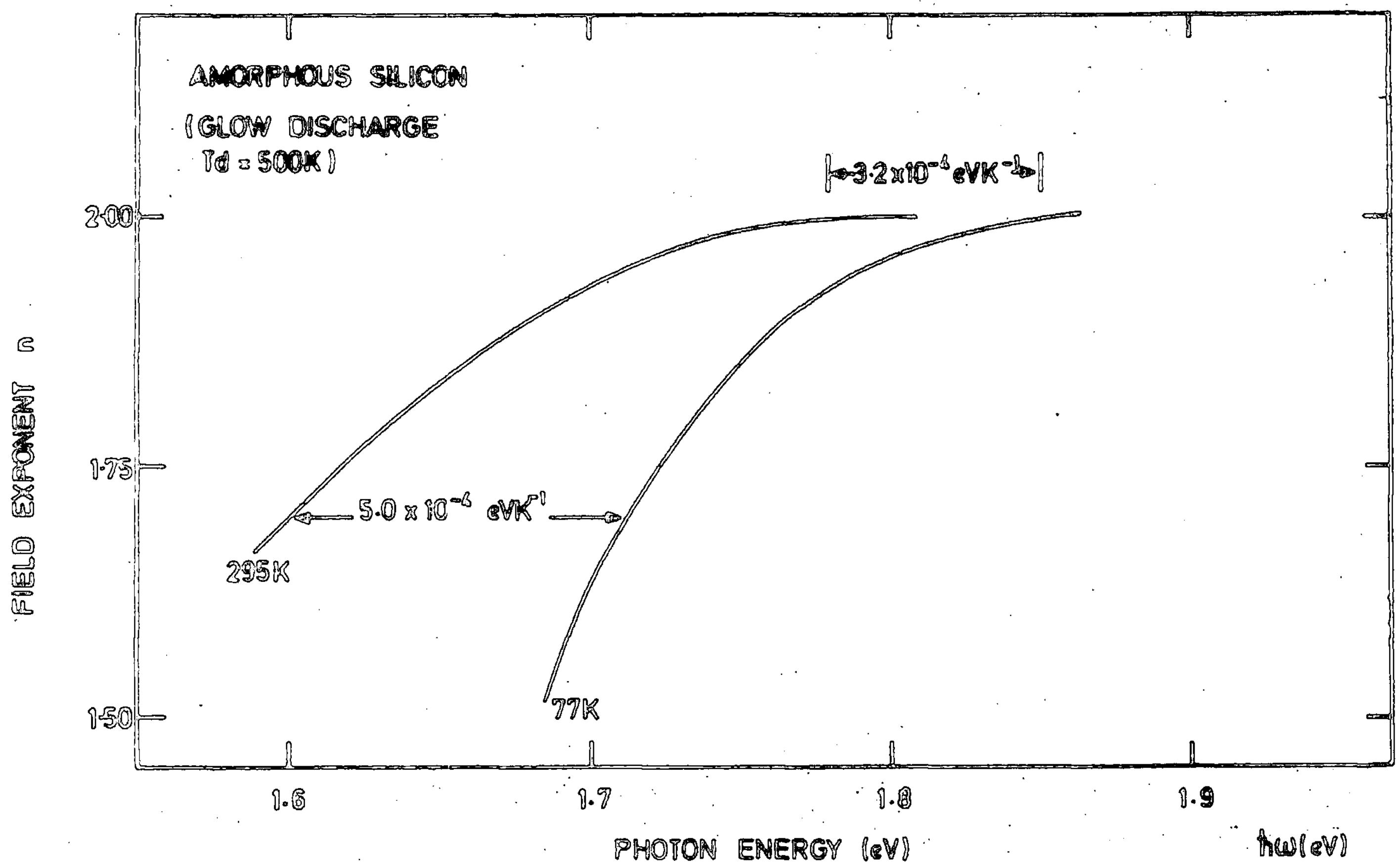

Figure 6.23 : Variation of the field exponent n of an undoped glow discharge α-Si sample at 295 and 77 K, with photon energy.

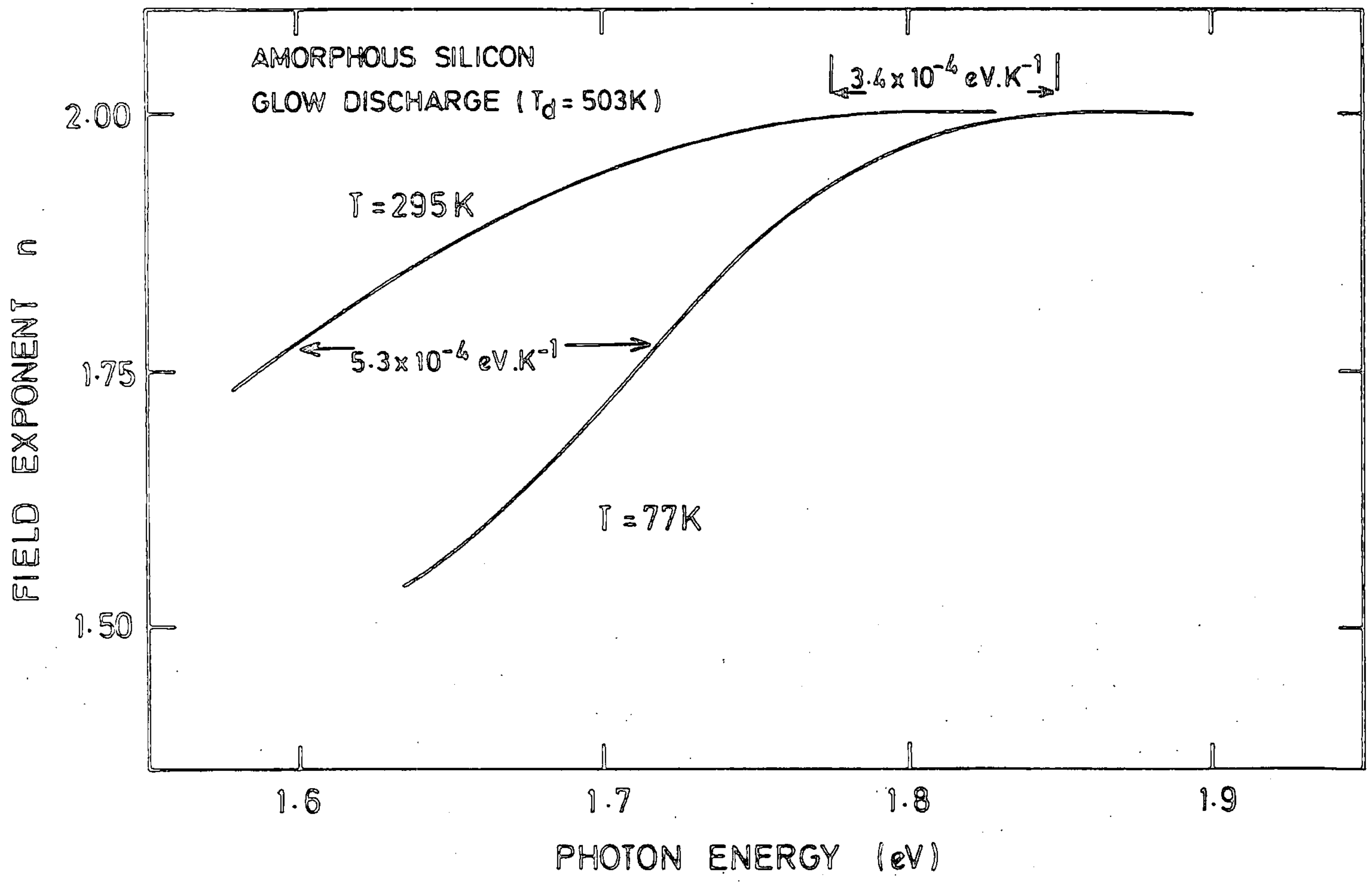

Figure 6.24 : Variation of the field exponent n of a doped glow discharge α-Si sample at 295 and 77 K, with photon energy.

by an internal electric field. A model has been suggested$^{(32)}$ whereby the application of an external electric field is predicted to decrease the slope of the exponential edge further. As a result, a linear decay of the relative change in the absorption coefficient, $\left(\frac{\Delta\alpha}{\alpha}\right)$, with increasing photon energies is expected. For some amorphous systems$^{(33)}$, this prediction is only fulfilled experimentally in the high energy regime of the electroabsorption spectrum where the model should not be valid. In the low energy regime of the electroabsorption spectrum the magnitude of $\left(\frac{\Delta\alpha}{\alpha}\right)$ increases with photon energy. This indicates that the slope of the exponential absorption edge increases with electric field. This behaviour is also observed in our experiments as shown in Figs 6.25 and 6.26 for glow discharge and sputtered films respectively. In both cases the magnitude of $\left(\frac{\Delta\alpha}{\alpha}\right)$ increases linearly with photon energies to a maximum value before decaying linearly towards higher energies.

Because we are dealing with localized states, large transition matrix elements are probable if both the initial and final states do not overlap and therefore an electric field could produce the Stark effect resulting in a red shift of the tail region. This model for an inorganic, amorphous solid, was first proposed by Roberts et al$^{(25)}$ who identified the quadratic Stark effect as the mechanism underlying the optical transition in the presence of an electric field in trigonal selenium. The energy states in this material are localized and the influence of an electric field is to produce the Stark effect. Al-Jalali and Weiser$^{(24)}$ have observed a somewhat similar structure in the electroabsorption spectrum of α-Si to those obtained in our measurements. These authors also attributed their results to the Stark effect. In the case of α-Si, because it does not possess a permanent dipole moment, a quadratic field dependence is to be expected and is in fact observed in our experiments on sputtered films as illustrated in Figs 6.17 to 6.19. Another strong point in favour of the Stark effect interpretation comes when one calculates an effective

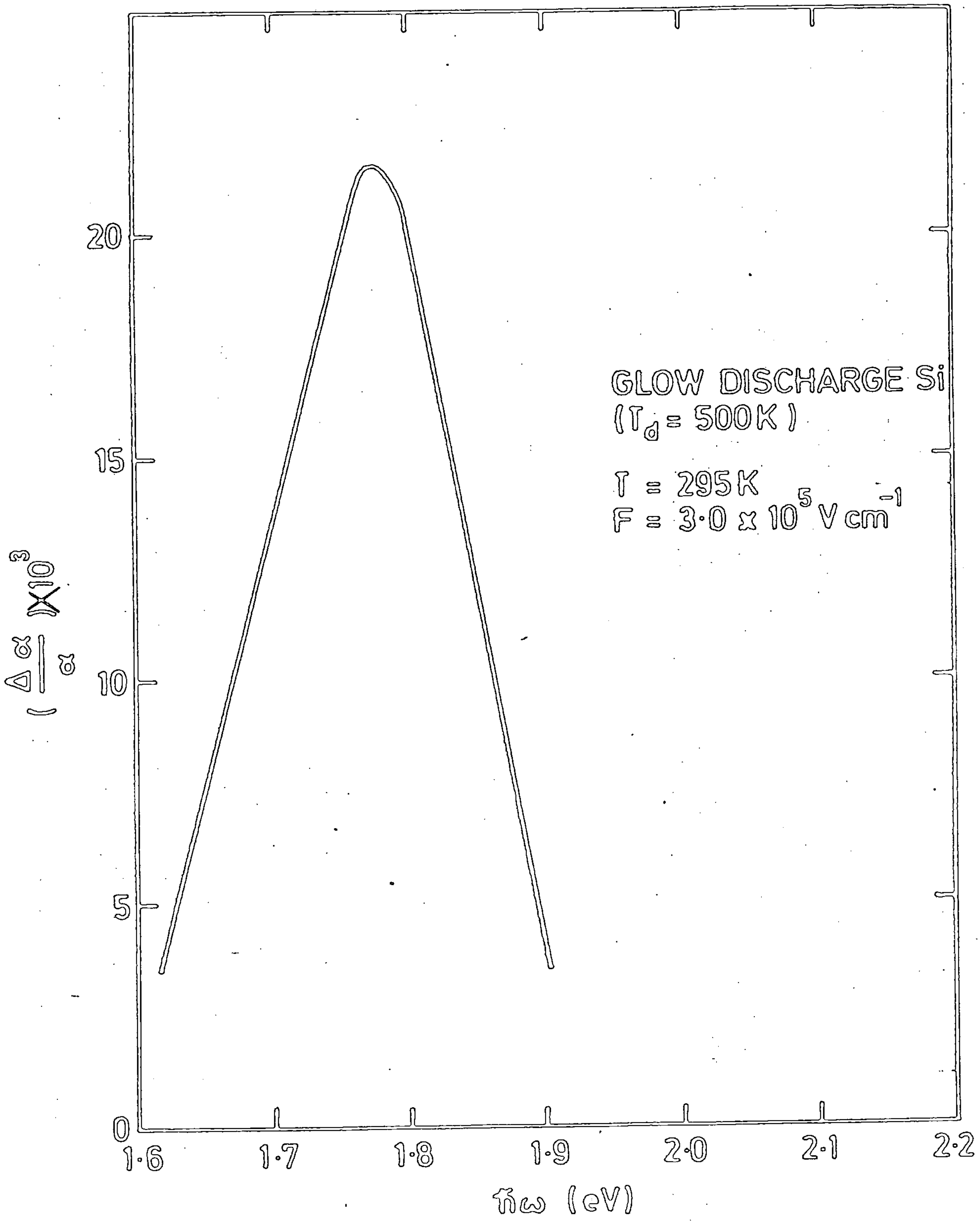

Fig 6.25 : Relative change in absorption coefficient of glow discharge produced α-Si as a function of photon energy.

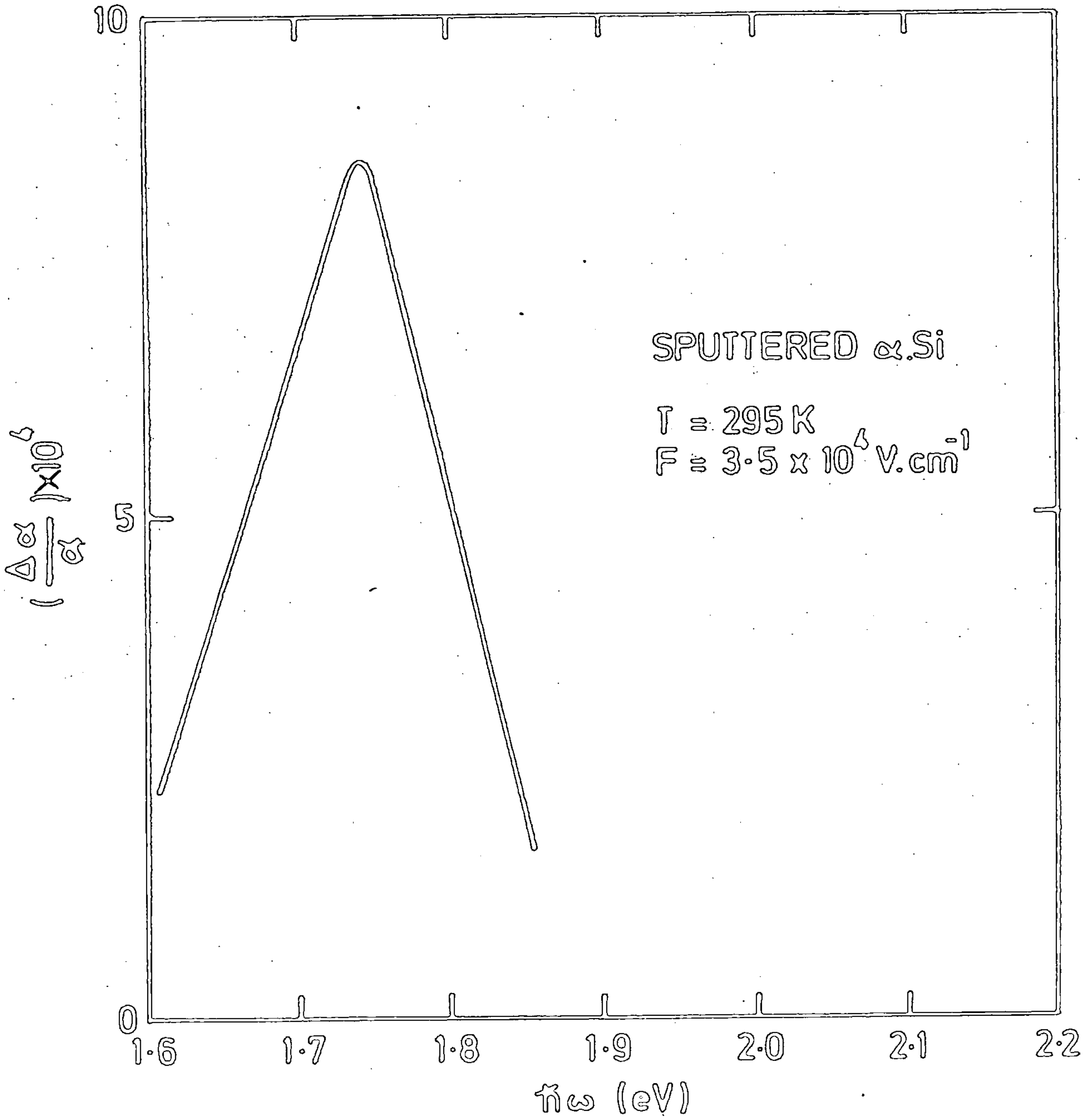

Fig 6.2^6 : Relative change in absorption coefficient of sputtered α-Si as a function of photon energy.

mass on the basis of free electron theory. A large and completely unrealistic value of the reduced effective mass ($\sim 10\ m_o$) is calculated from the data. The Stark effect is smaller for states lying deeper in the energy gap, probably due to a less dense population of those states. The magnitude of $\Delta\alpha$ therefore reduces as one moves towards energies deeper in the tail of localized states.

The decrease which occurs for energies above the peak arises because of the increased delocalization of the states. The lifetime of electrons will begin to be reduced rapidly by scattering due to random potentials that are present in α-Si. In this region of increasing absorption and decreasing localization of energy states, the electroabsorption response is reduced due to lifetime broadening of the states. The peak of the relative change in absorption, $\left(\frac{\Delta\alpha}{\alpha}\right)$, thus marks the energy where this broadening is dominant and indicates the onset of delocalization which increases gradually as evident from the decreasing value of $\left(\frac{\Delta\alpha}{\alpha}\right)$ with photon energies. This argument is strengthened by the fact that this peak coincides with $\hbar\omega_o$; the mobility gap deduced from the quadratic dependence of the absorption coefficient on photon energy.

6.5.1 Glow Discharge Films

A rather different field dependence of the change in absorption, $\Delta\alpha$, is observed in glow discharge produced α-Si as shown in Figs 6.23 and 6.24. For the glow discharge samples, a quadratic field dependence is observed only at the peak energy of the electroabsorption spectrum. At lower energies the signal increases more slowly with electric field as evident from the decreasing value of $n(< 2)$.

In general, the optical and electrical properties of glow discharge produced α-Si are different to those of sputtered films. The differences are thought to be due to the presence of hydrogen(34), the incorporation of which serves to neutralize the role of dangling bonds. Spear et al(10) believe that these differences are associated with the particular nature of the deposition process. Even though the diffraction pattern indicates that the glow discharge and sputtered films used in our measurements are in amorphous form, their states in the gap could be different. Both films exhibit band tailing, the amount of which will influence the field broadening of the absorption edge. A large density of states is also observed in glow discharge α-Si. The overlap between these states will reduce the transition matrix elements involved. An important difference between the sputtered and glow discharge films used in our measurements is that Langmuir-Blodgett film deposition is effective only on glow discharge samples but not on sputtered films. A subtle difference in the field dependence of the electroabsorption signal of sputtered and glow discharge films is therefore not entirely unexpected. The quadratic field dependence of the change in absorption, $\Delta\alpha$, is observed for sputtered α-Si. For glow discharge produced α-Si ; $\Delta\alpha$ is proportional to F^n (F is the electric field). The value of n depends on the photon energy considered ; n equals 2 at the energy corresponding to the peak of the electroabsorption spectrum and less than 2 at lower energies. In an attempt to understand this phenomenon, two explanations are put forward.

A. The Stark Effect

The quadratic Stark effect is observed at the peak of the electroabsorption spectrum. This material exhibits band tailing and transitions between these states are believed to be responsible for the Stark effect. The magnitude of this effect is however reduced for states deeper in the gap, in the region where $n < 2$. A large electric field could reduce the degree of localization of these states, and thus reduce the transition matrix elements involved. This process appears to be more effective at lower temperatures as indicated by a more drastic decrease in the value of n at 77 K ; this leads to a larger temperature coefficient than the one deduced at the peak of the electroabsorption spectrum. This is probably attributable to a change in the population of the tail states with temperature. The lower density of electrons at low temperatures results in a decrease in the value of n over a smaller energy range (see Figs 6.23 and 6.24).

The temperature coefficient of the energy shift, $\left(\frac{\Delta E}{\Delta T}\right)$, depends somewhat on the value of n. At the peak position where n takes the value 2, $\left(\frac{\Delta E}{\Delta T}\right) \sim 3.0 \times 10^{-4}$ eV.K^{-1} corresponding to the temperature shift of the absorption edge. However at n = 1.7, for example, $\left(\frac{\Delta E}{\Delta T}\right)$ is significantly larger and reaches the value 5.0×10^{-4} eV.K^{-1}. A large temperature shift at the onset of the photoconduction in glow discharge produced α-Si has also been observed by Spear et al$^{(18)}$. This can be explained if it is assumed, in addition to the widening of E_g with decreasing temperature as a result of electron-phonon interaction and dilation as in the crystalline phase, that the position of the mobility edge is also temperature dependent. The observed temperature shift is thus the resultant of the shift in the mobility edge and the shift due to the electron-phonon interaction and dilation. It is still not clear whether the large temperature coefficient observed independently at the onset of the photoconduction is related to those obtained from electroabsorption measurements. The phenomenon, however, suggests further that the behaviour of glow discharge as well as sputtered α-Si is controlled mainly by its localized states.

B. Mixed Response

An alternative explanation is that the observed electroabsorption signal is a mixture of the Franz-Keldysh and Stark effects. That is, where the slope is accurately 2 the Stark effect is completely dominant. However, increased delocalization in glow discharge produced samples, produces a small but measurable Franz-Keldysh effect, $\left(\frac{\Delta I}{I}\right)^{\prime\prime}$. The magnitude of the Stark effect is estimated by using data extrapolated from the energy range where this effect is observed experimentally. In this region, the observed $\left(\frac{\Delta I}{I}\right)$ is plotted against V^2 (V is the applied voltage) at a certain photon energy. The gradient of this curve, G, depends linearly on photon energy as shown in Fig 6.27. The magnitude of the Stark effect is therefore GV^2; a relationship we assume to be also correct at low energies. The magnitude of the Franz-Keldysh effect may then be found by using the following equation, namely $\left(\frac{\Delta I}{I}\right)^{0} = \left(\frac{\Delta I}{I}\right) - GV^2$. An attempt was made to fit the resulting Franz-Keldysh effect component to the free electron theory described in section 2.5. It was found that this component varies as the four-thirds of the electric field as shown in Fig 6.28 ; the equivalent effect to that which is obtained for indirect transitions in a free electron framework. However, it is not clear whether phonons are involved in the transition at these energies. Another hindrance is that the straight lines do not extrapolate to the origin.

At this stage, there is no conclusive explanation as to which mechanism is responsible for the slight perturbation to the optical absorption described above. Data from doped samples are very similar to those obtained from undoped samples suggesting that doping is not responsible for the change. However it is interesting to note that electroabsorption results (planar geometry) on glow discharge produced α-Si reported by Al-Jalali and Weiser(24) show that the electroabsorption response increases quadratically with electric field. Detailed studies on the field dependence of the electroabsorption response obtained from sputtered and glow discharge α-Si samples (sandwich structure) indicate that a subtle difference is observed. The results are presented for the first time here, and are interpreted mainly in terms of the Stark effect.

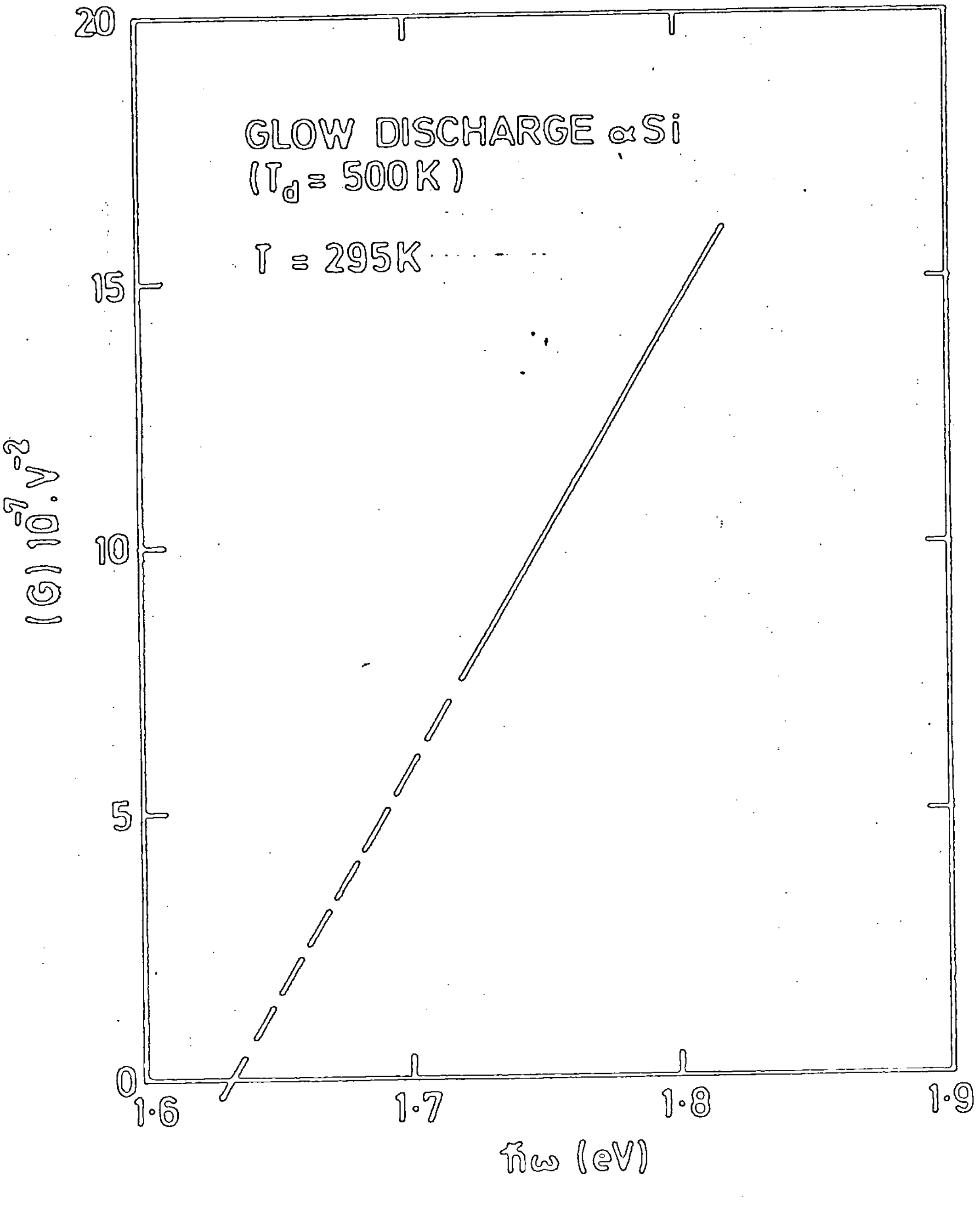

Fig 6.27 : Linear dependence of G on photon energy.

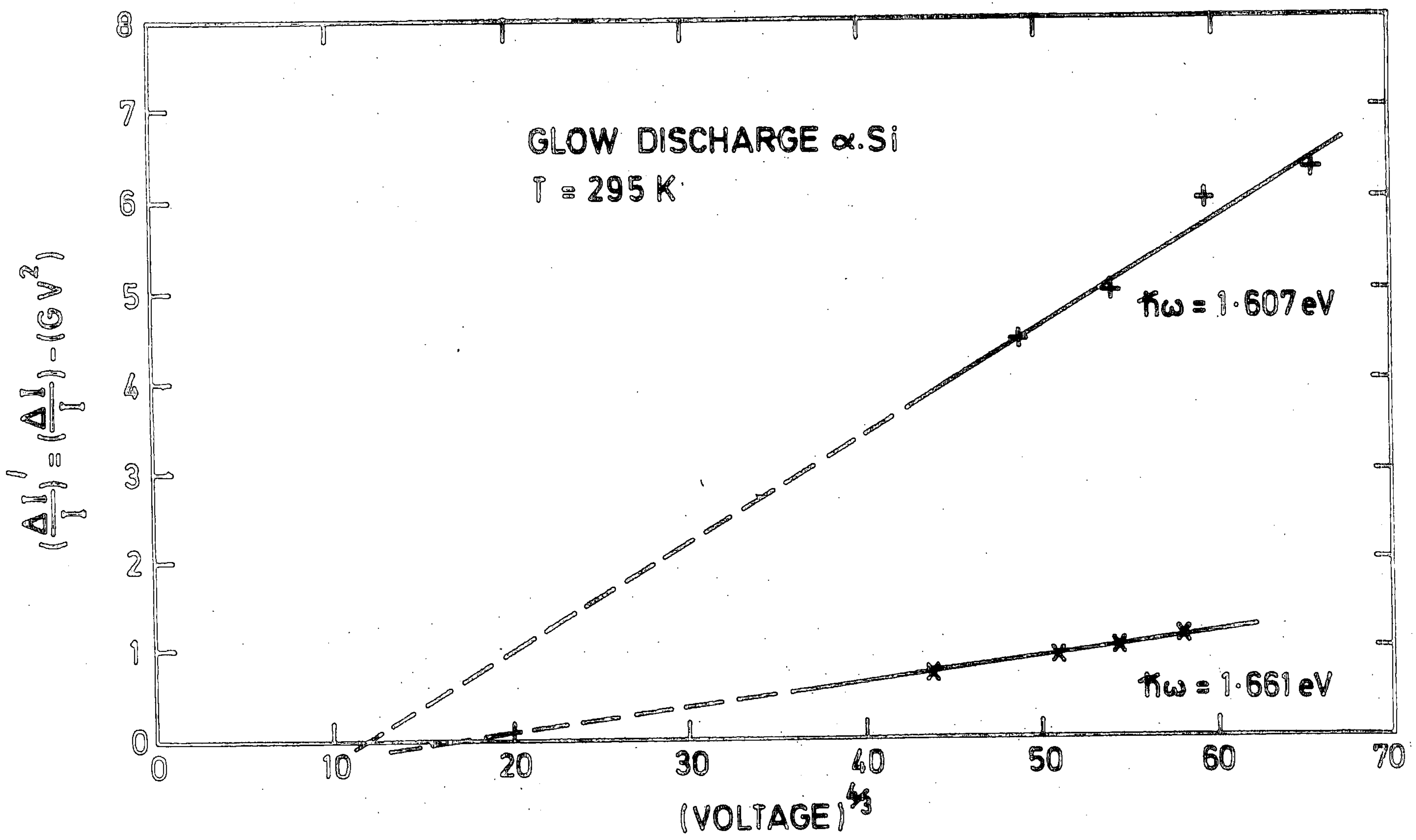

Fig 6.28 : Four-thirds dependence of the Franz-Keldysh effect component on the applied voltage.

CHAPTER 7

ELECTROABSORPTION STUDIES IN DIACETYLENE LANGMUIR FILMS

7.1 INTRODUCTION

Progress in the preparation technique of Langmuir-Blodgett 'built-up' organic multilayers has stimulated research towards further basic studies and possible technological applications of organic thin films. This technique can be used to prepare thin films by depositing a series of monolayers of a suitable organic material, with each monolayer being deposited upon the previous layer until the required thickness is reached. Provided certain conditions are carefully controlled, ordered Langmuir monomolecular layers can be obtained whose optical and electrical properties may be extremely useful.

The thinness and perfection of films of conventional Langmuir-Blodgett material coupled with their excellent insulating qualities can be capitalised upon in producing MIS transistors(1) and photovoltaic structures(2). For a review of the possible technological applications of Langmuir films, the reader is referred to a recent article by Vincett and Roberts(3). The films commonly used as dielectrics in these devices, however, have quite low melting point and therefore are unlikely to form the basis of practical devices. Work is currently in progress in the Applied Physics and Electronics Department at the University of Durham towards producing more stable materials, in particular suitably substituted diacetylenes(4). The diacetylene Langmuir films are produced in monomer form and then polymerized on the substrate using ultra-violet light. Two forms of polymer namely, 'blue' and 'red' forms are produced depending on the length of exposure time to ultra-violet light. The blue form which is obtained after a short exposure time will gradually transform to the red form as the exposure time is increased. The main objective of the work presented in this chapter is to investigate this interesting characteristic using electroabsorption technique. The thinness and excellent insulating properties of this film enable electroabsorption measurements to be performed. However, due to a limited time, only preliminary results are presented in this chapter after a description of the production of Langmuir films.

7.2 PREPARATION OF LANGMUIR FILMS

Langmuir films are prepared by depositing a small quantity of a solution of a suitable organic material onto a liquid surface, waiting for the solvent to evaporate and then compressing the monomolecular layer so produced until it forms a quasi-solid one molecule thick. The container which holds the liquid subphase upon which the monolayer floats is termed a Langmuir trough. In order to remove monolayers from the subphase (usually purified water), a suitable substrate is dipped through the quasi-solid and then removed. Provided certain stringent requirements have been met, one monolayer is transferred to the substrate during this process. An organic multilayer with high degree of structural perfection is assembled by repeatedly dipping the substrate through the subphase. Using this method, Langmuir films may be built up from an initial thickness of approximately 1.2 nm to depths in excess of one millimetre. Fig 7.1 illustrates the deposition process of the multilayers. Even though the method is simple in principle, a clean environment and great attention to experimental detail are essential in order to produce well ordered layers which are structurally stable. Furthermore, only a limited range of organic materials can be formed into Langmuir film multilayers. Both these points are discussed in the following sections.

7.2.1 Suitable Material for Langmuir Films

Various materials have been deposited using the Langmuir technique; these materials must possess both a hydrophobic and hydrophilic component (5)

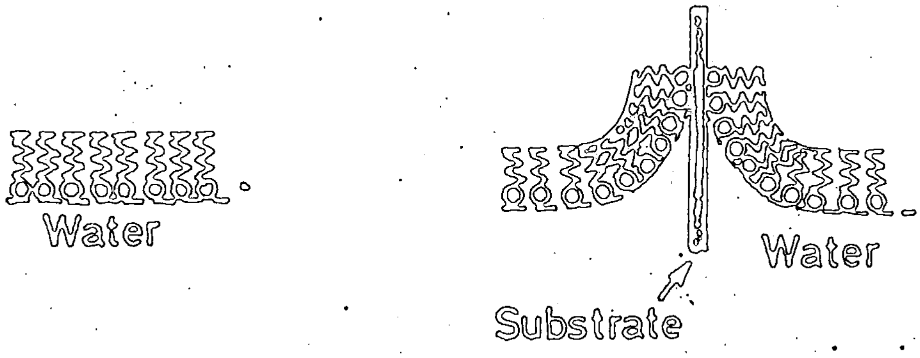

(a) Monolayer on the surface of the water.

(b) First layer on withdrawal.

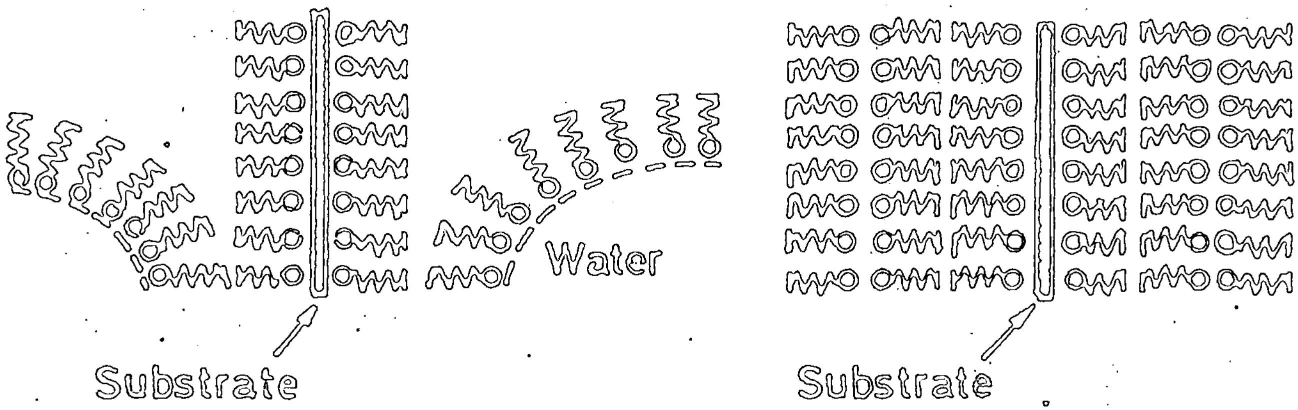

(c) Second layer (2nd Insertion)

(d) Slide with three layers (after 2nd Removal)

Figure 7.1 : Illustration of the build-up of a multilayer film from a Langmuir trough.

Furthermore to obtain multilayers as opposed to a monolayer, the hydrophilic group must normally be quite strong. An aliphatic side-chain is normally used as the hydrophobic part of the molecule. In order to avoid excessive water-solubility, the aliphatic component must also be quite large. Accordingly, suitable molecules generally contain one or more long (approximately 18 carbon) aliphatic hydrocarbon chains. Material such as fatty acids(5) whose structure is illustrated in Fig 7.2 satisfy these requirements.

The scope of the technique has also been considerably widened by the demonstration(6) that aromatic molecules with their extended π-electron orbitals can be handled on the Langmuir trough. These molecules, however, like the fatty acid salts cannot withstand temperatures in excess of a hundred degrees. Therefore, Langmuir films with greater thermal stability are required for the purpose of practical devices. One candidate is suitably substituted diacetylenes, monomer films so produced can readily be polymerized(7,8) under ultra-violet light to form chains containing conjugated double and triple bonds. Polymerisation does not destroy the layered structure of the films, which are temperature stable up to 230° C(4). The monomeric and polymeric forms of this material (abbreviated 12-8 diacetylene) are shown in Fig 7.3. It will be seen that the end groups of the monomer become the side groups of the polymer and therefore play a vital role in packing the monomeric units into a reactive configuration.

7.2.2 Preparation of Diacetylene Langmuir Films

The Langmuir trough for the deposition of the organic monolayers is normally kept in a very clean, dust free environment, and must be situated on an antivibration table. The area within which the solution containing suitable organic material is deposited, is defined by a constant perimeter PTFE coated glass fibre barrier system. The schematic diagram of the trough is shown in Fig 7.4.

The substituted diacetylene monomer (synthesized by Dr.D.Bloor,

FATTY ACID SALTS

$$[CH_3(CH_2)_{n-2}COO^-]_2\,Cd^{2+}$$

n = 18 CADMIUM STEARATE

n = 20 CADMIUM ARACHIDATE

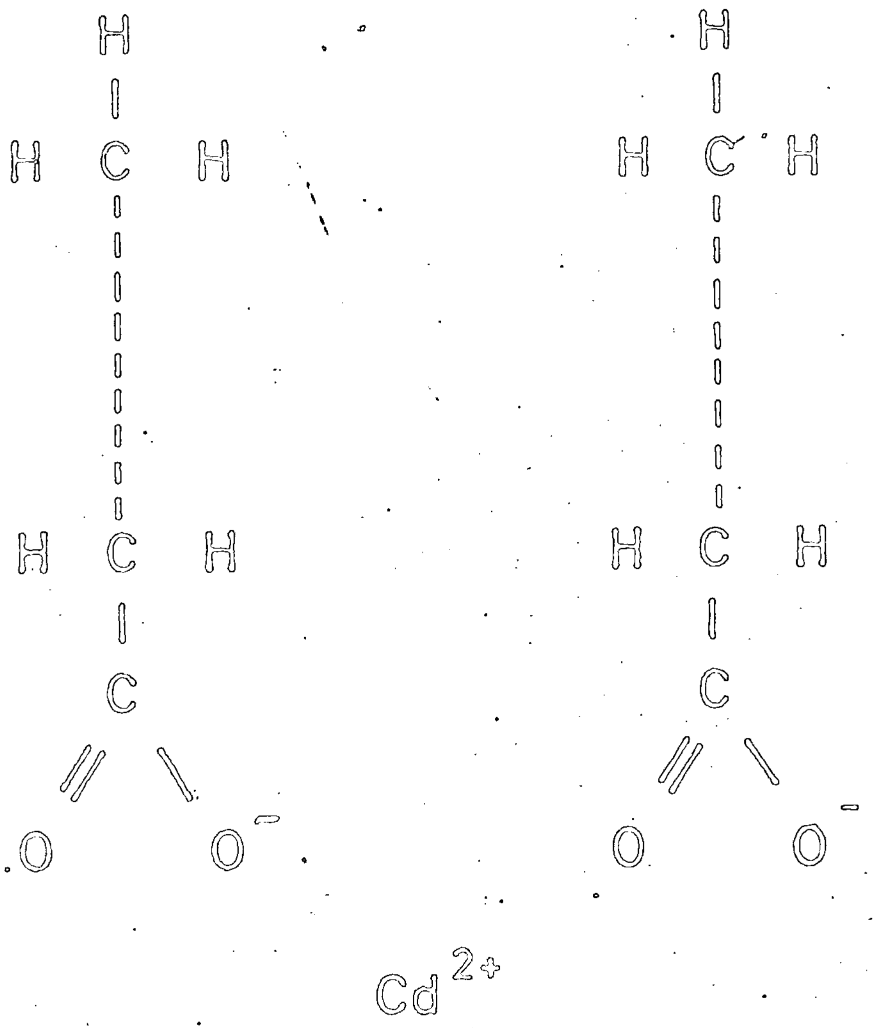

<u>Figure 7.2</u> : Structure of long-chain fatty acid salts showing the hydrophilic carboxyl (COOH) and hydrophobic components.

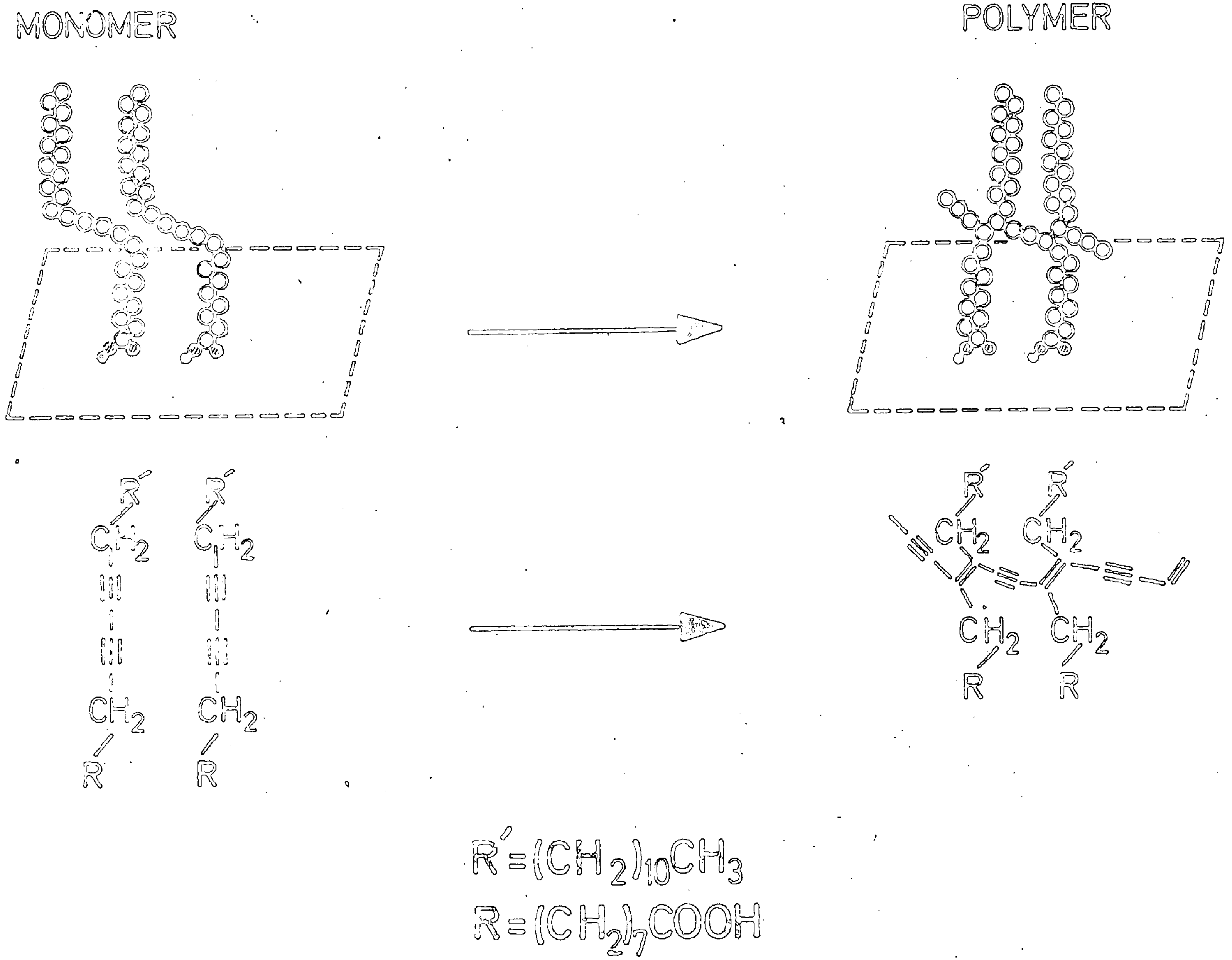

Figure 7.3 : Schematic diagram illustrating the formation of diacetylene Langmuir film polymer produced by UV irradiation on the monomer.

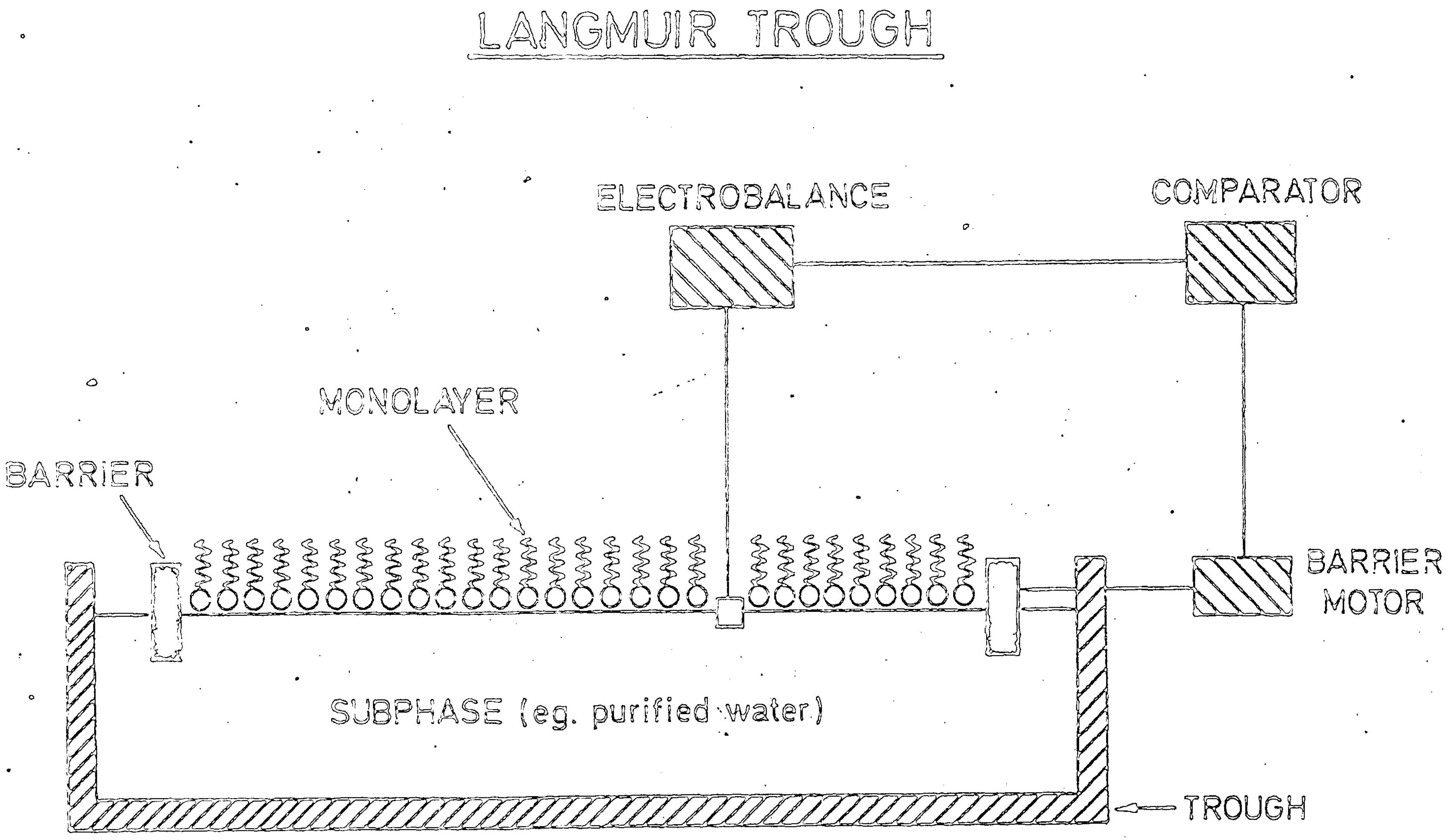

Figure 7.4 : Schematic diagram showing the main components of the Langmuir trough.

Q.M.C, London) was dissolved in chloroform and spread onto the surface of water obtained from a millipore 'Milli-Q' purification system. This aqueous subphase contained 2.5×10^{-4} M $CdCl_2$ and its pH at 17° C was adjusted to be in the range 6.2 to 6.4. In order to investigate the structure of the monolayer and establish optimum dipping conditions, isotherms must be recorded. These were achieved by compressing the monolayer at a constant rate and recording the surface pressure and area on an X-Y chart recorder. Such an isotherm is shown in Fig 7.5. There are three distinct regions to the curve corresponding to the different phases that the films can be in. In region A, the molecules are spread out corresponding to a gas phase ; some of the upright molecules in this phase tend to bend over due to the relatively large amount of surface available for them. Compression of the film decreases the surface area per molecule until eventually a quasi-solid is formed where the molecules are upright. This phase indicated by region B corresponds to the steeply rising part of the curve. A liquid phase occurs in region C, the transition from region A to B. Further increase in the surface pressure simply makes the film more compact, until finally at the top of the curve the monolayer collapses. It is best to dip a film at a pressure corresponding to the quasi-solid region ; in the main, we used a pressure of 15 $dynes.cm^{-1}$.

The compression process is achieved by means of a motor driven barrier system ; this system is coupled to a micro-balance which continuously monitors the surface pressure via a sensor in the liquid surface. The differential feedback system is capable of carefully maintaining the monolayers at a desired surface pressure which is of particular importance when dipping is in progress and molecules are being removed from the subphase. The films were dry when they emerged from the subphase and the process of deposition was monitored through the recorded values of the area and pressure. After the monomer monolayers had been deposited, the film was immediately polymerized by exposure to an intense 300 nm ultra-violet source. The films

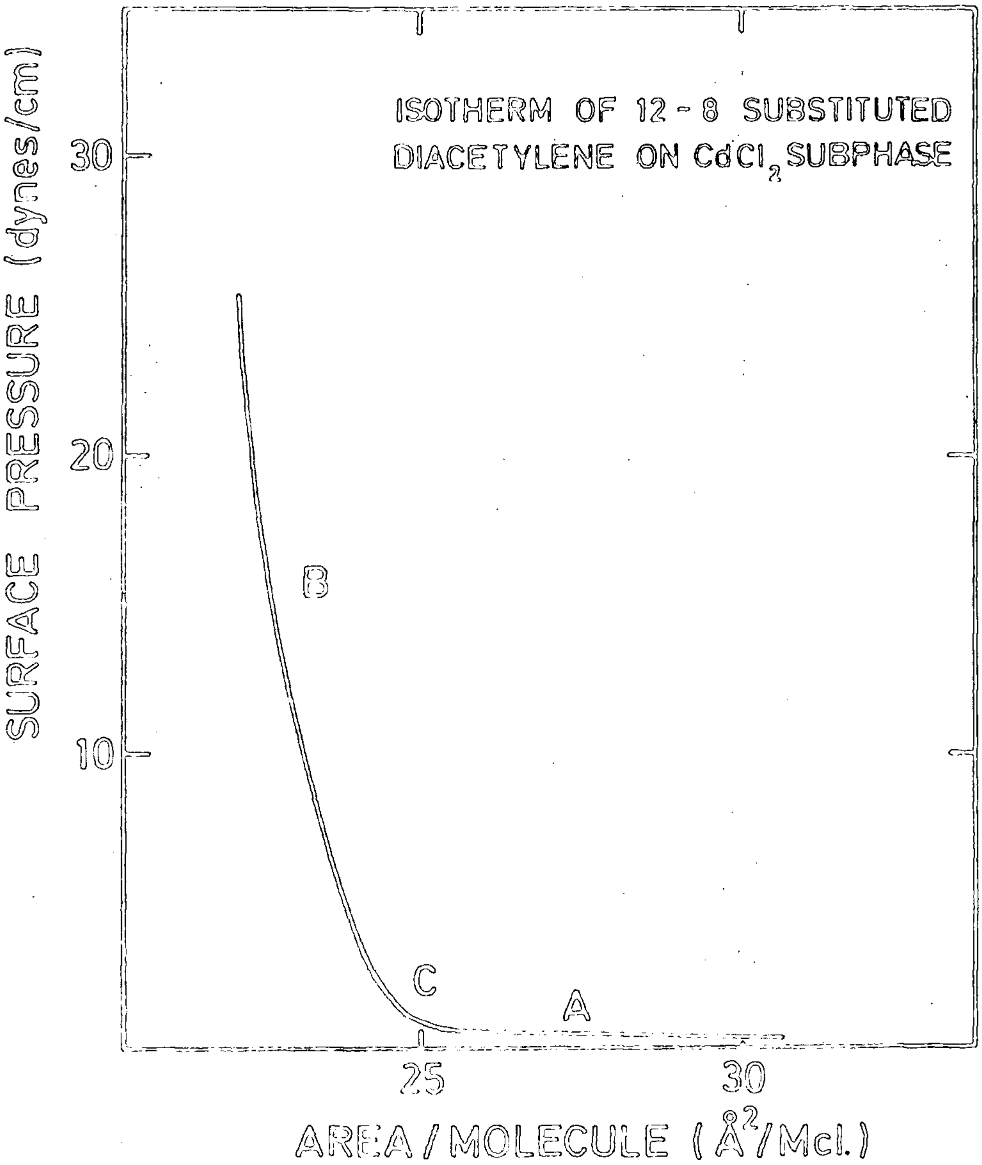

Figure 7.5 : Surface pressure - area isotherm obtained on (12-8) substituted diacetylene on $CdCl_2$ subphase.

were stored under dry nitrogen in a desiccator for three days before top contact were made. The metal (usually gold) evaporation onto the film was best done whilst the film was cooled using liquid nitrogen. Graphite water based paste was normally used for an electrical contact to the gold electrode.

7.2.3 Electrical Characteristics of Langmuir Films

The most commonly studied materials(9-11) are multi-layers of the fatty acid family, in particular its Cd salts, cadmium arachidate, cadmium stearate and cadmium palmitate. They have been studied in two forms : sandwiched between evaporated metals (MIM) or deposited on a semiconducting surface (MIS). The general conclusion is that the fatty acid Langmuir films are good insulators with dielectric strengths greater than 10^6 V.cm^{-1}. Polymeric materials are relatively new and their characterisation is less complete. However, d.c. measurements(4) indicate that polymerized diacetylene Langmuir films are very resistive with $\rho \sim 4 \times 10^{11}$ Ohm.cm at a field strength 5×10^5 V.cm^{-1}. A barrier limtied conduction process (Poole-Frenkel effect) has been inferred in this material from linear plots of log current versus square root of voltage which are independent of electrode polarity. The capacitance displays virtually no dispersion throughout the frequency range 70 Hz to 100 kHz, while the conductance varies according to the equation $G \alpha \omega^n$ with n of the order of unity signifying good insulator properties.

7.2.4 Diacetylene

In a form other than a Langmuir film,namely polydiacetylene single crystal, it consists of parallel chains of molecules with a backbone of conjugated single, double, and triple bonds. The strong interaction along the chain together with the small length of the repeat unit suggests some delocalization of electron along the polymer chain. These states were indeed observed utilizing the electric field effect on the reflectance (electroreflectance) in this material(12) and the onset of an interband type transition was observed at 2.44 eV

The polymer chains of polymerized diacetylene Langmuir films also consist of double and triple bonds which contribute the π-electrons along its backbone. It is therefore interesting to study whether delocalization also occurs in this material. Electroabsorption measurements should be able to establish whether this characteristic is also present in polymerized diacetylene Langmuir films.

7.3 EXPERIMENTAL RESULTS

The diacetylene Langmuir film polymer was prepared in the following manner. The monomer monolayers which were deposited onto quartz or glass slide substrates were immediately polymerized by exposure to an intense 300 nm ultra-violet source. Two forms of polymer were produced depending on the length of exposure time to ultra-violet light. After about one minute the colourless monomer turned to a 'blue' polymerised film. The absorption spectrum of the blue form polymer for 31 monolayers (the thickness of each monolayer is 3.3 nm(4)) recorded at room temperature is shown in Fig 7.6. For comparison, the absorption spectrum of a diacetylene monomer(8) is also shown in the figure. The monomer shows strong absorption in the ultra-violet region and displays no structure in the visible range. By contrast, the blue form polymer absorption is characterised by two broad peaks at 635 and 565 nm. This spectrum is similar to that reported by Tieke et al(8). This characteristic bluish colour has also been observed after solid state polymerisation of a number of other diacetylenes(13).

The polymerisation process is illustrated in Fig 7.3, the polymer chains consist of double and triple bonds which contribute the π-electrons along the backbone of this polymer. The blue form is due to active carbene chain ends in the polymerised diacetylene(8), the presence of which has been well established by ESR-spectroscopy(14,15).

A gradual change in colour with increasing exposure time occurs during polymerisation. The blue form eventually changes to a 'red' form after exposure for more than 5 minutes. The absorption spectra at two

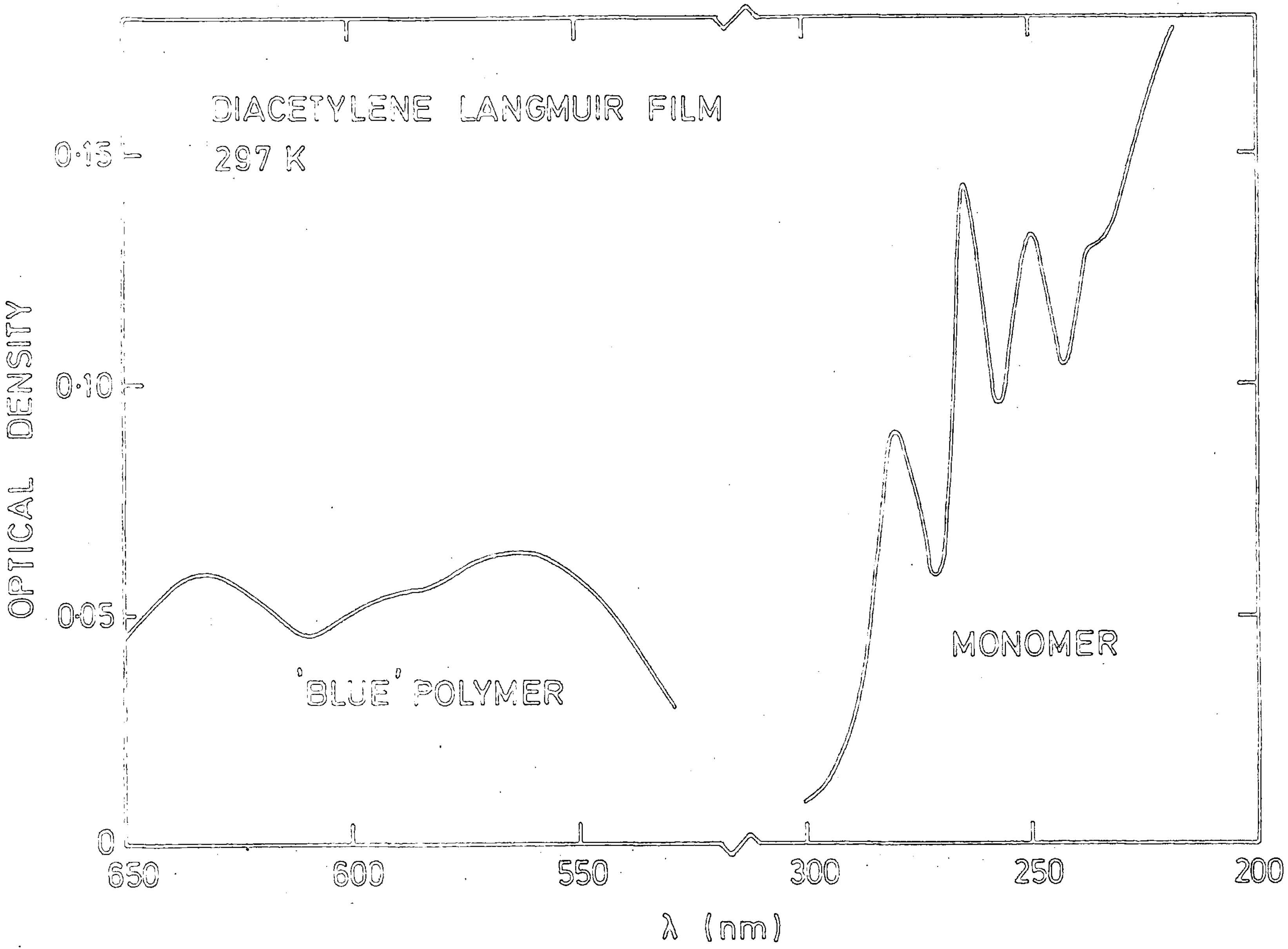

Figure 7.6 : Optical density of the blue form of polymerised diacetylene Langmuir film at 295 K, as a function of photon energy. For comparison, the optical density of a diacetylene monomer (8) is also shown.

different temperatures of the red polymer obtained after exposing 31 monolayers to ultra-violet radiation for about 15 minutes are shown in Fig 7.7. At room temperature, the spectrum is characterised by two peaks at about 535 and 500 nm. The blue peaks do not entirely disappear ; their magnitudes, however, are significantly smaller. This suggests that a small proportion of the blue form is still present. The spectrum is shifted by about 15 nm on cooling to 77 K. In addition,while the long wavelength of the red characteristic peak decreases, the short wavelength peak increases in intensity with decreasing temperature.

It has been suggested(8) that carbene chain ends in the blue form polymer can be destroyed thermally or by adding a swelling agent such as ethanol or chloroform ; the distorted polymer then can react with a neighbouring monomer to form cyclopropene which dominates the red polymer. It is therefore most likely that overexposure of the blue form polymer to ultra-violet light leads to a similar reaction producing the red form of polymerised diacetylene.

7.3.1 Electroabsorption

The main objective of the work reported in this chapter was the study of the effect of a large electric field on the optical absorption properties of the various form of diacetylene Langmuir film polymer. Limited time, however, allowed only detailed investigation of the red polymer form.

The electroabsorption measurements were performed on a sandwich structure sample so that the applied electric field was parallel to the polymer chain. A second harmonic (2f) signal was detected when the sinusoidal electric field was applied across the sample at a frequency of 3.0 kHz. This procedure was chosen to eliminate any effects due to polarisation of the specimen, as previously discussed in Chapter 4 for CdTe : Cl.

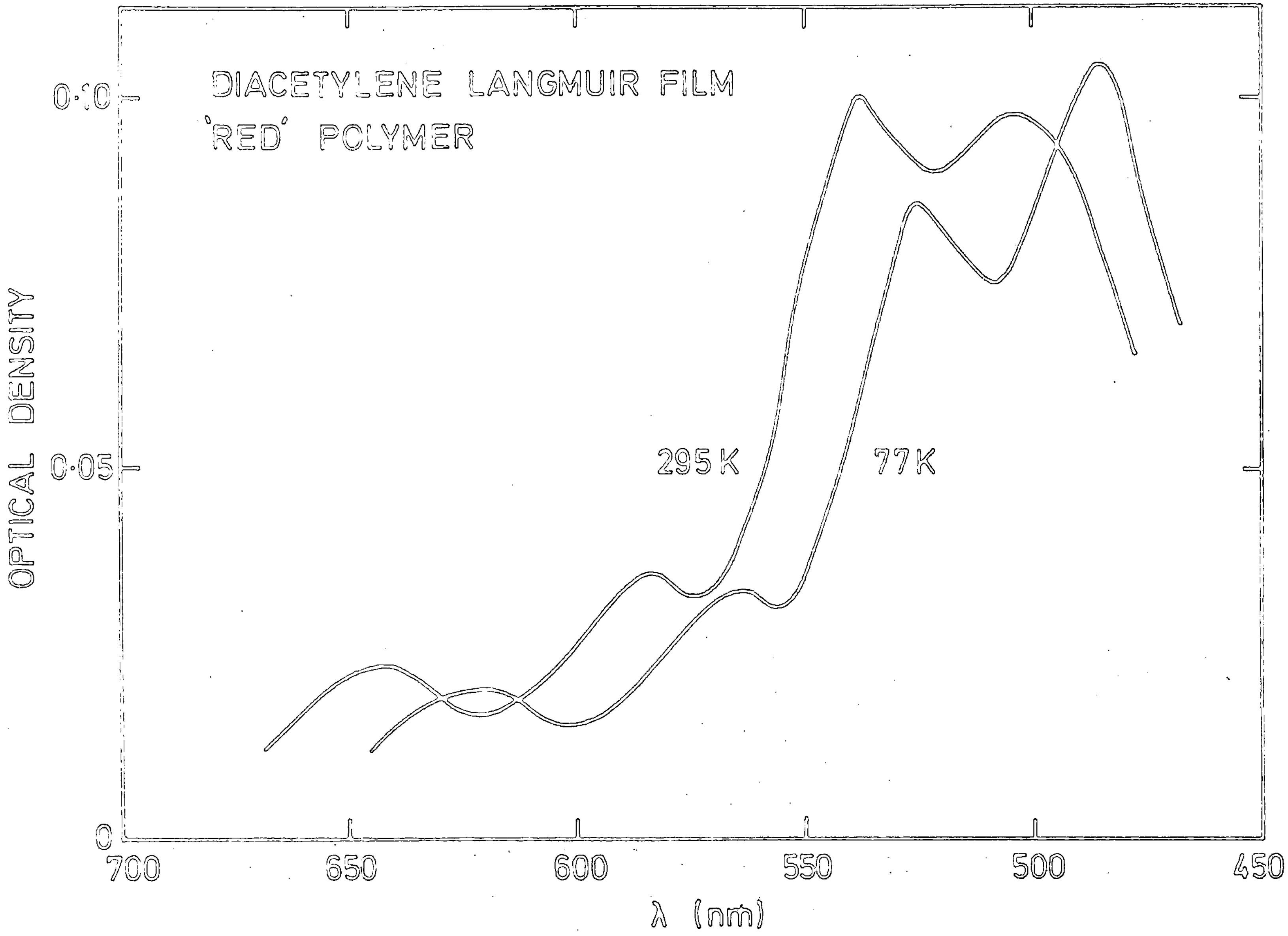

<u>Figure 7.7</u> : Optical density of the red polymerised diacetylene Langmuir film at 295 and 77 K, as a function of photon energy.

Fig 7.8 displays the electroabsorption spectrum obtained at room temperature from a 31 monolayer thick red form polymerised diacetylene film. This spectrum is entirely different from that observed in a polydiacetylene single crystal$^{(12)}$. The magnitude of the relative change in transmission $\Delta I/I$, is of the order of 10^{-6} (corresponding to a change in absorption of 1 part in 10^5) at a field strength of 10^5 V.cm^{-1}. This small signal is typical for organic materials where the Stark effect is expected to be the dominant electroabsorption mechanism. The electroabsorption spectrum approximates to the first derivative of the optical absorption spectrum in the range 530 to 585 nm. However, real and detectable differences are evident upon closer inspection of the curves. The cause is not fully understood. However, there is evidence of hidden structure in the absorption curves and their origin is also probably responsible for the observed differences.

The above characteristics were also observed at 77 K as shown in Fig 7.9. The spectrum is similar in structure and the peak magnitudes are similar to those recorded at room temperature. However, the spectra are shifted towards higher energies by about 15 nm corresponding to the shift in the absorption spectrum at this temperature.

At both temperatures, the magnitude of the electroabsorption response increase quadratically with electric field. Fig 7.10 illustrates this quadratic field dependence at room temperature. The fact that the straight line extrapolates to the origin, as shown in Fig 7.11, indicates the absence of space charge complications in these measurements.

7.3.2 Discussion of Results

Despite similarities in the structure of the polydiacetylene single crystal and the polymerised diacetylene Langmuir film, their optical transitions may respond differently to an external electric field. The electro-reflectance and electroabsorption spectra of the polydiacetylene single crystal suggest strongly that the π-electron states of the chain

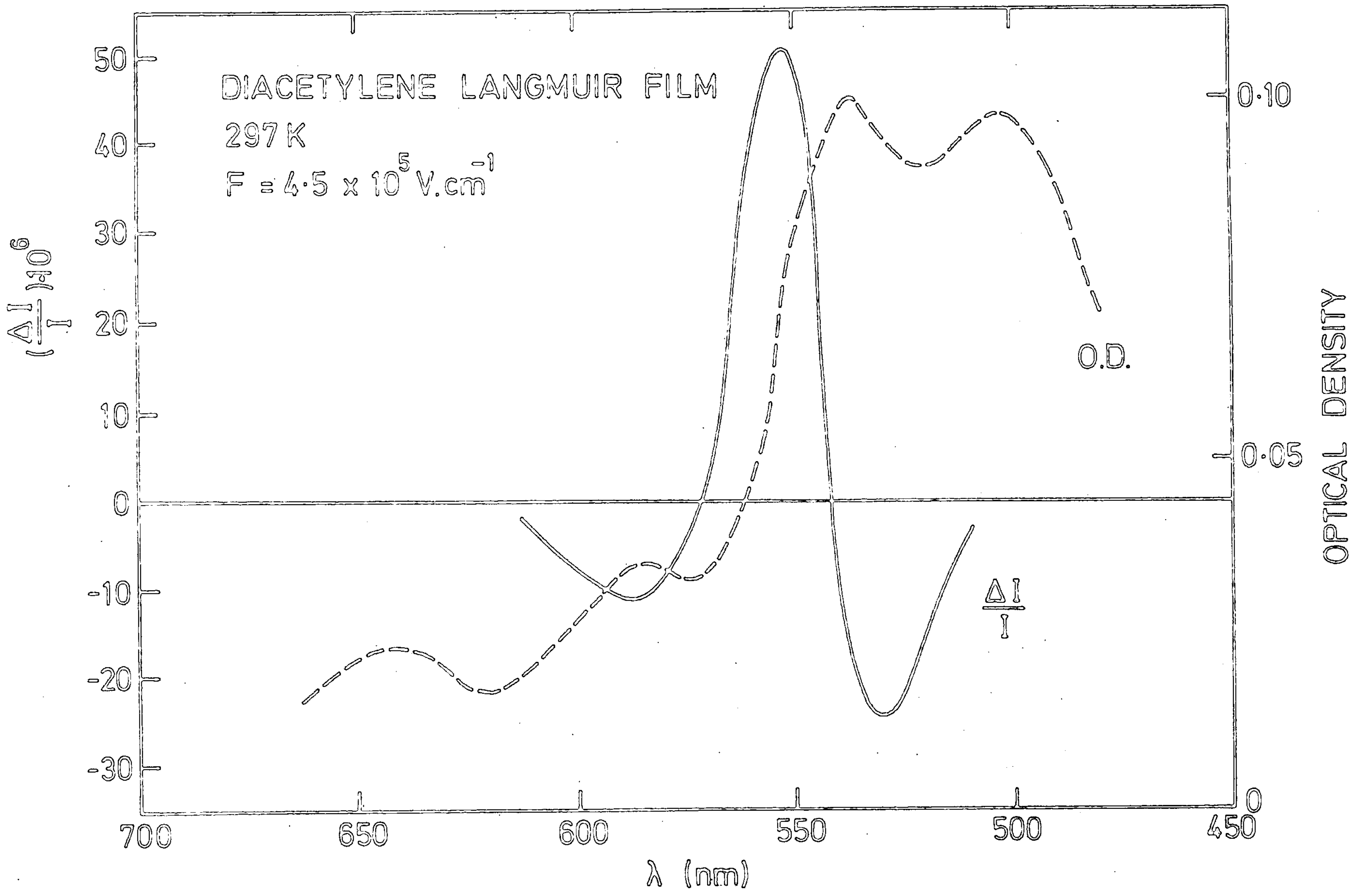

Figure 7.8 : Optical density and fractional change in the transmission of the red diacetylene polymer at 297 K, as a function of photon energy.

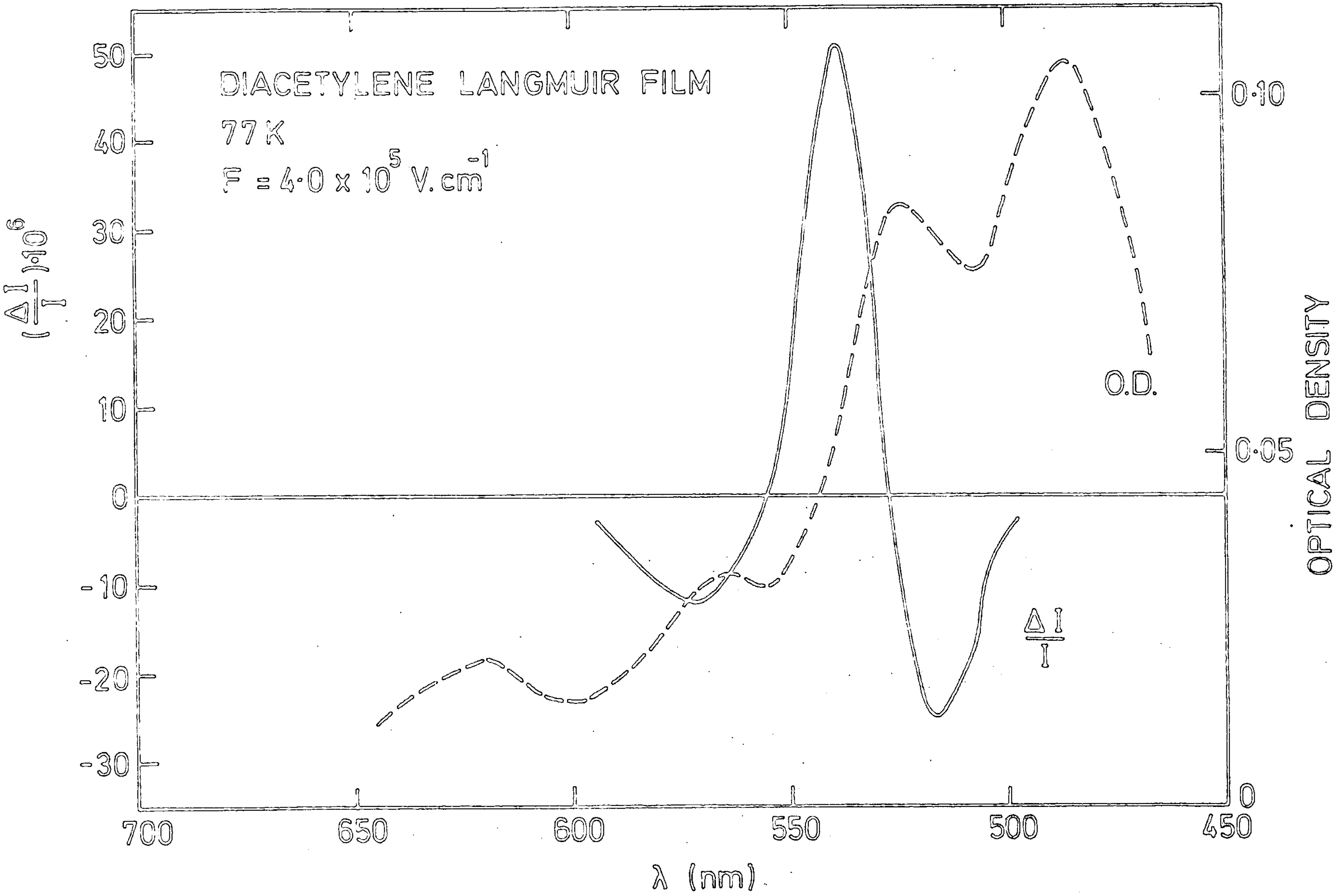

Figure 7.9 : Optical density and the fractional change in transmission of the red form of polymerised diacetylene Langmuir film at 77 K, as a function of photon energy.

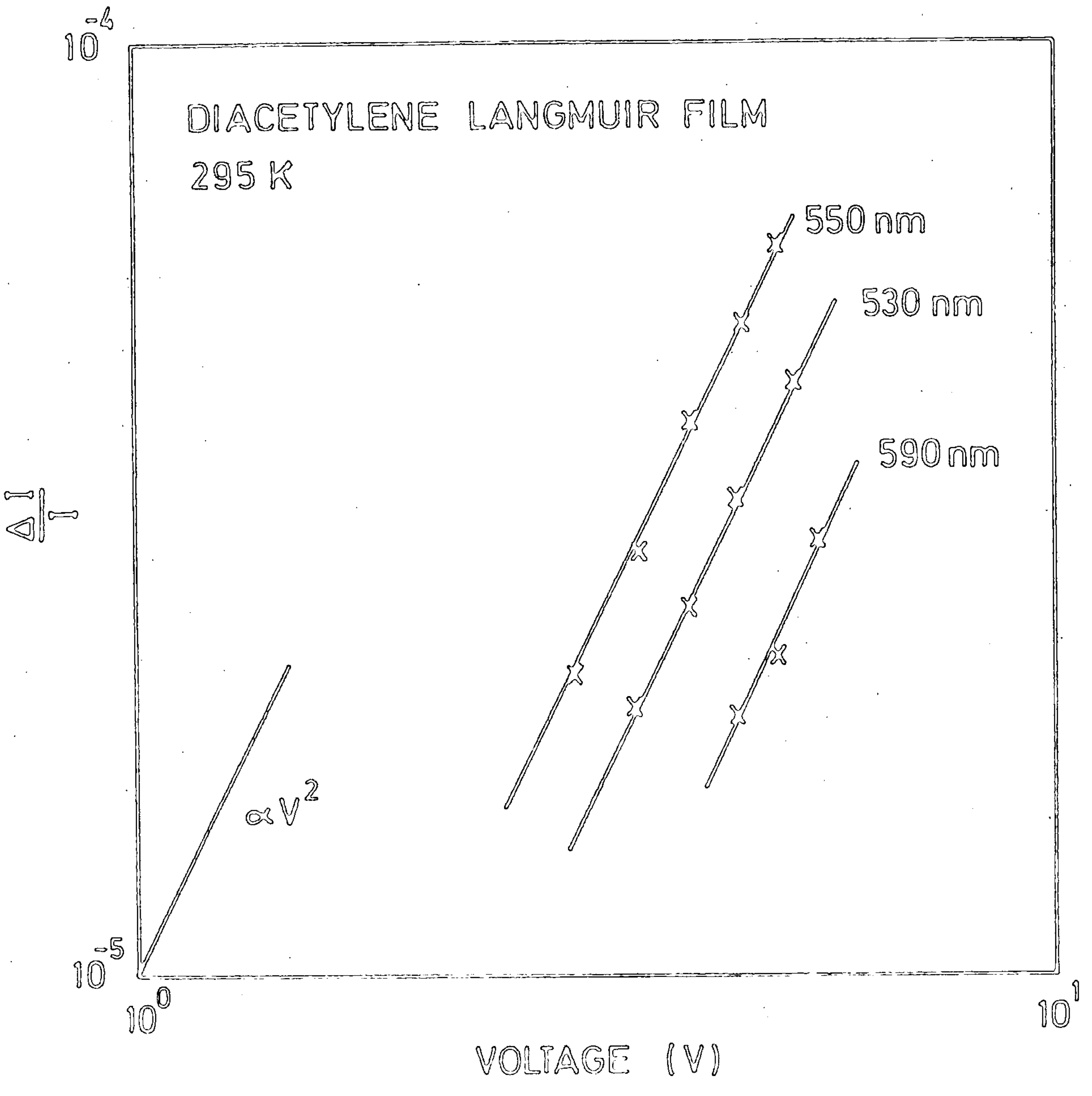

Figure 7.10 : Dependence of the fractional change in transmission of the red diacetylene polymer at 295 K on the applied voltage.

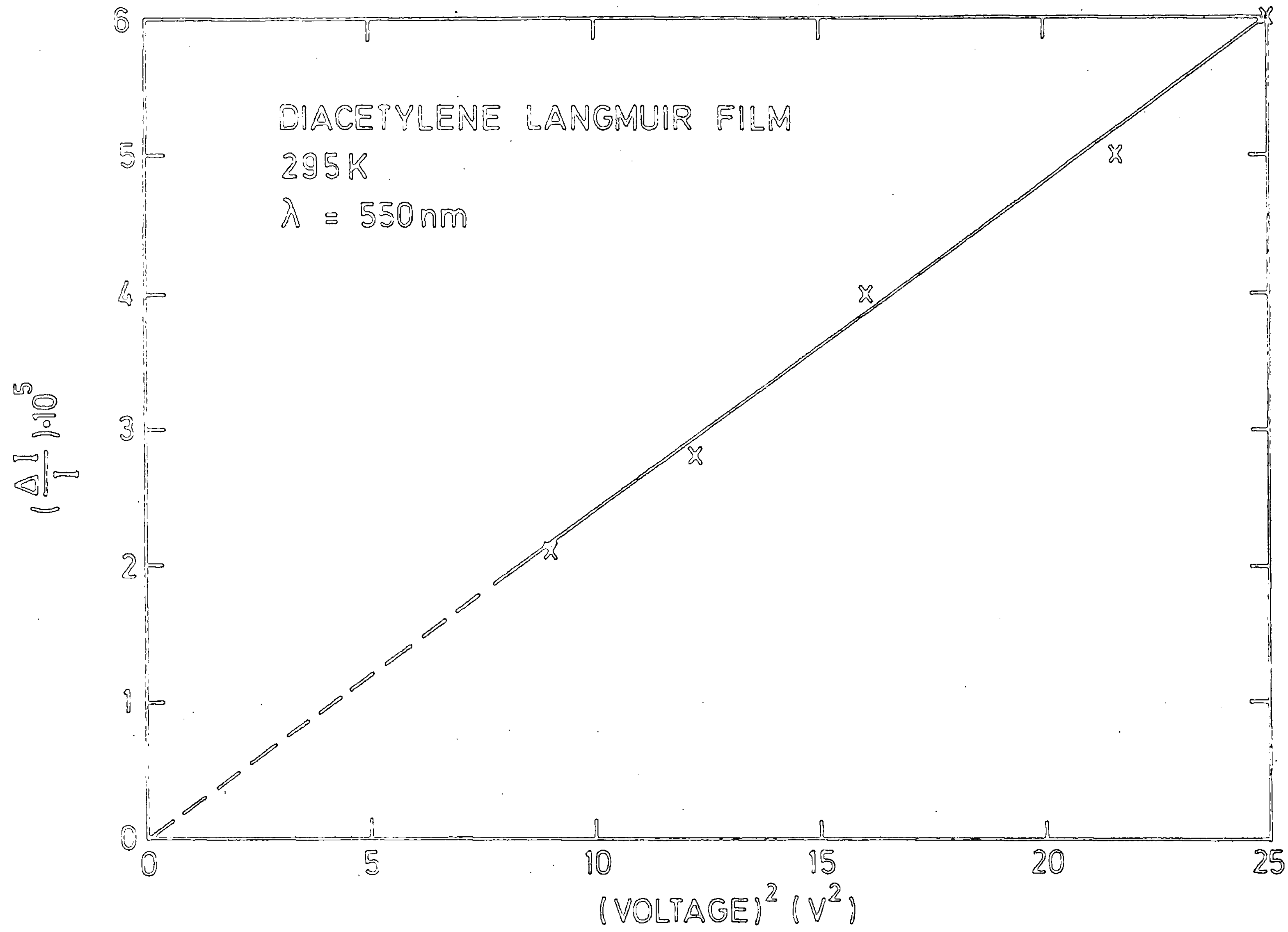

Figure 7.11 : Dependence of the fractional change in transmission of the red diacetylene polymer at 295 K on the applied voltage.

are delocalised along the chain as in an inorganic wide band semiconductor but strongly localised in the perpendicular direction similar to a conventional molecular crystal$^{(12)}$. However, our measurements indicate that the influence of an external electric field on the absorption of the polymerised Langmuir film is to produce the Stark effect. Even though the electroabsorption spectrum of the Langmuir film does not relate exactly to the first derivative of the corresponding absorption curve, the magnitude of the electroabsorption response is very small. This is a strong indication of the presence of the Stark effect. Further evidence that the Stark effect is observed is that a large reduced effective mass is obtained if one calculates its value within the framework of band to band type transitions.

The observed quadratic field dependence of the electroabsorption response indicates transitions from ground to excited states in this material which does not exhibit a permanent dipole moment. These data can therefore be used to calculate the difference in static polarizability, $\Delta\alpha$ between the excited and ground states of this material,as discussed in section 2.7.3. Using equation (2.51) and parameters appropriate to diacetylene Langmuir film, a value $\Delta\alpha = 36\ \mathring{A}^3$ is calculated. In view of the Lorentz correction involved in equation (2.51), this value is only approximate. However, it is in reasonable agreement$^{(16)}$ with estimates made of this parameter in other organic materials.

Attempts have also been made to determine the effect of polarized light upon the electroabsorption spectra. The spectra for two orthogonal directions of polarisation are shown in Fig 7.12. The resulting spectra are similar in shape, with the magnitude of the vertical polarisation being slightly larger than the corresponding spectrum for the horizontal polarisation. Geometrical considerations confirm the results of structural experiments showing that the diacetylene molecule and its associated side groups do not line up vertically with the substrate. If this were so, a

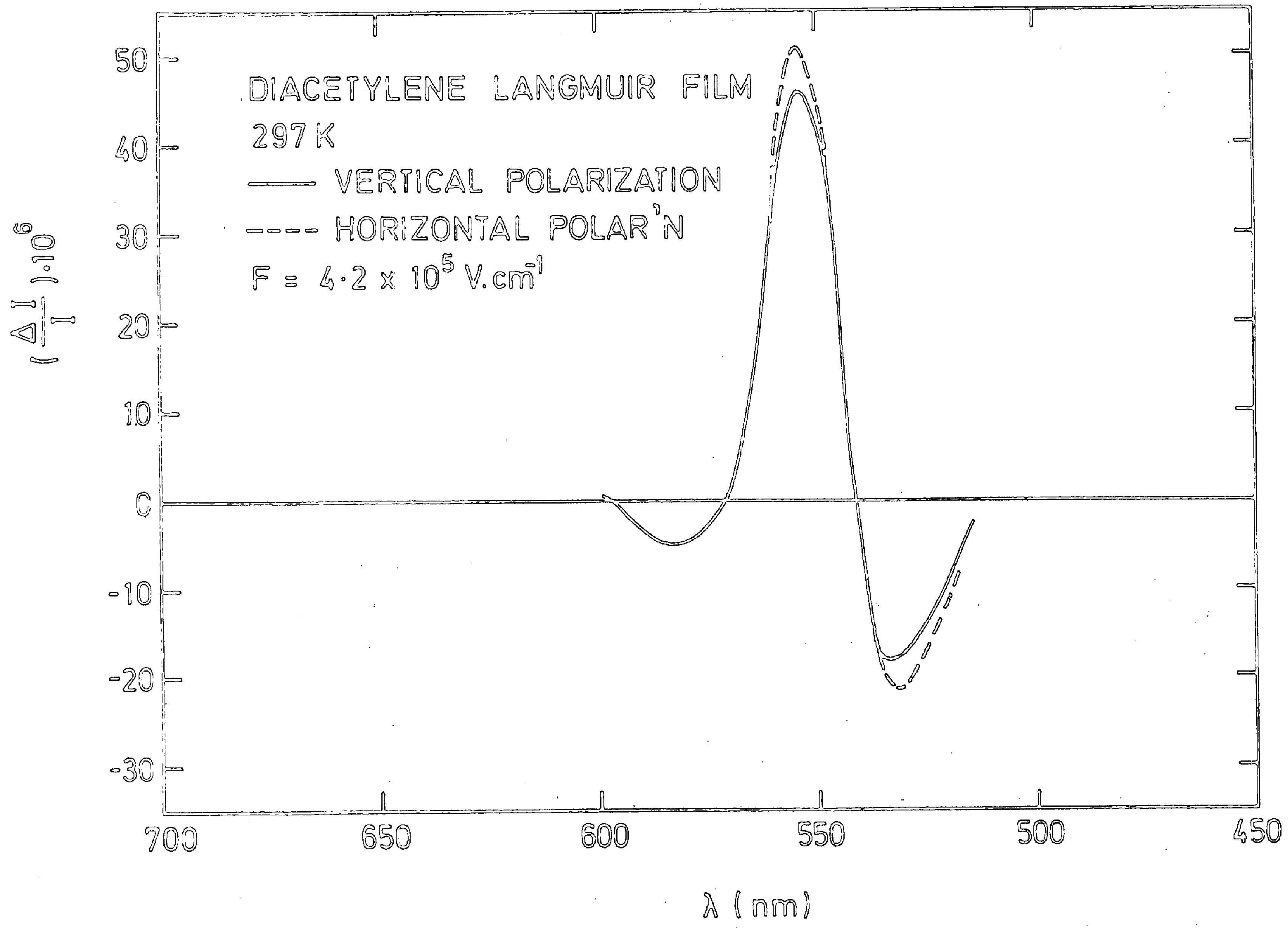

Figure 7.12 : Electroabsorption spectra of the red form of polymerised diacetylene Langmuir film at 295 K for vertical and horizontal polarisation of the incident light.

molecular size of approximately 3.6 nm would be measured. Experimental evidence suggests that the spacing between successive molecules is nearer 3.3 nm. This factor probably accounts for the small difference in the result obtained for different polarisation. That is, the anisotropy is not as large as might be expected if the side groups were vertical to the substrate. However, it is interesting to note that a large polarisation effect in polydiacetylene single crystal has been detected from electroreflectance measurements (12).

Time limitations prevented our undertaking a detailed investigation of other aspects of electroabsorption in diacetylene polymer films. Further experiments would be required on the blue form and on diacetylenes substituted with different side groups before a complete assessment can be made. However, these preliminary measurements indicate the value of the electroabsorption measurement in the study of organic material deposited using the Langmuir trough technique.

CHAPTER 8

CONCLUSIONS AND SUGGESTIONS FOR FURTHER WORK

8.1 INTRODUCTION

The main objective of this work has been to demonstrate the versatility of the electroabsorption technique. Various semi-insulators have been studied and the principal results obtained with each are summarized in this chapter. The investigation has also led to a new method for analysing optical absorption data when the applied electric field injects space charge into a specimen. Each of the following sub-sections deals with different aspects of the work and conclude with a discussion of how further experiments could clarify unresolved issues.

8.2 CADMIUM TELLURIDE

The principal aim of the electroabsorption study has been to determine the reduced effective mass of this II-VI compound. Other experiments such as infrared Faraday rotation and reflectance(1) and cyclotron resonance(2) had previously provided a value of 0.10 m_o for undoped single crystals ; the results of our data for semi-insulating crystals doped with chlorine were in good agreement. However, the average value of 0.105 m_o was only obtained after carefully controlling the experimental conditions. Our major conclusions concerning these particular experiments may be summarised as follows :

(1) Ohmic Contacts : D.C. and A.C. conductivity experiments are required to ensure that no barrier has been formed between the metal and semiconductor of the sandwich structures used in the electroabsorption measurements. Capacitance data have been useful in proving that the application of a voltage produces a uniform field distribution across the specimens.

(2) Frequency Dependence of the Electroabsorption Response : For particular semiconductors it is important to perform experiments

above a certain critical frequency. At lower frequencies (normally less than 1 kHz) we have proved that photogenerated carriers are responsible for producing a large spurious signal. This effect can also be monitored via a harmonic analysis of the electroabsorption spectrum. That is, a genuine response is detected at twice the frequency of the modulating field (second harmonic signal). However, a first harmonic signal can also exist due to an effective d.c. field produced by the crystal's photoconductivity. Further investigations, where both d.c. and a.c. fields were applied simultaneously have shown that, whereas the d.c. field has a negligible effect on the second harmonic signal, it produces drastic changes to the first harmonic signal.

(3) Field Dependence : A quadratic field dependence of the electroabsorption response has been observed in CdTe:Cl, If the measurements are performed in such a way as to eliminate contact and photoconductivity effects then the straight line graph of the change in absorption coefficient, $\Delta\alpha$ versus F^2, passes through the origin.

(4) Space Charge Effect : Current-voltage characteristics for semi-insulating CdTe:Cl display an Ohmic region followed by a Space Charge Limited Current (SCLC) region where $J \alpha V^2$. The measurements of the reduced effective mass m*, have initially been made in the linear J-V domain in order to avoid complications due to injected charge. However, with many semi-insulators, it is impossible to avoid space charge injection at the high fields required for electroabsorption and therefore it was thought to be useful if systematic experiments could be carried out in this region. Extensive investigations in the SCLC region have indicated that the amount of carrier injection decreases with increasing measuring frequency and is insignificant above a certain (typically ∿ 3 kHz) frequency. At this frequency the straight line graph of $\Delta\alpha$ versus F^2 indicating the quadratic field dependence of the electroabsorption response extrapolates to the origin. However, if similar plots were carried out at lower frequencies,

a family of straight lines was obtained which extrapolated to a focal point. Therefore, if one could not experimentally attain a high enough frequency to avoid space charge effects, one can assume that this focal point is a correct value, as is the origin. The gradient of a straight line connecting this focal point and the origin could thus be used to calculate m*. In the case of CdTe:Cl, excellent agreement has been obtained between the value of m* deduced in this way and that obtained in the Ohmic region.

Having established a procedure to cope with the complications of injected charge and photoconductivity, various other semi-insulators have been studied briefly. An attempt has been made to correlate the time constant corresponding to the frequency at which the space charge is just compensated with other parameters that characterise the specimens under study. Preliminary results have indicated that the depth of impurity levels are probably related to the time constants measured for these crystals.

These experiments on CdTe:Cl firmly establish electroabsorption as a reliable technique to measure the reduced effective mass of semiconductors compensated with deep trapping centres in order to make them more insulating. The focal point observed in the plot of the change is absorption, $\Delta\alpha$, versus F^2 is worthy of further theoretical study.

8.3 SEMICONDUCTOR ALLOY SYSTEM $Cd_xZn_{1-x}S$

The electroabsorption technique has never been used previously to measure the reduced effective mass as a function of alloy composition. Single crystals of CdS and ZnS have been used in our experiment. In the previous sub-section we have summarized our results for another II-VI semiconductor CdTe and mentioned how the Franz-Keldysh effect could be used to determine the reduced effective mass. Both CdS and ZnS have rich excitonic spectra and therefore this provided an opportunity to display another use of the electroabsorption technique. The results in this case have been interpreted in terms of the Stark effect which has enabled the energy position of the lowest bound exciton states to be precisely located, thus allowing the determination of the reduced effective masses of the excitons in the two semiconductors and their alloys. The effective mass, as predicted theoretically, has been found to vary linearly with the energy gap of the material.

A great degree of attention has been paid recently to ternary and quaternary alloys of III-V and II-VI compounds ; the band gap and lattice constants of these materials can both be controlled according to composition, a facility that provides considerable potential for opto-electronic devices. Accordingly, it would be interesting and very useful to follow the variation of the reduced effective mass as a function of the energy gap in these materials using the electroabsorption technique.

For example, the energy gap of the $Cd_xHg_{1-x}Te$ alloy system varies between -0.02 eV for HgTe and 1.5 eV for CdTe, a useful range for infrared detectors. For electroabsorption measurements it would be necessary to grow epilayers of $Cd_xHg_{1-x}Te$ on relatively conducting substrates so that all the field is dropped across the ternary. In view of the small energy gap, it would also be essential to cool the samples during the electroabsorption measurements. Another important alloy system is $Ga_xIn_{1-x}As_yP_{1-y}$. This quaternary system can be deposited on conducting InP crystals and is very useful in laser devices. It would be particularly useful to look at the variation of the effective mass with band gap in this system to see whether the interesting conducting band structure of the end members is retained in the quaternary alloys.

8.4 AMORPHOUS SILICON

Amorphous silicon is believed to have considerable potential as a low cost material in a variety of electronic applications. A major problem is likely to be the attainment of reproducible material on which to fabricate these devices. Electroabsorption provides a technique for monitoring the subtle differences that occur between films prepared under different conditions. The results of the electroabsorption studies of α-Si carried out in this work may be summarised as follows :

(1) The electroabsorption spectrum has indicated that only transitions involving localized states can respond to electric field modulation. This has enabled us to determine the energy where the onset of delocalisation occurs.

(2) The electroabsorption response may be attributed to the Stark effect.

(3) Careful investigation of the electroabsorption response has shown that, whereas a quadratic field dependence has been observed for sputtered films, a change in absorption coefficient, $\Delta\alpha$, proportional to F^n (where the value of n depends on the photon energy considered) has been seen for glow discharge produced films. In the latter case a value of n equal to 2.0 has been obtained only at the peak of the electroabsorption spectrum and decreased with decreasing photon energy in the low energy règime of the spectrum. Measurements at lower temperatures have indicated that a larger decrease in the value of n occurred resulting in a larger temperature coefficient of the energy shift $\frac{\Delta E}{\Delta T}$, for smaller values of n (< 2). For example a value of $\frac{\Delta E}{\Delta T}$, $\sim 5.0 \times 10^{-4}$ eV.K^{-1} is obtained at n = 1.7 as compared to only $\sim 3.2 \times 10^{-4}$ eV.K^{-1} for n = 2 at the peak of the electroabsorption spectrum. Two possible mechanisms have been suggested to explain the effect ; one based purely on the Stark effect and the other on a combined Franz-Keldysh and Stark picture. It is interesting to note that Spear et al(3) have reported a large temperature coefficient of the energy position where the onset of photoconduction occurs in glow discharge produced α-Si. They have attributed the temperature coefficient to a change in the position of the mobility edge with temperature. However, theoreticians are not convinced of their interpretation but our experimental evidence seems to confirm that an effect occurs which is at least formally equivalent to an

effective change in the mobility edge with temperature.

Electroabsorption measurements coupled with surface analytical techniques on samples prepared under different conditions, in particular at different substrate temperature T_d, will probably eventually reveal the mechanism responsible for the effect mentioned above. The degree of band tailing in amorphous semi-conductors can also be learnt from electroabsorption experiments. It would therefore be useful to extend these current measurements to disordered films of a variety of materials produced in different ways.

8.5 DIACETYLENE LANGMUIR FILM

Organic layers which are well ordered and structurally stable can be prepared using the Langmuir-Blodgett technique. The thinness and high dielectric strength of these films are well suited to electroabsorption experiments. The diacetylene compound we have investigated possesses an interesting feature. It can be polymerised to produce blue and red forms which are more stable chemically than the monomer. Due to time constraints it was only possible to carry out a preliminary study of the red form. The main conclusions reached this far are :

(1) The observed change in the absorption coefficient is extremely small (one part in 10^5 for a field strength of 10^5 V.cm^{-1}) and is attributed to the quadratic Stark effect.

(2) The change in static polarizability $\Delta\alpha$, between the excited and ground states of the molecule has been calculated to be 36 Å^3 which is in reasonable agreement with estimates made for the same parameter in other organic materials.

The optical properties of the polymerised diacetylene films depend somewhat on the exposure time during the u.v. polymerisation process. In addition, side groups of the polymer chain have considerable influence on their optical and electrical properties. Further experiments would therefore be required on the blue form and on diacetylenes substituted with different side groups before a complete assessment could be made.

8.6 SUMMARY OF APPLICATIONS OF ELECTROABSORPTION TECHNIQUE

Much work has already been published in the electroabsorption field and different experimental and theoretical groups have made notable contributions during the past twenty years. In this investigation an attempt has been made to put the technique on a sound experimental footing and to show the wide range of areas where it can be useful. The thesis therefore concludes with a list of general applications of electroabsorption experiments.

(1) Electroabsorption is a very powerful experimental tool in obtaining information concerning singularities in the energy band structure and phonon spectra of semi-insulating solids. Being a differential technique the features are better resolved than in a corresponding absorption spectrum.

(2) The technique can be used to detect the presence of small quantities of impurities in semiconductors and enables an analysis of the impurity state symmetry to be performed.

(3) The detection of the Franz-Keldysh effect using the electroabsorption technique provides a reliable method for the determination of the reduced effective mass in semi-insulators.

(4) The technique can be used to detect the exciton spectrum in semi-insulating inorganic solids which allows the energy position of the lowest bound exciton state to be located precisely. The exciton electroabsorption which is interpreted in terms of the Stark effect can be used to calculate the reduced effective mass of the exciton.

(5) The technique provides a sensitive method for studying the structure and reproducibility of organic and inorganic thin films. For example, structure due to the intrinsic disorder in the films can be separated from other features in the spectrum.

(6) An investigation of band tailing effect in inorganic solids may be performed using the electroabsorption technique. This is achieved by looking at the field dependence of the electroabsorption signal as a function of

photon energy as demonstrated in Chapter 6 for amorphous silicon.

(7) Electroabsorption experiments are an extremely sensitive method for detecting the Stark effect in organic materials with a consequent evaluation of the change in the static polarizability of the molecular crystals.

It is to be hoped that electroabsorption will eventually become a standard tool for the study of solids. It is relatively inexpensive to assemble the required equipment and provided precautions are taken, the benefits available are large.

References to Chapter 1

1. J. Stark, Ann. d. Phys. 43 (1919) p 965.

2. A. Lo Surdo, Accad.Lincei Atti 22 (1913) p 665.

3. W. Franz, Z. Naturforsch 13a (1958) p 484.

4. L. W. Keldysh, Sov.Phys. JEPT 7 (1958) p 788.

REFERENCES TO CHAPTER 2

1. T.S.Moss, 'Optical Properties of Semiconductors', Butterworth Publication (1959) p 36.

2. H.Y.Fan, M.L.Shepherd and W. Spitzer, Photoconductivity Conf., Wiley New York (1954/56).

3. G.G.Macfarlane, T.P.McLean, J.E.Quarrington and V.Roberts, J. Phys. Chem. Solids, 8 (1959) p 390.

4. J. Frenkel, Phys.Rev. 37 (1931) p 1276.

5. G. Wannier, Phys.Rev. 52 (1937) p 191.

6. P.W. Baumeister, Phys.Rev. 121 (1961) p 359.

7. R.Elliott, Phys. Rev. 108 (1957) p 1384.

8. R.S.Knox, 'Theory of Exciton', Solid State Physics, Suppl.5 (1963).

9. J.O.Dimmock, 'Semiconductors and Semimetals', 3 (1967) p 259.

10. F. Urbach, Phys.Rev. 92 (1952) p 1324.

11. F.Stern and J.Dixon, J.Appl.Phys. 30 (1959) p 268.
J. Tauc, Materials Rev. Bull. 5 (1970) p 721.

12. D. Redfield, Phys. Rev.130 (1963) p 916,
140 (1965) A2056.

13. D.L.Dexter, Phys.Rev. Letts. 19 (1967) p 383.

14. J.Dow and D.Redfield, Phys.Rev. B 5 (1972) p 594.

15. G.G.Roberts, S.Tutihasi and R.C.Keezer, Phys.Rev. 166 (1968) p 637.

16. N.F.Mott and E.A.Davis, 'Electronic Processes in Non-crystalline Materials', Clarendon Press, Oxford (1979) p 288.

17. H.P.D. Lanyon, Phys. Rev. 130 (1963) p 134.

18. E.A.Davis and N.F.Mott, Phil.Mag. 22 (1970) p 903.

19. R.A.Street, T.M.Searle, I.G.Austin and R.S.Sussmann, J.Phys.C: Solid State Physics 7 (1974) p 1582.

20. J.Tauc and A.Menth, J.Non-Cryst.Solids 8-10 (1972) p 569.

21. A.Terenin in H.Kallman and M.Silver (Ed) ' Sympos.on Electrical Conductivity in Organic Solids' Durham N.C.(Interscience N.Y.1961).

22. W.Franz, Z. Naturforsch 13a (1958) p 484.

23. L.W.Keldysh, Sov.Phys. JEPT 7 (1958) p 788.

24. C. Zener, Hippel Z. Physik, 67 (1931) p 707,
68 (1931) p 39.

25. K. Tharmalingham, Phys. Rev. 130 (1963) p 2204.

26. C.M.Penchina, Phys. Rev. 138 (1965) A924.

27. J. Callaway, Phys. Rev. 130 (1963) p 549.

28. T.S.Moss, J.Appl.Phys: Suppl to V32(1961) p 2139.

29. J.Calloway, Phys. Rev. 134 (1964) A998.

30. D.E.Aspnes, Phys.Rev. 147 (1966) p 554.

31. D.E.Aspnes, Phys.Rev. 153 (1967) p 972.

32. J.C.Philips, B.O.Seraphin, Phys.Rev.Letts, 15 3 (1965).

33. D.E.Aspnes, P.Hadler and D.F.Blossey, Phys. Rev. 166 (1968) p 921.

34. Y. Hamakawa, F.A.Germano and P.Hadler, Phys. Rev. 167 (1968) p 703.

35. J.Stark. Ann.d.Phys. 43 (1919) p 965.

36. C.B.Duke and M.E.Alferieff, Phys. Rev. 145 (1966) p 583.

37. H.I.Ralph, J.Phys. C : Solid State Phys. 1 (1968) p 378.

38. J.D.Dow and D.Redfield, Phys. Rev. B 1 (1970) p 3358.

39. R. Enderlein, Phys. Stat.Sol. 26 (1968) p 509.

40. D.F.Blossey, Phys. Rev. B2 (1970) p 3976.

41. D.F.Blossey, Phys. Rev. B3 (1971)p 1382.

42. A.L. Surdo, Accad.Lincei Atti 22 (1913) p 665.
J.Stark, Ann.d.Phys. 43 (1919) p 965.

43. L. Pauling and E.Wilson, 'Intro. to Quantum Mechanics'
McGraw-Hill, N.Y.(1935).

44. L. I.Schiff, 'Quantum Mechanics', MgCraw-Hill.

45. R.M.Hochstrasser ; Acc.Chem.Research 6 (1973) p 263.

46. W.Liptay, 'Modern Quantum Chemistry', Vol.3,Academic Press, N.Y.(1965)

47. D.L.Dexter, Nuovo Cim 7 (1958) p 245.

48. Y.Toyozawa, Prog.Theor.Phys. 12 (1959) p 111.

REFERENCES TO CHAPTER 3

1. M. McGinnity, Ph.D. Thesis (1979) Durham University.

2. J.I.Polanco, G.G.Roberts and M.B. Myers, Phil.Mag. 25 (1971) p 117.

References to Chapter 4

1. B. Lunn and V. Bettridge, Rev. Phys. App. 12 (1977) p 151.

2. D. De Nobel, Philips Res.Repts 14 (1959) p 361 and 430.

3. W. G. Pfann, J. Metals, N.Y. 4 (1952) p 747.

4. N.V. Agrinskaya and O.A. Matveev, Sov.Phys. Semicond. 10 No.1 (1976) p 96.

5. C. Kittel in "Introduction to Solid State Physics". Wiley, New York (1967).

6. M.G.Williams, R.D. Tomlinson, M.J.Hampshire, Solid State Commun. 7 (1969) p 1831.

7. G.F.J.Garlick, T.M.Hough and R.A.Fatehally, Proc.Phys. Soc. London 72 (1958) p 925.

8. D.T.F. Marple, Phys. Rev. 150 (1966) p 728-

9. M.L.Cohen and J.K.Bergstrasser, Phys. Rev. 141 (1966) p.789.

10. J. Chelikowsky and M.L.Cohen, Phys. Rev. B14 (1976)p 556.

11. B. Segall, Phys. Rev. 150 (1966) p 734.

12. J.L.Freeouf, Phys. Rev. B 7 (1973) p 3810.

13. D.G.Thomas, J.Appl. Phys. 32 (Supp) (1961) p 2298.

14. E.J.Danielewicz and P.D.Coleman, Appl.Opt. 13 (1974) p 1164.

15. A.J.Strauss, Rev.Phys. Appl. T12, No.2 (1977) p 167.

16. Y.F.Tsay, S.S.Mitra and J.F. Vetelino, J.Phys. Chem.Solids, 34 (1973) p 2167.

17. K.K.Kanazawa and F.C.Brown, Phys. Rev. 135 (1964) A1757.

18. B. Segall and D.T.F. Marple in "Physics and Chemistry of II-VI Compounds" Edited by M.Aven and J.S. Prener (1967) Wiley, N.York, p 317.

19. D.L. Rode, Phys. Rev. B 2 (1970) p 4036.

20. R. Triboulet and Y.Marfaing, J. Electrochem. Soc. 120 (1973) p 1260.

21. P. Höschl, P. Moravec, A. Martinaitis and A. Skalas, Phys.Stat. Sol. (a) 48 (1978) K43.

22. N.V. Agrinskaya and O.A.Matveev, Sov.Phys. Semicond. 12 (2) (1977) p 187.

23. A.J.Strauss, Rev.Phys.Appl.12 (1977) p 167.

24. M.V.Alekseenko, E.N.Arkadeva, V.S.Kisilenko, L.V.Maslova, O.A.Matveev, S.P.Prokof'ev, S.M.Ryvkin and A.Kh. Khusainov, Fiz. Tekh.Poluprov, 8 (1974) p 550 (Sov.Phys.Semicond. 8 (1974) p351).

25. J.Gu, T.Kitahara, K.Kawakami and T.Sakaguchi, J.Appl.Phys. 46 (1975) p 1184.

26. M.C.Petty, I.M.Dharmadasa and G.G.Roberts, J.Phys.D.Appl.Phys. 13 (1980) p 1899.

27. P.S. Kareev, N.N.Orlova, V.N.Saurin and L.N.Strel'tsov, Fiz. Tv. Tela. 7 (1965) p 1271.

28. L.N. Strel'fsov and L.I.Verbitskaya, Neorganichaskie Materialy 4 (4) (1968) p 618.

29. G.A.Babonas, E.Z. Krivaite, A.Y. Raudonis and A.J.Shilieka, Institute of Semicond.Phys. (Conf. 1968 on Semiconductor) p 400.

30. Yu. N. Berozashrili, A.V. Dundua and D. Sh. Lordkipanidze, ShETF. Pis.Red. 15(2) (1972) p 95.

31. R.M.Akopyan, Yu.N. Berozashvili, A.V.Dundua and D.Sh.Lordkipanidze, Zh.Eksp.Teor.Fiz. 65 (1973) p 2007.

32. E.Lorentz, F.T.Novik and O.A.Trofimov, Fiz. Tekh.Poluprovodn, 10 (1976) p 549.

33. G.Neu, Y. Marfaing, R.Triboulet and M.Escorne, Rev.Phys. Appl. 12 (1977) p 263.

34. G.G.Roberts and F.W.Schmidlin, Phys. Rev. 180 (1969) p 785.

35. C. Canali, M.A.Nicolet and J.W.Meyer, Solid Stat.Electronics, 18 (1975) p 871.

36. K.P.Pande and G.G.Roberts, IEEE Trans. Nucl. Sci. NS-24 (1977) p 2017.

37. A.Zoul and E.Klier, Czech. J.Phys. B 27 (1977) p 789.

References to Chapter 5

1. C.B.Duke and M.E.Alferieff, Phys.Rev.145 (1966) p 583.

   C.B.Duke, Phys.Rev.Letters 15 (1965) p 625.

2. S. Oktik, G.J.Russell and J.Woods, (To be published in Solar Cell).

3. R.Hill, Royal.Soc.Conf.(C21) U.K.Section of the International Solar Energy Soc.(1980) p 25.

4. L. Clark and J.Woods, J.Crystal Growth 314 (1968) p 126.

5. K.F.Burr and J.Woods, J.Crystal Growth 9 (1971) p 183.

6. B.Ray, "II-VI Compounds", Pergamon Press (1969).

7. T.K.Bergstresser and M.L.Cohen, Phys.Rev.164 (1967). p 1069.

8. P.Eckett, O.Madelung and J.Treusch, Phys.Rev.Letters 18 (1967) p 656.

9. M.L.Cohen and T.K.Bergstresser, Phys.Rev. 141 (1966) p 789.

10. D.C.Reynolds, C.W.Litton and T.C.Collins, Phys.Stat.Sol.9 (1965)p 645.

    D.C.Reynolds, C. W.Litton and T.C.Collins, Phys.Stat.Sol.12 (1965) p 3.

11. F.A.Junga, K.F.Cuff and R.B.Horst, Bull.Am.Soc.Phys. 11 (5) (1966) p 754.

12. E.A.Davis and E.L.Lind, J.Phys.Chem.Solids 29 (1968) p 79.

13. M.S.Brodin, M.V.Kurik and N.I.Vitrikhovskii, Proc.Int.Conf. on the Phys. of Semicond.Kyoto (1966) p 127.

    J.Phys. Soc. Japan, 21 Suppl. (1966).

14. D.G.Thomas and J.J.Hopfield, Phys.Rev. 116 (1959) p 573.

15. T.S.Moss "Optical Properties of Semiconductor", Butterworth Pub, (1959) p 215,220.

16. C.K.Coogan, Proc.Phys.Soc.London, 70 (1957) p 845.

17. D.C.Reynolds, S.J.Czyzak, R.C.Allen and C.C.Reynolds, J.Opt.Soc. Amer. 45 (1955) p 136.

18. S.J.Czyzak, W.M.Baker, R.C.Crance and J.B.Howe, J.Opt.Soc.Amer. 47 (1957) p 240.

19. B.Segall and D.T.F.Marple, "Physics and Chemistry of II-VI Compounds", (M.Aven and J.S.Prener, Eds) North Holland (1967).

20. H.Yoshinaga, Phys.Rev. 100 (1955) p 753.

21. R.E.Drews, E.A.Davis and A.Leiga, Phys.Rev.Lett. 18 (1967) p 1194.

22. W.E.Spear and J.Mort, J.Proc.Phys.Soc. 81 (1963) p 130.

23. M.Fugita et al, J.Phys. Soc.Japan 20 (1965) p 109.

24. M.Aven and C.A.Mead, Appl.Phys. Lett. 7 (1965) p 8.

25. K.W.Boer, H-J.Hansch and U.K.Kummel,Naturwissenschaften 45 (1958) p 450. p 460.

26. K.W.Boer,Z.Phys. 155 (1959) p 184.

27. K.W.Boer, H-J.Hansch and U.K.Kummel, Z.Physik 155, p 170.

28. K.W.Boer and R.Rompe, Ann.Phys. 5 (1960) p 200.

29. R.Williams, Phys.Rev. 117 (1960) p 1487.

30. E. Gutsche and H.Lange, Phys.Stat.Solidi 4 (1964) K21.

31. E.Gutsche and H.Lange, Phys.Stat.Solidi 13 (1966) K131.

32. B.B.Snavely, Solid. Stat. Commun. 4 (1966) p 561.

33. B.B.Snavely, Phys.Rev. 167 (1968) p 730.

34. Nobugasu Hase and Masami Onuki, J.Phys.Soc.Japan 28 (1970) p 956.

35. E. Gutsche and H. Lange, Phys.Stat.Sol. 32 (1969) p 293.

36. R. Damaskova and K. Patek, Z.Physik, 164 (1961) p 428.

37. G. Shachar, Y.Brada, E.Alexander and Y.Yacobi, J.Appl.Phys.41 (1970) p 723.

38. Y.Brada, I.T.Steinberger and B.Stone, Phys.Letters 38A (1972) p 263.

39. B.G. Yacobi and Y.Brada, Phys.Rev.B 10 (1974) p 665.

40. N.Hemmatt and M.Weinstein, J.Electrochem. Soc. 114 (1967) p 851.

41. D.F.Blossey, Phys.Rev. B2 (1970) p 3976.

42. M.V.Kurik, Physics Lett. 24A (1967) p 742.

References to Chapter 6

1. D.E.Carlson and C.R.Wronski, Appl.Phys.Lett. 28 (1976) p 671.
2. D.E.Carlson and C.R.Wronski, J.Electron.Mater. 6 (1977) p 95.
3. S.K.Bahl and S.M.Bhaget,J. Non-cryst.Solids 17 (1975) p 409.
4. W.Paul, G.A.N. Connell and R.J.Temkin, Adv.Phys. 22 (1973) p 531.
5. W.Paul, A.J.Lewis, G.A.N.Connell and T.D.Moustakas, Solid.Stat. Commun. 20 (1976) p 969.
6. R.C.Chittick, J.H. Alexander and H.F.Sterling, J.Electrochem.Soc. 116 (1969) p 77.
7. P.G. Le Comber, A. Madan and W.E.Spear, J.Non-cryst.Solids, 11 (1972) p 219.
8. W.E.Spear and P.G.Le Comber, Solid.Stat.Commun.17 (1975) p 1193 ; Phil.Mag. 33 (1976) p 935.
9. D.E.Polk, J.Non-cryst.Solids. 5 (1971) p 365.
10. W.E.Spear, Proceedings of 5th Conf. on Amorphous and Liquid Semiconductor, Garmisch (1973) p 1.
11. N.F.Mott and E.A.Davis in 'Electronic Process in Non-Crystalline Material', Clarendon Press, Oxf (1979) p 366.
12. J. Stuke, Proceedings of 7th Conf.on Amorphous and Liquid Semiconductors, Edinburgh (1977) Ed. W.E.Spear, p 406.
13. P.A.Thomas, M.H. Brodsky, D.Kaplan, D. Lepine, Phys.Rev. B 18 (1978) p 3058.
14. D. Kaplan, Physics of Semiconductors 1978 : Inst.Phys. Conf. Ser. No. 43, p 1129.
15. D. Adler, Phys.Rev. Lett. 41 (1978) p 1755.
16. W. Beyer and J. Stuke, Proceedings of 5th Conf. on Amorphous and Liquid Semiconductors, Garmisch (1973) Ed. W.E.Spear, p 251.

17. P.G.Le Comber and W.E.Spear, Phys.Rev.Lett 25 (1970) p 509.

18. W. E. Spear, D. Allan, P. LeComber and A. Ghaith, Phil. Mag. B 41 (1980) p.419.

19. P.G.Le Comber, W.E.Spear and R.A.Vaughan, Proceedings of 5th Conf. on Amorphous and Liquid Semiconductors, Garmisch (1973), Ed. W.E.Spear, p 245.

20. D. Engemann and R.Fischer, Proceedings of 5th Conf.on Amorphous and Liquid Semiconductors, Garmisch (1973) Ed. W.E.Spear, p 947.

21. E.C.Freeman, D.A.Anderson and W.Paul, Bull. Am.Phys.Soc. 24 (1979) p 399.

22. H. Okamoto, Y. Nitta, T. Adachi and Y. Hamakawa, Surface Sci.86 (1979) p 486.

23. D.E.Aspnes and J.E.Rowe, Phys.Rev.Lett. 26 (1971) p 1429.

24. S. Al.Jalali and G.Weiser, J.Non-cryst. Solids, 41 (1980) p 1.

25. G.G.Roberts, B.S.Keating and A.V.Shelley, J.Phys. C:Solid State Phys. 7 (1974) p 1595.

26. S.G.Tomlin, Brit.J.Appl.Phys. (D) 2, 1 (1968) p 1667.

27. R.S. Sussmann, B.T.Debney and R.S.Walker, Plessey Report on Amorphous Silicon Solar Cells, (1979) p 6.

28. B. Esser, Phys.Stat.Sol.(b) 51 (1972) p 735.

29. V.C.Bonch Bruevich, Phys.Stat.Sol.42 (1970) p 35.

30. J.D.Dow and D.Redfield, Phys.Rev. B1 (1970) p 3358.

31. J.D.Dow and D.Redfield, Phys.Rev. B5 (1972) p 594.

32. R.A.Street, T.M.Searle, I.G.Austin and R.S.Sussmann, J.Phys. C : Solid St.Phys. 7 (1974) p 1582.

33. R.S.Sussmann, I.G.Austin and T.M.Searle, J.Phys. C: Solid St.Phys 8 (1975) L182.

34. G.A.N.Connell and J.R.Pawlik, Phys.Rev.B 13 (1976) p 787.

References to Chapter 7

1. G.G. Roberts, K.P. Pande and W.A.Barlow, Solid St. Elect.Devices 2 (1978) p 1969.
2. I.M. Dharmadasa, G.G.Roberts and M.C.Petty, Electronics Letts.16 (1980) p201.
3. P.S.Vincett and G.G. Roberts, Thin Solid Films, 68 (1980), p 135.
4. K.K. Kan, M.C. Petty and G.G. Roberts, Proc.Raleigh Conf.on the Physics of MOS Insulators (Pergamon, New York, 1980), p 344.
5. G.L. Gaines in 'Insoluble Monolayers at Liquid Gas Interface' Interscience, New York (1966).
6. G. G. Roberts, T.M. McGinnity, W.A.Barlow and P.S.Vincett, Thin Solid Films 68 (1980) p 223.
7. V. Enkelmann, R.J. Leyner and G. Wegner, Makromol Chem.7 (1979) p 180.
8. B. Tieke, G. Leiser and G. Wegner, J. Polymer Sci : Polymer Chem. Edition, 17 (1979) p 1631.
9. R.M.Handy and L.C.Scala, J. Electrochem Soc. 113 (1966) p 109.
10. M.H.Nathoo and A.K.Jonscher, J. Phys. C. 4 (1971) p L301.
11. B. Mann and H. Kuhn, J.Appl.Phys. 42 (1971) p 4398.
12. L. Sebastian and G. Weiser, Chem.Phys.Letters 64 (1979) p 396.
13. G. Wegner, Pure and Appl.Chem. 49 (1977) p 443.
14. H. Eichele, M. Schwoerer, R. Huber and D. Bloor, Chem.Phys.Letters 42 (1976) p 342.
15. G. V. Stevens and D. Bloor, Chem.Phys.Letters 40 (1976) p 37.
16. C. Cojan, G.P.Agrawal and C. Flytzanis, Phys.Rev. B 15 (1977)p909.
    M.A. Kurzmack and M.M. Malley, Chem.Phys. Lett. 21 (1973)p 385.

References to Chapter 8

1. D.T.F. Marple, Phys.Rev. 129 (1963) p 2466.

2. K. K. Kanazawa, and F.C. Brown, Phys.Rev. 135 (1964) p A1757.

3. W. E. Spear, D. Allan, P. LeComber and A. Ghaith, Phil. Mag. B 41 (1980) p.419.